The Occurrence, Distribution, and Concentration levels of Critical Raw Materials from the Coal Discard of the Witbank Coalfield.

School of Chemical and Metallurgical Engineering

Xolisa Nkwamza

A dissertation submitted in fulfilment of the requirements for the degree of Masters of Sciences in Chemical Engineering at the University of the Witwatersrand University, South Africa.

Supervisor: Dr N. Malumbazo

June 2025

Declaration

I, Xolisa Nkwamza, hereby declare that the dissertation titled: “The occurrence, distribution, and concentration levels of critical raw materials from coal discards of the Witbank coalfield”, submitted in fulfillment for a Master of Sciences degree in Chemical Engineering (MSc. Eng) at the University of Witwatersrand, is my own work, unless specified otherwise, and this dissertation has not been submitted for an equivalent or higher qualification at any other tertiary institution.

Signed at Johannesburg, on the……day of ……, 2025

Xolisa Nkwamza

Acknowledgement

Firstly, I give thanks to the Almighty God for granting me the strength, wisdom, and opportunity to complete this project. I also give thanks to my mother Florence Nkwamza and my sister Thabisa Nkwamza for their unwavering support, love, and encouragement throughout this journey.

I would like to express my sincere gratitude to my supervisor Dr. Nandi Malumbazo for her guidance and support throughout this project. I also acknowledge the funding provided by Seriti, which enabled me to conduct this research.

I extend my appreciation to the Seriti team, particularly Mr. Johannes and Mr. Nkosi, for their assistance in sampling. I also thank Zamani Company for their expertise in drilling, which was crucial to this project. Special thanks to Mr. Xolani Ngubeni and his colleague Ms. Mthethwa for facilitating access to the TIMA at Eskom, and to Mr. Skhwiri, our driver from Witwatersrand University, for his assistance during sampling.

I acknowledge the use of free Python software for data analysis and visualization.

List of Publication/s

Nkwamza, X. and Malumbazo, N., 2025. The modes of occurrence, distribution and enrichment of critical raw materials (Ga, Sr, Zr and Ba) within coal discards of the Witbank Coalfield, South Africa. International Journal of Coal Geology, 104870.

Abstract

This study investigates the modes of occurrence, distribution, and concentration levels of critical raw materials (CRMs) within coal discard dumps from the Witbank Coalfield, South Africa. Traditionally regarded as waste, these coal discards have been found to contain economically significant concentrations of CRMs, including Ba, Ga, Sr, Zr, and other valuable elements. Two contrasting coal discard dumps an older, decommissioned dump (CD1) and a younger, active dump (CD2) were selected for sampling and analysed using a suite of analytical techniques such as thermogravimetric analysis (TGA), bomb calorimetry, Fourier-transform infrared spectroscopy (FTIR), X-ray diffraction (XRD), scanning electron microscopy with energy-dispersive spectroscopy (SEM-EDS), automated mineralogy (TIMA), X-ray fluorescence (XRF), and inductively coupled plasma mass spectrometry (ICP-MS). Sampling at CD1 was conducted systematically by depth profiling, while CD2 samples were collected unsystematically at the surface. Samples were categorized into four lithological groups: bright coal discard, moist coal discard, clay-rich coal discard, and reddish oxidized coal discard.

Results indicate that both CD1 and CD2 contain high-volatile bituminous coal discards, with CD1 exhibiting average values of 4.49 wt% moisture, 21.91 wt% volatile matter, 38.53 wt% fixed carbon, 34.78 wt% ash, and a calorific value of 18.11 MJ/kg. CD2 showed slightly different values: 6.46 wt% moisture, 20.29 wt% volatile matter, 38.14 wt% fixed carbon, 35.11 wt% ash, and 17.55 MJ/kg calorific value. FTIR analysis revealed characteristic absorption bands including O-H, C-H, C=C, C-O, C-C, M-O, Si-O, and Si-O-Si in samples from both dumps. Mineralogically, quartz and kaolinite dominate, accompanied by minor amounts of barite, zircon, apatite, illite, muscovite, and ilmenite. Major oxides in both dumps are dominated by SiO_2 and Al_2O_3, however, Al_2O_3 content remains below 40%, classifying these as low-alumina coal discards. CD1 is comparatively enriched in Fe_2O_3, CaO, MnO, MgO, Ba, Ga, Sr, Cu, Ni, and rare earth elements plus yttrium (REY), whereas CD2 displays higher concentrations of SiO_2, Fe_2O_3, P_2O_5, SiO_2, Na_2O, Be, Co, Li, Nb, Mo, Pb, Rb, Zr, V, and Zn. On average, CRM concentrations are higher in CD1 compared to CD2.

Vertical variability of CRMs in CD1 was clearly evident, with depth-dependent trends noted for Ba and Sr, especially within 0–1 m and 3–4 m depth intervals. Sr is also widely distributed throughout CD2. Ba predominantly occurs in barite, while Sr exists mostly in barite in CD1 and

is primarily associated with phosphate and carbonate minerals in CD2. Zr associates strongly with zircon, Ga occurs within kaolinite and organic matter, and Li shows intimate organic associations. REYs are hosted by Fe-bearing and phosphate minerals in CD1 but by Ca-rich aluminosilicates in CD2. Nb associates with both aluminosilicate and Ti-bearing minerals in CD1, but shows organic associations in CD2. Mo is mainly found in Ti-bearing minerals in CD1 and organic matter in CD2. Co occurs in Mn-, Ca-, Na- and Ti-bearing minerals in CD1 but is limited to Ca, Fe, Mn-carbonate in CD2. Cu exhibits strong organic affinity in CD1 and occurs in phosphate and chromite minerals in CD2. Pb associates with organic matter in CD1 and is found in apatite, chromite, Ti-, and Mg-bearing minerals in CD2. Ni, Be, and Zn show organic affinity in both dumps, while Rb is mainly hosted by illite and muscovite.

The study highlights the influence of hydrogeochemical processes and igneous intrusions on CRM enrichment and mineral associations within coal discards. The findings underscore the potential for coal discard dumps to serve as secondary sources of CRMs, offering promising opportunities for sustainable resource recovery and economic value addition. Furthermore, CRM extraction from coal discards could help mitigate the environmental risks posed by stockpiled waste materials. Based on results, it is recommended that further research focus on optimizing flotation and selective leaching techniques to enhance CRM recovery potentials.

Table of Content

List of Figures

List of Tables

Abbreviations

A – Ash content

ASTM – American Society for Testing and Materials

ATR – Attenuated Total Reflection

CCBs – Coal Combustion Byproducts

CD1 – Coal Discard 1

CD2 – Coal Discard 2

CRMs – Critical Raw Materials

CV – Calorific Value

FC – Fixed Carbon content

ISO – International Organization for Standardization

KPa – Kilopascal

LOI – Loss off Ignition

M – Moisture content

MV – Volatile Matter content

SRMs – Strategic Raw aterials

TGA – Thermogravimetric Analysis

Chapter 1: Introduction

1.1 Background

Coal discards are the byproducts generated from coal mining and beneficiation, traditionally considered as waste. They consist of low-grade coal, minerals, and other impurities (Misz-Kennan & Fabiańska, 2011; Vo et al., 2022). These materials accumulate in large quantities, leading to environmental pollution and substantial land use (Lloyd, 2000). However, from an economical point of view, these coal discards may contain significant amount of critical raw materials (CRMs), increasingly considered as valuable secondary sources (Dai et al., 2017; Lin et al., 2018b; Thompson et al., 2018; Wang et al., 2022; Zhao et al., 2019). Critical raw materials are materials that are in high demand, difficult to replace, and face supply risks due to their scarcity or geopolitical factors (Ferro & Banollo, 2019). These materials include precious metals, rare earth (REEs), and other valuable metals. They are indispensable for manufacturing batteries for electric vehicles, magnets for wind turbines, phosphors for lighting, catalysts in refineries, and energy storage systems crucial to renewable energy technologies (Ferro & Banollo, 2019; Lin et al., 2018, 2018a, 2018c). Their unique and reliable properties make them irreplaceable in many sectors including electronics, healthcare, aerospace, and defence (Ferro & Banollo, 2019).

The importance of CRMs is particularly critical in achieving global decarbonization goals by 2050, with surging demand driven by renewable energy deployment and electric vehicle adoption during the post-COVID-19 recovery period (IEA, 2021; World Bank, 2020; Karal & Shah, 2022). However, supply chains for CRMs face vulnerabilities from geopolitical tensions, environmental concerns, resource depletion, and fluctuating global demand, all of which have broad economic and social implications (European Commission, 2023). Therefore, identifying alternative and sustainable sources of CRMs is essential. Studies show that coal byproducts, such as coal discards, contain significant concentrations of CRMs, making them promising secondary sources beyond traditional ore mining (Dai et al., 2017; Lin et al., 2018b; Thompson et al., 2018; Wang et al., 2022; Zhao et al., 2019). South Africa, with extensive coal reserves notably in the Witbank Coalfield, is well-positioned to contribute to CRM supply both locally and internationally (Khan et al., 2022). Their main focus in South Africa has been on the modes of occurrence and concentration of REEs in fly ash, coal ash, and coal (Moroeng et al., 2024; Rerani et al., 2024). However, the geochemistry of coal discards has not been explored thoroughly.

The Witbank Coalfield, located in Mpumalanga Province, is one of South Africa's largest and most productive coal mining areas. Despite environmental challenges from carcinogenic substances such as xylenes, toluene, and benzene, as well as high concentrations of CO, CO_2, and CH_4 (Pone et al., 2007), it remains a key coal source for local use and export market. Its extensive coal reserves and continuous mining activities present an opportunity to valorize coal discards as CRM reserves. This approach can enhance both the economic benefits and environmental sustainability of coal operations in the region.

1.2 Problem Statement and Rationale

1.2.1 Problem statement

Historically, the Witbank Coalfield has been one of the largest coal-producing regions in the country, generating massive quantities of coal discards as byproducts of mining and beneficiation. While these discards are often seen as waste, they may contain valuable CRMs such as REEs, lithium (Li), boron (B), scandium (Sc), strontium (Sr), barium (Ba), vanadium (V), manganese (Mn) and titanium (Ti) which are essential component for high-technology industries. However, the occurrence, distribution, and concentration of these CRMs within Witbank's coal discards are not well understood. This lack of comprehensive data limits the opportunities for their recovery, while the accumulation of unmanaged coal discard piles continues to present significant environmental hazards.

1.2.2 Rationale

The exploration of CRMs within coal discard from the Witbank Coalfield is crucial for several reasons:

- Resource recovery: due to the ever-changing markets trends, finding alternative sources for CRMs has become critical as the global market for them continues to grow. Coal discards are normally given minimal attention even though they may contain important components that are vital to various industries.
- Environmental impact: the management of the stockpiles is an environmental problem because the disposal and contaminant-potential of coal discards have been identified. Understanding the chemical composition of coal discards will help inform environmentally sustainable management practices.
- Economic potential: benefits attached to the extraction of CRMs from coal discards are that it will create employment and income for people engaged in coal mining business.
- Technological innovation: this information is useful because it may help promote research into the occurrence and distribution of CRMs in coal discard and improve technologies for extraction and processing. This can lead to more efficient and environmentally friendly resource recovery methods.
- Policy and Regulation: collecting detailed information about chemical and radioactivity contents of CRMs in coal discard can help to formulate effective policy and regulation concerning coals extraction and utilization, as well as waste disposal and lessening environmental impacts.

1.3 Hypotheses

- The modes of occurrence of CRMs in coal discards are strongly influence by hydrogeochemical processes, leading to significant differences between the two dumps.
- The spatial distribution of CRMs within coal discards varies across coal discard dumps in the Witbank Coalfield.
- Coal discards from legacy dump contain high concentrations of CRMs.

1.4 Research Questions

- Which CRMs are present in the coal discards of the Witbank Coalfield?
- How are these CRMs distributed spatially and concentrated across two selected coal discard dumps?
- How do the characteristics of coal discard, such as age, depth, and geological composition affect the occurrence and concentration of CRMs?

1.5 Research Aim and Objectives

1.5.1 Aim

The primary aim of this study is to investigate the occurrence, distribution, and concentration levels of CRMs in coal discards from two selected coal discard dumps within the Witbank Coalfield. The secondary aim is to assess the potential of these dumps as secondary sources of CRMs and explore opportunities for sustainable resource recovery.

1.5.2 Objectives

- To compare the modes of occurrence and spatial distribution of CRMs between the two dumps.
- To quantify CRMs, present in coal discards from the two dumps.
- Provide recommendations for sustainable resource management and the development of innovative technologies for CRM recovery from coal discard.

1.6 Scope

The coal discards selected for this study originate from bituminous coal primarily used for electricity generation. Conventional analytical techniques will be applied to characterize representative bulk samples of the coal discard. Particle size fractions of 50, 75, and 212 μm will be used for different analyses: the 212 μm fraction for coal quality assessment and TIMA analysis, the 75 μm fraction for XRF, and the 50 μm fraction for FTIR, XRD, SEM-EDS, and ICP-MS

analyses. The dissertation is sub-divided into six chapters, each with a specific focus outlined as follows:

Chapter 1

The Introduction discusses the origin of coal discards, role of CRMs, importance of this project, hypotheses, research questions, and research aim and objectives.

Chapter 2

Provide a review of literature regarding the geological setting of the study area, origin and formation of coal, coal components, coalification stages, production of coal discards, review of CRMs list by countries, mineral occurrence in coal, modes of occurrence of elements in coal and its by-products, previous studies on the Witbank Coalfield.

Chapter 3

Coal discard preparation and characterization using conventional analytical techniques.

Chapter 4

Experimental results obtained are presented and notable observations, particularly, the lithology, quality, mineralogy, geochemical composition of coal discards and concentration levels of critical raw materials.

Chapter 5

Discuss how these critical raw materials are spatially distributed across coal discard dump, how are they occurring in terms of both organic and inorganic matters, the geological factors that contributed to their enrichment and both economic and environmental implications of CRMs

Chapter 6

Provides conclusions and recommendations made based on the experimental results.

Chapter 2: Literature Review

2.1 Geological Setting

The Witbank Coalfield is situated in the northeastern Mpumalanga Province of South Africa (Fig. 1). Its geological setting features a sequence of volcanic rocks, shales, quartzites, mudrocks, sandstones, dolomites, banded iron formations, conglomerates, and diamictites associated with the Rooiberg Group (Eriksson et al., 1993; Eriksson and Altermann, 1998). Overlying this sequence are the organic-rich sandstones, shales, coal seams, mudstones, siltstones, and minor conglomerates of the Vryheid Formation (Jones and Wagener, 2017; Soeder and Borglum, 2019).

Structurally, the coalfield lies in the northern sector of the Main Karoo Basin (MKB), an area shaped by glacial erosion during Paleozoic glaciations that once covered the Gondwana supercontinent (Hancox and Gotz, 2014). Five major paleovalleys trending NNE-SSW have been identified: Grootvlei, Vischkuil, Coronation, Bank, and Arnot. These valleys significantly influence the distribution, thickness, and continuity of coal seams, especially the economically important No. 2 seam, leading to complex facies patterns and irregular seam geometries across the region (Hancox and Gotz, 2014).

Except where dolerite intrusions have tilted the layers, the coal seams and surrounding strata are generally flat to gently undulating, dipping regionally less than one degree toward the south and southeast (Hancox and Gotz, 2014). The coal-bearing rocks mainly belong to the Vryheid Formation within the Ecca Group (Fig. 2). This formation consists of alluvial deposits, multiple interbedded coal seams (Nos. 1 to 5), siltstones, limestones, sandstones, diamictites, and the pre-Karoo basement complex (Cadle and Cairncross, 1987; Hancox and Gotz, 2014). Among the coal seams, the No. 2 seam stands out for its thickness averaging around 7 meters and high-quality coal. It is extensively mined through both opencast and underground methods. The other seams, Nos. 1, 3, 4, and 5 (from the bottom up), range in average thickness from 1 to 2.5 meters and are generally thinner and of lower quality but are still economically exploited throughout the coalfield.
Stratigraphic relations among these seams are as follows: the No. 1 seam lies beneath siltstones and sandstones and above siltstones, sandstones, diamictites, and basement rocks. The No. 2 seam is bounded by siltstones and interlaminated sandstone-siltstone layers. The No. 3 seam is overlain by siltstones and sandstones and underlain by thick sandstones. The No. 4 seam is situated below a thick sandstone layer and above both siltstones and sandstones. Lastly, the No. 5 seam is enclosed

within siltstone layers. The uppermost layer consists of alluvial deposits, which protect the coal seams from erosion (Fig. 2).

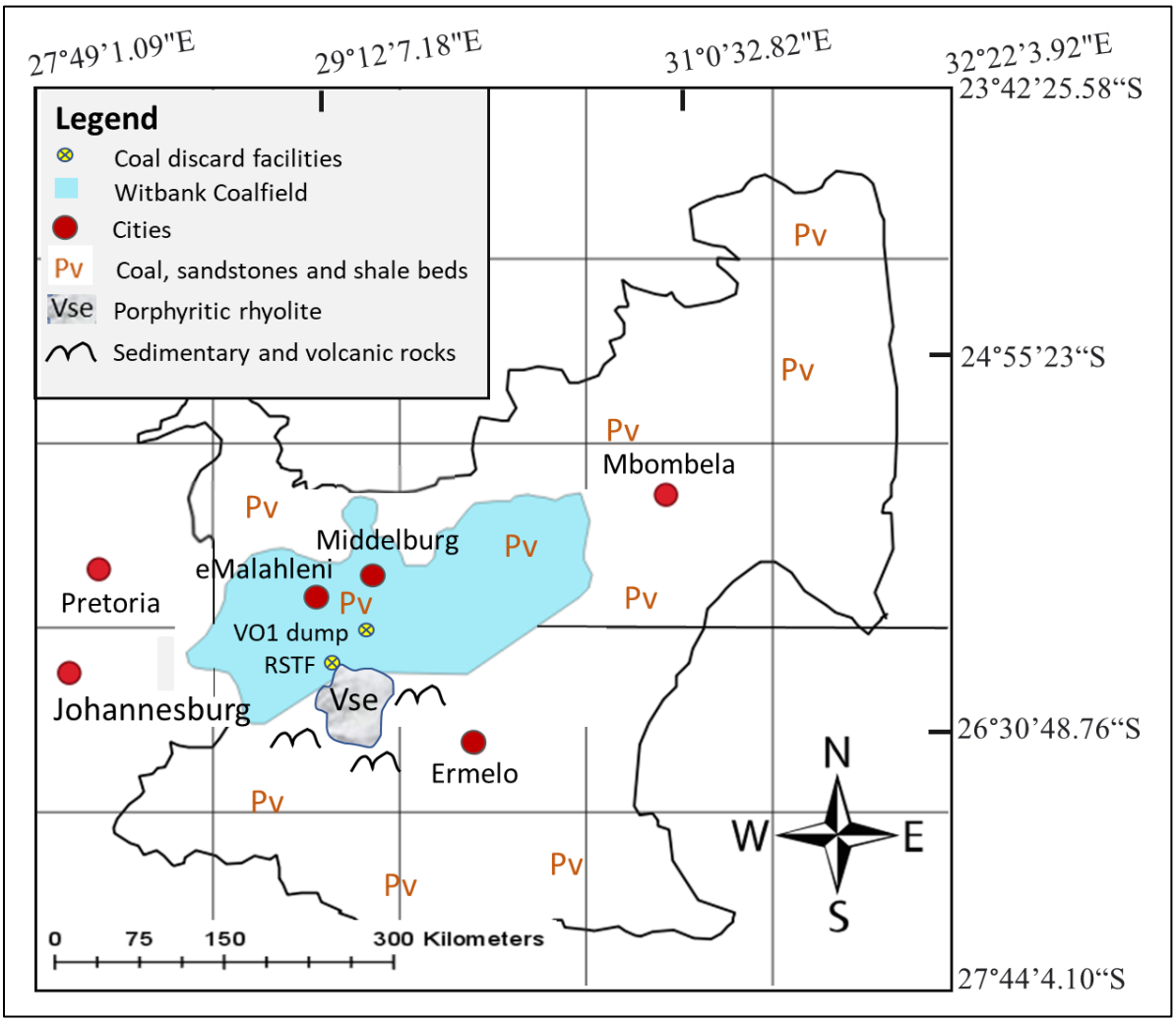

Figure 1: Map showing the Witbank Coalfield in Mpumalanga Province, highlighting coal discard facilities (VO1 and RSTF), major cities geological units including coal, sandstones, shale beds, porphyritic rhyolite, and sedimentary and volcanic rocks (Nkwamza & Malumbazo, 2025).

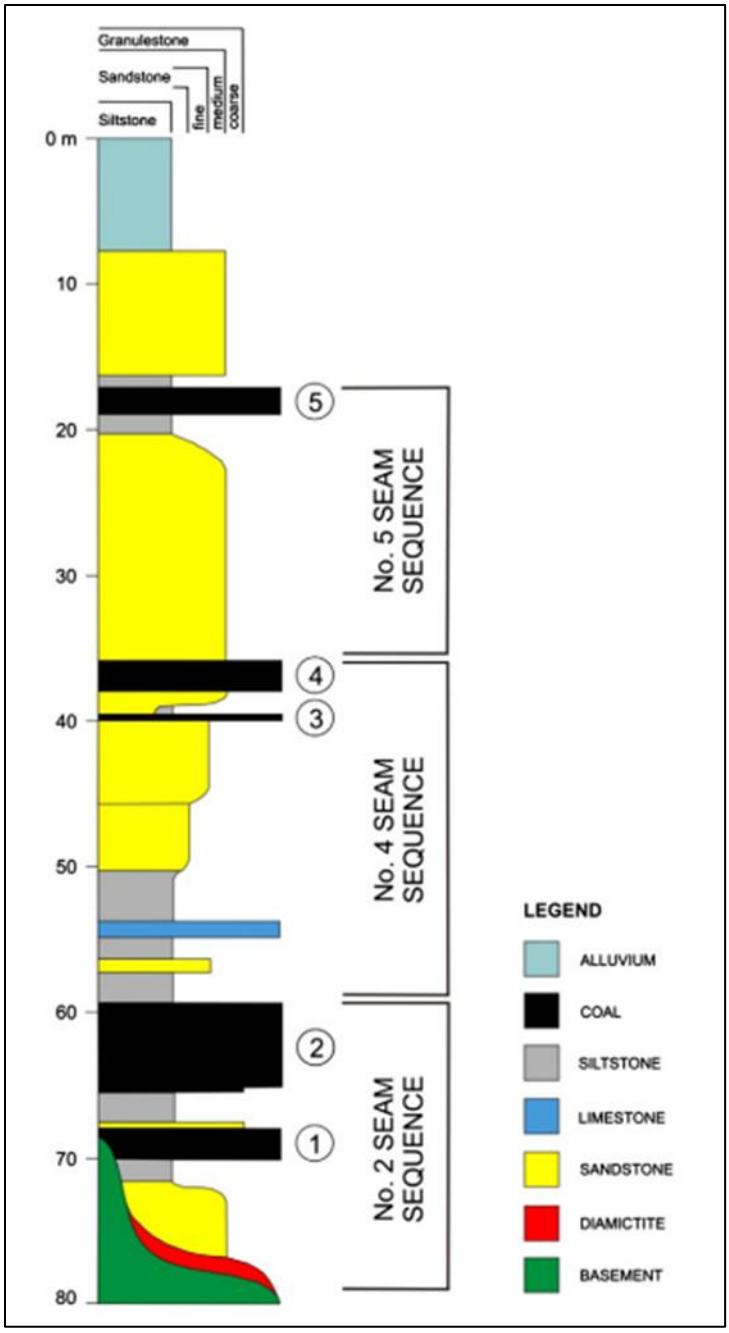

Figure 2: Generalized stratigraphic sequence of the Vryheid Formation subset of Ecca Group in the Witbank Coalfield, showing interbedded coal seams, siltstones, sandstones, and alluvial cover (Hancox and Gotz, 2014).

2.2 COAL

2.2.1 Overview

Coal is a unique commodity because it contains a mixture of organic matter and a proportion of minerals, which effectively dilute the organic component. This complexity makes coal challenging to beneficiate, as it exhibits considerable variation in rank and non-uniform chemical composition (Falcon & Falcon, 1978; Falcon & Ham, 1988; Orem & Finkelman, 2005). As a result, its chemical and physical properties can differ widely, even between samples from the same seam, influencing their behavior during industrial processing. Therefore, understanding the mineralogical and geochemical characteristics of coal is essential before its utilization.

Globally, coal remains a primary energy source. In South Africa, coal accounts for approximately 80% of the country's electricity generation and supports 6.7% of diesel fuel consumption. It also plays a significant role in the overall energy sector, excluding contributions from hydropower renewable sources (Pierce & Ferreira, 2022). It also accounts for approximately 12% of foreign exchange earnings (Hassan, 2023). Despite its extensive use, coal also holds untapped potential as an economic source of valuable materials beyond energy production.

2.2.2 Origin and formation of coal

South African coal reserves were formed between 250 and 300 million years ago, when the region was still part of the super-continent 'Gondwana' (Cairncross, 2001). During the Permian period, extensive swamps developed, where coal-bearing sediments accumulated in environments such as shallow intercontinental seas, continental lakes, and stable continental depressions along glacial valley margins. The variability in topography and sedimentary conditions influenced the decomposition stages of the vegetation. Most of the vegetation remained in place, while a smaller fraction was transported by flooding into adjacent lakes, deltas, and shallow seas. Concurrently, minerals eroded from nearby mountains were carried inland by water (Falcon & Ham, 1988).

The predominant swamp vegetation comprised hardwoods from deciduous trees and woodlands, contributing to differences in plant tissue composition and size in structures like leaves, pollen, and waxy exudates. These factors fostered the formation of mineral-rich peat swamps with diverse compositions, which over time transformed into thick coal seams. Falcon & Ham (1988) noted that these coal seams generally developed at shallow burial depths, resulting in nearly horizontal, shallow seams that are relatively inexpensive to mine. However, the coal-bearing strata were regularly intruded by igneous bodies, subjecting the coal to elevated temperatures and pressures. This altered coal rank and caused an uneven distribution of elements within the seams. The transition from peat to bituminous coal in Figure 3 involves the reduction of hydroxyl, carboxylic acid groups, and hydrophilicity, typically occurring when carbon content reaches around 89% (Brown, 1962).

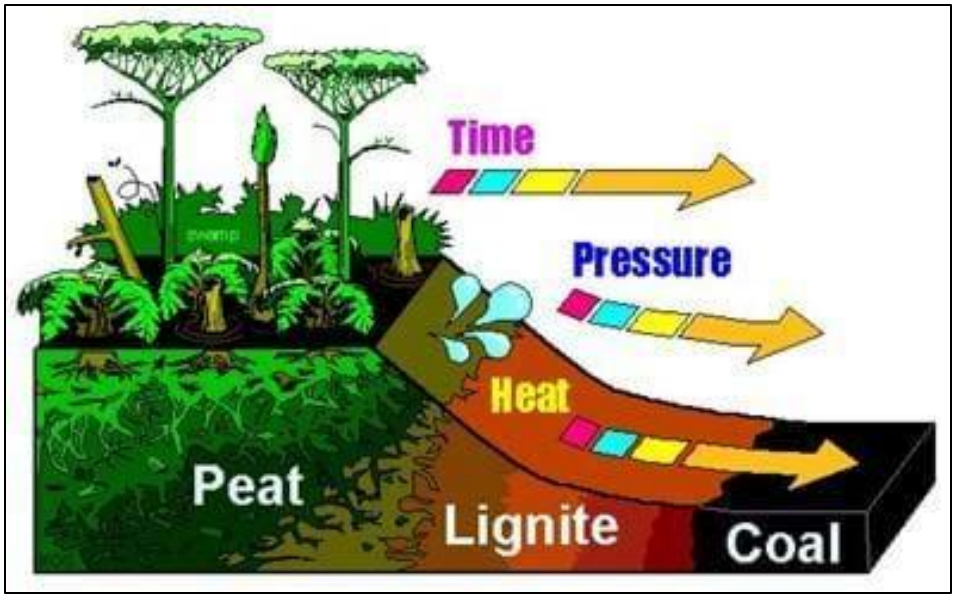

Figure 3: The formation of coal over millions of years (DMP, 2008).

2.2.3 Coalification stages

This is the process whereby the lowest rank coal 'peat' is consecutively transformed into higher rank coals such as lignite, sub-bituminous, bituminous, and anthracite. It is made up of three coalification stages:

1. Sedimentation stage: plant material accumulates and decays under anaerobic conditions in water bodies. Simultaneously, minerals are deposited alongside the organic matter. The coal's grade is influenced by the relative amounts of both mineral content and organic material present (Falcon ,1977).
2. Diagenetic stage: the decayed plant debris consolidates into banded layers. Biochemical transformations and compaction alter the chemical composition and proportion of organic matter. These changes produce precursor materials that eventually form the macerals observed in fossilized coal. The nature of these precursors plays a critical role in determining the coal's rank and performance.
3. Metamorphic stage: this final stage is controlled by temperature, pressure, and time. These factors drive coalification, influencing the coal's rank and final geochemical characteristics, thereby defining the properties of the mature coal deposit (Brown, 1962).

Coalification is characterized by major changes in coal's chemical composition, such as the enrichment of carbon at the expense of hydrogen and oxygen as coal maturation increases (see Table 1).

Table 1: The major changes in coal rank as a function of coal's chemical composition (Falcon, 1977).

Rank	Carbon [%]	Hydrogen [%]	Oxygen [%]	Nitrogen [%]
Wood	50	6	43	0.5
Peat	59	5	33	2,5
Bituminous	82	5	10	2
Lignite	70	5,5	23	1
Anthracite	93	3	2,5	1
Graphite	100	0	0	0

2.2.4 Coal components

Coal consists of two microscopic components: the organic matter (macerals) and the inorganic mineral matter. The macerals are classified into three main groups: vitrinite, liptinite, and inertinite.

Vitrinite originates from the woody parts of plants such as bark, twigs, and branches. It is characterized by relatively high oxygen content, elevated volatile matter, and a reflectance range of approximately 0.5 to 10% (Falcon and Falcon, 1987). The colour of vitrinite varies with coal rank, appearing white in anthracite and dark grey in high-volatile bituminous coals. Liptinite, also previously known as exinite, forms from spores, resin bodies, and algae during peatification. It is notable for its high hydrogen content and lower reflectance, ranging from 0.0 to 10%. Like vitrinite, its colour depends on coal rank, ranging from white in anthracite to black and brown in high-volatile bituminous coal. Inertinite derives from oxidized organic material (humus) and is distinguished by its high carbon content, higher reflectance values (0.7 to 10%), low combustion rates, and resistance to processes such as coking, hydrogenation, and devolatilization. Its colour shifts with rank, typically yellow-white in anthracite and medium grey in high-volatile bituminous coal (Falcon and Falcon, 1987). Mastalerz et al. (1993) studied the relationship between vitrinite and inertinite. They found that as the carbon content in vitrinite increases, the oxygen content decreases, suggesting that vitrinite becomes more aromatic in character over time.

Minerals present in coal can be grouped into:

1. Clay minerals: illite, smectite and kaolinite etc.
2. Sulfide minerals: pyrite, marcasite, sphalerite etc.
3. Carbonate minerals: calcite, dolomite, ankerite, and siderite, etc.
4. Oxide minerals: hematite, magnetite, quartz, etc.
5. Other minerals: limonite-goethite, apatite, feldspars, zircon etc.

These minerals occur with macerals in the matrix of coal particles (Falcon & Falcon, 1987)

2.2.5 Coal rank

Coal rank is the system used to categorize coal based on the degree of metamorphism or maturation that the coal seam has undergone over a period. The rank of coal is controlled by geological time, temperature, and to a lesser degree pressure and burial depth. The main categories of coal rank are

presented in Table 1. The rank of carboniferous coals in Europe and North America is typically determined by the contents of both volatile matter and fixed carbon (Falcon & Falcon, 1987). The carboniferous coals with high fixed carbon and volatile matter contents are considered as high rank coal (Czajka, 2018). However, these traditional parameters are not well-established for shallow South African coals. In South Africa, the most reliable measure of rank is the reflectance of vitrinite, determined petrographically under oil immersion (Falcon & Falcon, 1987). The simple reason is Gondwana coals and Carboniferous coals differ notably in their maceral composition, with Gondwana coals being rich in inertinite and Carboniferous coals dominated by vitrinite. Because inertinite contains higher carbon and lower volatile matter compared to vitrinite, traditional coal rank standards based on volatile and fixed carbon content do not apply well to these coals.

2.2.6 Coal discard production

Global coal production is approximately 8.8 billion tons per year (IEA, 2025), with a global coal reserve of 1.14 billion tons (IEA, 2020). The quantity and type of coal available in a specific area result in various coal discards. South Africa has 1.5 billion tons of coal discards stockpiled in the coal mining regions (DOE, 2001). These coal discards are produced during extraction, transportation, processing, and combustion of coal (Figure 4). These discards are categorized based on their origin in a mine processing scheme.

1. Aggregates discarded consist of overburden and coarse rejects separated during coal processing, and they are deposited in spoil heaps.
2. Washery discards consist of finer fractions from the washing plant, and they are disposed of in slurry form in tailing facilities (Vo et al., 2022).

These discards are further classified based on their particle sizes and place of origin. Coarse-grained (10-250 mm) comes from suspension plant, fine-grained (0.5-30 mm) are generated by sedimentation processes, and very fine-grained (<1 mm) are generated by floatation processes (Misz-Kennan & Fabiańsk, 2011).

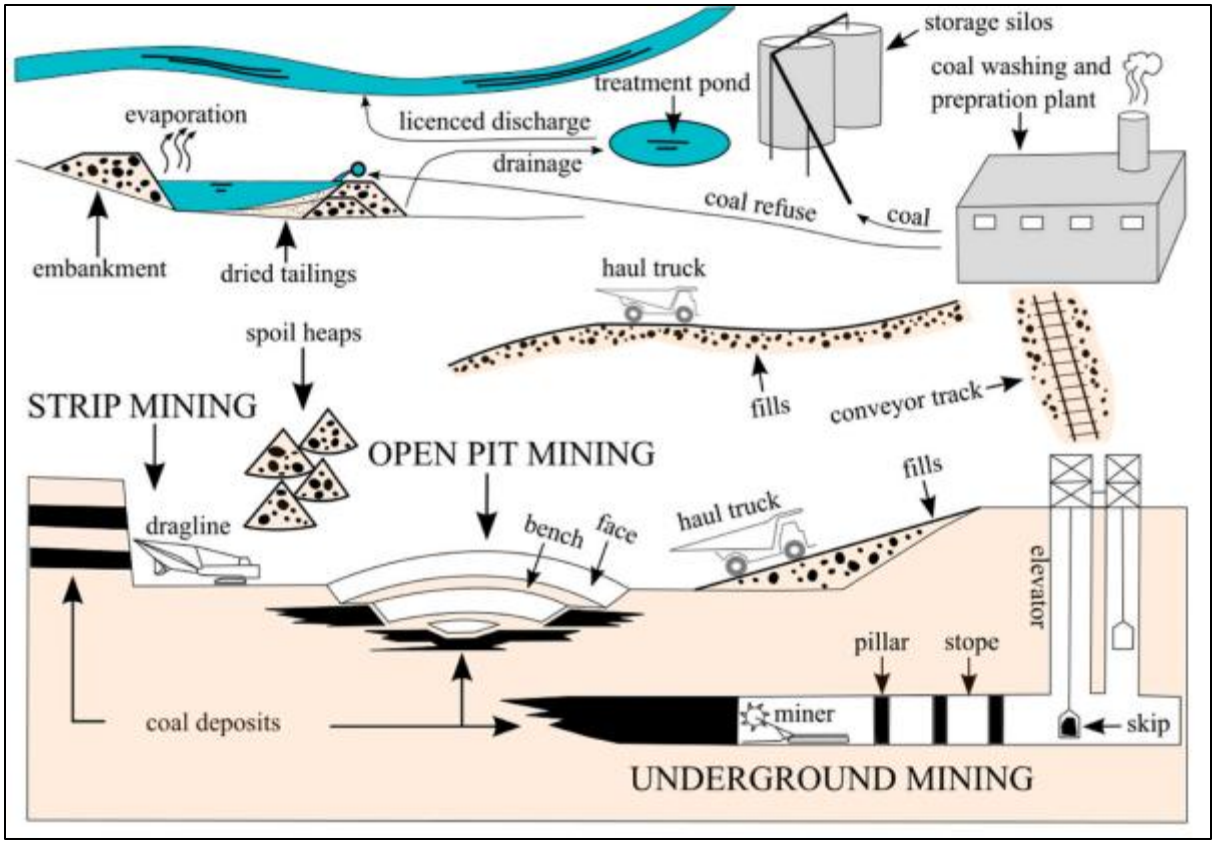

Figure 4: Coal discard production (Vo et al., 2022).

2.2.7 Environmental impacts of coal discards

Approximately 10 million tons of coal ash are produced during coal combustion annually. Of this, only about 30% is utilized by the construction industry, while the remaining 70% accumulates in coal discard piles. These coal discards act as reservoirs for various toxic elements such as Sb, As, Be, Cd, Cr, Hg, Ni, Pb, Se, and U (Mashishi et al., 2023). Leaching of these elements from the discards can lead to contamination of soil, surface water, and groundwater (Orem & Finkelman, 2005). Because these contaminants are present in both soil and water, they can be absorbed by plants, which may slow plant growth and introduce toxins into the food chain, posing risks to animals and humans alike (Adriano, 1986).

A particularly important concern involves sulfides within coal discards, especially pyrite. When pyrite is exposed to oxygen and moisture, it undergoes oxidation, producing ferrous sulfate and sulfuric acid. This acid generation leads to acid mine drainage (AMD), which severely impacts

aquatic ecosystems in both active and abandoned mining areas. Moreover, pyrite oxidation releases chalcophile trace elements into the water, which tend to precipitate in oxygen-rich surface waters and accumulate in stream sediments, further affecting water quality and sediment composition (Orem & Finkelman, 2005).

2.3 Critical Raw Materials (definition, uses and applications)

Critical raw materials are materials that are in high demand, difficult to replace, and have considerable risk associated with securing their supply. These materials are often essential to produce a wide range of goods and technologies, including those in the renewable energy sector, defense, electronics, and other high-tech industries (Ferro & Banollo, 2019). They are essential for all kinds of economic benefits from energy to the fourth industrialization revolution that might improve the quality of modern lives. The global demand for CRMs continues to grow owing to the inevitable population growth and improvement in the standard of living (Lin et al., 2018b). They are distinct from strategic raw materials (SRMs), which are important for the technology that supports the twin green and digital and defense and aerospace objectives (U.S DOD, 2019).

They have numerous applications in the global economy, for instance, REY are non-substitutable in electronics, emerging innovations, health care, oil refinery, steel, automative, aerospace, defense, clean and high-tech products (Ferro & Banollo, 2019; Lin et al., 2018a). Lithium and cobalt are utilized in energy storage for battery manufacturing, borates in wind turbines, and dysprosium, neodymium, and praseodymium are essential in the manufacturing of motors for electric vehicles (EVs) and wind generators. Dysprosium is more vulnerable due to its demand and smaller proportion in rare earth ores (Szczepanski, 2020).

2.3.1 Overview of CRMs listed by countries

Different nations have different CRMs lists, yet terminology, data support, and assessment frameworks vary. The EU labels this category of materials as ‘Critical Raw Materials’ (European Commission, 2023), whereas Canada employs the term ‘Critical Minerals’ (Government of Canada, 2022). These are semantically related terms, as critical minerals may not exclusively denote minerals but could encompass any raw materials. At this point, the terminology is standardized and designates all such materials as critical raw materials.

2.3.1.1 CRMs for South Africa

South Africa is renowned for its extensive reserves of platinum group metals (PGMs), accounting for about 90% of the world's resources (European Commission, 2023). As the role player in the production of PGMs, it plays a significant role in the manufacturing of hydrogen production technologies and catalytic converters, which are essential for reducing carbon emission and advancing clean energy solutions (WBG, 2020). In addition to PGMs, South Africa also produces a range of raw materials such as copper, vanadium, chromium, and manganese, which are required for steel production and battery technologies (European Commission, 2023). However, South Africa is still in its infancy stage of establishing a framework for CRMs. As the demand for CRMs continues to grow owing to technological advancement and the global transition to green economy, South Africa will have to meet both national and international requirements (Khan et al., 2022).

As a result, the Council for Scientific and Industrial Research (CSIR) produced list of CRMs for South Africa (Figure 5). This council noted that the methodologies for critical assessment employed by other countries like the EU, the U.S., and Canada are not suitable for South Africa due to complex variables and insufficient local data (Khan et al., 2022). In addition to that, South Africa is still a developing country, distinguishing itself from above-mentioned established countries (World Data, 2020). It is also grappling with significant energy supply challenges in the form of load-shedding (Ibrahim et al., 2021). In response to these challenges, the CSIR has associated CRMs with emerging technologies, speculating on the potential future influence of transformative technologies such as clean energy, digital advancements, and the industrial revolution of South Africa (Khan et al., 2022). The CRM list in South Africa comprises of 43.6% REEs (specifically lanthanides + Scandium + Yttrium), 20.5% precious metals, 17.9% base metals and 17.9% other materials.

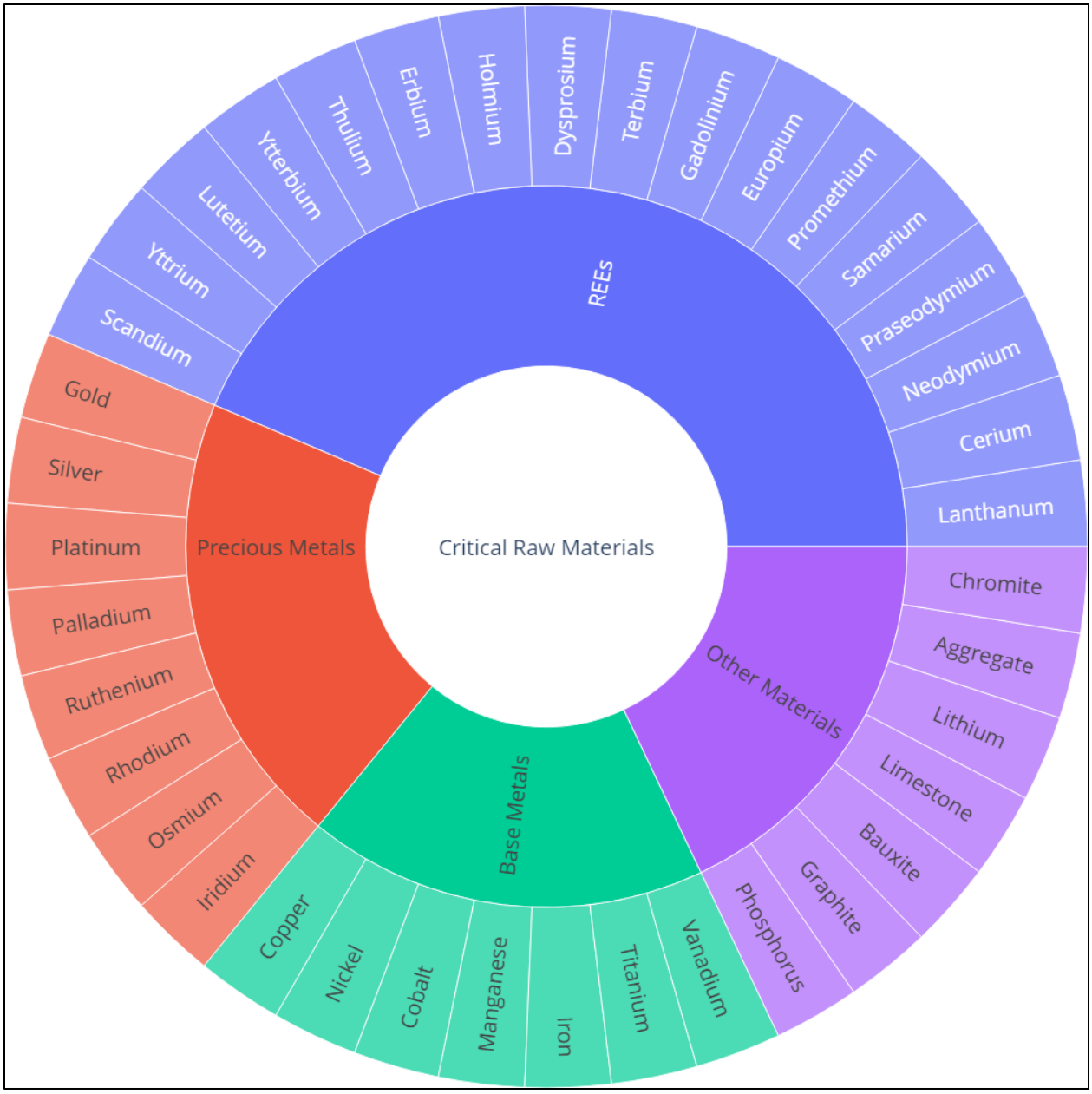

Figure 5:CSIR's proposed list of CRMs for South Africa (Khan et al., 2022).

Apart from vast reserves of PGMs, South Africa is also renowned for its extensive reserves of coal. Coal, as a cheap and complex earth commodity, is primarily used as a source of energy (Cairncross, 2001; Hancox & Gotz, 2014). Coal mining and processing in South Africa have produced massive quantities of coal discards, which are stockpiled in the mining provinces, imposing environmental and spatial challenges. This presents an opportunity to explore and harness other raw materials

such as REEs, Li and Sc from coal, coal ash, and coal discards. Numerous studies have reported these materials contain significant concentration of REEs, exceeding the cut-off grade for extraction (Harrar et al., 2022; Rerani et al., 2024). On going research initiatives are focusing on assessing the availability and feasibility of extracting these materials from coal and its by-products. These efforts aim to significantly bolster South Africa's position in the global CRMs market and reduce its reliance on importing such materials. This will make South Africa to be a role player in the global supply chain and contribute to broader sustainability efforts aimed at addressing climate changes and promote resource efficiency.

2.3.1.2 CRMs for Canada

Canada released its first list of critical minerals in 2021, identifying 31 minerals considered essential to the country's economy, including PGMs and REEs (Government of Canada, 2022). This list was updated in 2024 (Figure 6), adding three new minerals and expanding the total to 34 (Government of Canada, 2024). Minerals are included based on three main criteria: their importance to Canada's economic security and supply risk, their role in supporting the transition to a low-carbon economy, and their status as reliable sources of strategic materials for Canada's partners and allies (Government of Canada, 2024, 2022; Ralph et al., 2023).

The list was developed through consultations with provincial, territorial, and industry experts and is subject to comprehensive review every few years (Government of Canada, 2022). However, the methodology behind the list's creation is not fully disclosed, limiting the ability to critically assess its robustness. This suggests that Canada's critical minerals framework is still in an early stage of development.

The overarching objectives of the Canadian government list of critical minerals is to support six national strategies, such as driving exploration, research, and development; expediting responsible project development; constructing sustainable infrastructure; advancing reconciliation with indigenous people; cultivating a diverse workforce and thriving communities; and enhancing global leadership and security (Government of Canada, 2022).

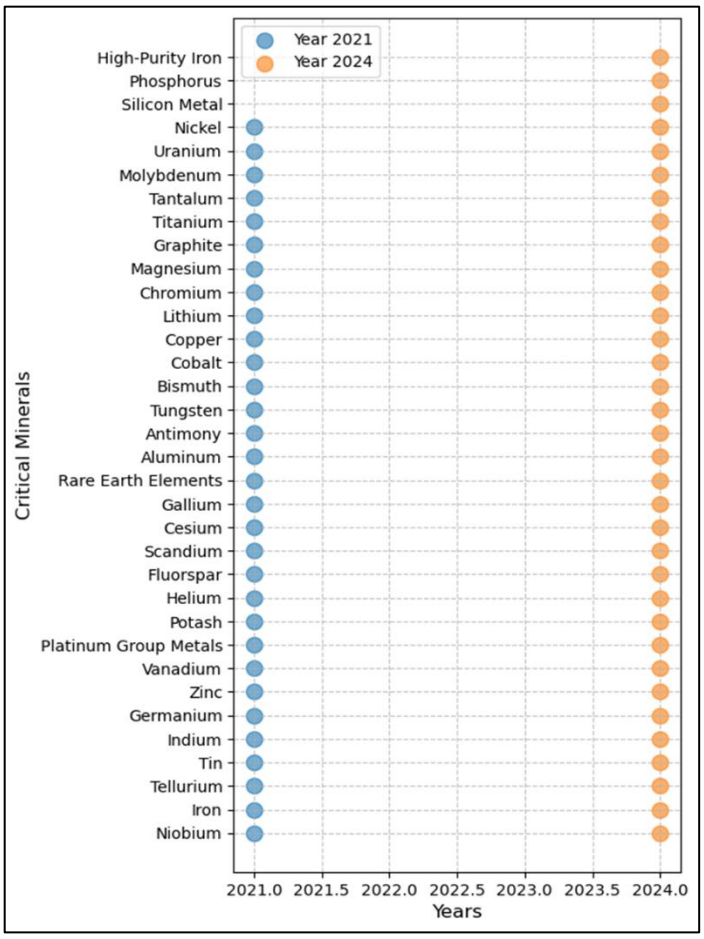

Figure 6: Canada's 2021 and 2024 list of critical minerals (Government of Canada, 2024, 2022; Ralph et al., 2023).

Canada is renowned for its rich geological resources and significant reserves of essential minerals. The country is home to over 60 critical minerals and is a top producer of Co, C, Li and Ni. These minerals are essential for the manufacturing of batteries and electric vehicles for the future. It is also known as the second-largest global producer of Nb, which is indispensable for the aerospace industry. Lastly, it is also fourth-largest global producer of In, which is the key component in the manufacturing of advance vehicle and semiconductors (Government of Canada, 2022). This suggest that Canada can supply even more critical minerals to both domestic and international markets.

Canadian government has conducted a preliminary analysis to identify regions with high prospect for critical minerals (Figure 7). These regions include remote areas, rural areas, and indigenous communities. The government of Canada acknowledges that these regions are still at various stages of processing and mining (Government of Canada, 2022).

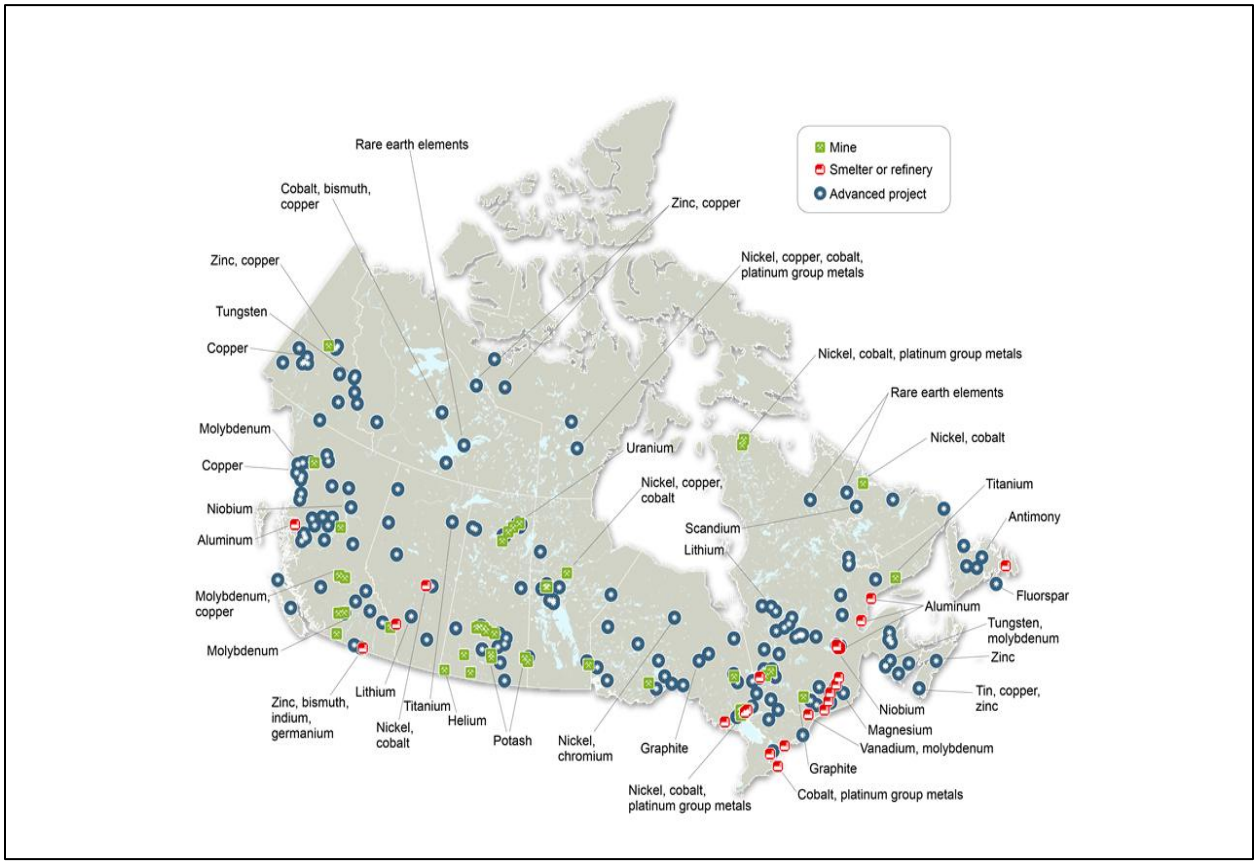

Figure 7: Canadian regions rich in critical minerals excluding the newly added critical minerals (Government of Canada, 2022).

Canada is among other countries that have recognized the potential of coal combustion by-products (CCBs) as potential source of critical minerals, particularly REEs and other value minerals. Canada acknowledged that the demand for REEs is expected to increase due to their indispensability in clean energy technologies. This country also realizes that the currently supply of REEs is not sufficient to meet both local and international future requirements, therefore it is of foremost importance for Canada to explore alternatives source of critical minerals. Among others coal and

its by-product have emerged as potential source of REEs owing to their abundance, environmental and economic incentivizes for reuse (Bishop et al., 2023).

Canadians have gained a deeper understanding of the evolution of the CRM lists and the alterations they have undergone over time. This comprehension has empowered them to evaluate the current and future significance of such lists.

2.3.1.3 CRMs for United States (U.S.)

The U.S. Department of Energy defines critical minerals as those essential to energy production and subject to a high risk of supply disruption (U.S. Department of Energy, 2019). The initial list of critical minerals was introduced in 2010, with special emphasis on clean technologies. This early strategy identified five REEs and In as particularly critical in the short term (U.S. Department of Energy, 2010). The strategy was based on three key pillars: diversifying supply sources, developing substitutes and alternatives for critical minerals, and improving recycling and reuse practices. Its ultimate objective was to establish the U.S. as a leader in clean technology production by ensuring secure and sustainable access to these essential materials.

The U.S. Department of Energy evaluated mineral criticality based on two main factors: their importance to clean energy technologies and the risk of supply disruption (U.S. Department of Energy, 2010). In the short term, Dy, Nd, Tb, Y, Eu, and In were classified as critical minerals due to their essential roles in magnets, batteries, LEDs, solar photovoltaic coatings, and catalytic converters. Whereas Ce, La, and Te were considered near critical, despite their high importance for clean energy, they presented a moderate supply risk (Figure 8).

In the medium term, Dy, Nd, Tb, Eu, and Y remained critical minerals, reflecting their continued high demand and supply vulnerability. While In, Li, and Te were categorized as near critical minerals, given their high clean energy relevance but moderate supply risk (Figure 9). These elements are primarily vital for producing batteries, solar panels, and thermoelectric devices (U.S. Department of Energy, 2010).

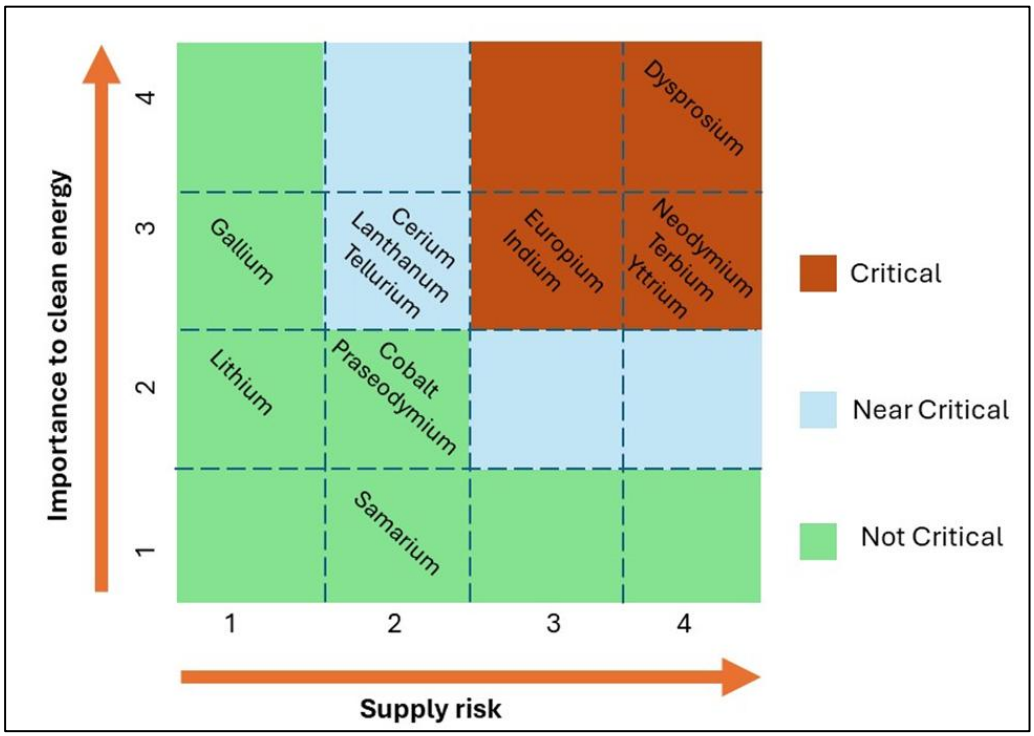

Figure 8:Short-term (0-5 years) criticality assessment matrix (U.S. Department of Energy, 2010).

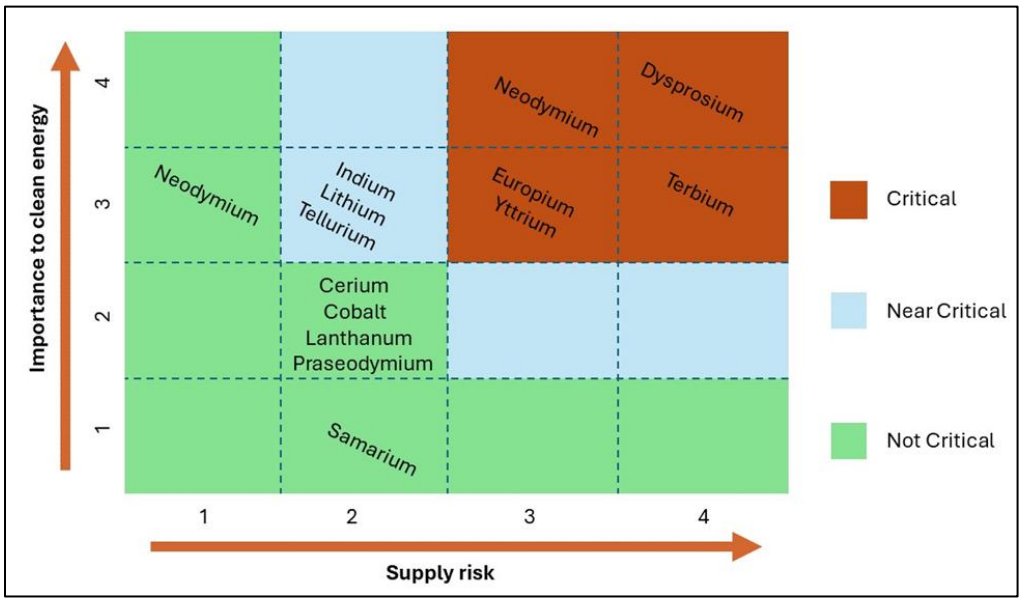

Figure 9: Long-term (5-15 years) criticality assessment matrix (U.S. Department of Energy, 2010).

Like the EU, the U.S has effectively established a framework for CRMs and revised its list periodically. The U.S geological survey released a list of 54 critical minerals in 2018, followed by a list of 51 critical minerals in 2022 (Figure 10). Noteworthy, helium, potash, rhenium, strontium, and uranium were removed in the year 2022 list while nickel and zinc were added indicating approximately 5.56 % decline in the number of critical minerals in period of 4 years (U.S. Geological Survey, 2022, 2024). The fact that more minerals have been removed, and few have been added, suggests a demand shift and supply chain stability for other minerals.

The U.S. is renowned for its massive coal reserves (American Coal Ash Association, 2017). The four ranks of coal are utilized as follows lignite is used as fuel in electric power plants, sub-bituminous coals used to generate electricity, bituminous coals are used to generate electricity and coke for metallurgical industry, and lastly anthracite coals are used as a domestic heating fuel (Penny State University, 2024). The U.S produces vast quantities of coal by-products, of which 50% of coal ash is used to make construction materials such as bricks and cements (American Coal Ash Association, 2017). Hower et al. (2017) declared that these coal and its by-byproducts that are kept in tailing facilities contain large potential resources. As a result, the U.S. Government of Energy funds extensive research to explore the occurrence, abundance, and recovery of critical minerals from such materials (National Energy Technology Laboratory, 2018).

Indeed, ongoing research has showed significant concentration levels of certain critical minerals in the U.S. coals, for instance the U.S. coals have been found to contain 721 ppm of Ti and 266 ppm of Ba (Lin et al., 2018a), 430 ppm of P_2O_5 P, 1.86 wt% of Fe and 0.18 wt% of Mg (Orem & Finkelman, 2005), 2400 ppm of REEs in low-ash (Hower et al., 2018), 200 to 3000 ppm of REY on ash basis, marine shale coal related contain 200 to 800 ppm of REY on ash basis (Mastalerz et al., 2020), moisture-free coals contain 65.5 ppm REY (Lin et al., 2018) and lastly the total mean concentration of REEs (sum of La, Y, Sc) in ash from Appalachian sources was 591 ppm and the total fraction of REEs such as Nd, Eu, Tb, Dy, Y, and Er in fly ash was found to be 34-38% higher than in conventional ores (Targaart et al., 2016).

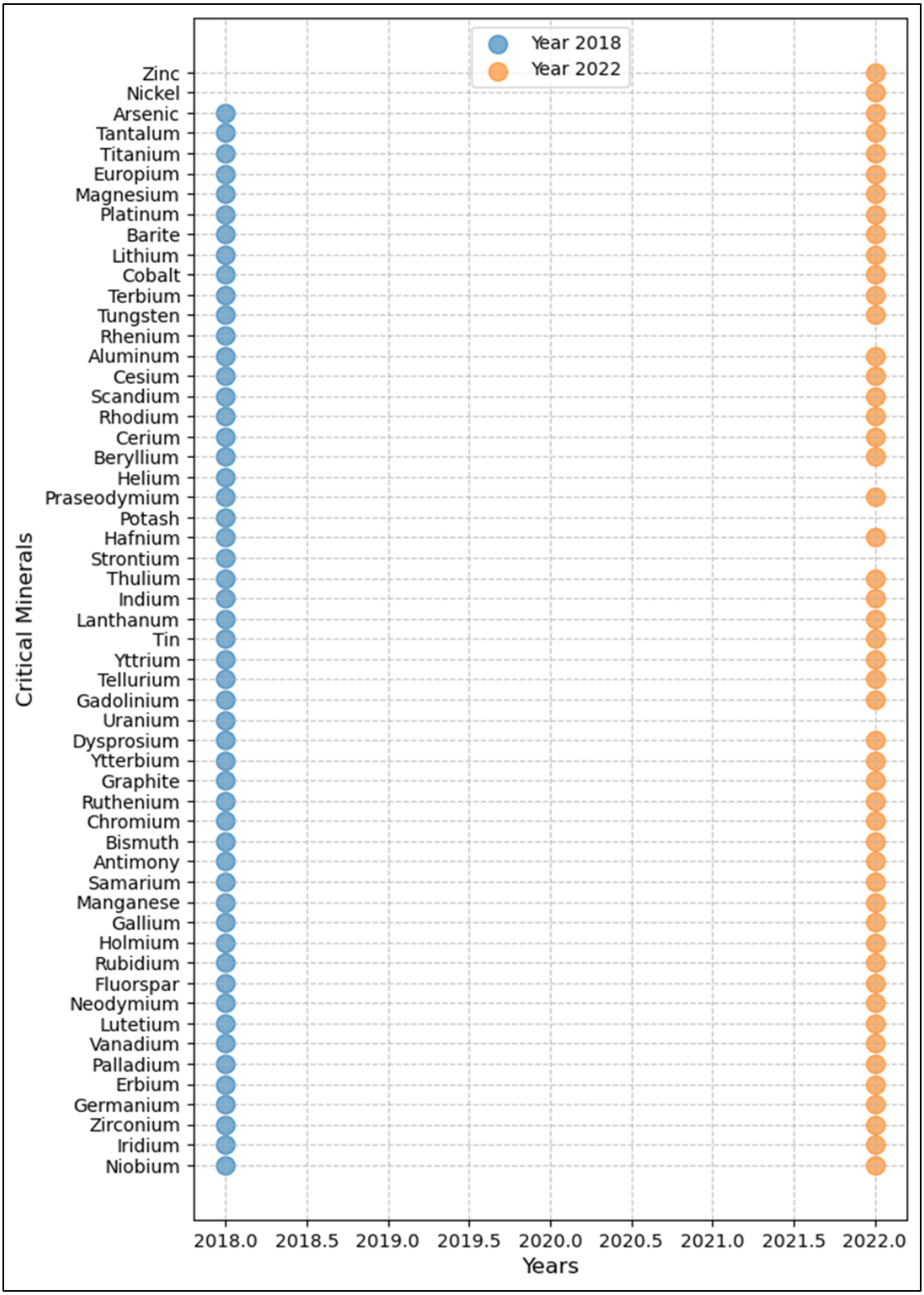

Figure 10: Changes in timeframes for the U.S critical mineral list from 2018 to 2022 (U.S Geological Survey, 2024, 2022).

2.3.1.4 CRMs for European Union (EU)

The EU's CRM efforts began in 2008 with the 'Raw Material Initiative'. This initiative aimed to address concerns about the security of the supply of raw materials essential for European industries (European Commission, 2008). The initiative had three main objectives: ensuring fair access to resources in developing countries, promoting stable domestic raw material supplies, and enhancing resource efficiency and recycling. The aim was to use this initiative to influence international policy and geopolitical engagement, such as achieving national self-sufficiency. For instance, policies towards developing countries focused on human rights, governance, conflict, and stability. In line with the EU CRM approach, the first set of 14 CRMs was identified in 2011 based on their higher supply risk and economic impact compared to other raw materials (European Commission, 2011).

The EU list of CRMs is regularly updated every three years, to reflect changing economic, technological, and geopolitical factors. More CRMs have been added than removed over the three-year intervals (Figure 11). The average growth rate is 1.67 CRMs per year from 2011 to 2023 (European Commission, 2023). The impacts of the COVID-19 pandemic and the Russia-Ukraine war significantly influenced the addition and/or removal of raw materials. For instance, the EU introduced the category of strategic raw materials (SRMs) in response to the Russia-Ukraine war in 2022, although it had been previously defined in the foresight document (European Commission, 2023). Even though the European Union faces several challenges in securing a stable and sustainable supply of CRMs due to several factors such as geopolitical dynamics, supply chain vulnerabilities, environmental concerns, and technological dependencies. The European Union has been successful in initiating efforts to address raw materials and establishing a framework for CRMs.

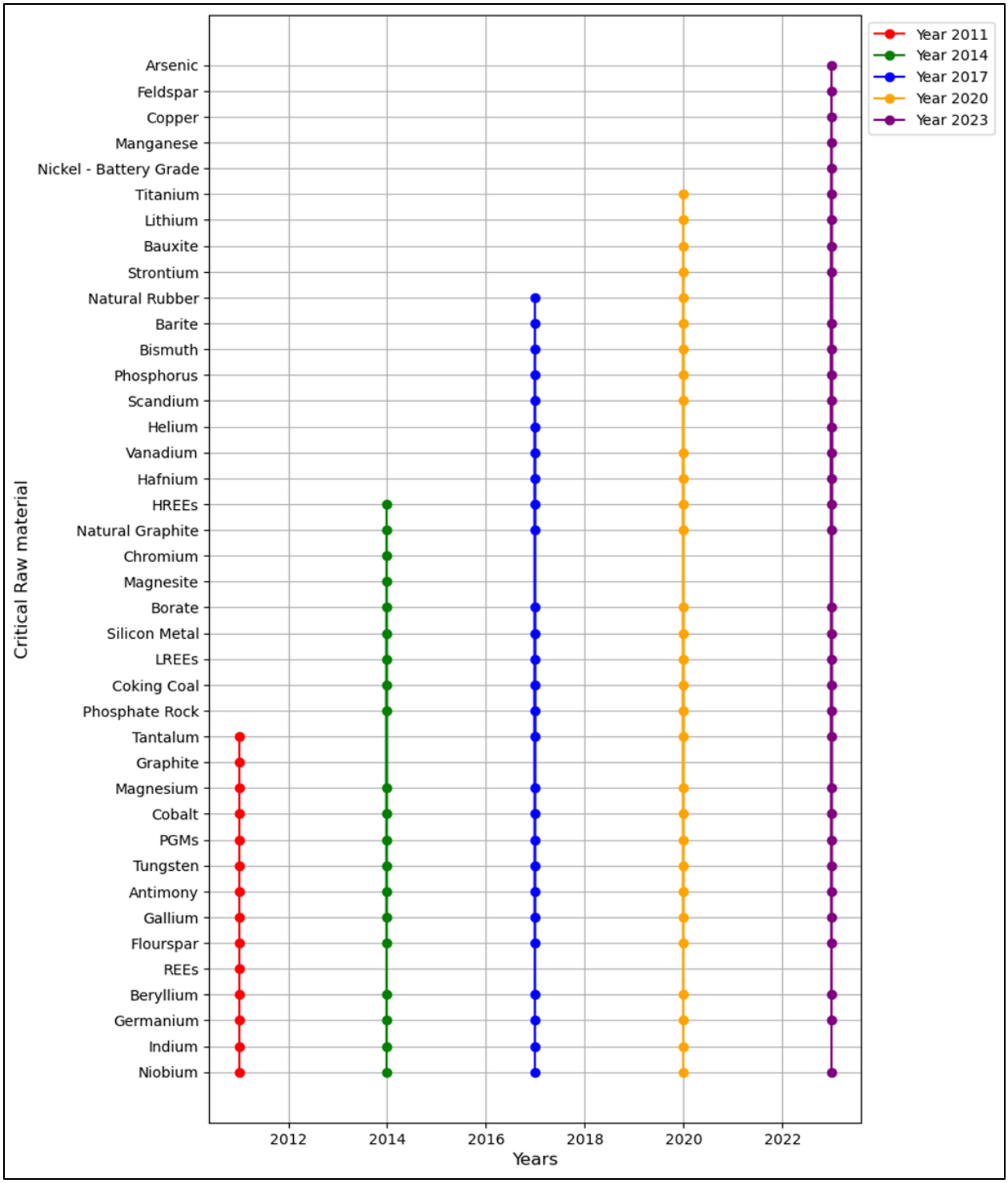

Figure 11: Changes in period for the EU CRM list from 2011 to 2023 (European Commission, 2011, 2014, 2017, 2017a, 2020, 2020a, 2023).

The EU has recognized how Li and REEs are increasingly replacing oil and gas at the heart of its economy (European Commission, 2022). Amidst the global shortage of Li, REEs and other materials, the EU has identified coal and its by-products as potential reservoirs for such materials. Studies have shown that coal deposits and coal by-products such as fly ash, coal ash and coal discard can contain significant concentrations of these materials. For instance, a study on the Polish coal ash and fly ash found that coal ash contains Pb at 131 ppm, Ce at 31 ppm, Sb at 10 ppm, Be at 30 ppm, while coal ash contains Se at 21 ppm. The study noted that Mo contents in both coal ash and fly ash were above the average in the Earth's crust (Bielowicz, 2021).

2.4 Mineral occurrence in coal

Studies on the mineralogy of coal have been carried out extensively in South Africa, China, Australia, Canada, India, European countries, Pakistan, and United State of America. Over 200 minerals have been found in coal and belong to various mineral groups such as silicates, sulfides, sulfates, carbonates, phosphates, and oxides (Finkelman et al., 2019). The main mineral groups and their associated minerals are presented in Table 2. The presence of mineral matter in coal provides valuable information about the geological history and depositional conditions of the coal-bearing strata (Ward, 2002).

Coal contains both crystalline and amorphous minerals, each with distinct origins and characteristics. Crystalline minerals appear as well-defined crystals, grains, or aggregates of diverse mineral species. In contrast, amorphous minerals mainly consist of volcanic glassy materials and meteoritic debris lacking a defined crystal structure. Alongside these solids, coal also contains liquid and gas phases, as well as fluid inclusions within mineral grains (Vassilev & Vassileva 1996).

Crystalline minerals in coal form through multiple processes. They may be introduced into the peat by sediment input through epiclastic (physical weathering) and pyroclastic (volcanic) mechanisms. Biogenic components, such as microorganisms and plant residues, also contribute minerals during peat accumulation. Additionally, minerals can precipitate within the swamp environment during early diagenetic stages.

Minerals in coal are often visible in hand specimens and can be identified during the examination of drill cores, outcrops, or mine exposures. They commonly occur as thick pyrite-rich clay bands, rounded pellets or nodules, dispersed crystals within the coal matrix, or as coatings and fillings along fractures and cleats. Microscopic investigation revealed that many mineral grains intimately associate with organic matter, existing as isolated euhedral crystals, fragmented detrital particles, microscopic nodules, or even sub-microscopic crystalline aggregates closely embedded within the coal fabric (Shao et al., 2022).

This intricate mineral-organic association reflects coal's complex genesis and influences its physical, chemical, and combustion properties.

Table 2: Mineral deposits present in coal (Dai et al., 2021; Finkelman et al., 2018).

Mineral deposits	**Mineral**	**Chemical Formula**
Silicates	Kaolinite	$Al_2Si_2O_5(OH)_4$
	Illite	$KAl_2(AlSi_3)O_{10}(OH)_2$
	Montmorillonite	$Na(AlMg)Si_4O_{16}(OH)_2$
	Chlorite	$(MgFeAl)_6(AlSi)_4O_{10}(OH)_8$
	Quartz	SiO_2
	Feldspar	$KAlSi_3O_8$
Carbonates	Calcite	$CaCO_3$
	Siderite	$FeCO_3$
	Dolomite	$CaMg(CO_3)_2$
	Ankerite	$Ca(Fe,Mg)CO_3$
	Aragonite	$CaCO_3$
Sulfides	Pyrite	FeS_2
	Marcasite	FeS_2
	Sphalerite	ZnS_2
	Galena	PbS
	Chalcopyrite	$CuFeS_2$
Sulfates	Gypsum	$CaSO_4 \cdot 2H_2O$

	Barite	$BaSO_4$
	Anhydrite	$CaSO_4$
	Coquimbite	$Fe_2(SO_4)_3{\cdot}9H_2O$
	Szomolnokite	$FeSO_4{\cdot}H_2O$
	Natrojarosite	$NaFe_3(SO_4)_2(OH)_6$
	Thernadite	Na_2SO_4
	Bassinite	$CaSO_4{\cdot}½H_2O$
	Celestite	$SrSO_4$
Phosphates	Apatite	$Ca_6F(PO_4)_3$
	Goyazite	$SnAl_3(PO_4)_2(OH)_5.5H_2O$
Other Minerals	Anatase	TiO_2
	Boehmite	AlO(OH)
	Hematite	Fe_2O_3
	Goethite	$Fe(OH)_3$
	Zircon	$ZrSiO_4$

2.4.1 Silicates

Silicate minerals in coal occur in multiple forms depending on their type and origin. Clay minerals are the most common silicate minerals in coal. They are derived from chemical precipitation and detrital clastic transports (Shao et al., 2022). Clay minerals such as kaolinite, illite, muscovite, and montmorillonite are commonly found as fine-grained, platy, book-page, or flaky textures, often dispersed within organic matrix, coating organic matter or filling voids and fractures. For example, kaolinite in the Late Permian C1 coal from Yunnan Province has an authigenic origin, formed in situ within the depositional environment (Li et al., 2020). In the Taoshuping deposits, kaolinite is present as thin bands and associated with vitrinite. In a few cases, a small portion of kaolinite is found in a vermicular structure within collodetrinite or as fillings in cellular spaces (Wang et al., 2012). Similarly, in the Datong coalfield, kaolinite was found in two forms, firstly as aggregates filling the cell cavities in organic matter suggesting authigenic origin and as striped kaolinite from terrigenous clastic transport (Shao et al., 2022).

Quartz is the most common silicate mineral present in coal. In the Late Permian C1 Coal, the presence of quartz indicates past volcanic activity and magmatic alteration. Quartz associated with volcanic activity appears as angular fragments or elongated particles embedded within a kaolinite matrix. Conversely, quartz related to magmatic origins tends to display subangular to subrounded grains with serrated edges (Li et al., 2020). Wang et al. (2012) reported that volcanic quartz is closely linked to organic matter and typically occurs as euhedral crystals or melt-formed grains. In Taoshuping coals, quartz appears as irregular grains within bands of collodetrinite, fusinite, semifusinite, cutinite, and macrinite, suggesting an authigenic origin. Meanwhile, detrital quartz derived from terrigenous sources occurs as solitary grains within the coals (Wang et al., 2012). This variation in quartz morphology and origin reflects the complex depositional and post-depositional history of coal, affecting its mineralogical and chemical properties.

2.4.2 Carbonates

Calcite is the most common carbonate mineral found in coal, followed by siderite and dolomite. Lesser amounts of ankerite and aragonite are also present. These minerals are primarily authigenic, forming within the coal seams as cleat infillings (Vassilev & Vassileva, 1996). They exhibit both syngenetic and epigenetic origins. Wang (2017) identified three main modes of calcite occurrence in coal. First, calcite can be present in veins filled with organic matter or other minerals, indicating an epigenetic origin. Second, network-like calcite veins are associated with multiphase fluid activity. Third, calcite may occur as clusters or prism-shaped particles occupying pores within organic material. Syngenetic calcite appears as individual grains, lenses, or fills cell cavities. Li et al. (2016) reported that calcite formation can result from limestone dissolution followed by the precipitation of Ca and Mg within fractures in coal seams. This mineral diversity and textural complexity reflect the dynamic geochemical environment influencing coal formation and mineralization.

Siderite predominantly forms during the syngenetic stage of coal development under oxygen-deficient conditions (Dai et al., 2015). The presence of syngenetic siderite within coals indicates deposition in non-marine environments (Vassilev and Vassileva, 1996). Typically, siderite precipitates authigenically during diagenesis and manifests as small nodules or as infillings within organic matter. Most siderite coexists with pyrite, while a smaller fraction is distributed throughout

the kaolinite matrix because both siderite and pyrite form under similar reducing, low-oxygen conditions rich in iron and sulfur. During coal diagenesis, iron is commonly available in the environment, and sulfur from organic matter or external sources reacts with iron to form pyrite. When sulfur is limited, iron may instead combine with carbonate ions to precipitate siderite.

Dolomite, another authigenic mineral, typically occurs in coal seams as coal concretions developed in warm, saline environments. Syngenetic dolomite presents as discrete grains, lenses, or fills cellular pores (Querol et al., 2001). Both calcite and dolomite commonly occur near igneous intrusions, where hydrothermal fluids facilitate their formation (Shao et al., 2022). This mineral assemblage reflects complex geochemical and environmental interactions during coal formation, influencing coal's properties and behavior during utilization.

2.4.3 Sulfides

Sulfide minerals in coal exhibit both syngenetic and epigenetic origins. Pyrite is the dominant sulfide mineral found, with lesser occurrences of marcasite and sporadic findings of chalcopyrite, bornite, and pyrrhotite (Dai et al., 2021). The presence of pyrite in some coals is attributed to Fe derived from mafic volcanic ash and S from seawater (Dai et al., 2011). Additionally, Li et al. (2016) reported pyrite formation resulting from the precipitation of epithermal fluids. Syngenetic and epigenetic pyrites are typically associated with marine depositional environments, while syngenetic pyrite also forms in sulfate-rich groundwater. Epigenetic pyrite commonly occurs as cleat fillings within coal seams (Ward, 2002). Morphologically, pyrite displays a range of forms including isolated euhedral crystals, framboidal structures, irregular shapes, fracture infillings, and aggregates of euhedral crystals (Ma et al., 2022). Marcasite, an orthorhombic allotrope of pyrite with a less stable crystal structure, rarely occurs as cleat fillings in coal. It forms mainly during late epigenetic processes under low-temperature and acidic conditions. In coal, marcasite is found as radial and spheroidal crystalline clusters (Wang et al., 2016). This mineral variability highlights the complex geochemical conditions influencing sulfide mineralization in coal seams.

2.4.4 Sulfates

Gypsum and barite are the most common syngenetic sulfates minerals present in coal (Finkelman et al., 2018; Liu et al., 2018; Ward, 2002). Vassilev and Vassileva (1996) reported that these

minerals formed during epigenetic process and occur as long prismatic crystals and in some instances as crack infilling. Liu et al. (2018) explained that gypsum is formed by the precipitation of dissolved sulfate and calcium. They reported that substantial portions of Fe, Ca, and Fe exist as dissolved salts, ionic forms bounded in carboxylates, and metal cations in organometallic complexes. They highlighted that Al, Ca, and Fe are present in organic complexes, but a small portion of Ca and Al are present in water soluble and non-mineral organic form.

2.4.5 Phosphates

Apatite is the most prevalent mineral in coal, with REE-bearing minerals such as monazite and xenotime occurring less frequently but still present in many coal deposits (Dai et al., 2015, 2018; Ward, 2016). Apatite primarily occurs as prismatic crystals and in a few cases as clusters. Apatite is primarily associated with the influence of hydrothermal fluids (Permana et al., 2013), volcanic ash input (Zhao et al., 2012) and terrigenous detritus (Dai et al., 2013). The apatite mineral in the Datong coal mine suggested an authigenic origin as it occurred as crystal particles in the pores of coal seam (Shao et al., 2022). The occurrence of apatite and aluminophosphates of the crandallite group as both syngenetic cell and pore infillings or epigenetic cleat and fracture fillings in the coal seam is attributed to earlier remobilization of phosphate (Ward, 2002).

2.4.6 Other minerals

Zircon and monazite occur within the kaolinite matrix in coal as subhedral to euhedral grains (Li et al., 2020). Anatase is present both as cubic crystals within kaolinite and as elongated strips in boehmite (Shao et al., 2022). Zircon typically appears as euhedral or square-shaped crystals, however, a minor fraction exhibits volcanic origin, identified by bubble cavities (Li et al., 2020). In the Datong Coalfield, detrital zircon grains are predominantly rounded and massive, displaying platy or tetrahedral crystal habits (Shao et al., 2022). Monazite occurs as discrete spherulitic aggregates within coal (Li et al., 2020). This mineralogical diversity within the kaolinite matrix highlights the complex provenance and depositional history of coal-forming environments.

Well-developed anatase crystal structure is associated with hydrothermal alteration (Dai et al., 2014). Anatase originating from terrigenous sources in the Taoshuping coals occurs as single

irregular grains and/or as filling in cellular spaces in the organic materials (Wang et al., 2012). Hematite and magnetite in coal are associated with oxidation during weathering. They occur as fine-grained, anhedral to subhedral particles and often as inclusion in oxidized zones of coal (Wagner et al., 2019). On the other hand, ilmenite is considered as detrital, deposited with other minerals during the sedimentary process. It occurs as fine-grained, detrital particles and often associated with heavy mineral assemblages. In some cases, it occurs within the coal matrix (Farjana et al., 2021).

2.5 Mode of occurrence of CRMs in coal and coal by-products

Mode of occurrence refers to how CRMs are chemically bound and disseminated within a material. It provides valuable insights into the origin of CRMs, the geochemical processes undergone by the peat and coal, and crucially, how the CRMs will behave during coal cleaning, utilization, leaching and disposal (Dai et al., 2021). It is crucial to understand the chemical form and association of CRMs in coal, as this will help in successfully devising technologies that can economically extract CRMs from coal.

2.5.1 Types of mode of occurrence

There are three types of mode of occurrence: inorganic, organic and intimate organic associations. Inorganic associations/minerals refer to those elements that hosted by macroscopically or microscopically discrete mineral phases and ion-exchangeable forms. Organic associations describe elements that are chemically bound by the organic matter in coal such as carboxylates in low rank coal, while intimate organic associations include elements adsorbed onto organic surfaces, dissolved in pore water, and hosted in very fine-grained minerals within coal. These elements are adsorbed on the surface of the organic matter and sometimes are dissolved in water pores of the coal (Dai et al., 2021).

2.5.2 Mode of occurrence of major elements in coal and coal by-products

Major elements are elements with a concentration exceeding 0.1 wt%, however, in certain instances, the concentration of TiO_2, MnO, K_2O, Na_2O, and P_2O_5 may be below 0.1 wt% (Dai et al., 2021). These include elements associated with organic matter (C, H, O, N, and S) and those associated with inorganic compounds (SiO_2, TiO_2, Al_2O_3, Fe_2O_3, MnO, CaO, MgO, K_2O, Na_2O, Cr_2O_3, and P_2O_5) (Dai et al., 2017, 2011; Yuan et al., 2019).

Table 3: Probable mode of occurrence of major elements in coal (Dai et al., 2021; Finkelman et al., 2018).

Major elements	**Mode of Occurrence in Coal**
SiO_2	Found in quartz and silicate minerals (e.g., clays like kaolinite, illite, and montmorillonite).
TiO_2	Associated with Ti-bearing minerals such as rutile (TiO_2), anatase, and ilmenite ($FeTiO_3$).
Al_2O_3	Found in clay minerals like kaolinite, illite, and montmorillonite; can also occur in feldspars.
Fe_2O_3	Associated with pyrite (FeS_2), hematite (Fe_2O_3), and siderite ($FeCO_3$); can also occur in mixed oxides.
MnO	Found in manganese carbonates (e.g., rhodochrosite), oxides, and silicate minerals.
CaO	Present in calcite ($CaCO_3$), dolomite ($CaMg(CO_3)_2$), or gypsum ($CaSO_4 \cdot 2H_2O$).
MgO	Found in dolomite ($CaMg(CO_3)_2$), magnesite ($MgCO_3$), and other magnesium-bearing silicates.
K_2O	Associated with clay minerals like illite and feldspars.
Na_2O	Present in feldspars, clay minerals, and saline minerals like halite (NaCl).
P_2O_5	Found in phosphate minerals such as apatite ($Ca_5(PO_4)_3(F,Cl,OH)$).
Cr_2O_3	Occurs in chromite ($FeCr_2O_4$) and other chromium-bearing spinels.

Silicon (Si)

In general, Si is the most dominant inorganic element in coal. It is predominant in silicate minerals such as quartz (Spears & Booth, 1999). Si is also found as part of aluminosilicates, contributing to the mineral matter in coal (Dai et al., 2019). A negligible portion of Si is associated with organic matter (Wigley et al., 2000).

Aluminum (Al)

Al is the second dominant inorganic element in coal. It primarily occurs in mineral forms such as boehmite (Li et al., 2016), illite/smectite layers, mullite, illite and kaolinite, and to a lesser extent as micas and feldspar, along with at least 30 other aluminum-bearing minerals (Finkelman et al., 2019). In addition to mineral forms, non-mineral Al exists as organometallic complexes (Liu et al., 2018; Grigore & Sakurovs, 2016). Al in coal interacts with other elements such as Si, to form alumino-silicate minerals that are thermally stable during combustion (Dai et al., 2019). While Al is primarily inorganic, a small portion is associated with organic matter (Liu et al., 2018).

Iron (Fe)

Fe in coal primarily occurs in mineral forms such as pyrite, siderite, ankerite, hematite, magnetite, ilmenite, goethite, lepidocrocite, limonite, coquimbite, melanterite, rozenite, szomolnokite, jarosite, copiapite, vivianite, chromite, to a lesser extent as marcasite and in few instances as bornite, pyrrhotite, chalcopyrite, arsenopyrite, and mackinawite (Dai et al., 2021; Finkelman et al., 2018; Querol et al., 2001). Some Fe-bearing minerals are chlorite, micas, mixed layer clay, garnet, montmorillonite, pyroxene, vermiculite, ferroselite, eskebornite, amphiboles, olivine, tourmaline, and interlayered berthierine/chamosite (Dai et al., 2021; Finkelman et al., 2018, 2019; Li et al., 2021; Ward, 2002). Even though Fe is in inorganic form, in low rank coals, Fe is associated with organic matter (Dai et al., 2021, 2011). The content of Fe as pyrite decreases with increasing specific gravity of the coal fraction (Huggins & Huffman, 1996). This could lead to a high content of Fe in carbonate minerals (Querol et al., 2001).

Magnesium (Mg)

The presence of Mg in coal is attributed to rock fragmentation and deposition of detrital minerals. Mg is primarily associated with clay and carbonates minerals (Dai et al., 2021; Finkelman et al., 2019, 2018). The occurrence of Mg in high rank coals is associated with siderite, ankerite, magnesite and dolomite, where it substitutes either Ca or Fe and in clay mineral such as illite it occurs as adsorbed cations while in low rank coals a portion of Mg is associated with organic matter (Dai et al., 2021). Mg, Ca, and Fe have similar ionic radii, charges, and electronegativity. Under certain conditions Mg^{+2} may substitute either Fe^{+2} or Ca^{+2} in carbonate minerals and adsorbs onto clay mineral surfaces. Other Mg-bearing minerals in coals are smectite, pyroxene, olivine, biotite, garnet, chlorite, vermiculite, talc, chromite, clinoptilolite, amphiboles, bischofite, augite, chrysotile, diopside, heuland, spinel, and interlayered berthierine/chamosite (Dai et al., 2021; Finkelman et al., 2019; Li et al., 2021).

Calcium (Ca)

Ca is primarily associated with carbonate and sulfate minerals such as calcite, anhydrite, and gypsum and to a lesser extent with phosphate, organic minerals, silicates, hydroxides, and zeolites (Dai et al., 2021; Finkelman et al., 2018). Ca may replace Mg and Fe in mineral structures within the coal matrix and be present as exchangeable cations on the surface of clay minerals. Dai et al. (2021) noted that the actual mode of occurrence of Ca is partly attributed to the rank of coal. In high-rank coals, Ca is mainly hosted by carbonate minerals, while in low-rank coal, a portion of Ca is associated with organic matter.

Sodium (Na)

Na in coal is associated with feldspars, tourmaline, smectite, analcime, pyroxenes, clinoptilolite and paragonite and to a lesser extent, with halite, Na-Autunite, dawsonite, sideronatrite, natrojaronite, blodite, natroalunite, glauberite and thenardite (Finkelman et al., 2019; Ward, 2002). Na's occurrence in coal depends on its rank. Na in high-rank coal is hosted by clay minerals, while in low-rank coal it is associated with organic matter (Swaine, 1990).

Titanium (Ti)

Ti in coals occurs as Ti-oxides (Figure 12), as rutile and anatase. In a few instances it is present in mineral form such as ilmenite, brookite and brannerite (Finkelman et al., 2018; Yuan et al., 2019). In low-rank coals, it is associated with organic matter (Finkelman et al., 2018; Swaine, 1990). Ti is also found within vitrinite (Van Alphen, 2005). Selective leaching studies by Finkelman et al. (2018) revealed that Ti is associated with organic matter (~15% in low-rank coals) and aluminosilicates (~70% in low-rank coals and ~65% in bituminous coals). Dai et al. (2015) found Ti in kaolinite in Paleozoic coal in Inner Mongolia, China, where it either substitutes for Al in clay minerals or occurs as separate Ti-bearing phases. This mode of occurrence was similarly observed in coals from the Gunnedah Basin in Australia.

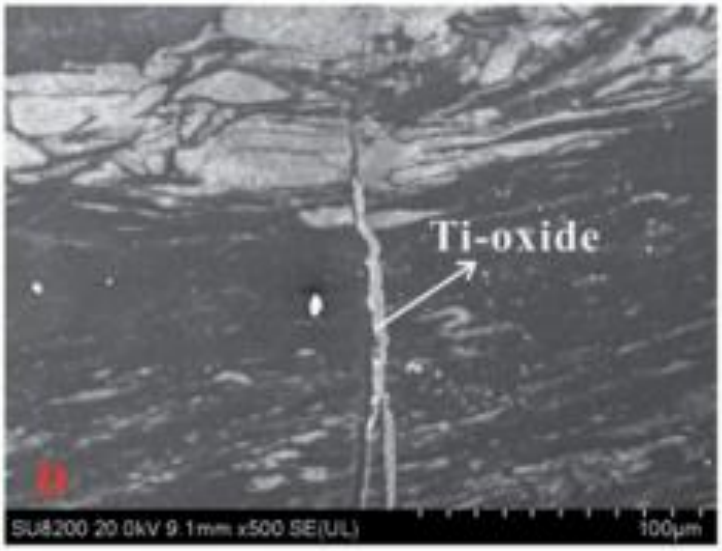

Figure 12: Epigenetic Ti-oxides (Yuan et al., 2019).

Manganese (Mn)

A substantial portion of Mn in coal is attributed to water soluble carbonate minerals (Spears & Booth, 1999). Mn is primarily found in siderite, calcite and ankerite (Qiao et al., 2020; Querol at al., 2001; Valentim et al., 2013) while in carbonate-poor coals it is found in organic matter or associated with clay mineral such as illite (Huggins & Huffman, 1996; Swaine, 1990). Other Mn-bearing minerals are pyrite, garnet, chlorites, pyroxenes, messelite, tourmalines, pennantite,

allanite, and epidote (Finkelman et al., 2019). Swaine (1990) reported that organic matter is the major carrier of Mn in low-rank coals.

Potassium (K)

K primarily occurs in clay minerals, particularly illite, and interlayered illite/smectite (Swaine, 1990). Finkelman et al. (2018) reported that their leaching experiments showed a small portion of K is associated with organic matter. Other K-bearing minerals are muscovite, amphiboles, microline, roscoelite, magnesioarfvedsonite, orthoclase, biotite, clinoptilotite, sanidine, whiillite and heulandite (Dai et al., 2017, 2018; Erkoyun et al., 2019; Falcon 1978) and to a lesser extent jarosite, natroalunite, alunite, kalinite, natrojarosite and alum-K (Dawson et al., 2012; Lipiarski et al., 2004).

Chromium (Cr)

The mode of occurrence of Cr in coal is a challenge, and the confidence level of mode of occurrence is 2 (Finkelman, 1994). Many studies have shown multiple modes of occurrence of Cr in coal, for instance some studies showed that 75% of Cr is associated with aluminosilicates while 25% is associated with sulfides (Querol et al., 2001; Huggins & Huffman, 1996). Spears & Booth (1999) reported that silicate minerals, specifically illite are the major carriers of Cr in coals. Swaine (1990) concluded that Cr in low-rank coals is organically associated.

Phosphorus (P)

P primarily occurs in minerals, particularly in P-bearing minerals such as goyazite, crandallite group minerals, REE-bearing phosphate, and apatite (Dai et al., 2015, 2021; Finkelman et al., 2018). In addition, P also occurs as an autochthonous phosphate in tonsteins, not just in the form of detrital apatite (Dai et al., 2021). Swaine (1990) mentioned that there is a possibility of organic P compound in coal, although there is no direct evidence for organically bound P.

2.5.3 Mode of occurrence of trace elements in coal and coal by-products

Trace elements are elements with a concentration of less than 0.1 wt%. However, in some cases, the concentration of F, Cl, Se, Be, REY, Ge, U, and As may be greater than 0.1 wt% (Dai et al., 2021). The modes of occurrence of trace elements vary widely and include sulfides, carbonates, oxides, silicates, organic association, and others (Table 4).

Table 4: Probable mode of occurrence of trace elements in coal (Dai et al., 2021; Finkelman et al., 2018).

Element	**Mode of Occurrence in Coal**
Ba (Barium)	Found in barite ($BaSO_4$), with clay minerals, or adsorbed onto organic matter.
Ce (Cerium)	Part of the rare earth elements (REEs); associated with phosphate minerals (e.g., monazite, apatite) or clays.
Co (Cobalt)	Found in pyrite and other sulfides; can occur in organic matter.
Cu (Copper)	Present in chalcopyrite ($CuFeS_2$), other sulfides, and organic associations.
Ga (Gallium)	Commonly associated with clay minerals or coal's organic fraction.
La (Lanthanum)	Part of the REEs; associated with phosphate minerals, clays, or organic matter.
Li (Lithium)	Associated with clay minerals, feldspars, or organic matter.
Mo (Molybdenum)	Present in pyrite or other sulfides; can occur in organic matter.
Nb (Niobium)	Associated with heavy minerals like rutile, ilmenite, or silicates.
Nd (Neodymium)	Part of the REEs; associated with phosphate minerals or clays.
Ni (Nickel)	Found in pyrite, other sulfides, or bound to organic matter.
Pb (Lead)	Present in galena (PbS), other sulfides, or adsorbed onto organic matter or clays.
Pr (Praseodymium)	Part of the rare earth elements (REEs); associated with phosphate minerals (e.g., monazite, apatite) or clays.
Sc (Scandium)	It occurs in phosphate minerals, clay minerals, or adsorbed onto organic matter.

Sr (Strontium)	Present in carbonates like calcite, aragonite, or phosphates like apatite.
Y (Yttrium)	Part of the REEs; associated with phosphate minerals, clay minerals, or organic matter.
Zn (Zinc)	Found in sphalerite (ZnS), other sulfides, or adsorbed onto organic matter.
Zr (Zirconium)	Present in zircon ($ZrSiO_4$) or other heavy mineral

Barium (Ba)

Ba is present in coal in multiple forms. It primarily occurs in witherite, barite (Hao et al., 2022; Swaine, 1990), barytocelestine, and gorceixite (Swaine, 1990) as part of crystal structure. It also occurs in crandallite primarily as a substitute for Ca within its crystal structure (Bytnar & Makowska, 2017; Hao et al., 2022). In low-rank coals, it primarily occurs in organic matter through carboxyl group (Bytnar & Makowska, 2017; Hao et al., 2022; Ward, 2002).

Strontium (Sr)

Sr is primarily associated with sulfates, phosphates, carbonates, and clay. In high-Ge and Low-Ge, it occurs in gypsum along with Ca (Liu et al., 2021). Sr-bearing minerals are gorceixite, goyazite, crandallite, barite, calcite, celestine, strontianite, gypsum, and clay (Dai et al., 2013, 2015; Spiro et al., 2019; Swaine, 1990). Some rare Sr-bearing minerals are heulandite, clinoptilolite (Çelik et al., 2021) and svanbergite (Çelik et al., 2021; Li et al.,2016). Swaine (1990) reported that most Sr is predominant in organic matter in low-rank coals.

Lithium (Li)

Li is primarily associated with silicates minerals (Dai et al., 2021) and to a lesser extent with organic matter (Wang et al., 2022). Li-bearing minerals are svanbergite (Li et al., 2016), illite, montmorillonite, detrital mica, and tourmaline (Sun et al., 2022). Li also occurs in kaolinite in the form of ions adsorbed on the surface (Li et al., 2016; Shao et al., 2022; Sun et al., 2022). Zhao et

al. (2019a) reported that the presence of Li in coals is due to hydrothermal fluids generated by magmatic activities but to Wang et al. (2022) is due to volcanic eruption.

Gallium (Ga)

Ga is primarily associated with clay minerals (Dai et al., 2021) and in some cases it is present in sulfide minerals such as sphalerite (Dai et al., 2021; Davidson & Rythoven, 2023). Ga occurs in kaolinite, gibbsite, goethite, and boehmite as a substitute for Al within their crystal structures due to similar radii and charges (Finkelman et al., 2019; Li et al., 2016; Shao et al., 2022). The few other Ga-bearing minerals are disapore, goyazite (Finkelman et al., 2019) and svanbergite (Li et al., 2016).

Rare earth elements and Yttrium (REY)

REY in coals occurs in multiple forms (Figure 13). The modes of occurrences of REY are associated with their geological origins such as detrital inputs from source rocks via wind and water, mineralized REY-rich fluids, and volcanic ash deposits (Dai et al., 2021; Fu et al., 2022). The main mode of occurrence of REY in high-REY coals is fine-grained authigenic and organic compounds (Seredin & Dai, 2012). Ca-bearing REE-phosphate minerals such as monazite are the major carriers of REY (Zhao et al., 2019). Lighty-REY such as La, Ce, Pr and Nd are hosted by phosphate minerals whilst heavy-REY (from Sm to Lu) are hosted by phosphate minerals and organic matter (Zhao et al., 2019a). REEs are enriched in Ca and Fe rich aluminosilicates (Kolker et al., 2017), in Al and Si rich aluminosilicates (Thompson et al., 2018) and in Al and P rich aluminosilicates (Pan et al., 2018). Major REE-bearing minerals are monazite, xenotime, cerium-rich minerals (Hower et al., 2018; Rerani et al., 2024), kaolinite, and boehmite (Shao et al., 2022).

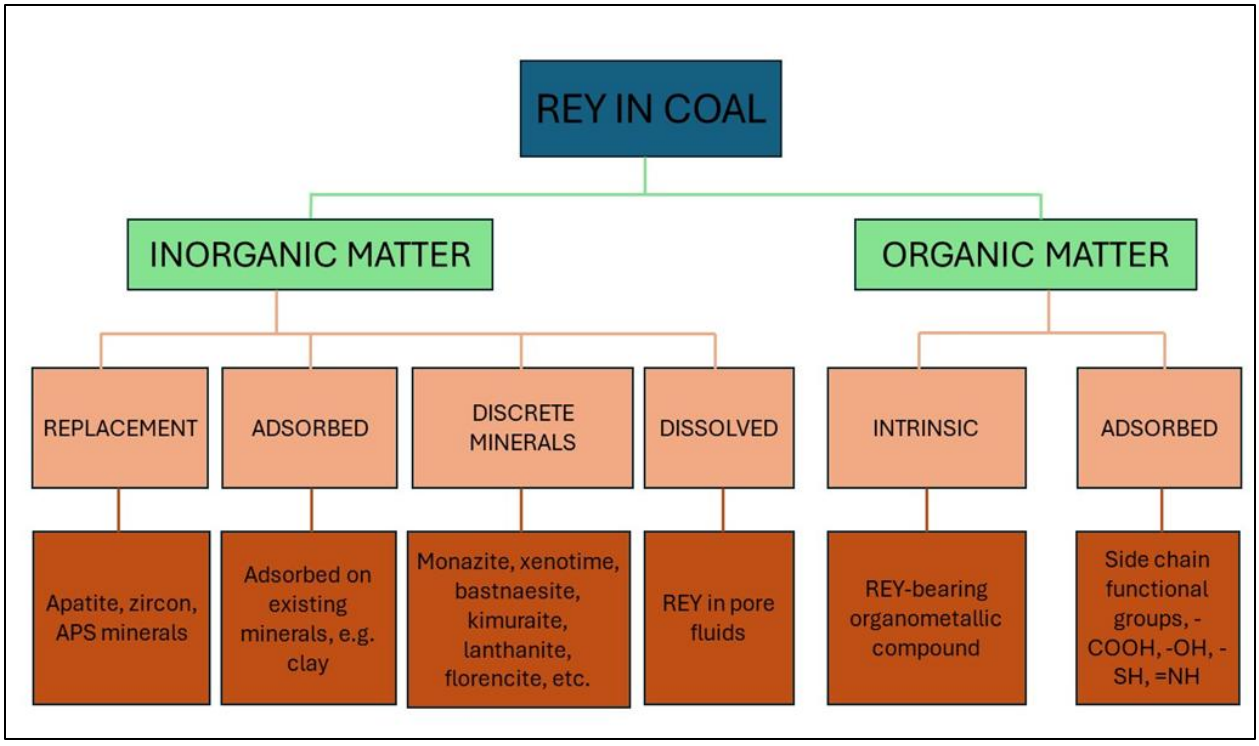

Figure 13: General mode of occurrence of REYs in coal (Fu et al., 2022).

Zirconium (Zr)

Zr primarily occurs as part of the mineral zircon (Swaine, 1990; Yuan et al., 2019) and in few cases, it occurs in organic matter and typically substitutes Fe within the pyrite crystal lattice (Yuan et al., 2019). The substitution usually takes place in pyrite associated with other heavy minerals. Notably, its incorporation is limited due to the difference in ionic radii and crystal structure between Zr and Fe. It may occur in pyrite as part of composite minerals grains, where pyrite is intergrown with other Zr-bearing minerals and as an impurity. In certain instances, it exists as part of pyrite aggregates, where pyrite is found along Zr-bearing minerals or zircon (Yuan et al., 2019).

Beryllium (Be)

The mode of occurrence of beryllium requires further refinement. Its mode of occurrence was investigated using indirect methods and has not yet been supported by direct methods. In many coals, Be is associated with organic matter (Swaine, 1990). Querol et al. (2001) reported that

aluminosilicate minerals are the main carriers of Be. Spears & Booth (1999) also reported that Be is associated with pyrite, carbonate, silicate, and organic matter. Dai et al. (2015) found that Be may occur as part of the mineral hydrous beryllium sulfate.

Cobalt (Co)

Co in coal occurs in many forms. There is an elevated level of uncertainty concerning the mode of occurrence of Co in coal (Finkelman, 1994). It is associated with pyrite (Swaine, 1990; Wigley et al., 2000), linnaeite-group mineral, organic matter (Swaine, 1990), aluminosilicates, carbonates (Querol et al., 2001), and to a lesser extent with illitic clay minerals (Wigley et al., 2000). Other Co-bearing minerals are cattierite and siegenite (Dai et al., 2015).

Molybdenum (Mo)

Mo in coals has multiple modes of occurrence (Swaine, 1990). It is primarily associated with organic matter and sulfides (Dai et al., 2021; Querol et al., 2001). Its mode of occurrence also depends on the rank coal, in high-rank coals, it is mainly found in sulfides and to a lesser extent in silicates, carbonates, sulfates and organic matter while in low-rank coals it is mainly found in silicates and to a lesser extent in sulfide and organic matter (Finkelman et al., 2018). Tian et al. (2013) reported that Mo has a strong association with pyrite. Riley et al. (2012) concluded that most of Mo existed in organic matter, and a small proportion of Mo existed in shielded grained or resistant minerals.

Niobium (Nb)

Nb primarily occurs in zircon, anatase and rutile (Dai et al., 2021; Li et al., 2017) and in rare cases it occurs in organic matter (Dai et al., 2015). Geological processes play a significant role in the concentration levels of Nb in coal. For instance, no Nb has been found to occur in authentic zircon (Dai et al., 2014). Nd is incorporated in the crystal structure of a perovskite-structured barium niobate (Hower et al., 2018).

Scandium (Sc)

Sc in coals primarily occurs in organic matter and aluminosilicate in varying proportions (Dai et al., 2021; Swaine, 1990). Swaine (1990) stated that the mode of occurrence of Sc is investigated by indirect methods such as selective leaching, statistical analysis, and density fraction and rarely by direct methods such as in situ analysis. Sc predominantly exists in organic matter (Arbuzov et al., 2014).

2.6 Previous work done at Witbank Coalfield

This coalfield has been the focus of extensive geochemical research due to its significant coal production and related environmental challenges. Thwala (2020) investigated the acid-generating potential by analyzing groundwater chemistry and acid-base accounting predictions. The study revealed that the Arnot and Goedehoop collieries have high concentrations of sulfide mineral, mainly pyrite. Thwala (2020) concluded that certain coal seams and discard facilities act as hotspots for sulfurous minerals, indicating a high risk of acid mine drainage (AMD) issues in these areas.

Pinetown et al. (2007) utilized XRD and XRF to investigate the mineralogical and geochemical composition of coal-bearing succession in the Witbank Coalfield. They found that quartz, kaolinite, dolomite, and pyrite were dominant minerals. These findings correlate with acid mining drainage potential, as pyrite oxidation is a significant contributor to AMD in the region. Similarly, Netshitungulwana et al. (2022) found that Witbank coalfield is dominated by sub-bituminous and high-volatile bituminous coals, with high content of kaolinite and quartz and minor content of pyrite, and carbonate while anatase and mica were present as accessory minerals. They noted the enrichment of Co, As, W, Zn, Yb, U, Se, Pb in stream sediments downstream of mining sites, emphasizing the need for effective environmental management strategies.

The geochemical investigation conducted by Maya et al. (2015) showed that Fe, Mn, and Ti were dominant major elements in the studied part of the Witbank coalfield, while their remote sensing technique identified areas with high concentration of heavy elements such as As and Pb. Recent research in the Witbank Coalfield revealed that monazite and xenotime were the major carriers of

REY +Sc (Modiba & Wagner, 2024; Rerani et al., 2024). It also revealed that the coal seams are primarily composed of kaolinite and quartz along with dolomite and pyrite. The analysis concluded that the average concentrations of light rare elements (LREEs) in the coal samples were notably higher than those of medium and heavy rare earth elements (MREEs and HREEs), suggesting a potential for economic extraction of these elements from coal deposit (Modiba & Wagner, 2024).

Furthermore, studies have shown that coal from Witbank contains critical elements such as Li, Sr, Zr and Ba, which are increasingly sought after for various industrial applications. Netshitungulwana et al. (2022) reported that the concentrations of Ba ranged from 62 to 931 ppm, Sr from 8.5 to 302 ppm and Zr from 45 to 838 ppm, whilst Pinetown et al. (2007) reported that the concentrations of Ba ranged from 5.68 to over 3000 ppm while of Sr and Zr from 2.85 to over 2000 ppm. The concentration and occurrence of Li in this coalfield are rarely reported.

The Witbank Coalfield remains a critical resource for South Africa's energy needs but poses significant environmental challenges due to its geological characteristics and historical mining practices. Continued research into the geochemical composition of trace elements in coal byproducts such as discard and fly ash is essential for combating global shortage of CRMs while mitigating the environmental impacts of coal discards.

Chapter 3: Method and Materials

3.1 Introduction

There were four research procedural stages followed to achieve this study's objectives. These stages are schematically represented in Figure 14 as field trips and sampling, coal discard quality assessment, mineralogical analysis, and geochemical analysis.

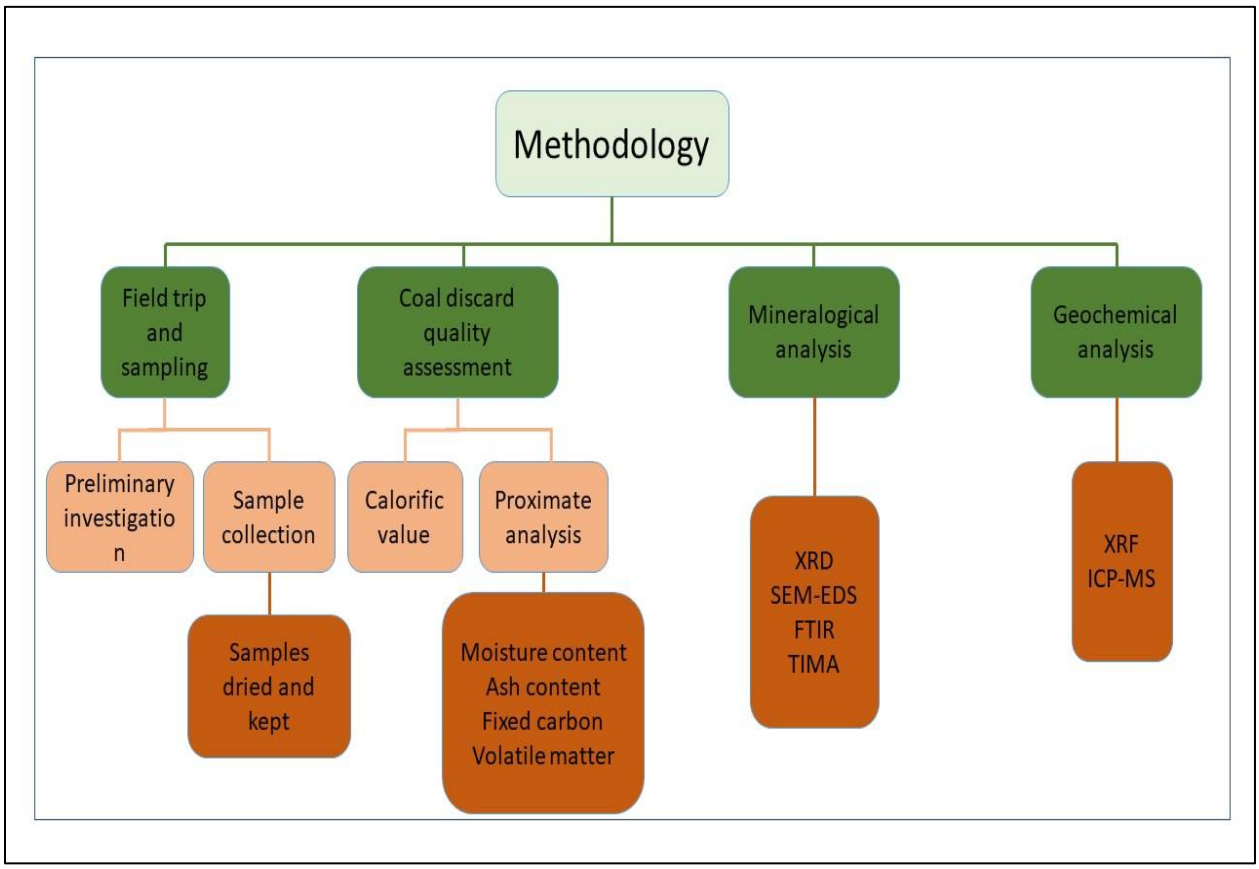

Figure 14: Schematical diagram for research procedural stages.

Based on Figure 14, the first stage, 'field trip and sampling' was executed through a field trip and inspection, collection, and storage of samples. The second stage is 'coal discard quality assessment', which involves determination of calorific value and proximate analysis parameters such as moisture, ash, fixed carbon (by calculation), and volatile matter contents. The third stage was the 'mineralogical analysis,' which involved X-ray diffraction (XRD), scanning electron microscopy coupled with energy dispersive spectroscopy (SEM-EDS), Fourier-transform infrared spectroscopy (FTIR), and Tescan integrated mineral analyzer (TIMA). The fourth stage was

'geochemical analysis', which involves the quantification of elements using X-ray fluorescence (XRF) and inductively coupled plasma mass spectrometry (ICP-MS).

3.2 Locality of the Study Area

The Coal Discard 1 (CD1) and Coal discard 2 (CD2) are situated within the Witbank Coalfield, located in the Mpumalanga Province of South Africa (Figure 15). The south-eastern part of the CD1 dump sits over the igneous intrusions from the Rooiberg Group (Figure 15).

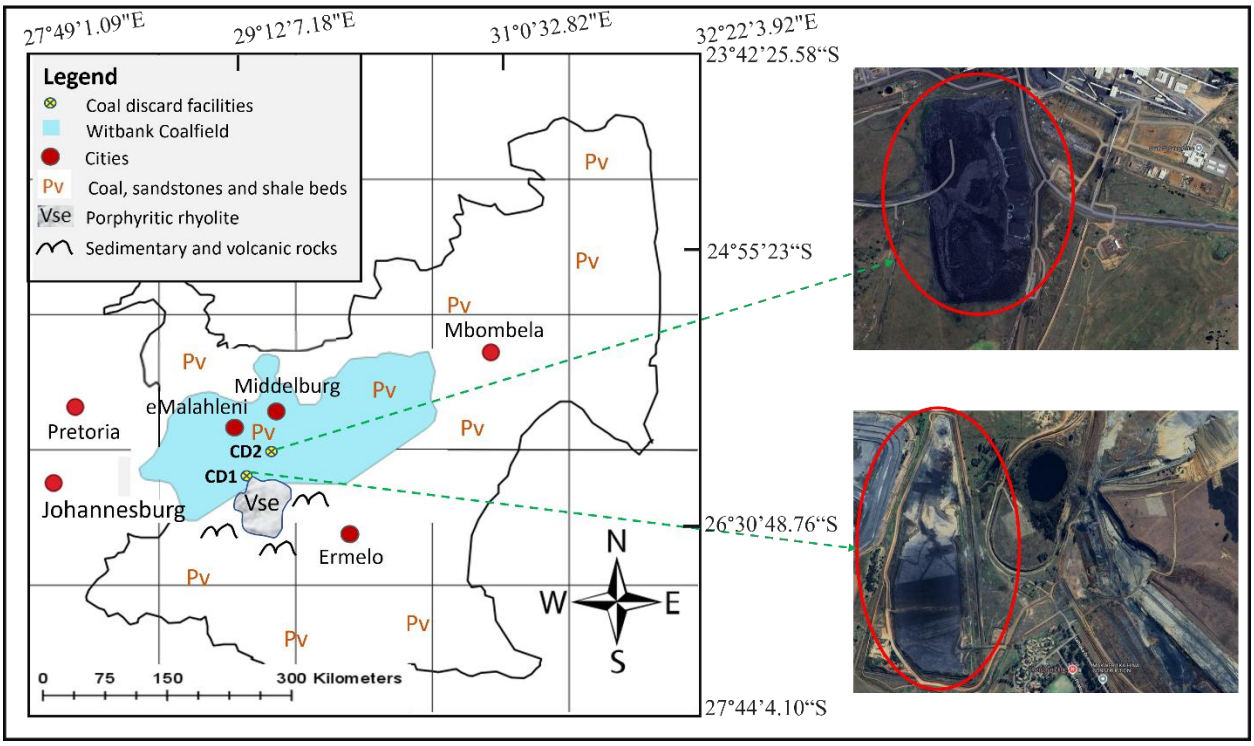

Figure 15: The map of the study area in the Mpumalanga Province.

3.3 Field Trip and Sampling

The adequate investigation and comprehensive collection of coal discard samples from the study areas was made possible by the considerable number of field trips.

3.3.1 Field Trip

The two coal discard dumps visited are CD1, located in Ogies, and CD2, located in Middelburg, both are in Witbank Coalfield in Mpumalanga Province. CD1 is a decommissioned dump (established in 1988 and decommissioned in May 2002), while CD2 is still an operational and new dump. The sites were selected for investigation due to their accessibility, contrasting ages, and differing operational statuses. However, the criteria pursued in the selection of the coal discard dumps were as follows:

For CD1 dump:

1. May contain what is deemed as good coal quality in modern days, which could not be processed by older technologies around the 1980s to early 1990s.
2. Well maintained and formal discard dump.
3. Effects of age, spontaneous combustion, and weathering on the mode of occurrence of elements in coal discards.

For CD2 dump:

1. Effects of age and coal quality.
2. Non-formal discard dump.

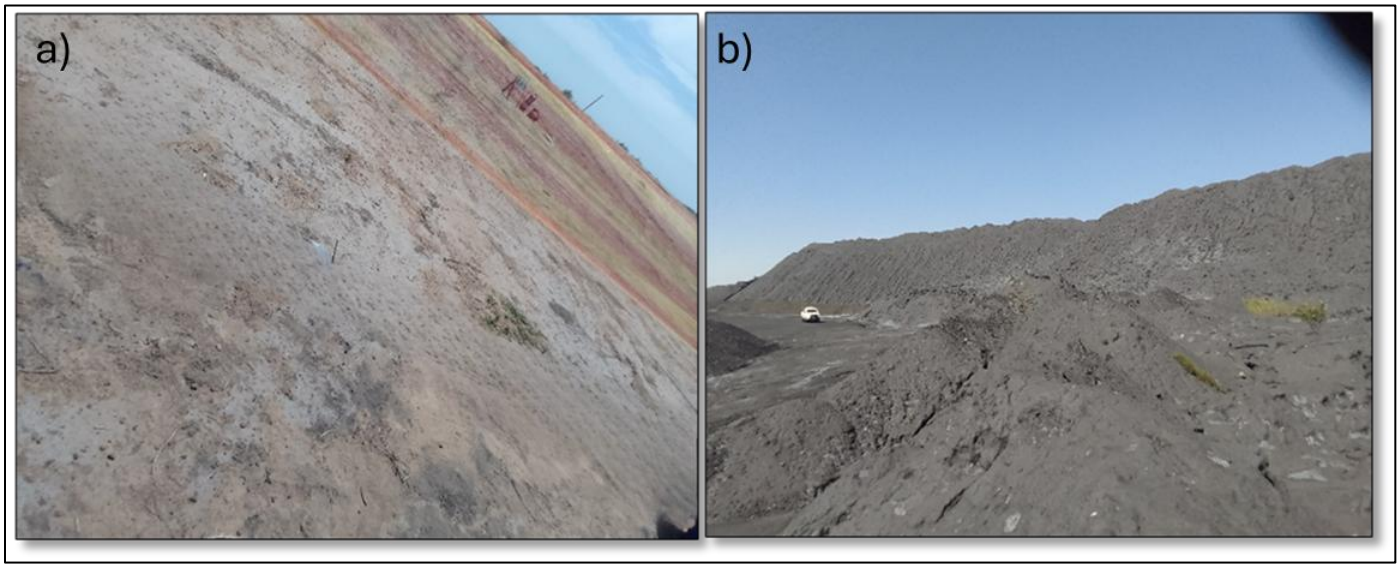

Figure 16: Pictures of coal discards dump taken during site visit a) CD1 dump and b) CD2 dump.

During the field trip inspection, the CD1 dump was rehabilitated and well maintained as illustrated in Figure 16a. While mechanical components such as pipelines and pump stations were removed, the penstock, under drainage, effluent trenches, and return water dam were not decommissioned and remained operational. Conversely, it was observed that deposition is still taking place in CD2 dump as illustrated in Figure 16b.

The collected samples were systematically labelled following a conventional pattern as demonstrated in Figure 17. The CD1 dump has an estimated volume of 6.4 million cubic meters, while the size of the CD2 dump remains unknown. After collection, all samples were carefully packed in plastic bags for transport from Mpumalanga to Johannesburg for subsequent analysis. Upon arrival, samples were air-dried and stored in the laboratory. In total, ninety-four coal discard samples were obtained, comprising seventy samples from the CD1 dump collected using a drill rig truck, and twenty-four samples from the CD2 dump. This careful sampling and handling procedure ensured the integrity and representativeness of the samples for accurate laboratory analysis.

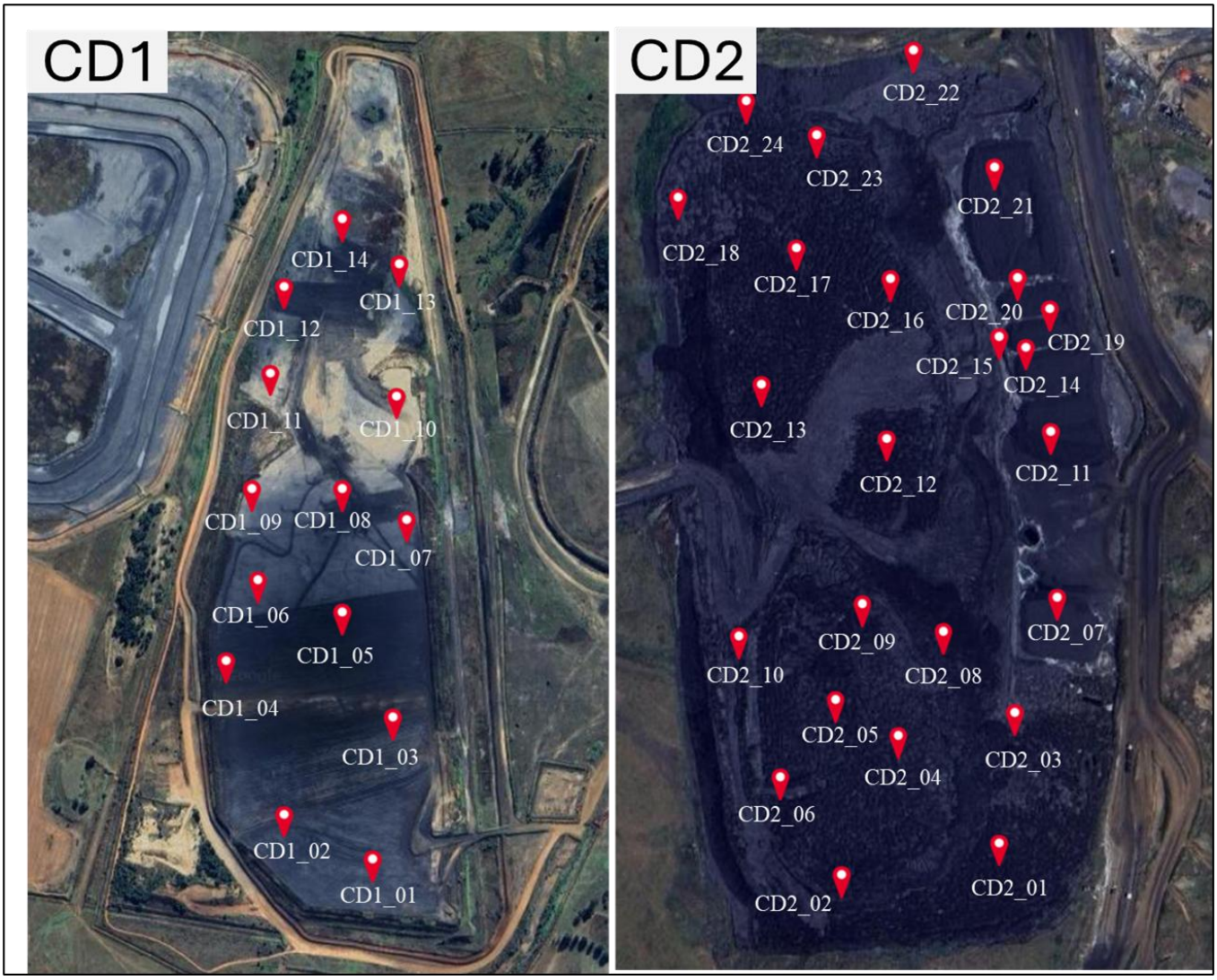

Figure 17: Google map extract for CD1 and CD2 dumps.

3.3.2 Sampling

The location and number of samples required from both sites were already known through desktop study mapping and a field trip. The core samples were obtained from the CD1 dump through drilling using a drill rig truck (Figure 19 A1), and the lump samples from the CD2 dump were collected using a shovel (Figure 19 A4). Fourteen (14) drilled core samples from CD1, each measuring 5 m deep and 80 mm (about 3.15 in) in diameter (Figure 19 A2 and A3). Each core was segmented into 1-meter intervals (0-1 m, 1-2 m, 2-3 m, 3-4 m, 4-5 m) and labelled as CD1_01 up to CD1_14 (0-1 m up to 4-5m) as shown in Figure 19 A2 and A3. The CD2 samples were obtained

in the form of lumps characterized by a weight distribution spanning between 5 to 7 kilograms per bag and put on a plastic bag to avoid contamination, labelled as CD2_01 – CD2_24 as shown in Figure 19 A4.

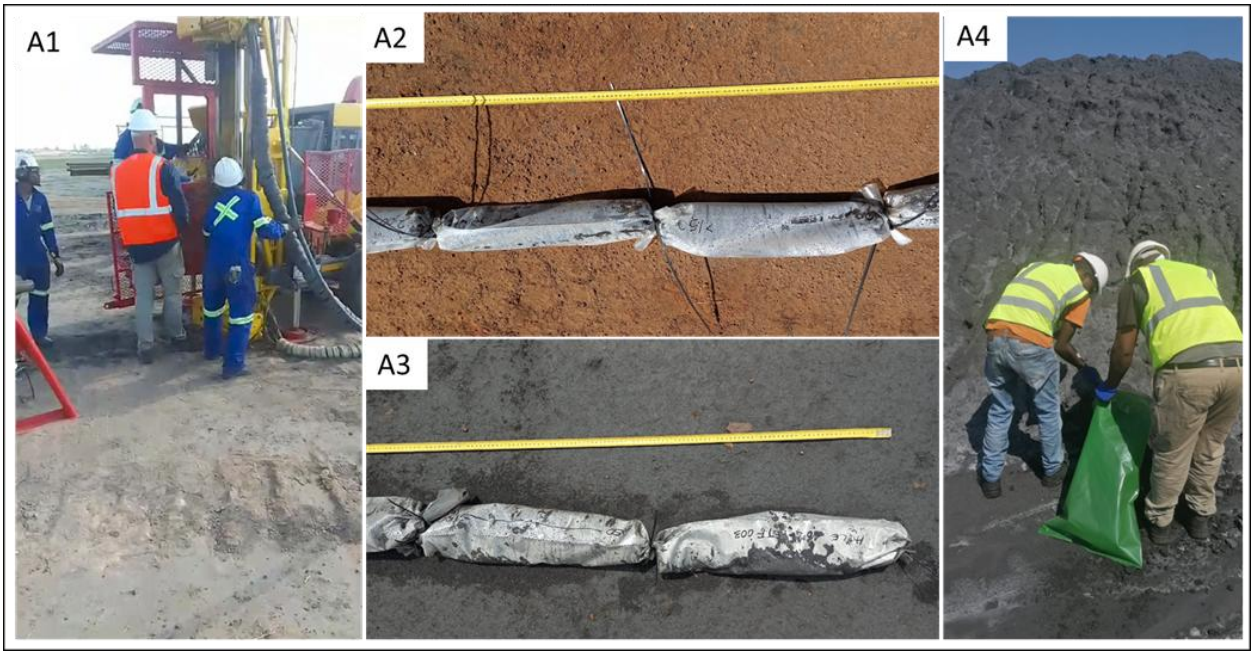

Figure 18: Drilling and sampling, A1 shows drill rig truck at CD1 dump, A2 and A3 show unconsolidated drilled core samples from CD1 dump, and A4 shows sampling at CD2 dump.

3.4 Sample Preparation

All samples were first air-dried before being crushed using a jaw crusher. The crushed material was then split into representative sub-samples using a sample splitter. From these, two opposing representative portions were extracted and ground further to pass through 212, 75, and 50 µm sieves. To prevent cross-contamination, stringent cleaning protocols were implemented. After processing each sample, the jaw crusher and splitter were cleaned with compressed air. The bowl and pestle of the end runner mill were thoroughly cleaned using acetone and wiped with a clean roll. Likewise, each sieve used in the analysis was washed with water and dried with compressed air before reuse.

3.5 Coal Discard Quality Assessment

The coal discard quality assessment techniques used in this study include proximate analysis and calorific values. The proximate analysis parameters such as moisture, ash, volatile matter and fixed carbon contents were determined following established international standards for coal and coke. The calorific values of the coal discards were also determined following established international standards for coal and coke.

3.5.1 Proximate Analysis

Proximate analysis was conducted on all samples that passed through the 212 μm sieve, following the ASTM D5142-09 standard (ASTM International, 2009). This analysis was performed using TGA 701 Leco equipment to obtain critical information on the physicochemical properties of the coal discard samples. These properties will assist in assessing coal discards' suitability for specific applications such as energy generation or other industrial processes, and the effects of each parameter on the mode of occurrence of CRMs.

In the TGA 701 Leco equipment, each crucible received a staged addition of 1 g of a representative sample. The proximate analysis procedure involves multiple steps. Initially, nitrogen was introduced for drying, starting at room temperature (around 20 °C) and gradually increasing to 107 °C at a heating rate of 8 °C/min, aiming to determine the moisture content through mass loss measurements. Subsequently, volatile matter content was then assessed by monitoring mass loss within the temperature range of 107 to 950 °C. Following this, a combustion process in an oxygen environment was carried out, focusing on mass loss between 650 and 750 °C. The residual mass after these steps represented the total ash content of the sample. The fixed carbon content was then calculated as 100 % minus the sum of moisture content, volatile matter content, and ash content. The results obtained are documented in Tables A1 and A2.

3.5.2 Calorific Value

The calorific value was conducted after proximate analysis following the ASTM D5865-07 standard (ASTM International, 2007) using a Leco AC 500 bomb calorimeter. This analytical procedure was undertaken to ascertain the fundamental chemical property of coal discards. The chemical properties will assist in understanding the combustion efficiency of coal discards. Specifically, assessing the quantity of heat released per unit mass during combustion processes. The bomb calorimeter was calibrated according to the manufacturer's guidelines, ensuring the cleanliness and integrity of all components. A standard calibration was performed using 1 g of benzoic acid, thoroughly dried to eliminate any moisture. This calibration process involves igniting the benzoic acid in the calorimeter to record the temperature rise, repeated for reliability. Each sample, representing 1 g, was burnt in a closed vessel under an oxygen atmosphere at a high pressure of 3 000 kPa, and the amount of heat released was measured. The temperature was maintained at 25 °C via circulating cooling water using a pump. The system uses an electronic thermometer with an accuracy of 0.0001 to measure the temperature every six seconds, with the results obtained within 4.5 to 7.5 minutes. The results obtained are documented in Tables A1 and A2.

3.6 Mineralogical Analysis

The mineralogical analysis of the coal discard samples involved the use of FTIR, XRD, TIMA, and SEM-EDS. FTIR detected molecular bonds, enabling the identification of minerals, organic compounds, and alterations in coal discards based on absorption spectra. XRD was employed to identify and quantify the mineral phases by measuring the diffraction patterns of crystalline structures. TIMA was utilized to quantify the mineral phases in coal discard samples. While SEM-EDS provided high-resolution images and elemental composition of the sample surface to realize mineral morphology and microstructure.

3.6.1 FTIR Analysis

The FTIR analysis was conducted at the School of Chemical and Metallurgical Engineering at Witwatersrand University. FTIR has been used extensively to analyze coal in terms of functional groups (Martin & Chao, 1988; Fuller et al., 1982: Painter et al., 1981). The ninety-four (94) samples were ground to pass through a 50 µm sieve to ensure elevated surface area and improve IR absorption. Initially, the background scan was run without the sample in place to account for any atmospheric interference in a Bruker Tensor II FTIR spectrometer. Thereafter, the background spectrum was saved for automatic subtraction from the sample spectrum. About 25 mg was placed on the ATR crystal. A light pressure was applied to ensure good contact between the sample and the ATR crystal. The spectra range was set between 4000 and 400 cm^{-1} with a resolution of 4 cm^{-1} and 32 scans were collected for each sample. After each run the ATR crystal was cleaned with isopropanol to avoid contamination. The spectra were analyzed to identify functional groups present within the samples, with focused attention on both organic materials and mineral constituents, including carbonates, silicates, and clays. This approach facilitated a detailed characterization of the chemical structures governing the coal's physicochemical properties, revealing key insights into its organic compounds and mineralogical composition.

3.6.2 XRD Analysis

The XRD analysis was conducted at the Microscopy and Microanalysis Unit (MMU) at the University of Witwatersrand. Initially, a total of ninety-four samples were ground to pass through a 50 µm sieve to ensure homogeneity. About 1.2 g of the powdered sample was poured into the cavity of the sample holder and then flattened to ensure that the x-ray beams uniformly interact with the sample. During XRD analysis, the minerals phases in a sample were identified by comparing the positions and intensities of the diffraction peaks to those of the mineral reference standard from a database. This analysis was conducted using a BRUKER D2 PHASER advanced diffractometer with Cu Kα radiation (λ = 1.5406 Å) at 30 kV and 10 mA. Scan ranges were performed from 5 to 90° at a step size of 0.02° and a count of 2 seconds per step. The resulting data were analyzed using EVA software, which facilitates phase identification and quantification by comparing the measured peaks to entries in the ICDD PDF-4 database.

3.6.3 SEM-EDS Analysis

The SEM-EDS analysis was done at the School of Chemical and Metallurgical Engineering at the University of Witwatersrand. The primary function of the SEM-EDS is to generate a 3-D image of the sample's surface using a focused beam of electrons that scans across it, providing an exceptional depth of field. In addition, SEM-EDS is a powerful analytical technique for investigating the mode of occurrence of mineral deposits. It allows detailed examination of mineral textures, grain sizes, morphologies, and their spatial associations within the coal matrix (Marchant & Lawrence, 1991). According to Orem & Finkelman (2005), SEM-EDS remains the most effective method for identifying minerals with diameters as small as 1 µm, providing critical insights into coal mineralogy and facilitating thorough characterization of coal constituents. Twenty samples were ground to pass through a 50 µm sieve to ensure homogeneity. About 0.5 g of the sample was mounted on stubs coated with a thin layer of carbon to ensure electrical conductivity. SEM-EDS was conducted using a ZEISS EVO MA10 microscope equipped with an Oxford Instrument EDS detector (Figure 19). Secondary electron (SE) and backscattered electron (BSE) imaging were used to determine the morphology and microstructure of the specimen, while EDS provided semi-quantitative elemental analysis. High-resolution images were captured to examine the mineral associations, and EDS spectra were collected to identify elemental composition of specific phases.

Figure 19: Typical image of SEM-EDS (left) and samples prepared for analysis (right).

3.6.4 TIMA Analysis

The TIMA analysis was done at Eskom Research, Testing and Development Centre in Johannesburg. A total of twenty samples were ground to pass through a 212 µm sieve to ensure homogeneity according to Eskom standard used for TIMA analysis. About 2 g of each sample was added into a wax container filled with warm wax. The mixture was stirred until even distribution of coal discard throughout the wax. The mixture was then placed in a furnace, where temperatures were decreased from 110 °C to 50°C, to ensure complete homogenization of the wax and coal discard and to create a stable pellet for TIMA analysis (Figure 20). Subsequently, the pellet was air-cooled and ready for polishing. The polishing was done according to EN 12407 for geological materials. The silicate carbide papers with decreasing grit sizes from P1000 to P4000 were used to remove any coarse irregularities and expose the coal discard.

Then the polished samples were subjected to carbon coating to ensure sufficient electrical conductivity. A high throughput was achieved with multiple TIMA EDS detectors operating over 2 million counts per second, using low-count EDX spectra to identify minerals at each measurement grain segment (Hrstka et al., 2018). The TIMA system (Figure 20), equipped with a field-emission scanning electron microscope (FE-SEM) and EDS, was used to perform automated mineralogical analysis. BSE imaging and EDS were employed to identify and quantify the mineral phases and their associated phases. Particle maps were generated to study the mineral textures, liberation, and distribution of desired elements.

Figure 20: Typical image of the TIMA (left) and samples prepared for analysis (right).

3.7 Geochemical Analysis

The mineralogical analysis of the coal discard samples involved the use of XRF to determine major and trace elements, and ICP-MS for precise quantification of trace elements.

3.7.1 XRF Analysis

The XRF analysis for major elements was done at Council for Geosciences (CGS) following a methodology given by Cloete (2012). Ninety-four samples were ground to pass through a 75 µm sieve, and 50 g of each sample was taken to CGS for analysis. Initially, the samples were dried for

at least 3 hours at 100℃ and then roasted at 1000 ℃ for at least 3 hours to oxidize Fe^{+2} and S which were detrimental to the Pt ware used to prepare glass disks. The loss of ignition (L.O.I) and moisture (H_2O^-) were determined gravimetrically during the drying and roasting steps. The glass disks were prepared by fusing 1 g roasted sample and 10 g flux consisting of 49.50% $Li_2B_4O_7$, 49.50% $LiBO_2$, and 1% LiBr at 950 ℃. The glass disks were then analyzed by a PANalytical Axios X-ray fluorescence spectrometer equipped with a 4 kW Rh tube. The XRF analysis for trace elements was done at the University of Pretoria. Initial 12 g samples and 3 g Licowax were mixed and pressed into a powered briquette by a hydraulic press with the applied pressure at 25 tons. The pressed powder pellets were analyzed for the trace elements by a PANalytical Zetium X-ray fluorescence spectrometer equipped with a 4 kW Rh tube.

3.7.2 ICP-MS Analysis

The ICP-MS analysis was conducted at the University of Witwatersrand. Ninety-four coal discard samples were ground to pass through a 50 μm sieve. Approximately 250 mg from each sample was weighed and transferred into the Teflon vessel. The samples underwent acid digestion using a mixture of 6 ml of 55% of nitric acid (HNO_3), 2 ml of 32% hydrochloric acid (HCl), 1 ml of 48% hydrofluoric acid (HF), 0.5 ml of 30% hydrogen peroxide (H_2O_2) and 1 ml of H_2O. The solutions were digested by heating from 55 ℃ to 100 ℃ for 10 min, from 100 ℃ to 200 ℃ for 5 min and holding at 200 ℃ for 35 min. Thereafter, the vessels were cooled at room temperature while the stopper was closed. The solutions were transferred into 50 ml tubes and diluted with 18 MΩ deionized waters. The solutions were then filtered through 0.45 μm filters before ICP-MS analysis. Calibration was carried out using multi-element standards, and the internal standards (e.g., Rh, Re) were employed to correct matrix effects and instrumental drift. Certified reference materials were analyzed to validate the accuracy of the method. Concentrations of target elements were determined based on the calibration curves, and the results were reported in μg/g.

Chapter 4: Results

This chapter presents the results of the experimental investigations conducted to characterize coal discard samples. The results are divided into four main categories, core logging and sample description, coal discard quality assessment (techniques employed are TGA and bomb calorimeter), mineralogical analysis (techniques employed are FTIR, XRD, SEM-EDS and TIMA) and geochemical analysis (techniques employed are XRF and ICP-MS). The results from these techniques are presented below, providing a comprehensive understanding of the coal discard properties.

4.1 Core Logging and Sample Description

The samples collected during this study are presented in Tables 5 and 6, primarily focusing on coal discards from various depths in CD1 and on the surface in CD2. These samples were categorized into distinct lithologies, including bright, moist, clay-rich, and reddish coal discards, with observations on texture, moisture, and mineral content. For example, bright coal discards commonly displayed shiny minerals such as mica or pyrite, whereas moist coal discards were characterized by their black, crumbly, and wet nature. Clay-rich discards featured visible layering with variable moisture content. Within the CD1 dump, bright coal discards dominated the 0–1 m interval, while clay-rich discards were more common in deeper intervals (1–5 m). The CD2 dump mostly consisted of black, moist, crumbly coal discards, except for specific samples (CD2_05, CD2_09, CD2_11, CD2_13, CD2_15, CD2_21, CD2_22, CD2_23, and CD2_24). Bright and reddish coal discards were observed in CD1, while dull coal discards predominated in CD2.

Table 5: Lithology and observations at CD1 dump.

Depth interval (m)	Sample_ID	Lithology	Observation
0 - 1 m	CD1_01	Bright coal discard	Some shiny crystals indicating mica and/or pyrite
	CD1_02	Bright coal discard	Some shiny crystals indicating mica and/or pyrite
	CD1_03	Moist coal discard	Black, crumby, higher moisture content
	CD1_04	Moist coal discard	Black, crumby, higher moisture content
	CD1_05	Bright coal discard	Some shiny crystals indicating mica and/or pyrite
	CD1_06	Reddish coal discard	Higher mineral content
	CD1_07	Bright coal discard	Some shiny crystals indicating mica and/or pyrite
	CD1_08	Bright coal discard	Some shiny crystals indicating mica and/or pyrite
	CD1_09	Bright coal discard	Some shiny crystals indicating mica and/or pyrite
	CD1_10	Bright coal discard	Some shiny crystals indicating mica and/or pyrite
	CD1_11	Bright coal discard	Some shiny crystals indicating mica and/or pyrite
	CD1_12	Moist coal discard	Black, crumby, higher moisture content
	CD1_13	Moist coal discard	Black, crumby, higher moisture content
	CD1_14	Bright coal discard	Some shiny crystals indicating mica and/or pyrite
1 -2 m	CD1_01	Clay coal discard	Black with visible clay layers, high moisture
	CD1_02	Clay coal discard	Black with visible clay layers, low moisture
	CD1_03	Clay coal discard	Black with visible clay layers, low moisture
	CD1_04	Clay coal discard	Black with visible clay layers, low moisture
	CD1_05	Clay coal discard	Black with visible clay layers, high moisture
	CD1_06	Clay coal discard	Black with visible clay layers, low moisture
	CD1_07	Moist coal discard	Black, crumby, higher moisture content
	CD1_08	Moist coal discard	Black, crumby, higher moisture content
	CD1_09	Clay coal discard	Black with visible clay layers, high moisture

	CD1_10	Clay coal discard	Black with visible clay layers, high moisture
	CD1_11	Clay coal discard	Black with visible clay layers, high moisture
	CD1_12	Clay coal discard	Black with visible clay layers, high moisture
	CD1_13	Clay coal discard	Black with visible clay layers, low moisture
	CD1_14	Clay coal discard	Black with visible clay layers, high moisture
2 - 3 m	CD1_01	Clay coal discard	Black with visible clay layers, moisture
	CD1_02	Clay coal discard	Black with visible clay layers, low moisture
	CD1_03	Clay coal discard	Black with visible clay layers, high moisture
	CD1_04	Clay coal discard	Black with visible clay layers, low moisture
	CD1_05	Moist coal discard	Black, crumby, higher moisture content
	CD1_06	Moist coal discard	Black, crumby, higher moisture content
	CD1_07	Clay coal discard	Black with visible clay layers, low moisture
	CD1_08	Moist coal discard	Black, crumby, higher moisture content
	CD1_09	Clay coal discard	Black with visible clay layers, high moisture
	CD1_10	Clay coal discard	Black with visible clay layers, high moisture
	CD1_11	Moist coal discard	Black, crumby, higher moisture content
	CD1_12	Clay coal discard	Black with visible clay layers, low moisture
	CD1_13	Clay coal discard	Black with visible clay layers, high moisture
	CD1_14	Clay coal discard	Black with visible clay layers, high moisture
3 - 4 m	CD1_01	Clay coal discard	Black with visible clay layers, high moisture
	CD1_02	Clay coal discard	Black with visible clay layers, high moisture
	CD1_03	Clay coal discard	Black with visible clay layers, high moisture
	CD1_04	Clay coal discard	Black with visible clay layers, low moisture
	CD1_05	Moist coal discard	Black, crumby, higher moisture content
	CD1_06	Moist coal discard	Black, crumby, higher moisture content
	CD1_07	Clay coal discard	Black with visible clay layers, moisture
	CD1_08	Moist coal discard	Black, crumby, higher moisture content

	CD1_09	Clay coal discard	Black with visible clay layers, high moisture
	CD1_10	Clay coal discard	Black with visible clay layers, low moisture
	CD1_11	Clay coal discard	Black with visible clay layers, high moisture
	CD1_12	Clay coal discard	Black with visible clay layers, moisture
	CD1_13	Clay coal discard	Black with visible clay layers, moisture
	CD1_14	Clay coal discard	Black with visible clay layers, moisture
4 - 5 m	CD1_01	Clay coal discard	Black with visible clay layers, low moisture
	CD1_02	Clay coal discard	Black with visible clay layers, low moisture
	CD1_03	Clay coal discard	Black with visible clay layers, high moisture
	CD1_04	Moist coal discard	Black, crumby, higher moisture content
	CD1_05	Moist coal discard	Black, crumby, higher moisture content
	CD1_06	Clay coal discard	Black with visible clay layers, low moisture
	CD1_07	Clay coal discard	Black with visible clay layers, low moisture
	CD1_08	Moist coal discard	Black, crumby, higher moisture content
	CD1_09	Reddish coal discard	Higher mineral content
	CD1_10	Clay coal discard	Black with visible clay layers, high moisture
	CD1_11	Clay coal discard	Black with visible clay layers, high moisture
	CD1_12	Clay coal discard	Black with visible clay layers, low moisture
	CD1_13	Clay coal discard	Black with visible clay layers, low moisture
	CD1_14	Clay coal discard	Black with visible clay layers, low moisture

Table 6: Lithology and observations at CD2 dump.

Sample_ID	Lithology	Observations
CD2_01	Moist coal discard	Black, crumby, higher moisture content
CD2_02	Moist coal discard	Black, crumby, higher moisture content
CD2_03	Moist coal discard	Black, crumby, higher moisture content
CD2_04	Moist coal discard	Black, crumby, higher moisture content
CD2_05	Clay coal discard	Black with visible clay layers, low moisture
CD2_06	Moist coal discard	Black, crumby, higher moisture content
CD2_07	Moist coal discard	Black, crumby, higher moisture content
CD2_08	Moist coal discard	Black, crumby, higher moisture content
CD2_09	Clay coal discard	Black with visible clay layers, high moisture
CD2_10	Moist coal discard	Black, crumby, higher moisture content
CD2_11	Clay coal discard	Black with visible clay layers, low moisture
CD2_12	Moist coal discard	Black, crumby, higher moisture content
CD2_13	Clay coal discard	Black with visible clay layers, low moisture
CD2_14	Moist coal discard	Black, crumby, higher moisture content
CD2_15	Clay coal discard	Black with visible clay layers, high moisture
CD2_16	Moist coal discard	Black, crumby, higher moisture content
CD2_17	Moist coal discard	Black, crumby, higher moisture content
CD2_18	Moist coal discard	Black, crumby, higher moisture content
CD2_19	Moist coal discard	Black, crumby, higher moisture content
CD2_20	Moist coal discard	Black, crumby, higher moisture content
CD2_21	Clay coal discard	Black with visible clay layers, high moisture
CD2_22	Clay coal discard	Black with visible clay layers, low moisture
CD2_23	Clay coal discard	Black with visible clay layers, low moisture
CD2_24	Dull coal discard	Higher mineral content

4.2 Coal Discard Quality Assessment

The physicochemical properties (proximate analysis and calorific value) of CD1 and CD2 dumps are presented in Tables 7 and 8, respectively. The CD1 results exhibit trends in the proximate analysis parameters such as moisture (M), volatile matter (VM), fixed carbon (FC) and ash content (A); and calorific values (CV) across different depth intervals, in the same manner CD2 exhibits its trend of the same parameters across the dump.

4.2.1 CD1 Dump

The physicochemical properties of coal discards vary across different intervals. For instance, the moisture content ranges from 2.61 wt% in CD1_09 at the 4-5 m interval to 7.42 wt% in CD1_03 at the 0-1 m interval. The average moisture content is 4.78 wt%, suggesting a significant variation in moisture content across the samples. The volatile matter content varies from 7.66 wt% in CD1_09 at the 4-5 m interval to 23.49 wt% in CD1_06 at the 4-5 m interval. The average volatile matter content is 21.91 wt% indicating the presence of high organic matter in most samples. Similarly, the ash content ranges from 25.43 wt% in CD1_08 at the 4-5 m interval to 84.13 wt% in CD1_09 at the same interval. The average ash content is 34.78 wt%, indicating a significant variation across the samples, with most samples at 4-5 m interval having the highest ash content. The elevated ash content observed in these samples indicates a significant proportion of mineral matter within the coal discards. The fixed carbon content varies from 5.62 wt% in CD1_09 at the 4-5 m interval to 46.18 wt% in CD1_05 at the 1-2 m interval, with an average of 38.53 wt%. The calorific value ranges from 0.12 MJ/kg in CD1_09 at the 4-5 m interval to 22.94 MJ/kg in CD1_05 at the 4-5 m interval, with an average of 18.11 MJ/kg. The lowest organic fraction in CD1_09 aligns with high ash content in this sample, suggesting it has high inorganic material.

4.2.1.1 Depth Intervals Comparisons

Figure 21 shows that the physicochemical properties of coal discards vary across different depth intervals. The moisture content is initially observed to decrease reaching its lowest value of 4.41 wt% at 2-3 m interval, then slightly increases at the intervals of 3-4 m and 4-5 m, while volatile matter content increases slightly from 0-1 m to 1-2 m but then decreases steadily from 1-2 m downward. It reached its lowest value of 21.15 wt% at the interval of 4-5 m. Similarly, ash content decreases from 0-1 m to 1-2 m but then increases from 1-2 m onward and reaches its highest value of 36.38 wt% at the interval of 4-5 m. The fixed carbon content increases from 0-1 m to 1-2 m (peaking at 40.23 wt%) but then decreases from 1-2 m onwards, opposing the ash content. Finally, the calorific value is inconsistent, it increases sharply from 16.60 MJ/kg at 0-1 m to 19.01 MJ/kg at 1-2 m. It decreases between 1-2 m and 2-3 m but shows a slight increase at the 3-4 m and 4-5 m intervals. The calorific value correlates with fixed carbon trends, peaking at 1-2 m interval and stabilizing later.

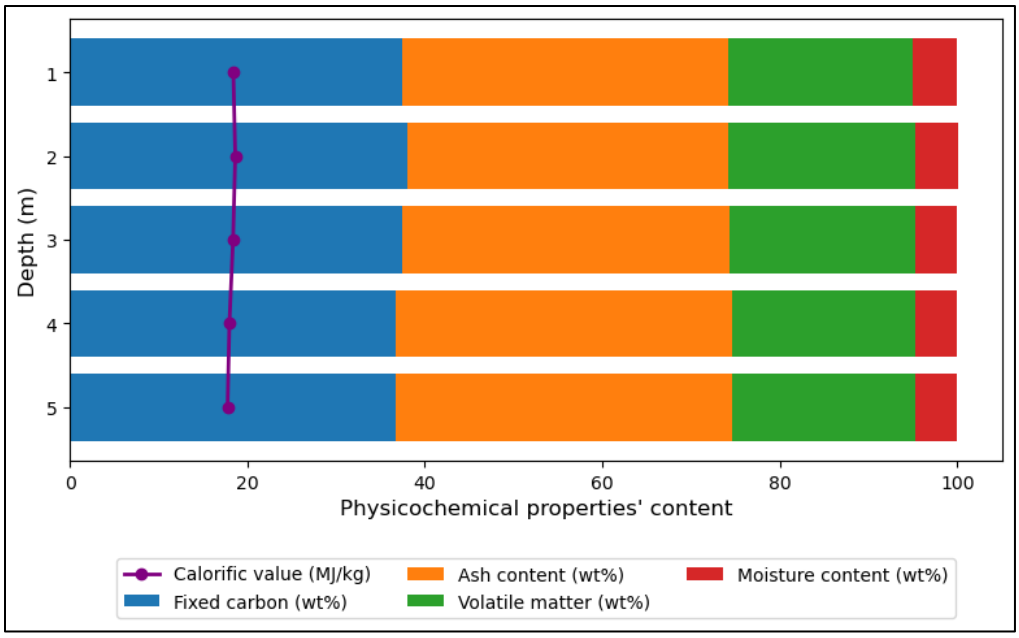

Figure 21: Physiochemical properties of CD1 samples per depth interval.

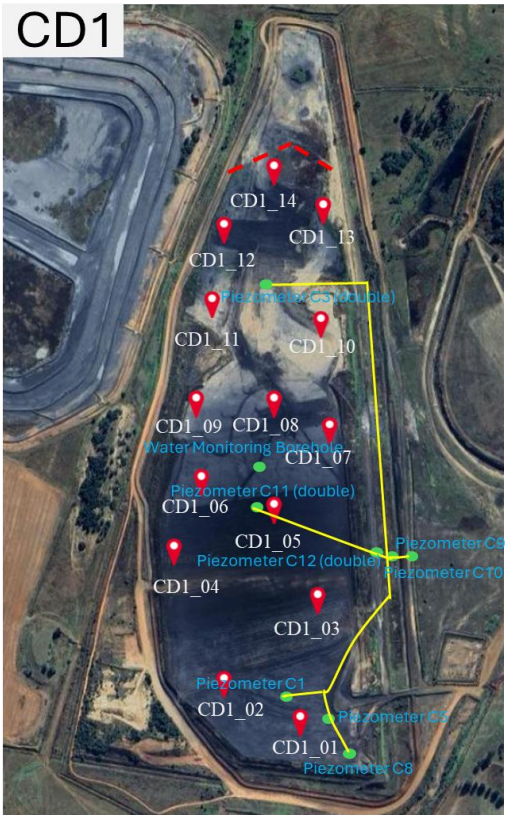

Figure 22: Schematic diagram showing the chemical composition variation across the CD1 dump.

The following were the final observations made on the CD1 dump which is also illustrated in Figure 22:

1. Physicochemical composition variation was observed on samples CD1_01, CD1_04, CD1_06, CD1_09, and CD1_12.
2. All these samples are at the dump's western side at the edge.
3. As the depth increases, the FC increases whilst ash is decreasing (CD1_01 & CD1_06).
4. In some (CD1_04, CD1_09 and CD1_12), as the depth increases, ash increases whilst FC increases.
5. The rest of the coal discard still has high FC.
6. VM and M are constant throughout the coal discard.

4.2.2 CD2 Dump

The moisture content ranges from 4.49 wt% in CD2_05 to 9.09 wt% in CD2_10, with an average of 6.46 wt% notably higher than that found in CD1 (Table 7). Similarly, the volatile matter content ranges from 18.93 wt% in CD2_15 to 21.39 wt% in CD2_07. The average volatile matter is 20.29 wt%, slightly lower than that found in CD1. The ash content ranges from 29.79 wt% in CD2_06 to 51.23 wt% in CD2_24, with an average of 35.11 wt%, slightly higher than that found in CD1 (Table 7). In the same manner, the fixed carbon content varies from 24.66 wt% in CD2_24 to 41.44 wt% in CD2_06. The average fixed carbon content is 38.14 wt%, slightly less than that reported in CD1. The calorific value ranges from 10.77 MJ/kg in CD2_24 to 19.48 MJ/kg in CD2_06. The average calorific value is 17.55, slightly less than that found in CD1. These variations in physicochemical properties may be attributed to the age difference between the two coal discards, with CD1 dump being the older dump and having slightly higher organic fractions (VM, FC and CV) than CD2 dump suggesting that it retained good quality coal that could not be processed by older technologies.

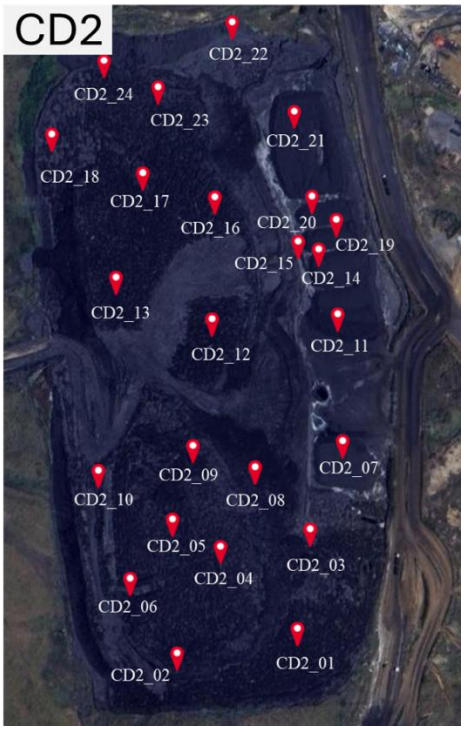

Figure 23: Schematic diagram showing the chemical composition variation across the CD2 dump.

The following conclusions were made for CD2 dump as illustrated in Figure 23:

At the south end of the coal discard:

1. FC and M are predominantly high.
2. Low ash content.

At the north end of the coal discard:

1. FC and M are predominantly low.
2. High ash content.

Overall assessment:

1. VM and CV (except for CD2_24 – 10.8 MJ/kg) are constant throughout the dump (19 to 20 wt%) and (15.5 to 19.5 wt%).
2. Ash content ranges from 31 to 51 wt%.
3. M content ranges between 4 to 9 wt%.
4. FC content ranges from 24.5 to 41.4 wt%.

4.2.3 Key observations: Comparison between CD1 and CD2 samples.

The Department of Energy (DOE) reported that coal discards from Witbank have the following physicochemical properties (DOE, 2001).

1. At least 18 wt% fixed carbon content,
2. 1.434 million tons of coal discards exhibited a volatile matter ranging from 28-30 wt% and,
3. 1.605 million tons of coal discards exhibited a calorific value of at least 21 MJ/kg.

The classification system from ASTM D388-99 (ASTM International, 1999) was employed to calculate the dry, mineral-matter-free basis for each parameter (Equation A1).

Table 7: Physicochemical properties results and comparison.

Physicochemical properties	CD1			CD2			DOE (2001)		
	Min	max	average	min	max	average	min	max	average
Moisture content (wt%)	2.61	7.42	4,78	4.49	9.09	6,46	-	-	-
Volatile matter (wt%)	7.66	23.49	21,91	18.93	21.39	20,29	8	30	19
Ash content (wt%)	25.43	84.13	34,78	29.79	51.23	35,11	10	70	40
Fixed carbon (wt%)	5.61	46.18	38,53	24.66	41.44	38,14	18	58	38
Calorific value (MJ/kg)	0.12	22.94	18,11	10.77	19.48	17,55	8	26	17

It is important to note that ASTM D388-99 (ASTM International, 1999) primarily addresses vitrinite-rich coals, and its application to inertinite-rich coal discards such as these may not fully capture their rank characteristics. Inertinite-rich coals generally exhibit higher vitrinite reflectance values at the same rank compared to vitrinite-rich coals, which can influence interpretations based solely on proximate analysis. Although the fixed carbon content and calorific value in CD2 samples are slightly lower than those in CD1, this difference may reflect variations in maceral composition and degree of oxidation rather than a true difference in coal rank. The older CD1 discards may have undergone significant oxidation or mineral alteration due to prolonged environmental exposure, potentially influencing their physicochemical properties. Petrographic analysis, which would reveal maceral proportions and mineralogical changes, would provide stronger evidence to clarify these effects. These findings suggest that these coal discards have potential applications in power generation and other uses where high-energy coal is required (Steyn & Minnitt, 2010).

4.3 Mineralogical Analysis

4.3.1 FTIR Analysis

The FTIR analysis was conducted to determine the functional groups present in the coal discards of the Witbank Coalfield. The FTIR spectra of the coal discards present functional group adsorption peaks at corresponding wavelengths between 450 and 4000 cm^{-1} (Figure 24, 25, 26, 27, A1, A2, A3). The peaks are assigned according to current literature (Fuller et al., 1982; Georgakopoulos, 2003; Martin & Chao, 1988; Oikonomopoulos et al., 2013; Öztaş & Yürüm,

2000; Painter et al., 1981; Xue et al., 2023). The FTIR spectra showed the signals of both organic and inorganic materials. Organic materials such as hydroxyl group (O-H), saturated aliphatic group (methyl and methylene), aliphatic ring, and aromatic rings. The inorganic material exhibited spectral features indicative of quartz, clay minerals (kaolinite, illite, and muscovite), and oxides, with Si-O and Si-O-Si, Al-OH, and C-Cl bands.

4.3.1.1 CD1 Dump

4.3.1.1.1 The 0-1 m interval

A prominent O-H stretching vibration between 3600 and 3700 cm^{-1} is present in all the samples. The C-H aliphatic stretching vibrations between 2800 and 3000 cm^{-1} and 1300 and 1400 cm^{-1} suggest the presence of aliphatic hydrocarbons (C-H). The intensity of peaks varied slightly across the coal discard samples, with CD1_06 and CD1_14 having the most prominent peaks, suggesting greater variations in organic matter concentration. The C=C aromatic rings stretching vibrations are observed between 1500 and 1600 cm^{-1}, signifying aromatic hydrocarbons. The peak is less prominent in CD1_06, indicating a lack of aromatic compounds in weathered samples. The C-O stretching is observed at around 1251.9 cm^{-1}, signifying the presence of carbonyl groups and carbonate minerals. The less prominent peak in CD1_06 suggests the limited presence of carbonyl groups and carbonate minerals in the weathered sample. The saturated aliphatic C-C at about 1029 cm^{-1} and C-Cl are observed in the range 690 and 760 cm^{-1} in all the samples. This indicates the complexity of the hydrocarbon structure. The Al-OH peak at 912.17 cm^{-1} indicates hydroxyl aluminum bearing minerals such as clay minerals. The presence of Si-O and Si-O-Si peaks at 1007.60 and 535.30 cm^{-1} varies slightly, with CD1_06 showing the most prominent peak, which suggests an abundance of silicate minerals. The presence of M-O peaks at 466.71 cm^{-1} is consistent across all the samples and indicates the metal-oxygen minerals such as hematite, magnetite, rutile, and ilmenite. For illustration purposes, the CD1 FTIR spectra are shown in Figure 24.

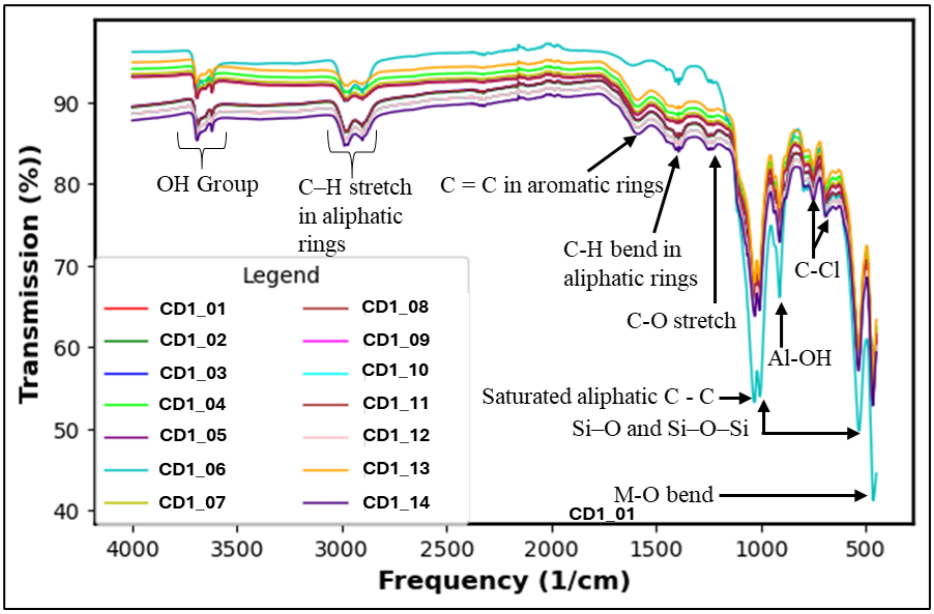

Figure 24: FTIR spectra for samples at the 0-1 m interval.

4.3.1.1.2 The 1-2 m interval

The FTIR spectra for the 1–2 m interval are illustrated in Figure 25. The O-H (3600-3700 cm^{-1}) and Al-OH (912.17 cm^{-1}) peaks are prominent, indicating the consistent presence of clay minerals in all the samples. Samples CD1_04, CD1_09 and CD1_13 have more pronounced C-H stretch (2800–3000 cm^{-1}) and C-H bend (1300 and 1400 cm^{-1}) peaks, indicating the presence of more aliphatic hydrocarbons. In the same samples, the C-O (1251.9 cm^{-1}) stretch is more pronounced than the rest of the samples, suggesting an abundance of carbonyl groups in organic matter and carbonate minerals. The C-C (1029 cm^{-1}) and C-Cl (690-760 cm^{-1}) peaks are also more prominent in the samples, indicating the complex nature of organic structures. The aromatic hydrocarbons are consistent throughout the samples. The prominence of peaks for Si-O and Si-O-Si and M-O vary slightly, except for samples such as CD1_04 and CD1_14 which have a more prominent peak, suggesting strong presence of both silicate and metal-bearing minerals.

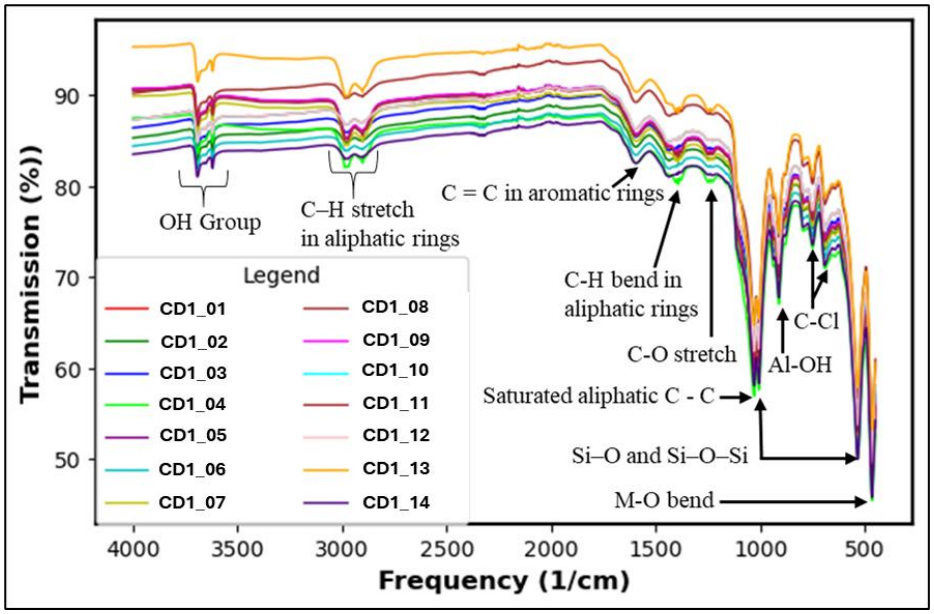

Figure 25: FTIR spectra for samples at the 1-2 m interval.

Intervals 2-3 m, 3-4 m and 2-5 m have a presence of the same stretching frequencies, and more information can be obtained in Figure A1, A2 and A3.

4.3.1.2 CD2 Dump

The FTIR spectra for CD2 are illustrated in Figure 26 and 27. Samples CD2_02, CD2_10 and CD2_12 exhibit the least prominent peaks for O-H at the range 3600-3700 cm^{-1} indicating a decrease in the hydroxyl group. The least prominent peaks for the samples have been noted in C=C stretch, showing a decline in aromatic compounds. CD2_10 also exhibits the least prominent peaks, indicating a less complex structure of organic compounds. Samples CD2_05 and CD2_09 exhibit the most prominent peaks at different ranges, such as 912.17 cm^{-1}, 1007.60 cm^{-1}, 690, 760 cm^{-1}, 535.30 cm^{-1}, and 466.71 cm^{-1} highlighting the presence of different functional groups and the presence of oxide, silicate, and hydroxide minerals (Figure 26). CD2_14, CD2_16 and CD2_24 exhibit the least prominent peaks for C-H stretch at high frequency and transmission. CD2_14 also exhibits the most prominent peaks for silicate, metal oxides, hydroxides at low frequency, and transmission (Figure 27).

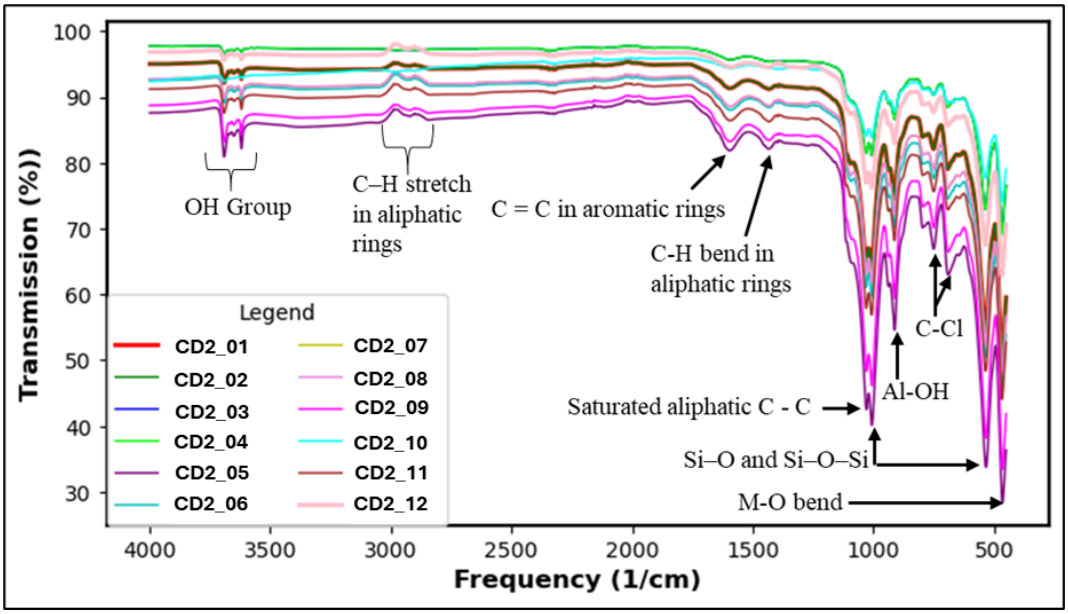

Figure 26: FTIR spectra for the first 12 CD2 samples.

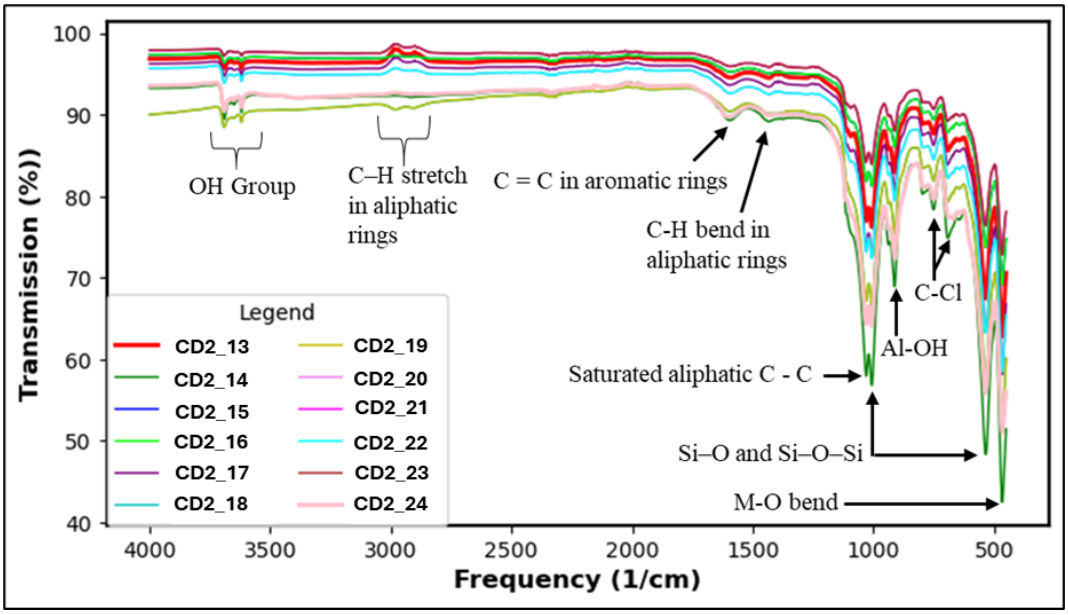

Figure 27: FTIR spectra for the last 12 CD2 samples.

4.3.1.3 Key Observations

The CD1 samples were mostly dominated by silicate minerals while CD2 samples were dominated by silicate minerals and organic matter. The absence of C-O stretches in CD2 samples indicates the absence of carbonyl groups in organic matter and the low content of carbonate minerals. The weathered sample CD1_06 at 0-1 m and CD1_09 at 4-5 m intervals have the most of prominent peaks, suggesting an increase in inorganic materials and a small proportion of organic materials. In both coal discard dumps, the functional groups identified by low transmission and low frequency were more prominent and clearer for a few samples.

4.4 XRD Analysis

The XRD results showed that the major crystalline phases present in the two coal discard dumps of the Witbank Coalfield were quartz and kaolinite. Minor phases of calcite, ankerite, pyrite, muscovite, dolomite, magnetite, berlinite, and brushite were also detected (Tables 7 and 8).

4.4.1 CD1 Dump

At the 0–1 m interval, quartz was more abundant in the reddish coal discards, while kaolinite and calcite levels are generally low. Bright coal discards from this interval exhibite higher concentrations of magnetite, pyrite, and ankerite. At 1-2 m interval, quartz content remains relatively stable within clay and moist coal discards, whereas kaolinite become more dominant, indicating shifts in clay mineral proportions. Magnetite also increases in the clay coal discards. At 2–3 m interval, clay coal discards show elevated levels of magnetite, pyrite, and berlinite. The 3–4 m interval is characterized by an increase in quartz associated with clay-rich coal discards containing lower kaolinite content. Dolomite and calcite concentrations remain consistent, while pyrite and berlinite peaked, suggesting enhanced diagenetic alteration. Magnetite levels also remain significantly high at this depth. Finally, at the 4–5 m interval, quartz in reddish coal discards reach its highest abundance, accompanied by a sharp decline in kaolinite.

Table 7: Mineralogical composition (wt%) of CD1 dump per depth interval in m.

0-1 m	**CD1_01**	**CD1_02**	**CD1_03**	**CD1_04**	**CD1_05**	**CD1_06**	**CD1_07**	**CD1_08**	**CD1_09**	**CD1_10**	**CD1_11**	**CD1_12**	**CD1_13**	**CD1_14**
Q	41,11	42,90	44,54	45,54	40,22	64,77	44,39	46,89	43,30	44,42	44,24	42,61	41,96	44,81
K	24,00	23,45	23,48	17,68	30,26	13,02	23,72	23,60	21,79	23,23	23,98	24,50	23,90	24,12
D	9,35	9,35	9,17	9,64	8,95	8,65	9,08	8,95	9,87	9,14	9,09	9,24	9,54	9,02
C	14,49	14,66	14,26	15,28	13,79	6,17	13,99	13,76	15,89	14,14	14,06	14,31	15,08	13,92
A	1,95	1,93	1,61	2,41	1,23	1,12	1,49	1,21	2,56	1,56	1,51	1,69	2,09	1,39
M	3,31	2,47	1,93	3,25	1,24	2,89	2,14	1,20	1,84	2,02	2,00	2,29	1,88	1,78
Mu	2,88	2,74	2,75	3,28	2,51	2,43	2,83	2,80	2,95	2,70	2,89	3,01	2,86	3,18
B	0,47	0,45	0,49	0,44	0,48	0,38	0,49	0,52	0,45	0,46	0,51	0,53	0,96	0,46
P	2,43	1,82	1,42	2,39	0,91	1,13	1,57	0,88	1,36	1,48	1,47	1,68	1,38	1,31
1-2 m	**CD1_01**	**CD1_02**	**CD1_03**	**CD1_04**	**CD1_05**	**CD1_06**	**CD1_07**	**CD1_08**	**CD1_09**	**CD1_10**	**CD1_11**	**CD1_12**	**CD1_13**	**CD1_14**
Q	40,91	39,76	46,24	52,30	48,78	53,16	47,32	44,22	41,29	44,87	45,09	43,87	44,82	45,86
K	24,02	24,33	22,70	14,46	25,33	25,63	22,49	25,35	21,97	22,74	23,08	23,22	22,91	22,40
D	9,25	9,43	9,09	9,29	8,61	9,05	9,00	9,04	9,21	9,26	9,10	9,20	9,09	9,10
C	14,36	14,82	14,11	14,52	13,13	6,93	13,91	13,98	14,24	14,47	14,08	14,24	14,01	14,04
A	1,84	2,16	1,50	1,84	0,77	1,42	1,35	1,39	1,97	1,76	1,54	1,69	1,43	1,49
M	3,06	3,40	1,78	2,40	0,74	1,89	1,56	1,57	4,47	2,06	2,13	2,53	1,66	1,96
Mu	2,88	2,95	2,57	2,52	1,64	0,56	2,52	2,50	3,00	2,58	2,67	2,70	2,63	2,50
B	0,44	0,45	0,47	0,41	0,31	0,46	0,53	0,48	0,50	0,49	0,47	0,46	0,85	0,48
P	2,25	2,50	1,31	1,77	0,54	0,39	1,14	1,15	3,29	1,52	1,57	1,86	1,22	1,44
2-3 m	**CD1_01**	**CD1_02**	**CD1_03**	**CD1_04**	**CD1_05**	**CD1_06**	**CD1_07**	**CD1_08**	**CD1_09**	**CD1_10**	**CD1_11**	**CD1_12**	**CD1_13**	**CD1_14**
Q	45,13	40,15	50,47	50,86	51,93	54,07	46,19	44,81	43,25	47,80	44,02	44,05	44,33	48,08
K	19,91	18,35	14,64	12,33	19,65	25,69	22,49	24,92	22,00	23,08	23,10	23,74	23,55	19,92
D	9,13	9,43	9,09	9,63	8,84	8,95	9,05	9,00	9,14	8,86	9,18	9,11	9,10	9,09

C	14,07	14,72	14,06	15,27	13,59	6,81	14,02	13,92	14,14	13,63	14,31	14,12	14,05	14,09
A	1,68	2,54	1,74	2,43	1,09	1,27	1,48	1,34	1,76	1,11	1,69	1,57	1,53	1,56
M	3,16	6,37	3,58	3,42	1,03	1,38	1,99	1,39	3,43	1,06	2,26	2,20	2,19	2,25
Mu	3,12	2,98	2,80	2,95	2,41	0,57	2,53	2,39	3,03	2,44	2,67	2,82	2,79	2,88
B	0,48	0,41	0,46	0,48	0,40	0,41	0,48	0,47	0,48	0,41	0,48	0,42	0,84	0,40
P	2,33	4,69	2,63	2,51	0,76	0,01	1,46	1,02	2,52	0,78	1,66	1,62	1,61	1,65
3-4 m	**CD1_01**	**CD1_02**	**CD1_03**	**CD1_04**	**CD1_05**	**CD1_06**	**CD1_07**	**CD1_08**	**CD1_09**	**CD1_10**	**CD1_11**	**CD1_12**	**CD1_13**	**CD1_14**
Q	46,70	42,45	48,96	45,78	51,56	55,09	47,69	45,24	59,66	45,57	43,05	41,78	42,59	47,11
K	18,07	17,77	17,74	12,03	18,24	23,94	17,14	25,13	10,14	21,20	25,50	23,37	23,12	18,65
D	9,25	9,48	9,18	9,89	8,96	9,00	9,23	8,96	8,66	9,23	9,07	9,37	9,12	9,33
C	14,40	14,88	14,27	15,83	13,81	6,89	14,34	13,82	13,21	14,40	14,04	14,70	14,10	14,62
A	1,93	2,50	1,77	3,04	1,32	1,40	1,86	1,28	0,95	1,79	1,48	2,02	1,71	1,95
M	3,54	5,48	2,98	5,37	1,72	1,96	3,26	1,44	1,59	2,57	1,93	2,92	3,22	2,80
Mu	2,67	2,84	2,35	3,11	2,17	0,64	2,93	2,45	4,24	2,45	2,53	2,72	2,67	2,92
B	0,46	0,39	0,44	0,51	0,44	0,51	0,45	0,50	0,31	0,47	0,53	0,52	0,90	0,51
P	2,60	4,03	2,19	3,95	1,27	0,44	2,39	1,06	1,17	1,89	1,42	2,15	2,37	2,06
4-5 m	**CD1_01**	**CD1_02**	**CD1_03**	**CD1_04**	**CD1_05**	**CD1_06**	**CD1_07**	**CD1_08**	**CD1_09**	**CD1_10**	**CD1_11**	**CD1_12**	**CD1_13**	**CD1_14**
Q	46,72	45,69	46,14	56,28	54,34	55,17	48,17	48,24	92,70	45,80	46,36	43,80	47,15	50,20
K	18,34	16,47	15,55	13,20	16,38	24,98	21,87	21,69	1,58	20,42	21,01	23,56	21,77	17,12
D	9,35	9,33	9,34	8,71	8,93	8,94	8,91	8,98	nd	9,25	9,08	8,97	9,03	8,94
C	14,54	14,49	14,50	13,31	13,78	6,75	13,74	13,85	nd	14,41	14,07	13,82	13,99	13,74
A	1,96	2,12	2,24	1,04	1,23	1,25	1,33	1,32	nd	1,82	1,58	1,47	1,44	1,46
M	3,19	4,48	5,24	1,84	1,26	1,50	2,07	1,57	nd	2,78	2,45	2,73	1,86	2,95
Mu	2,74	2,77	2,55	3,60	2,37	0,42	1,80	2,35	5,20	2,51	2,66	2,79	2,36	2,56
B	0,45	0,43	0,43	0,36	0,47	0,46	0,34	0,47	0,50	0,52	0,45	0,50	0,89	0,47
P	2,34	3,29	3,85	1,35	0,93	0,10	1,52	1,16	nd	2,04	1,80	2,01	1,37	2,17

Q-quartz, K-kaolinite, D-dolomite, C-calcite, A-ankerite, M-magnetite, Mu-muscovite, B-berlinite, P-pyrite and nd-not detected.

Quartz and kaolinite are the major minerals in CD1. In Figure 28, it was observed that quartz, muscovite, and berlinite have the most prominent peaks followed by kaolinite. Table 7 and Figure 28 showed that quartz was well distributed in massive quantities in sample CD1_01 at 0-1 m interval, followed by kaolinite and calcite. Other minerals were distributed in low quantities in the sample. The distribution of minor minerals varies throughout all the samples, for example, berlinite and ankerite were the most depleted minerals in the sample. Pyrite was among the less abundant phases identified in the sample, with a less pronounced peak at 2θ value of approximately 42°, confirming the presence of sulfide minerals (Figure 28). Presence of pyrite indicates that coal formation occurred under anaerobic conditions characteristic of peat swamp environments, with mineralization proceeding through both syngenetic deposition during sediment accumulation and subsequent epigenetic alteration during diagenesis (Li et al., 2016).

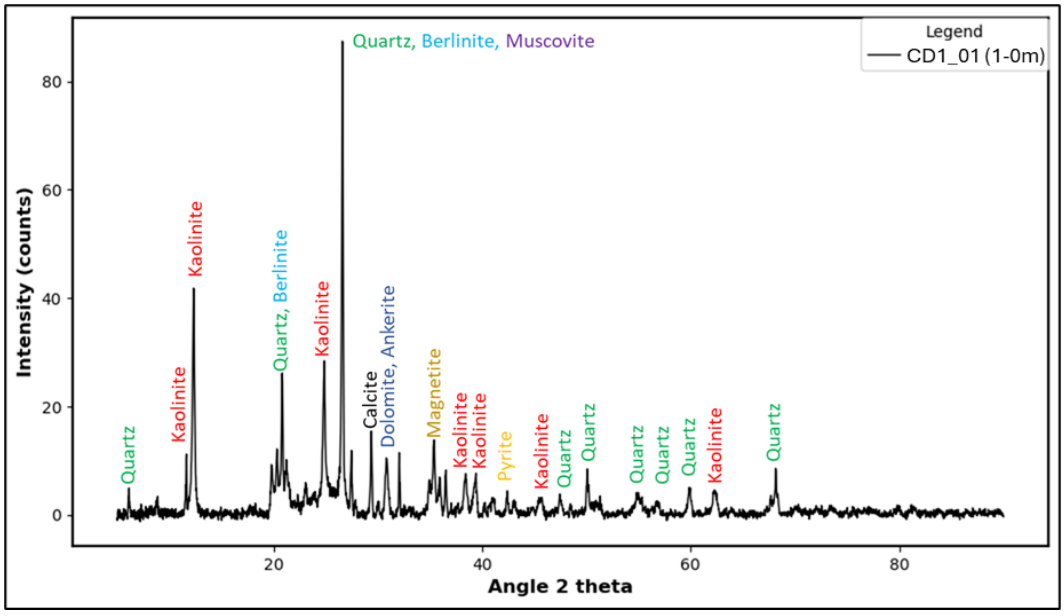

Figure 28: Sample CD1_01 at 0-1 m interval (observed pyrite).

Kaolinite was the second most abundant phase, and its peaks were identified at 2θ values of approximately 12°, 25°, 38°, 39°, 45°, and 63°, confirming its significant presence in the sample as illustrated in Figure 29. It might have been formed from weathered feldspar or other

aluminosilicate minerals. Its layered structure has implications for the adsorption of trace elements and potential interaction with organic matter (Vassilev et al., 2010).

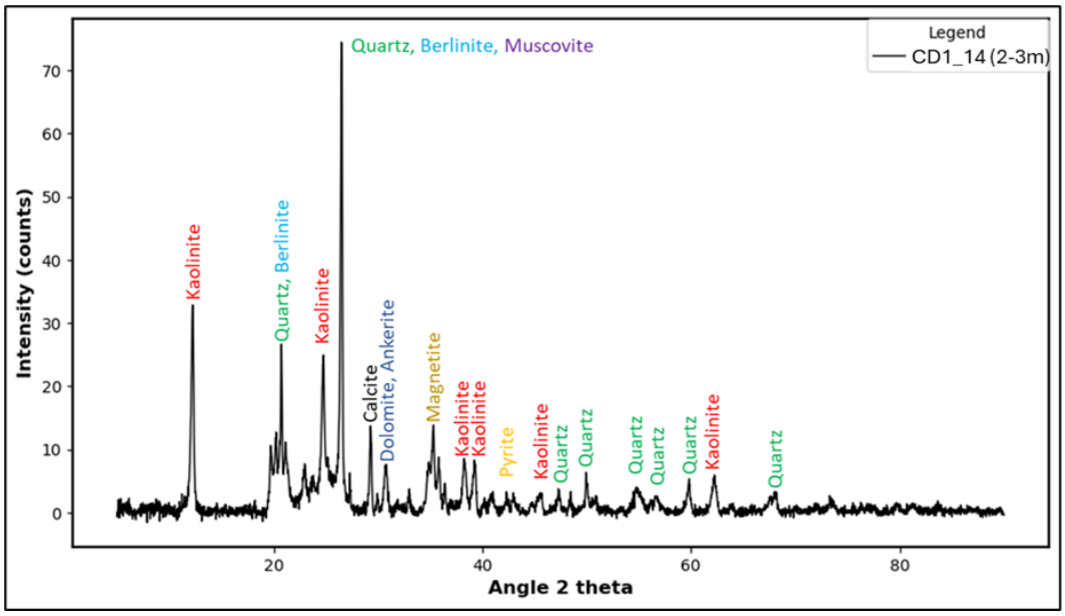

Figure 29: Sample CD1_14 at 2-3 m interval (observed kaolinite).

The presence of calcite and dolomite phases, along with small amount of ankerite suggest a significant carbonate fraction (Wang et al., 2017). Calcite was identified with a peak of 29° while dolomite and ankerite with overlapping peaks of 31° as illustrated in Figure 30. The presence of calcite in the sample suggests the contribution of biological activities such as microbial and shell fragments (Vassilev and Vassileva, 1996). The coexistence of dolomite and ankerite phases suggests varying fluid compositions. Dolomite was formed due to the precipitation of Mg-rich fluids, while ankerite was formed due to Mg-, or Mn- and Fe-rich fluids (Dai et al., 2021).

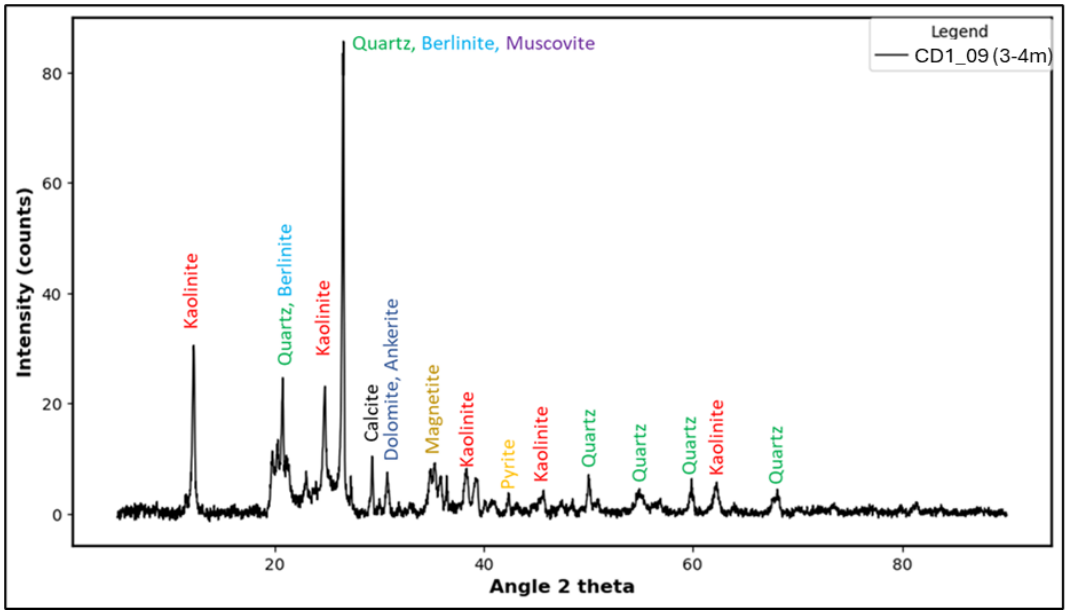

Figure 30: Sample CD1_09 at 3-4 m interval (observed calcite, dolomite and ankerite).

Quartz was the most abundant phase identified in the sample, with its prominent peaks at 2θ values at approximately 12°, 21°, 26°, 36°, 38°, 50°, 60° and 68° as illustrated in Figure 31. The high-intensity peaks reflect the robust crystalline structure of quartz. The abundance of quartz in the sample indicates its mechanical stability and resistance to chemical weathering during sediment deposition (Wang et al., 2012).

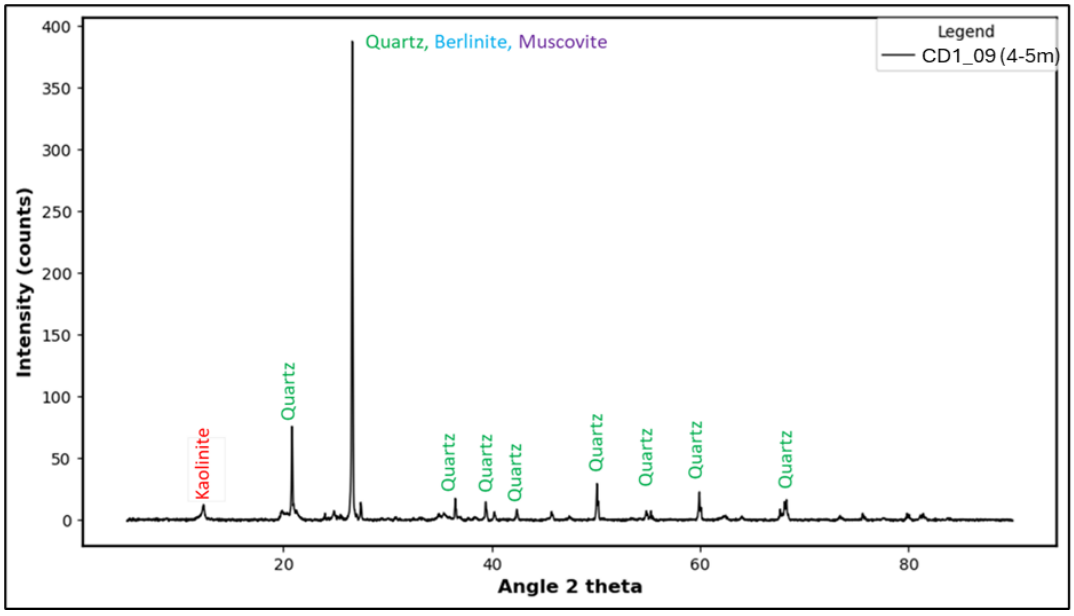

Figure 31: Sample CD1_09 at 4-5m interval (observed quartz).

4.4.2 CD2 Dump

Quartz and magnetite dominate in clay and dull coal discards, indicating lower organic matter content in these samples. In contrast, kaolinite, calcite, and pyrite are more abundant in moist coal discards, reflecting their higher organic richness. The presence of pyrite signals a potential for acid generation during oxidation. Brushite detected in dull coal discards suggests hydrothermal fluid interactions involving carbonate and phosphate minerals. Meanwhile, the notably high content of berlinite in clay coal discards points to possible mineral transformations influenced by phosphate-rich fluids. These mineralogical patterns provide insights into the depositional environment and post-depositional alteration processes affecting the coal seams.

Table 8: Mineralogical composition (wt%) of CD2 dump.

Sample_ID	Q	K	D	C	A	M	Mu	B	P	Br
CD2_01	40,08	37,23	4,38	4,63	3,50	3,04	2,97	2,36	1,63	nd
CD2_02	41,13	37,41	4,49	4,96	1,39	1,66	3,00	2,40	2,76	nd
CD2_03	45,39	36,29	2,40	4,68	1,27	1,61	3,21	2,32	2,72	nd
CD2_04	42,89	37,78	2,45	4,86	1,38	1,89	3,09	2,36	2,93	nd
CD2_05	43,57	37,08	2,40	5,67	1,25	1,54	3,17	2,36	2,67	nd
CD2_06	41,05	33,33	2,36	5,56	3,77	4,34	2,98	3,41	2,96	nd
CD2_07	39,18	36,81	2,47	4,89	1,40	3,95	3,86	2,36	4,97	nd
CD2_08	44,23	35,91	2,49	5,02	1,46	1,96	3,12	2,35	2,98	nd
CD2_09	41,32	37,56	2,47	4,86	1,33	1,50	4,05	2,41	3,65	nd
CD2_10	44,28	33,16	2,56	5,18	1,52	2,99	4,18	2,41	3,01	nd
CD2_11	63,64	20,63	1,55	1,50	1,15	2,38	3,02	2,91	2,29	nd
CD2_12	44,55	38,44	3,36	3,35	1,15	1,44	3,28	2,29	1,60	nd
CD2_13	45,82	30,95	2,48	8,30	1,35	1,64	3,39	2,44	2,74	nd
CD2_14	44,78	37,44	2,47	4,72	1,35	1,63	3,26	2,31	1,74	nd
CD2_15	48,35	36,62	2,28	2,26	1,13	1,52	3,27	2,15	1,66	nd
CD2_16	41,85	35,57	2,48	8,68	1,43	1,83	3,04	2,44	1,89	nd
CD2_17	44,90	33,32	2,39	8,27	1,24	1,63	3,24	2,29	1,74	nd
CD2_18	50,06	34,35	3,27	2,16	1,09	1,52	3,48	2,23	1,66	nd
CD2_19	45,03	40,16	2,44	2,60	1,23	1,30	3,20	2,22	1,50	nd
CD2_20	42,88	38,81	2,36	6,02	1,17	1,38	3,10	2,28	1,55	nd
CD2_21	41,13	28,52	2,40	7,46	2,23	6,01	3,05	5,30	3,42	nd
CD2_22	47,18	35,37	2,57	3,07	1,51	1,94	3,32	2,43	1,96	nd
CD2_23	56,58	22,06	2,87	4,03	2,04	2,88	3,97	2,52	2,66	nd
CD2_24	60,06	17,00	2,98	3,21	2,44	2,74	3,07	2,48	3,51	2,24

Q-quartz, K-kaolinite, D-dolomite, C-calcite, A-ankerite, M-magnetite, Mu-muscovite, B-berlinite, Br-Brushite, P-pyrite and nd-not detected.

Even in CD2 dump, quartz and kaolinite were observed to be the major phases. Just like in CD1 dump, the same minor phases were detected, including brushite which rarely occurs in coal. Even though berlinite was among the minor phases in the sample, its high-intensity peaks were detected at 2θ values of approximately 21° and 26° (Figure 32), coexisting with muscovite and quartz at around 26°. Berlinite's crystal structure is that of quartz, and its presence in the sample indicates phosphorus enrichment, from organic matter or groundwater interactions. Muscovite's prominent peak at 2θ approximately 26° (Figure 32) confirms progression of feldspar weathering. Rather than occurring solely as inclusions, muscovite represents an integral component of the mineral assemblage, reflecting its stability during sedimentary deposition and diagenetic alteration. It also reflects contributions from either metamorphic or igneous source rocks with limited alteration (Vassilev et al., 2010).

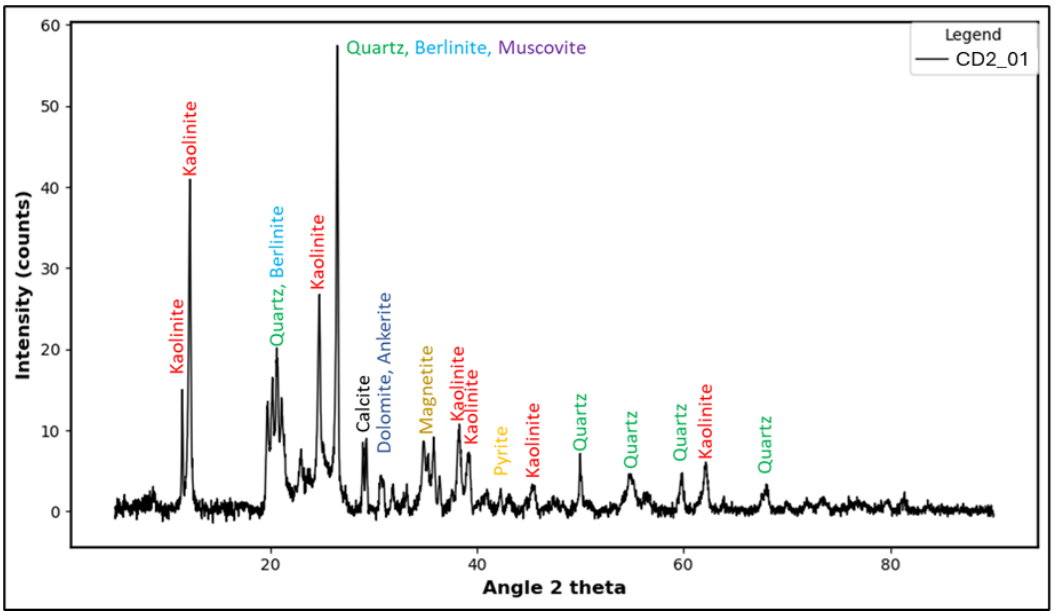

Figure 32: Sample CD2_01 (observed berlinite and muscovite).

A distinct peak at approximately 36°, corresponding to magnetite (Figure 33), indicates a minor iron-bearing phase. This suggests localized oxidizing conditions during coal formation and reflects detrital input from igneous or metamorphic rocks (Wagner et al., 2019).

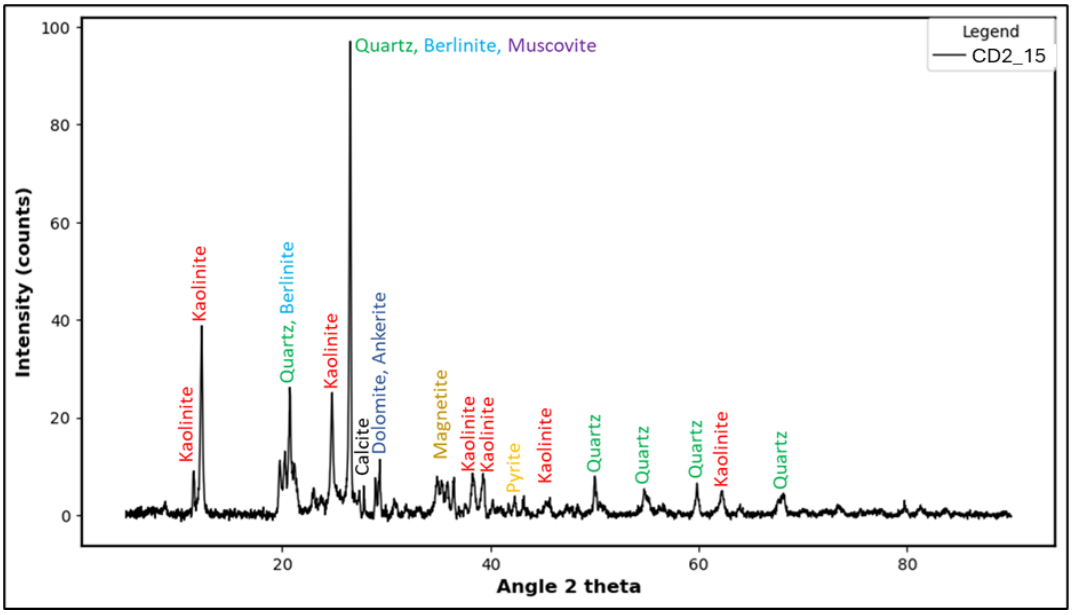

Figure 33: Sample CD2_15 (observed magnetite).

Brushite's prominent peak was identified at a 2θ value of approximately 11° (Figure 34). Its presence indicates that a small portion of calcium was incorporated into phosphate minerals. Its presence also indicates an early diagenetic transformation in phosphate sediments. It forms when phosphate-rich fluid interacts with dissolved calcium under acidic and low temperature conditions (Gong et al., 2024).

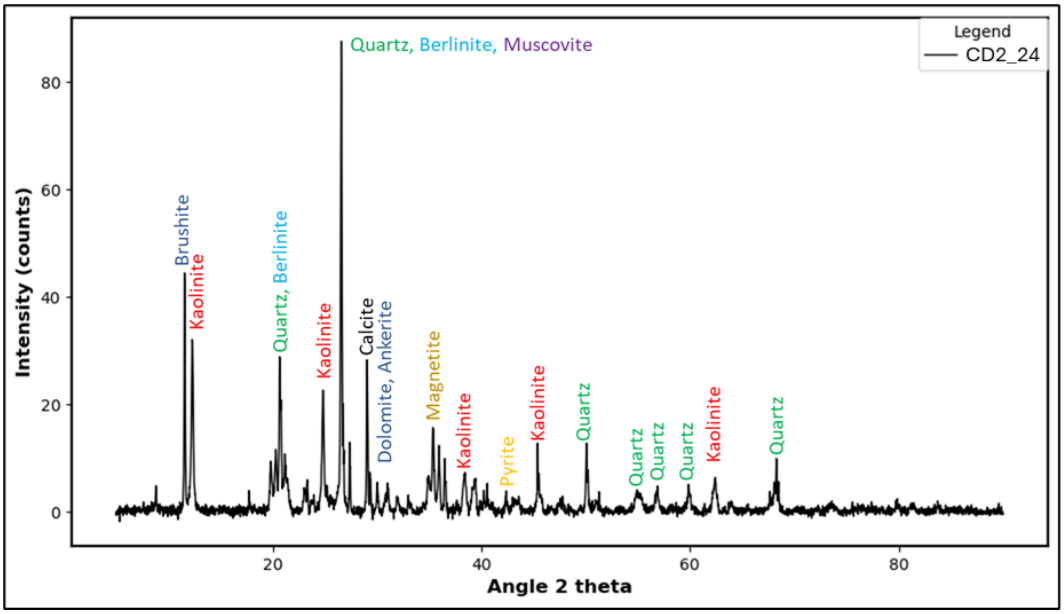

Figure 34: Sample CD2_24 (observed brushite).

4.5 SEM-EDS Analysis

The SEM-EDS analysis focused on the morphology and chemical composition of minerals present in the CD1 and CD2. XRD results revealed that both dumps share similar mineralogical compositions. While XRD identifies the crystalline minerals present, SEM-EDS provides complementary insight by revealing mineral morphology and determining the modes of occurrence. Specifically, SEM-EDS helps distinguish whether minerals are detrital (transported from external sources), authigenic (formed in place during sedimentation), or epigenetic (formed or altered after initial deposition). This combined approach enables a comprehensive understanding of the mineralogical characteristics influencing the coal discards.

4.5.1 Silicate Minerals

The principal silicate minerals in the CD1 and CD2 of the Witbank Coalfield are quartz and kaolinite, with minor amounts of muscovite, montmorillonite, and illite. Quartz grains exhibit angular to subangular particles with irregular morphologies, as illustrated in Figure 35a. This indicates detrital origin, suggesting limited transportation and minimal mechanical weathering. Montmorillonite appears as fine-grained, platy, and flaky aggregates with stacked morphology as

illustrated in Figure 35b, suggesting an intense chemical weathering during coal formation. The compacted and irregularly edged kaolinite with a blocky texture depicted in Fig. 7e reflects a more mature, diagenetically transformed phase, pointing to intense weathering of intermediate phases or feldspar (Figure 35c). In addition, some particles were porous and loosely packed, forming an irregular cluster, whereas in some areas they showed curled or crumpled sheet-like structures. The EDS spectrum in Figure 35c illustrates the presence of the major elements such as Si, O, C, and minor elements such as Al, Fe, and K. The dominance of Si and O suggests the presence of quartz. The EDS spectrum in Figure 35d shows major elements such as O, Si, Al, and minor elements such as Fe, K, and Ca. The high concentration of Si, O, Al suggests the presence of kaolinite while the presence of hematite and ilmenite suggest that kaolinite formed in oxidation environments.

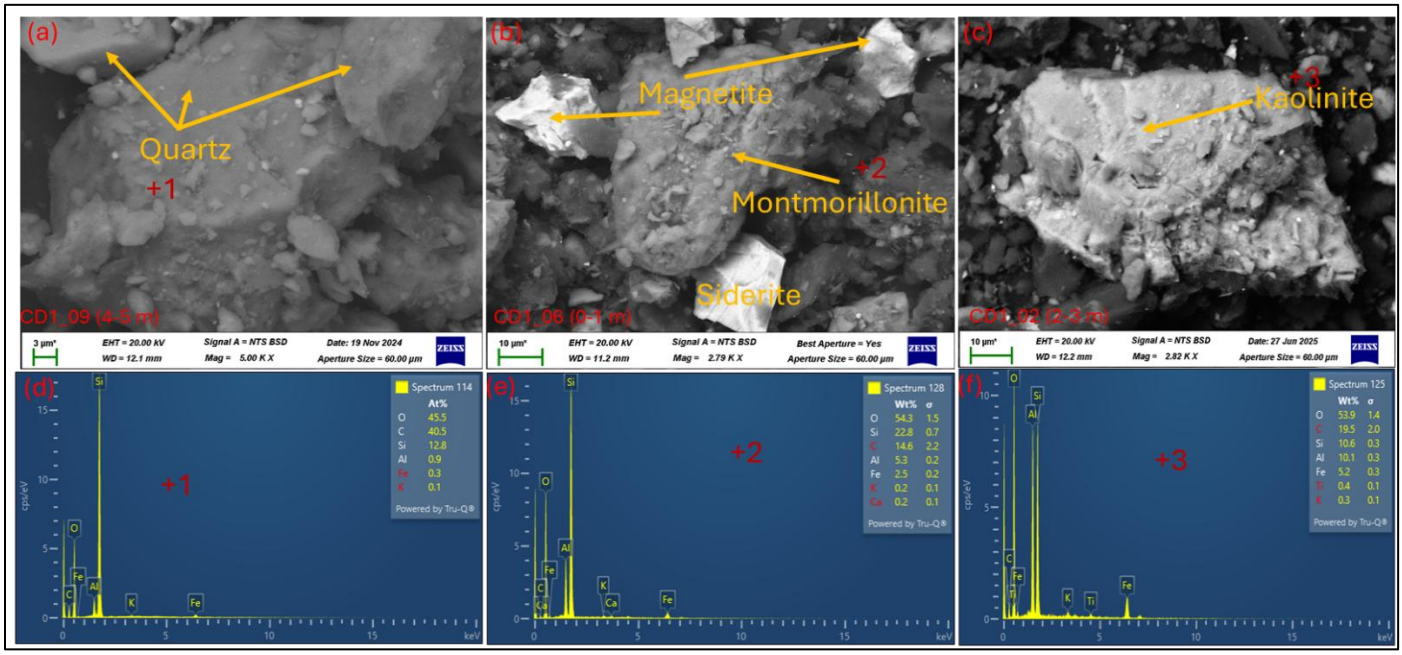

Figure 35: Silicate minerals in the coal discard samples, a) angular to subangular quartz, b) fine-grained, platy, and flaky montmorillonite aggregates, c) irregular edged kaolinite particle with a blocky texture d) EDS spectrum for point +1 in Figure 35a, e) EDS spectrum for point +2 in Figure 35b and f) EDS spectrum for +3 Figure 35c.

The muscovite particle appears as platy to angular with a smooth surface (Figure 36a). It is surrounded by fine-grained materials. The presence of muscovite reflects moderate diagenetic alteration of feldspar-rich sediments, consistent with low-energy depositional environments and chemical weathering conditions that favour mica stability (Finkelman et al., 2019). The illite particle appears as an elongated, sheet-like structure (Figure 36b), consistent with a detrital origin aligning with observations by Kang et al. (2024) that detrital illite typically exhibits discrete grain boundaries and elongated morphologies. "Its presence in coal discards is associated with feldspar weathering and indicative of higher-energy depositional environments typical of fluvial or deltaic systems (Ghosh et al., 2019). The EDS spectrum in Figure 36c showed the detected elements such as C, O, Al, Si, K, and a small amount of Fe and Mg were also detected. The high concentration of Al, Si and K confirms the muscovite and the presence of Fe and Mg suggests a possible substitution in the crystal structure. The presence of high carbon may be due to sample coating or organic matter association. The EDS spectrum in Figure 36d shows a high amount of O, Al, Si, K and a small amount of Ti, Fe and Mg. The presence of the Al-Si-K may be attributed to illite while Ti-Fe-Mg may be attributed to siderite. The lower carbon content compared to muscovite, suggests that illite was associated with kaolinite.

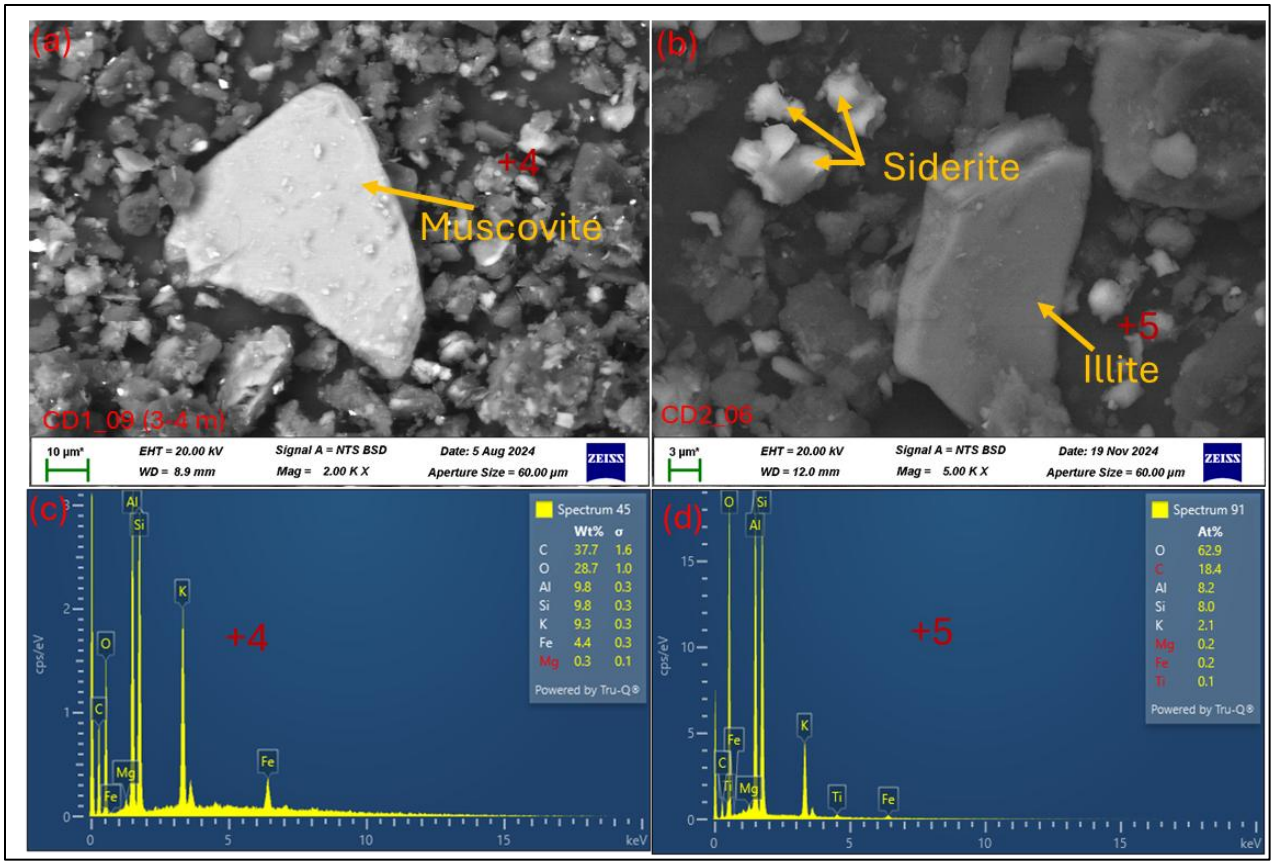

Figure 36: Silicate minerals in the coal discard samples, a) white platy to angular muscovite with a smooth surface, b) elongated, sheet-like structure of illite, c) EDS spectrum for point +4 in Figure 36a, and d) EDS spectrum for point +5 in Figure 36b.

4.5.2 Carbonate Minerals

Calcite and siderite were the dominant carbonate minerals in the Witbank coalfield. The siderite particles appear as small, bright, fragmented, or irregular shapes embedded in or surrounded by organic matter as illustrated in Figure 37a, suggesting an early diagenetic stage. The siderite particles have not fully crystallized, and the irregular shape indicates that precipitation took place under varying conditions, possibly low temperatures, or fluctuating pH levels (Wang et al., 2023). In Figure 37b, the siderite particle was more well-rounded, bright, and massive, suggesting a full crystallization. This indicates that siderite has precipitated under more stable diagenetic conditions where there was less involvement of organic matter (Wang et al., 2023). The EDS spectrum in Figure 37c exhibits high C and O, confirming a carbonate phase, while low Fe suggests that siderite

was mixed with calcite, dolomite or affected by carbon coating reducing the Fe-signal. The presence of Ca indicates that siderite occurs alongside calcite and dolomite. The EDS spectrum in Figure 37d shows a high Fe content, confirming the purity of siderite composition, while low C and O suggest reduced organic matter. The presence of Al and Si may suggest that siderite was associated with silicate minerals.

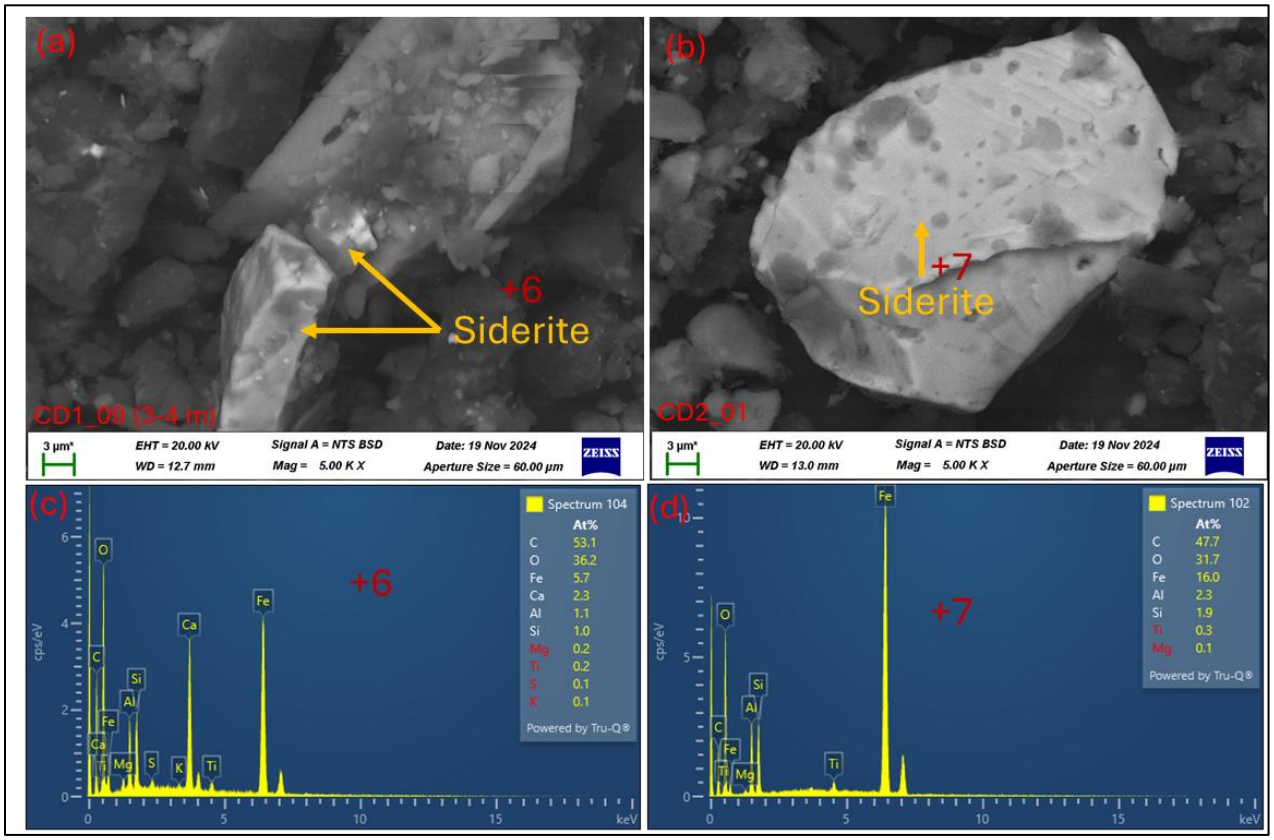

Figure 37: Carbonate minerals in the coal discard samples, a) small, bright, fragmented, or irregular particles of siderite, b) well-rounded, bright, and massive siderite particle, c) EDS spectrum for point +6 in Figure 37a, and d) EDS spectrum for +7 in Figure 37b.

Calcite and dolomite may originate from hydrothermal fluids or groundwater interactions (Shao et al., 2022). The calcite grains occur as irregular and fragmented particles within the organic matrix of coal (Figure 38a), indicative of precipitation influenced by organic matter. This morphology is consistent with early diagenetic formation, as well as potential later epigenetic alteration (Wang et al., 2017). Figure 38b shows a dolomite grain embedded within fine-grained particles. The rough

surface indicates weathering or possible diagenetic alteration. Figure 38c shows an EDS spectrum which shows high O, C, and Ca, confirming high purity of calcite and minor Al and Si, suggesting traces of silicate minerals. The presence of high O, C, Ca, and Mg confirms dolomite, while minor Fe, as well as trace Al, Si and P may indicate mixed phases.

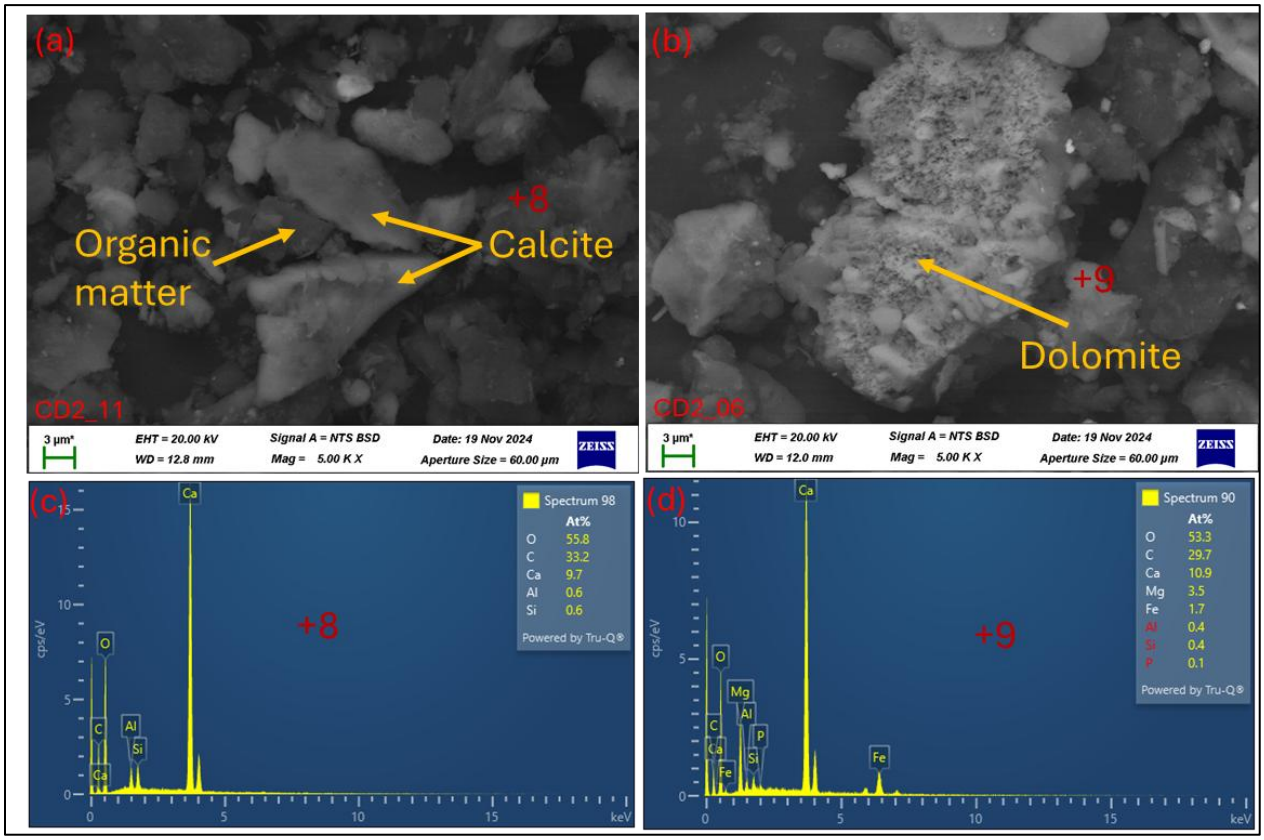

Figure 38: Calcite and dolomite a) irregular and fragmented particles of calcite, b) dolomite grains embedded in calcite, c) EDS spectrum for point +8 in Figure 38a, and d) EDS spectrum for point +9 in Figure 38b.

4.5.3 Sulfide Minerals

Pyrrhotite, rather than pyrite, is the main sulfide mineral identified in the two coal discard dumps of the Witbank Coalfield. Pyrrhotite is an iron sulfide mineral distinct from pyrite in crystal structure and physical properties. Its presence in coal-bearing sediments typically suggests decomposition of syngenetic pyrite. Sulfur content in coal, predominantly hosted by iron sulfides like pyrrhotite, is a key contributor to acid mine drainage potential (Orem & Finkelman, 2005;

Thwala, 2020). Marine influence via seawater during peat accumulation often controls the sulfur content in coal (Ma et al., 2022).

The pyrrhotite crystals exhibit euhedral to subhedral morphologies with bright, angular forms dispersed within a fine-grained matrix, as illustrated in Figure 39a. These well-defined crystal shapes indicate crystallization under relatively stable, near-equilibrium conditions that allowed orderly crystal growth. Figure 39b shows an EDS spectrum with strong peaks for sulfur (S) and iron (Fe), confirming the presence of iron sulfides. Additional low peaks of carbon (C), oxygen (O), aluminium (Al), and silicon (Si) relate to organic matter and clay minerals in the surrounding matrix. Pyrrhotite in these coal deposits may form via both syngenetic and epigenetic processes. Syngenetic pyrrhotite forms contemporaneously with peat accumulation, reflecting original depositional environments. In contrast, epigenetic pyrrhotite forms later, during diagenesis or post-depositional alteration, often precipitating from circulating fluids and modifying earlier mineral assemblages (Wang et al., 2017; Ma et al., 2022).

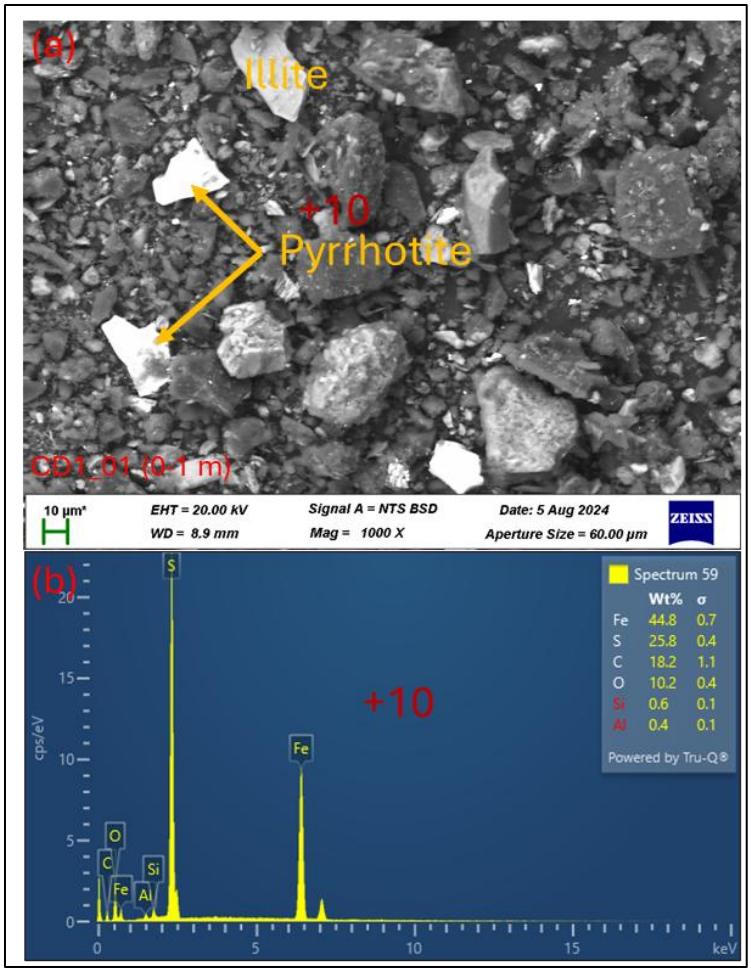

Figure 39: Sulfide mineral, a) bright white euhedral to subhedral crystal of pyrrhotite, b) EDS spectrum for point +10 in Figure 39a.

4.5.4 Sulfate Minerals

Barite is the only sulfate mineral detected by SEM-EDS in both coal discard dumps. In Figure 40a, it appears as a well-defined rectangular crystal form. Its bright white small angular crystal was embedded in a matrix of fine-grain particles, suggesting that barite formed through precipitation. Whereas in Figure 40b, it appears as a more elongated, blade-like crystal form. Its big and more irregular shape suggests unaltered grain. Similarly, in Figure 41a, it appears as a well-defined tabular, plate-like crystal with clear angular edges, suggesting minimal alteration and in Figure 41b, it appears as a more massive crystal form with a rough surface, indicating intense weathering or hydrothermal alterations. The prominent peaks of O, S and Ba in Figure 40c indicate high purity

barite, while the less prominent peaks were observed for Ba, S and O as shown in Figure 40d also confirming barite among other minerals.

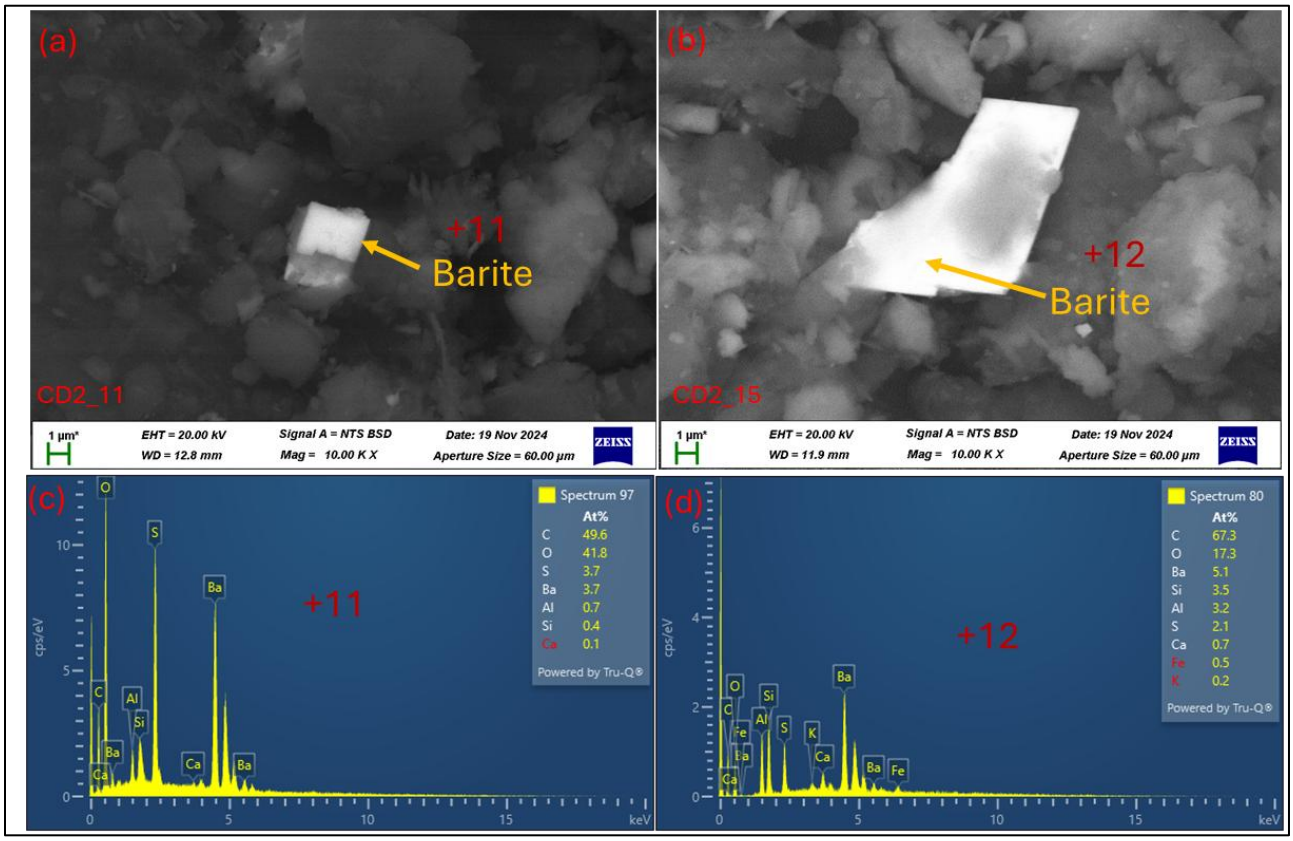

Figure 40: Barite in the coal discard samples, a) small, bright white, rectangular barite crystal within dark fine-grained matric, b) big elongated, blade-like barite crystal, c) EDS spectrum for point +11 in Figure 40a, and d) EDS spectrum for point +12 in Figure 40b.

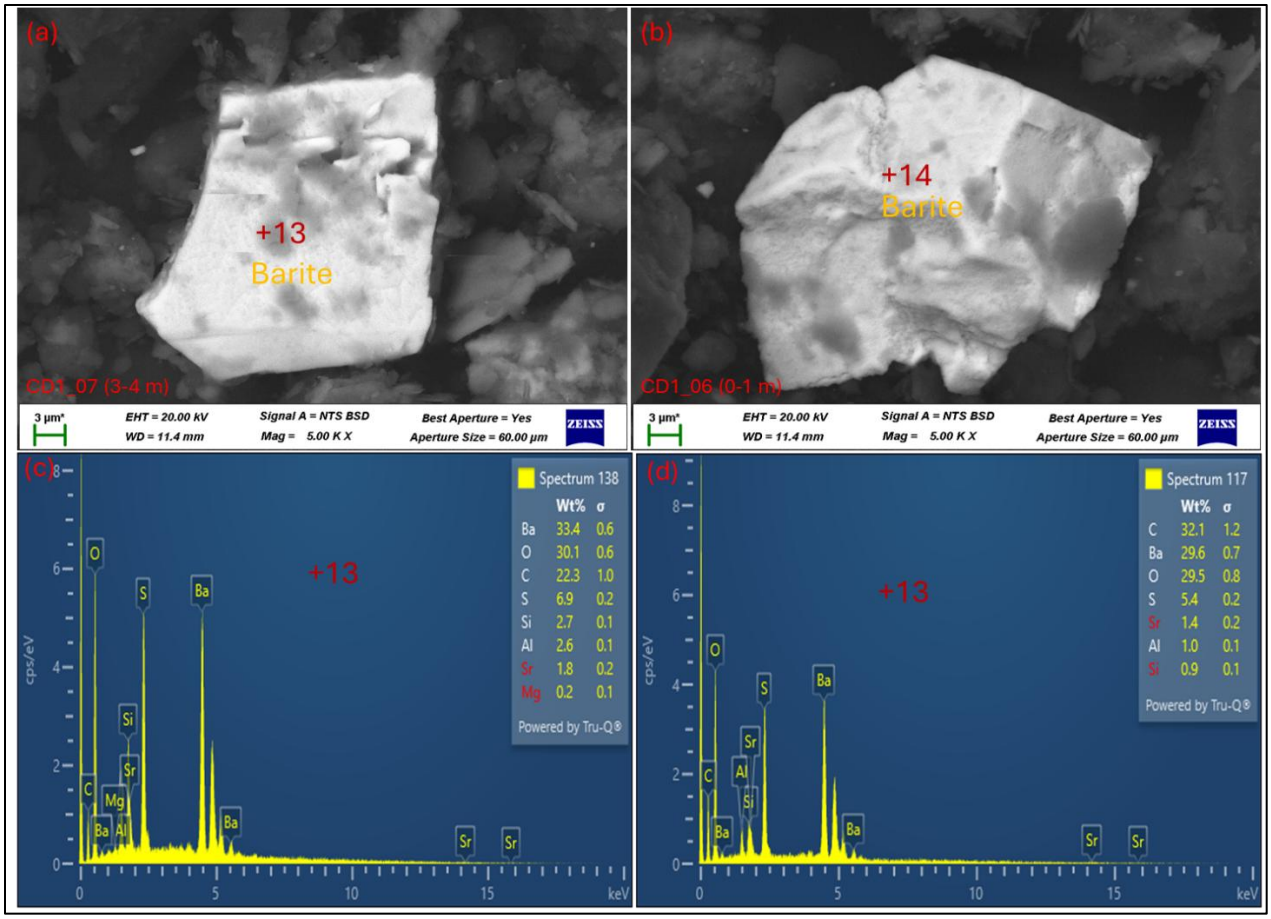

Figure 41: Barite, a) tabular, plate-like crystal with clear angular edges, and b) massive crystal form with rough surface, c) EDS spectrum for point +13 in Figure 41a, and d) EDS spectrum for point +14 in Figure 41b.

4.5.5 Other Minerals

Other minerals that have been detected by SEM-EDS were zircon, ilmenite, and magnetite. The presence of magnetite and ilmenite indicates oxidizing conditions in a micro-environment. In Figure 42a, magnetite had a bright-white, tabular, plate-like crystal with sharp edges, with some lines and small dark inclusions of amorphous organic matter on the surface, suggesting post-depositional alterations during coal formation. In Figure 43d, magnetite appears as a bright irregular shape that was partially covered by organic matter, suggesting that the organic matter was transported by hydrothermal fluids and adsorbed onto the surface of magnetite during mineral

precipitation (Wagner et al., 2019). High peaks of O and Fe confirm the high purity of the magnetite in the sample, as shown in Figure 42c.

Zircon is a resistant detrital mineral commonly sourced from weathered granitoids and sedimentary sources (Mapeo et al., 2019). It appears as a massive and round grain, with tiny cracks and small patches of organic matter on its smooth surface in Figure 42b, suggesting it was transported by terrigenous materials (Shao et al., 2022). In Figure 43b, zircon grains showed a well-developed, bright-white euhedral crystal form with a tetragonal prismatic structure (Shao et al., 2022). This suggests that these zircon grains have resisted weathering. Prominent peaks of Zr, Si, O, and Al suggest that zircon occurs with other minerals, making it less bright as shown in Figure 40d.

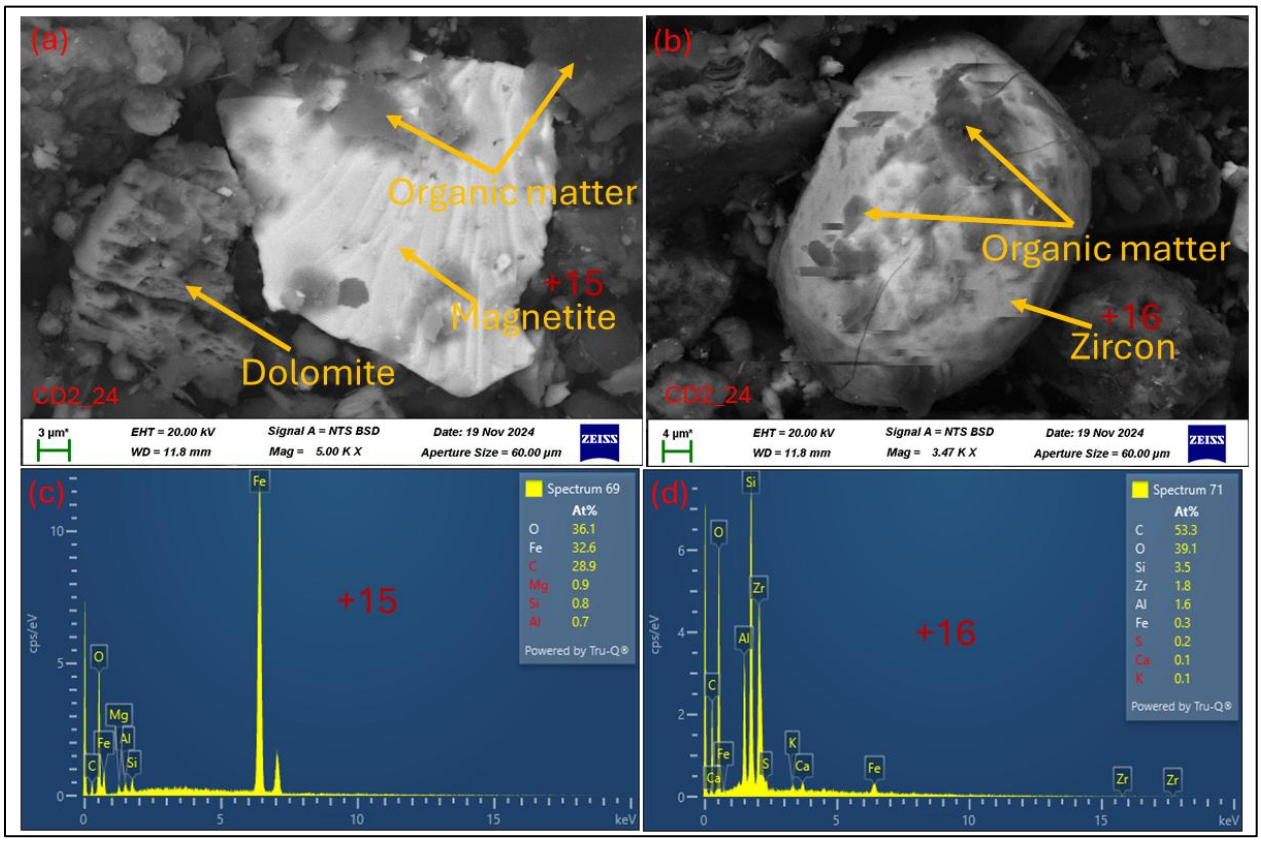

Figure 42: Other minerals, a) bright-white, tabular, plate-like magnetite crystal, b) massive and round zircon grain, c) EDS spectrum of point +15 in Figure 42a, and EDS spectrum of point +16 in Figure 42b.

Ti-hematite appears as an elongated, tabular crystal form as illustrated in Figure 43a, generally derived from mafic or heavy minerals (Farjana et al., 2021). Its rough surface and sharp edges suggest it went through minimal alteration in a situ environment. Prominent peaks of Fe, O, and minor peaks of Mg, Al, and Ti in Figure 42c, along with high concentrations of Fe, C, O and Ti, confirm the presence of ilmenite minerals among other minerals and organic matter.

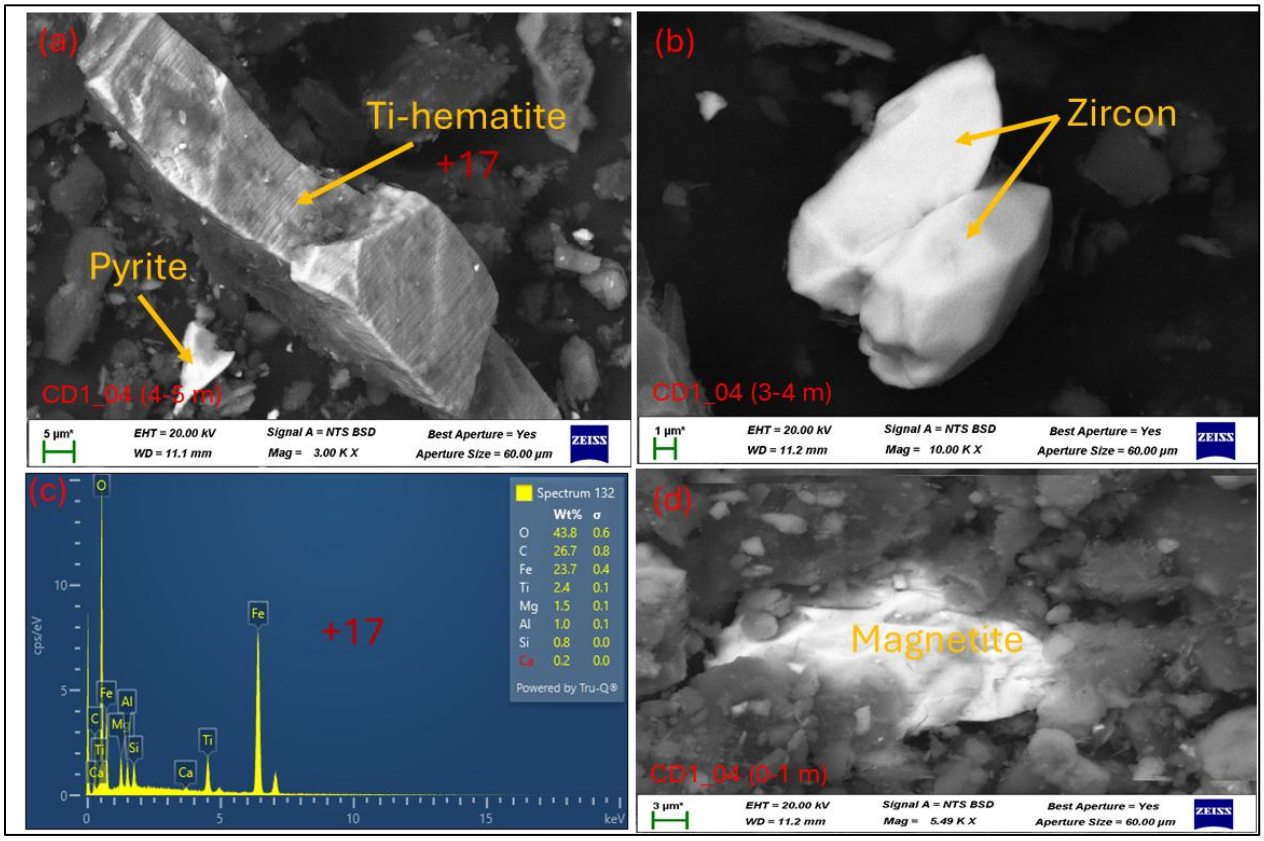

Figure 43: Other minerals, a) elongated, tabular crystal of Ti-hematite, b) white tetragonal prismatic structure of zircon, c) EDS spectrum of point +17 in Figure 43a, and d) white magnetite partially covered by organic matter.

4.6 TIMA Analysis

The TIMA was used to supplement XRD and SEM-EDS results by determining the mode of occurrence and providing insight into the distribution and association of CRMs in coal discards. Eight samples were selected for analysis based on their varied chemical composition. Five samples were from the CD1 dump at different depth intervals (CD1_09 at 0-1 m up to 4-5 m intervals) and three samples from the CD2 dump (CD2_06, CD2_15, and CD2_24).

Quartz and kaolinite are the major minerals in all the samples (Table 9). These results align with the XRD results. In the CD1 dump, the quartz content increased with depth while the kaolinite content decreased with depth. Kaolinite was the predominant mineral in all samples in CD1 dump, and in CD1_09 at 0-1 and 2-3 m intervals, while quartz was dominant in CD1_09 at 1-2, 3-4 and 4-5 m intervals. Sample CD1_09 at 0-1 m was found to contain high proportion of kaolinite, quartz, calcite, siderite, dolomite, pyrite, fusinite and vitrinite and microcline with other minerals occurring in trace amount less than 1 wt% including zircon, rutile, ilmenite, apatite, gypsum, illite, muscovite, albite, ferrosilite, biotite and gibbsite. CD1_09 at 1-2 m was found to be dominated by quartz, kaolinite, pyrite, calcite, fusinite and vitrinite and siderite while sample CD1_09 at 2-3 m was dominated by kaolinite, quartz, siderite, pyrite, vitrinite, fusinite, gypsum, calcite, microcline, illite, muscovite, rutile, and dolomite. Quartz, kaolinite, microcline, vitrinite, fusinite, pyrite, calcite, dolomite, and siderite dominated CD1_09 at 3-4 m, while quartz, kaolinite, fusinite, microcline and siderite were predominant in CD1_09 at 4-5 m. CD2 samples were dominated by kaolinite, quartz, vitrinite, siderite, fusinite, calcite, microcline, gypsum, muscovite, dolomite, biotite, rutile and pyrite.

Table 9: Quantitative modal analysis of coal discard samples using TESCAN TIMA.

Coal discard modal phases	CD1_09 (0-1 m)	CD1_09 (1-2 m)	CD1_09 (2 -3 m)	CD1_09 (3-4 m)	CD1_09 (4-5 m)	CD2_06	CD2_15	CD2_24
Liptinite	0,01	0,00	0,01	0,00	0,00	0,01	0,01	0,01
Vitrinite	6,58	1,74	4,53	2,94	0,32	7,90	10,23	3,13
Vitrinite (Oxidised)	5,04	1,19	1,84	2,70	0,23	6,66	13,47	3,13
RSF	1,30	0,33	0,84	0,60	0,22	0,87	1,39	0,36
SFusinite	4,89	1,23	4,07	3,53	1,50	6,74	8,15	2,29
Fusinite	10,97	2,62	11,03	8,10	5,57	15,94	16,90	6,09
Fusinite/Sc (Hi C)	5,15	1,16	3,35	4,37	2,71	8,04	9,20	4,35
Albite	0,32	0,16	0,24	0,15	0,09	0,25	0,22	0,42
Ferrosilite (Mg:Fe)	0,02	0,02	0,11	0,05	0,02	0,04	0,04	0,07
Kaolinite	10,38	4,65	23,04	8,16	7,98	19,16	15,75	11,44
Quartz	10,08	5,65	17,82	28,29	31,17	11,20	10,60	10,71
Alunite/Gibbsite	0,04	0,04	0,10	0,03	0,01	0,12	0,09	0,04
Chlorite/Biotite	0,21	0,44	0,45	0,37	0,30	0,29	0,25	1,28
Smectite Clay	0,00	0,00	0,01	0,00	0,01	0,02	0,00	0,00
Muscovite	0,48	0,38	1,83	0,36	0,20	1,42	1,62	0,58
Illite	0,44	0,36	1,68	0,65	0,76	0,80	0,74	0,67
Microcline	1,31	0,97	2,42	2,29	2,35	1,82	1,71	2,15
Pyrite	2,26	3,46	5,16	2,54	0,46	1,06	0,74	10,91
Gypsum	0,58	0,02	4,21	0,15	0,01	3,93	0,51	0,51
Calcite	5,22	2,49	3,87	1,73	0,33	3,05	1,56	7,74
Dolomite	1,42	0,84	1,01	1,06	0,16	1,42	0,86	2,64
Apatite	0,28	0,11	0,67	0,26	0,02	0,51	0,34	0,23
Siderite	1,82	1,85	6,16	1,73	2,15	2,57	1,23	3,66

Ilmenite	0,19	0,34	0,77	0,28	0,17	0,31	0,08	0,96
Rutile	0,52	0,58	1,07	0,51	0,60	0,51	0,31	1,01
Zircon	0,49	0,24	0,48	0,29	0,54	0,23	0,17	0,17
Others	1,38	0,73	2,98	1,98	2,01	1,81	1,77	1,74
Total	**71,37**	**31,57**	**99,82**	**73,13**	**59,90**	**96,67**	**97,94**	**76,32**

Figures 44 and 45 show mineral phases at different scales for each sample. Figure 44d shows that small illite phases occurred with biotite on the edges of microcline, suggesting that illite formed under hydrothermal or low-grade metamorphism conditions (Aja, 2019). In Figures 45b and c, muscovite particles were disseminated on the kaolinite, suggesting that kaolinite allows the adsorption of small particles of muscovite on its surface. This aligns with coal's inherent adsorptive properties (Dai et al., 2020). Siderite particles in Figure 44d were dispersed among quartz, clay minerals, and organic matter. They were also present alongside calcite and dolomite, indicating that carbonate minerals were precipitated during coal formation. Small particles of siderite were also distributed in pyrite, suggesting Fe-mineralization in high sulfuric conditions. The dolomite particles are embedded in calcite, which aligns with SEM-EDS results. The embedment of dolomite particles in calcite occurs because of incomplete calcite dissolution followed by the precipitation and replacement of Ca by Mg in a shallow marine environment (Querol et al., 2001). In Figures 44d, e and 45a, it can be observed that pyrite was mainly covered by small particles of kaolinite, dolomite and to a lesser extent, fusinite and quartz. The presence of small particles of ilmenite, fusinite (high C), dolomite, and kaolinite on the surface of pyrite reflects a very complex history of geological formation. This indicated that these minerals were deposited after pyrite crystallization. The same figures show that gypsum was found next to pyrite, this suggests that pyrite has undergone oxidation, where the sulfate ion reacted with calcium to form gypsum. Figures 44d and e show that small particles of calcite and dolomite were on the surface of gypsum, which indicates an incomplete transformation of these carbonate minerals to gypsum.

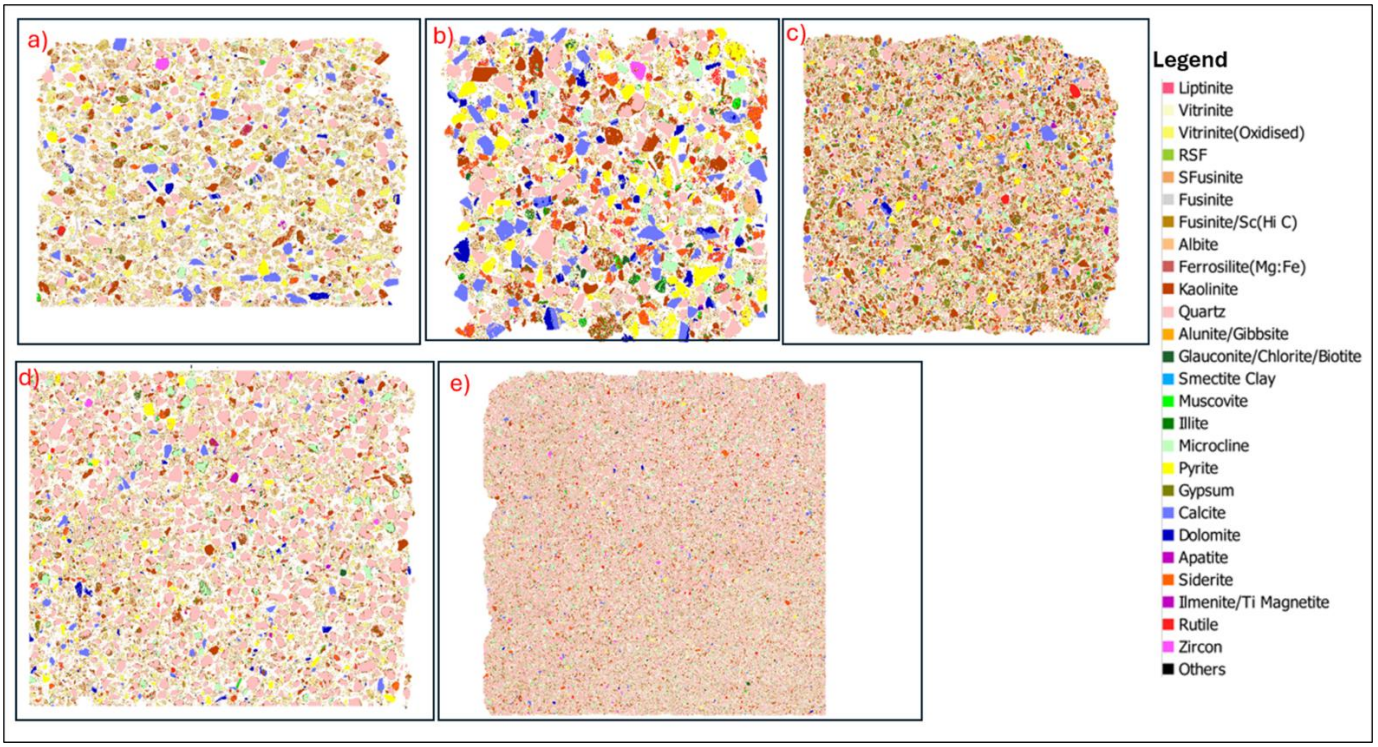

Figure 44: CD1 TIMA results for CD1_09 at difference scales, a) at 0-1 m interval (scale 2 mm), b) at 1-2 m interval (scale 1 mm), c) at 2-3 m interval (scale 2 mm), d) at 3-4 m intervals (scale 1 mm) and d) at 4-5 m (scale 5 mm).

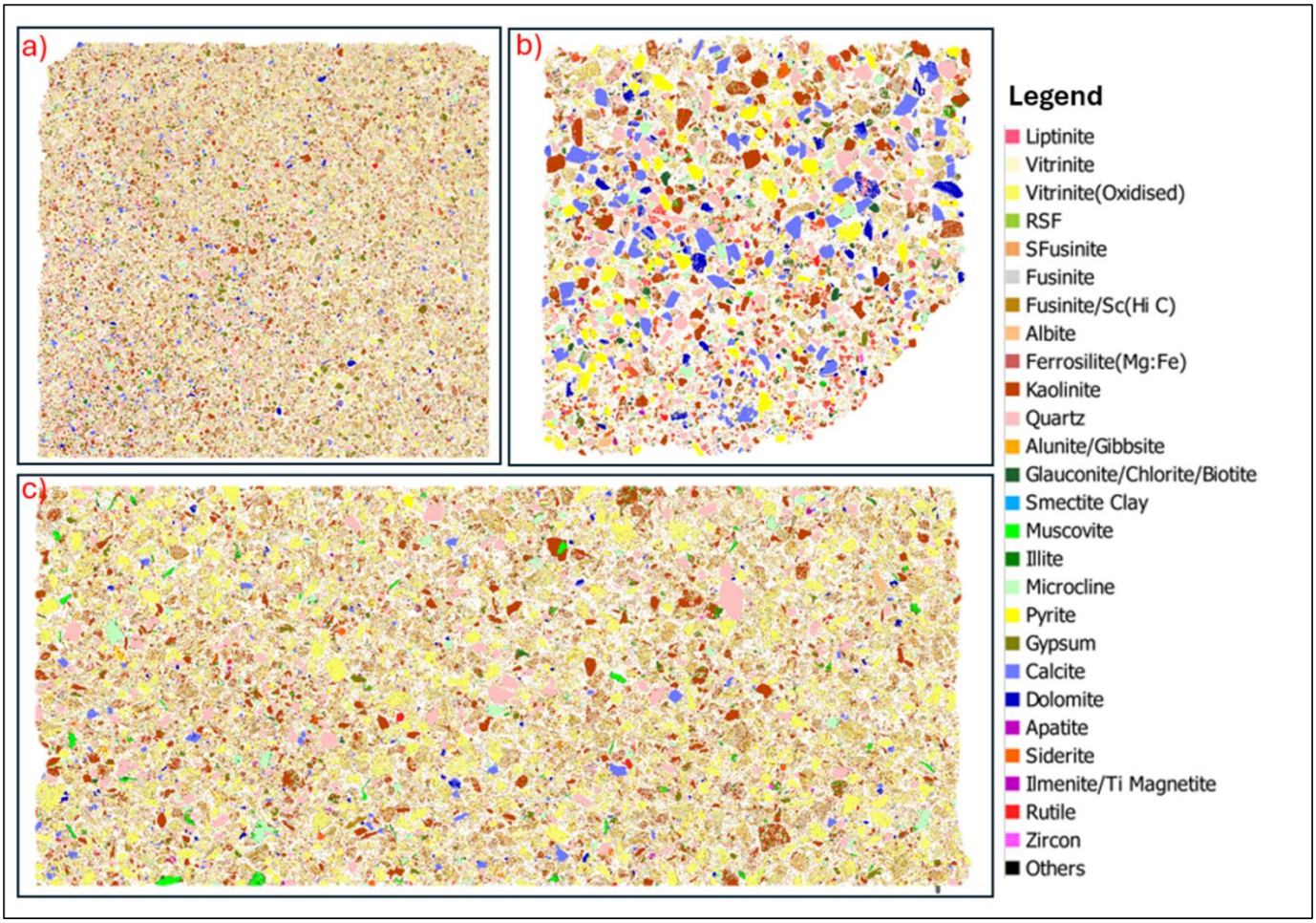

Figure 45: TIMA results for CD2 at different scales, a) CD2_06 (scale 5 mm), b) CD2_24 (scale 2 mm) and c) CD2_15 (scale 2 mm).

4.7 Geochemical Analysis

Geochemical analysis of CRMs is pivotal for understanding their distribution, abundance, and potential for extraction. This study employed a combination of XRF and ICP-MS to quantify the elemental composition of the samples. These techniques provided a comprehensive understanding of the major and trace element concentrations, enabling the identification and characterization of CRMs.

4.7.1 Major Oxides in CD1

The concentration levels of SiO_2, Al_2O_3 Fe_2O_3, TiO_2, MnO, MgO, CaO, Na_2O, K_2O, P_2O_5, and Cr_2O_3 as well as LOI vary across different sample depth intervals. The results are presented in Table 10. The concentration of silica ranges from 11.14 wt% in CD1_05 at the 1-2 m interval to 60.85 wt% in CD1_09 at the 4-5 m interval, with an average of 20.15 wt%. Similarly, the concentration of alumina ranges from 6.20 wt% in CD1_05 at the 1-2 m interval to 11.83 wt% in CD1_09 at the 4-5 m interval. The average Al_2O_3 content was 9.33 wt%, indicating a relatively low concentration of alumina in the samples (Dai et al., 2017; Zhu et al., 2016). The high silica and low alumina contents correlate to the high abundance of quartz and kaolinite from XRD and TIMA results and to a lesser extent correlate with lesser amount of muscovite, illite, and microcline.

The Fe_2O_3 concentration ranged from 1.08 wt% in CD1_05 at the 1-2 m interval to 9.37 wt% in CD1_02 at the 2-3 m interval, with an average of 3.72 wt%, while the concentration of CaO varies from 0.73 wt% in CD1_09 at the 4-5 m interval to 5.72 wt% in CD1_09 at the 0-1 m interval, with an average of 3.18 wt%. The low concentration of Fe_2O_3 is consistent with the limited occurrence of Fe-bearing minerals such as pyrite, siderite, and ferrosilite detected by TIMA and magnetite by XRD, while the low concentration of CaO correlates with the smaller amounts of calcite and apatite detected by TIMA and XRD. The concentration of MgO ranged from 0.52 wt% in CD1_09 at the 4-5 m interval to 1.21 wt% in CD1_01 at the 0-1 m interval, with an average of 0,87 wt%. The trace concentration of MgO may be attributed to minor phases of dolomite detected by TIMA and XRD. It can be inferred that the shallower intervals were enriched in carbonate minerals.

The rest of the oxides exhibit minimal proportion except for the loss of ignition (LOI), which shows the total content of organic matter and volatile elements. The average LOI is 60.79 wt%, indicating the CD1 can be combusted or volatilized. Coal discards may contain significant organic materials since kerogen is high in coals (Pone et al., 2007). In addition to that, the LOI was relatively stable across the 1-2 m interval samples, exhibiting the highest LOI at 63.42 wt%, indicating an increase in combustion or volatilization. Trace elements such as K, P, T, and Na were attributed to minor amounts of microcline, apatite, anatase, and albite, respectively, as detected by TIMA. The chromate concentration was the same throughout the sample.

Table 10: Geochemical composition (in wt%) of CD1 per depth interval.

0-1 m	SiO2	TiO2	Al2O3	Fe2O3	MnO	MgO	CaO	Na2O	K2O	P2O5	Cr2O3	LOI	Total
CD1_01	20.55	0.74	9.9	4.87	0.05	1.21	3.66	0.19	0.45	0.24	0.01	67.03	99.44
CD1_02	19.8	0.62	9.23	3.63	0.04	0.88	3.92	0.18	0.43	0.23	0.01	62.29	99.66
CD1_03	19.77	0.6	9.37	2.83	0.03	0.86	3.32	0.17	0.45	0.25	0.01	61.31	99.62
CD1_04	24.57	0.65	9.96	4.78	0.05	1.01	4.83	0.23	0.69	0.22	0.01	62.33	99.61
CD1_05	17.11	0.55	9.35	1.82	0.03	0.77	2.63	0.15	0.4	0.25	0.01	56.22	99.52
CD1_06	36.38	0.81	11.22	4.25	0.06	0.64	1.73	0.25	0.6	0.19	0.01	68	99.23
CD1_07	19.69	0.64	10.12	3.15	0.03	0.96	2.93	0.18	0.48	0.25	0.01	62.08	99.75
CD1_08	19.44	0.56	10.1	1.76	0.03	0.82	2.59	0.17	0.47	0.27	0.01	58.35	99.81
CD1_09	21.65	0.55	9.55	2.71	0.04	0.9	5.72	0.25	0.5	0.23	0.01	47.71	99.74
CD1_10	19.21	0.6	9.31	2.97	0.03	0.93	3.15	0.19	0.48	0.24	0.01	58.16	99.51
CD1_11	20.47	0.62	9.95	2.94	0.03	0.88	3.03	0.17	0.52	0.26	0.01	64.49	99.91
CD1_12	21.3	0.66	10.45	3.37	0.04	1.06	3.39	0.18	0.52	0.27	0.01	64.45	99.62
CD1_13	20.2	0.63	10.04	2.77	0.04	0.95	4.53	0.18	0.48	0.29	0.01	59.48	99.36
CD1_14	22.4	0.57	10.47	2.62	0.04	0.83	2.83	0.2	0.89	0.23	0.01	55.63	99.41
1-2 m	**SiO2**	**TiO2**	**Al2O3**	**Fe2O3**	**MnO**	**MgO**	**CaO**	**Na2O**	**K2O**	**P2O5**	**Cr2O3**	**LOI**	**Total**
CD1_01	20.45	0.75	10.08	4.5	0.04	1.01	3.47	0.18	0.44	0.23	0.01	66.96	99.38
CD1_02	21.53	0.71	9.7	5	0.04	0.93	4.15	0.19	0.48	0.23	0.01	64.62	99.44
CD1_03	18.12	0.59	9.1	2.62	0.03	0.81	3.1	0.16	0.39	0.24	0.01	60.63	99.74
CD1_04	17.65	0.63	8.97	3.54	0.04	0.89	3.71	0.17	0.39	0.21	0.01	57.69	99.47
CD1_05	11.14	0.36	6.2	1.08	0.02	0.53	1.67	0.09	0.26	0.16	0.01	14.99	99.56
CD1_06	17.58	0.63	9.52	2.78	0.03	0.95	2.84	0.16	0.38	0.24	0.01	63.92	99.64
CD1_07	17.66	0.59	9.03	2.29	0.03	0.76	2.81	0.14	0.39	0.27	0.01	57.54	99.5
CD1_08	17.11	0.58	9.28	2.31	0.03	0.82	2.9	0.14	0.37	0.25	0.01	60.48	99.56
CD1_09	21.89	0.82	9.79	6.58	0.05	1.05	3.29	0.22	0.57	0.26	0.01	69.46	99.81

CD1_10	18.43	0.59	8.83	3.04	0.04	0.87	3.64	0.16	0.41	0.25	0.01	62.55	99.37
CD1_11	18.89	0.62	9.24	3.14	0.03	0.9	3.06	0.17	0.47	0.24	0.01	73.24	99.66
CD1_12	18.93	0.66	9.62	3.72	0.04	1.02	3.29	0.16	0.41	0.24	0.01	64.82	99.54
CD1_13	18.41	0.6	9.33	2.44	0.03	0.96	2.96	0.16	0.43	0.23	0.01	59.38	99.56
CD1_14	17.43	0.61	9.04	2.89	0.03	0.94	3	0.16	0.37	0.25	0.01	60.78	99.76
2-3 m	**SiO2**	**TiO2**	**Al2O3**	**Fe2O3**	**MnO**	**MgO**	**CaO**	**Na2O**	**K2O**	**P2O5**	**Cr2O3**	**LOI**	**Total**
CD1_01	22.56	0.73	10.13	4.65	0.04	1.02	3.05	0.22	0.69	0.25	0.01	67.73	99.7
CD1_02	21.73	0.86	9.53	9.37	0.06	1.12	4	0.23	0.66	0.21	0.01	68.55	99.53
CD1_03	20.23	0.72	9.26	5.26	0.04	0.86	3.03	0.19	0.54	0.24	0.01	65.65	99.55
CD1_04	21.43	0.7	9.83	5.02	0.05	0.96	4.81	0.2	0.48	0.25	0.01	65.9	99.89
CD1_05	16.22	0.54	9.23	1.52	0.02	0.69	2.34	0.12	0.34	0.21	0.01	58.62	99.7
CD1_06	18.04	0.57	9.14	2.03	0.03	0.73	2.67	0.16	0.39	0.21	0.01	57	99.76
CD1_07	17.59	0.6	9.12	2.92	0.03	0.79	2.97	0.17	0.39	0.25	0.01	60.07	99.66
CD1_08	16.4	0.55	8.88	2.05	0.03	0.74	2.83	0.14	0.36	0.24	0.01	52.58	99.68
CD1_09	22.17	0.71	9.55	5.04	0.04	0.95	3.14	0.21	0.68	0.24	0.01	66.81	99.73
CD1_10	16.4	0.55	9.34	1.56	0.03	0.7	2.39	0.13	0.35	0.21	0.01	58.42	99.63
CD1_11	18.86	0.64	9.35	3.33	0.03	0.83	3.4	0.16	0.42	0.25	0.01	62.72	99.54
CD1_12	20.02	0.65	9.79	3.23	0.03	0.88	3.11	0.18	0.46	0.22	0.01	60.98	99.37
CD1_13	19.66	0.64	9.7	3.22	0.03	0.93	3.02	0.19	0.5	0.23	0.01	63.71	99.32
CD1_14	20.54	0.63	9.7	3.3	0.04	0.83	3.07	0.18	0.56	0.21	0.01	63.71	99.36
3-4 m	**SiO2**	**TiO2**	**Al2O3**	**Fe2O3**	**MnO**	**MgO**	**CaO**	**Na2O**	**K2O**	**P2O5**	**Cr2O3**	**LOI**	**Total**
CD1_01	19.05	0.69	9.03	5.21	0.04	0.96	3.53	0.2	0.51	0.24	0.01	61.6	99.46
CD1_02	20.73	0.84	9.06	8.05	0.05	1.05	4.24	0.23	0.61	0.2	0.01	67.93	99.89
CD1_03	16.48	0.63	8.3	4.38	0.04	0.87	3.34	0.17	0.43	0.23	0.01	59.64	99.5
CD1_04	23.17	0.82	9.76	7.9	0.06	1.07	5.63	0.24	0.54	0.26	0.01	66.61	99.72
CD1_05	14.53	0.58	8.3	2.54	0.03	0.77	2.67	0.12	0.34	0.23	0.01	57.66	98.98
CD1_06	18.54	0.59	9.27	2.88	0.03	0.8	2.78	0.17	0.49	0.26	0.01	57.79	99.77
CD1_07	20.85	0.67	9.96	4.79	0.04	0.99	3.44	0.2	0.57	0.23	0.01	64.88	99.64
CD1_08	16.62	0.57	9.22	2.12	0.03	0.78	2.67	0.15	0.38	0.26	0.01	56.5	99.61

CD1_09	38.33	0.58	7.58	2.34	0.03	0.59	1.78	0.21	0.6	0.16	0.01	51.97	99.66
CD1_10	17.29	0.58	8.63	3.78	0.03	0.86	3.52	0.17	0.4	0.24	0.01	60.47	99.61
CD1_11	17.38	0.62	9.39	2.83	0.03	0.86	2.99	0.15	0.38	0.27	0.01	59.92	99.69
CD1_12	19.39	0.67	9.5	4.29	0.04	0.9	3.97	0.17	0.39	0.27	0.01	63.81	99.57
CD1_13	18.8	0.71	9.49	4.73	0.04	0.95	3.09	0.17	0.41	0.26	0.01	64.7	99.38
CD1_14	21.05	0.67	9.74	4.12	0.04	0.87	3.85	0.21	0.55	0.26	0.01	63.1	99.54
4-5 m	**SiO2**	**TiO2**	**Al2O3**	**Fe2O3**	**MnO**	**MgO**	**CaO**	**Na2O**	**K2O**	**P2O5**	**Cr2O3**	**LOI**	**Total**
CD1_01	19.56	0.73	9.21	4.68	0.04	1.1	3.73	0.21	0.56	0.23	0.01	64.1	99.56
CD1_02	19.84	0.77	9.24	6.58	0.05	1.11	3.66	0.2	0.55	0.22	0.01	65.65	99.52
CD1_03	18.07	0.82	8.72	7.7	0.05	1.15	3.67	0.2	0.48	0.22	0.01	63.26	99.59
CD1_04	28.42	0.59	9.75	2.7	0.04	0.63	1.93	0.18	0.72	0.18	0.01	67.23	99.68
CD1_05	15.92	0.54	9.03	1.85	0.03	0.71	2.61	0.13	0.37	0.24	0.01	54.52	99.68
CD1_06	16.49	0.56	8.95	2.2	0.03	0.8	2.57	0.16	0.42	0.24	0.01	54.57	99.93
CD1_07	12.58	0.49	6.42	3.04	0.03	0.71	2.56	0.13	0.29	0.17	0.01	43.52	99.45
CD1_08	15.92	0.57	8.81	2.32	0.03	0.8	2.72	0.14	0.41	0.24	0.01	55.04	99.65
CD1_09	60.85	1.16	11.83	7.97	0.05	0.52	0.73	0.33	1.34	0.1	0.01	78	99.97
CD1_10	17.4	0.65	9.15	4.09	0.04	0.92	3.54	0.18	0.38	0.27	0.01	61.39	99.66
CD1_11	18.98	0.58	8.94	3.61	0.03	0.83	3.05	0.18	0.54	0.23	0.01	57.81	99.47
CD1_12	20.4	0.63	8.85	4.01	0.03	0.8	2.67	0.21	0.63	0.26	0.01	62.62	99.52
CD1_13	16.07	0.57	8.85	2.73	0.03	0.78	2.92	0.15	0.33	0.25	0.01	49.86	99.58
CD1_14	18.3	0.63	8.64	4.34	0.03	0.82	2.56	0.17	0.51	0.24	0.01	61.24	99.78
Average	**20.24**	**0.65**	**9.34**	**3.71**	**0.04**	**0.87**	**3.17**	**0.18**	**0.49**	**0.23**	**0.01**	**60.79**	**99.59**

4.7.2 Major Oxides in CD2

The concentrations of major oxides for CD1 dump are presented in Table 11. The concentration of silica oxide ranges from 19.59 wt% in CD2_07 to 33.83 wt%. Similarly, the concentration of alumina ranges from 10.25 wt% in CD2_15 to 18.84 wt% in CD2_11. The average concentrations of silica and alumina oxides were 23 wt% and 11.73 wt%, respectively, higher than those found in CD1 dump. This indicates a significant enrichment of silicate minerals in CD1 when compared to CD2. The concentration of Fe_3O_2 ranges from 1.77 wt% in CD2_21 to 5.94 wt% in CD2_24, with an average concentration of 2.69 wt%. The concentration of calcium oxide ranges from 2.16 wt% in CD2_18 to 4.61 wt% in CD2_24, with an average concentration of 2.86 wt%. The concentration of MgO ranges from 0.52 wt% in CD2_15 to 1.04 wt% in CD2_11. The low concentrations indicate the limited presence of carbonate minerals in CD2 dump.

Table 11: Geochemical composition (in wt%) of CD2 dump per sample.

Sample_ID	SiO_2	TiO_2	Al_2O_3	Fe_2O_3	MnO	MgO	CaO	Na_2O	K_2O	P_2O_5	Cr_2O_3	LOI	Total
CD2_01	20	0.7	11.2	2.26	0.03	0.62	2.5	0.18	0.5	0.4	0.01	61.1	99.3
CD2_02	20.6	0.7	11.1	2.44	0.03	0.66	2.9	0.18	0.5	0.4	0.01	60.5	99.6
CD2_03	22.7	0.7	11.1	2.37	0.03	0.63	2.6	0.19	0.6	0.4	0.01	58.4	99.6
CD2_04	21.5	0.6	11.1	2.77	0.03	0.62	2.8	0.18	0.5	0.4	0.01	59.3	99.6
CD2_05	21.8	0.6	11.5	2.27	0.03	0.66	2.6	0.19	0.6	0.4	0.01	58.9	99.5
CD2_06	20.5	0.7	10.9	2.85	0.03	0.62	2.5	0.19	0.5	0.4	0.01	60.5	99.8
CD2_07	19.6	0.7	10.5	2.87	0.03	0.68	2.8	0.18	0.5	0.4	0.01	61.3	99.6
CD2_08	22.1	0.7	10.7	2.88	0.03	0.58	2.9	0.19	0.6	0.4	0.01	58.6	99.8
CD2_09	20.7	0.6	11.4	2.21	0.03	0.69	2.8	0.21	0.5	0.4	0.01	60	99.9
CD2_10	22.1	0.7	11.3	2.93	0.03	0.69	3.1	0.18	0.6	0.4	0.01	57.6	99.6
CD2_11	33.8	1.1	18.8	3.49	0.05	1.04	4.5	0.28	0.9	0.7	0.02	35.2	99.5
CD2_12	22.3	0.7	12	2.12	0.03	0.73	2.4	0.22	0.7	0.3	0.01	58.2	99.6
CD2_13	22.9	0.7	12.7	2.4	0.03	0.75	2.8	0.21	0.6	0.4	0.01	56.4	99.6
CD2_14	22.4	0.7	11.9	2.4	0.03	0.71	2.8	0.2	0.6	0.3	0.01	57.5	99.5
CD2_15	24.2	0.6	10.3	2.23	0.03	0.52	2.3	0.19	0.7	0.3	0.01	58.3	99.9
CD2_16	20.9	0.6	11.1	2.69	0.03	0.59	2.9	0.19	0.5	0.4	0.01	59.6	99.4
CD2_17	22.5	0.6	11.4	2.4	0.03	0.68	2.5	0.19	0.7	0.3	0.01	58.1	99.5
CD2_18	25	0.6	11.3	2.23	0.03	0.62	2.2	0.21	0.8	0.3	0.01	56.6	99.6
CD2_19	22.5	0.7	10.9	1.91	0.03	0.76	2.6	0.23	0.7	0.3	0.01	58.9	99.5
CD2_20	21.4	0.6	11.2	2.03	0.03	0.63	2.4	0.19	0.6	0.3	0.01	60.3	99.6
CD2_21	20.6	0.6	11.4	1.77	0.02	0.75	2.5	0.22	0.6	0.3	0.01	60.9	99.6

CD2_22	23.6	0.6	11.4	2.85	0.03	0.76	3.1	0.2	0.6	0.4	0.01	56.1	99.7
CD2_23	28.3	0.8	13.5	4.24	0.04	0.85	4	0.24	0.7	0.5	0.01	46.2	99.6
CD2_24	30	0.8	13	5.94	0.05	0.61	4.6	0.24	0.7	0.4	0.01	43.2	99.8
Average	**23**	**0.68**	**11.73**	**2.69**	**0.03**	**0.69**	**2.86**	**0.2**	**0.62**	**0.38**	**0.01**	**56.74**	**99.61**

The concentrations of TiO_2, Na_2O, K_2O, P_2O_5, and Cr_2O_3 remain insignificant. A high concentration of Ti of 1.08 wt% was observed in CD2_11, which may be attributed to the presence of ilmenite and anatase. The LOI was slightly lower than that found in CD1. This is well aligned with physicochemical properties that were observed for CD2 samples, which were characterized by medium volatile matter and fixed carbon contents. Samples CD2_11, CD2_23 and CD2_24 had a high concentration of SiO_2, Al_2O_3, MgO, Na_2O, K_2O, P_2O_5, and low LOI, indicating that these samples have a high proportion of inorganic matter, which is not combustible.

4.8 Concentration of Trace Elements

The trace elements concentration of Ba, Be, Co, Cu, Ga, Li, Mo, Nb, Ni, Pb, Rb, Sr, Zn, Zr, Ce, La, Nd, Sc and Y were analyzed from the ninety-four (94) samples from the two coal discard dumps. These trace elements were selected based on their potential environmental and geochemical significance, as well as their detectability using XRF and ICP-MS analytical techniques. The results are summarized in Tables 12 and 13. These results show a significant variation in elemental concentration, reflecting the geochemical heterogeneity of coal. The XRF and ICP-MS data show that the concentrations of trace elements vary across depth intervals in CD1 and vary across CD2. These variations suggest that trace elements were not uniformly distributed throughout dumps, and they may be localized enrichment or depletion of these elements. It is important to note that only elements reliably detected by ICP-MS are reported (Tables 14 and 15).

4.8.1 Trace Elements Concentration via XRF in CD1

The XRF data show that trace elemental concentrations vary across different intervals for each sample as illustrated in Table 12. The concentration of Ba ranges from 487 ppm in CD1_09 at the 4-5 m interval to 3940 ppm in CD1_04 at the 3-4 m interval, with an average of 1157.66 ppm.

Similarly, the concentration of Zr ranges from 406 ppm in CD1_09 to 1020 ppm in CD1_09 at the 4-5 m interval, with an average of 495.39 ppm. The concentration of Sr ranges from 167 ppm in CD1_09 at the 4-5 m interval to 1570 ppm in CD1_05 at the 3-4 m interval, with an average of 1210.69 ppm. The second lowest concentrations of Ba and Sr and the second highest of Zr were found in CD1_06 at the 0-1 m interval. This indicates the enrichment of Zr and limited presence of Ba and Sr in weathered samples (CD1_06 at 0-1 m and CD1_09 at 4-5 m).

CD1_09 at the 4-5 m interval also showed the lowest concentrations of Ni, Nb and Y at 34 ppm, 14 ppm, and 41 ppm, respectively. The Cu concentration ranges from 3 ppm in CD1_07 at the 1-2 m interval to 128 ppm in CD1_03 at the 4-5 m interval, with an average of 78.19 ppm, indicating a significant variation across different intervals. In the same way, the Zn concentration ranges from 47 ppm in CD1_09 at the 3-4 m interval to 614 ppm in CD1_08 at the 2-3 m interval. The average concentration of Zn was 86.34 ppm, indicating its significant uneven distribution across different intervals in each sample. The concentrations of Ga, Mo, Pb, and Rb remained low and quite stable across each sample. The concentration of Pb remains undetected in most samples, followed by Cu, Mo, and Nb in a few samples.

Table 12: Concentration of trace elements (ppm) for CD1 per depth interval.

0-1 m	**Ba**	**Cu**	**Ga**	**Mo**	**Nb**	**Ni**	**Pb**	**Rb**	**Sr**	**Y**	**Zn**	**Zr**
CD1_01	1510	88	33	34	22	86	nd	47	1270	69	98	580
CD1_02	1450	66	36	41	22	76	nd	43	1200	66	79	488
CD1_03	1000	nd	32	30	18	71	41	nd	1260	62	76	473
CD1_04	1770	71	27	45	17	75	35	72	1080	56	97	564
CD1_05	762	87	38	27	23	74	nd	55	1400	70	74	425
CD1_06	614	60	26	36	17	55	nd	72	607	49	71	638
CD1_07	1030	84	38	nd	21	82	42	64	1280	68	97	473
CD1_08	669	64	35	37	23	72	nd	60	1340	69	71	421
CD1_09	1360	61	31	43	17	73	nd	42	1290	65	63	406
CD1_10	1090	71	33	32	23	74	nd	57	1240	69	133	477
CD1_11	946	76	36	nd	28	74	nd	63	1240	75	85	497
CD1_12	1340	80	37	45	20	79	31	55	1290	68	85	532
CD1_13	1190	62	29	41	21	66	nd	47	1480	72	67	502
CD1_14	913	64	32	31	nd	59	nd	93	1140	60	76	450
1-2 m	**Ba**	**Cu**	**Ga**	**Mo**	**Nb**	**Ni**	**Pb**	**Rb**	**Sr**	**Y**	**Zn**	**Zr**

CD1_01	1660	69	33	nd	15	87	37	40	1100	52	92	531
CD1_02	2080	59	36	35	nd	81	nd	43	1060	57	63	512
CD1_03	1080	62	34	33	24	90	nd	48	1300	73	74	461
CD1_04	1190	81	32	31	20	72	43	57	1320	60	69	498
CD1_05	739	82	37	nd	29	85	nd	53	1390	82	66	437
CD1_06	907	88	38	29	18	77	nd	47	1340	72	83	471
CD1_07	864	3	45	nd	25	86	nd	49	1300	64	75	470
CD1_08	757	79	3	36	22	83	nd	44	1370	72	71	456
CD1_09	1830	88	25	38	17	93	nd	53	1010	63	90	586
CD1_10	1120	80	31	37	18	86	nd	47	1300	nd	75	483
CD1_11	1020	81	38	33	24	78	nd	56	1250	64	75	488
CD1_12	1350	84	33	27	17	80	nd	50	1320	69	90	492
CD1_13	941	88	31	42	17	79	40	66	1270	63	83	491
CD1_14	933	89	38	30	20	75	nd	40	1320	74	77	448
2-3 m	**Ba**	**Cu**	**Ga**	**Mo**	**Nb**	**Ni**	**Pb**	**Rb**	**Sr**	**Y**	**Zn**	**Zr**
CD1_01	1410	91	32	35	19	76	nd	74	1010	65	82	531
CD1_02	1880	82	32	nd	nd	78	33	73	969	56	91	578
CD1_03	1100	83	40	37	19	75	nd	65	1080	60	82	525
CD1_04	2250	63	33	42	15	77	28	50	1100	60	70	508
CD1_05	714	70	37	32	23	91	nd	46	1270	72	74	416
CD1_06	676	71	42	nd	24	88	nd	52	1180	68	71	465
CD1_07	924	95	35	43	21	84	nd	44	1380	66	85	467
CD1_08	886	73	38	32	24	81	nd	51	1340	74	614	452
CD1_09	1360	77	37	40	22	61	nd	80	1100	59	95	503
CD1_10	609	74	40	19	21	91	nd	46	1260	66	74	410
CD1_11	1270	71	39	39	17	79	39	55	1200	54	81	477
CD1_12	1320	72	34	29	21	69	nd	54	1110	66	78	484
CD1_13	1190	74	34	54	20	74	31	66	1160	61	72	476
CD1_14	1210	70	34	26	22	70	nd	64	1070	64	74	472
3-4 m	**Ba**	**Cu**	**Ga**	**Mo**	**Nb**	**Ni**	**Pb**	**Rb**	**Sr**	**Y**	**Zn**	**Zr**
CD1_01	1240	75	35	32	26	73	nd	68	1270	68	74	532
CD1_02	1290	87	35	nd	21	71	37	66	1070	55	104	538
CD1_03	1160	86	34	46	22	86	34	65	1390	72	74	500
CD1_04	3940	71	32	39	nd	64	30	42	1060	48	81	480
CD1_05	708	117	48	40	25	70	nd	55	1570	71	78	509
CD1_06	816	78	35	32	24	71	nd	66	1280	67	70	440
CD1_07	1360	85	39	nd	16	75	nd	72	1100	62	98	463
CD1_08	802	87	35	nd	29	78	nd	51	1380	71	73	434
CD1_09	619	52	25	36	18	49	nd	64	762	50	47	620
CD1_10	1060	nd	38	31	18	72	nd	49	1360	59	77	474

CD1_11	978	107	36	nd	21	84	nd	nd	1300	72	87	450
CD1_12	1430	71	31	37	24	85	nd	41	1160	70	67	489
CD1_13	1470	89	29	47	18	91	nd	49	1160	64	83	467
CD1_14	1730	60	33	nd	20	77	nd	60	1170	58	67	452
4-5 m	**Ba**	**Cu**	**Ga**	**Mo**	**Nb**	**Ni**	**Pb**	**Rb**	**Sr**	**Y**	**Zn**	**Zr**
CD1_01	1430	105	26	27	21	70	nd	69	1270	67	84	551
CD1_02	1200	101	33	42	22	55	nd	66	1140	64	86	563
CD1_03	1120	128	30	44	nd	76	nd	49	1150	66	96	515
CD1_04	716	61	39	nd	26	58	nd	82	853	54	63	502
CD1_05	818	76	39	31	21	77	36	57	1400	74	71	440
CD1_06	669	91	39	40	19	75	nd	54	1420	70	84	445
CD1_07	1030	73	34	nd	18	72	35	51	1430	69	70	509
CD1_08	705	92	34	nd	21	76	40	65	1500	77	72	443
CD1_09	487	45	18	34	14	34	nd	89	167	41	69	1020
CD1_10	1330	99	43	37	23	80	nd	37	1370	72	92	463
CD1_11	831	93	35	nd	26	67	nd	71	1250	70	66	471
CD1_12	1070	82	36	36	21	82	nd	75	1160	60	70	472
CD1_13	883	89	36	34	27	69	nd	45	1470	72	65	467
CD1_14	1230	84	31	29	23	87	nd	71	1140	68	78	454
Average	**1157.66**	**78.19**	**34.03**	**35.83**	**21.08**	**75.51**	**36**	**57.53**	**1210.69**	**65**	**86.34**	**495.39**

nd-not detected

4.8.2 Trace Elements Concentration via XRF in CD2

The concentration values of trace elements in CD2 are summarized in Table 13. The average concentration of Ba was 668.25 ppm, which was approximately 57.73% of Ba in CD1. The average concentrations of Sr and Zr were 1220 ppm and 502.96 ppm, respectively. These findings show the reduction of Ba and enrichment of Sr and Zr in CD2. The lowest concentrations of Ni, Nb and Y were 55 ppm, 26 ppm and 59 ppm, respectively, which was quite above those found in CD1. The Cu average concentration remains quite stable across the two coal discard dumps. The average concentration of Zn was 114 ppm, which was 1.32 times larger than the one found in CD1. The concentrations of Ga, Mo, Pb, and Rb remained low and quite stable across each sample. Just like in CD1, the concentration of Pd remains undetectable in many samples, followed by Mo and Ni, and Cu in a few samples.

Table 13: Concentration of trace elements (ppm) for CD2.

Sample_ID	Ba	Cu	Ga	Mo	Nb	Ni	Pb	Rb	Sr	Y	Zn	Zr
CD2_01	629	101	44	28	25	82	47	66	1300	75	147	473
CD2_02	620	62	38	29	29	71	53	61	1350	74	99	490
CD2_03	727	71	40	29	28	nd	58	61	1170	73	114	539
CD2_04	653	70	28	29	25	72	nd	59	1260	75	125	519
CD2_05	688	75	39	22	25	74	nd	64	1250	74	107	470
CD2_06	587	92	39	32	24	84	nd	54	1360	75	118	491
CD2_07	625	85	40	35	33	83	nd	53	1350	81	121	497
CD2_08	623	65	33	nd	24	63	nd	59	1120	69	119	544
CD2_09	666	76	41	31	29	72	nd	56	1380	77	115	485
CD2_10	806	77	40	35	27	63	nd	50	1470	82	120	524
CD2_11	810	91	39	32	28	68	57	72	1400	76	113	506
CD2_12	591	61	38	28	24	56	nd	74	1140	76	105	436
CD2_13	644	82	40	35	27	72	nd	64	1340	74	121	468
CD2_14	664	80	39	39	30	65	nd	61	1190	75	131	456
CD2_15	724	58	39	42	24	55	nd	64	880	68	100	595
CD2_16	768	nd	36	nd	30	70	59	64	1440	77	105	504
CD2_17	687	60	39	nd	23	63	37	80	1090	62	114	462
CD2_18	693	60	34	nd	23	61	37	83	946	64	104	491
CD2_19	566	59	39	39	28	62	nd	81	976	69	115	492
CD2_20	572	64	38	23	27	65	nd	59	1140	77	123	450
CD2_21	753	59	47	nd	25	68	48	64	1270	68	104	451
CD2_22	705	66	38	28	23	72	nd	56	1260	73	101	540
CD2_23	631	61	32	42	26	67	nd	53	1220	77	110	535
CD2_24	606	62	31	41	17	65	45	54	978	59	105	653
Average	**668.25**	**71.17**	**37.96**	**32.58**	**26**	**68.39**	**49**	**63**	**1220**	**72.92**	**114**	**502.96**

nd-not detected

4.8.3 Trace Elements Concentration via ICP-MS for CD1

The ICP-MS results complement the XRF even though there were significant differences, but they exhibit a consistent pattern, with ICP-MS results showing slightly lower elemental values than XRF. The discrepancy between XRF and ICP-MS results for trace elements concentrations might be attributed to differences in analytical techniques, sample preparation, and/or instrument biases. XRF is a non-destructive technique that provides a more general estimate of general composition

while ICP-MS is a very sensitive technique, capable of detecting trace elements at lower concentrations (Table 14). .

The concentration of Ba ranges from 374.54 µg/g in CD1_09 at the 4-5 m interval to 3426.22 µg/g in CD1_04 at the same interval, with an average of 960.85 µg/g. The average concentration of Ba was 1.2 times smaller than the one provided by XRF, higher than the World Hard Coal (WHC) average concentration of 150 µg/g (Dai et al., 2012a; Ketris & Yudovich, 2009). The Sr concentration ranges from 91.91 µg/g in CD1_09 at the 4-5 m interval to 556.51 µg/g in CD1_05 at the 3-4 m interval, with an average of 344.94 µg/g, which was 3.51 times lower than the one provided by XRF.

Ga concentration ranges from 70.98 µg/g in CD1_02 at the 4-5 m interval to 456.80 µg/g in CD1_04 at the same interval. The average concentration of Ga was 141.07 µg/g, higher than 30 µg/g cut-off grade of Ga (Dai et al., 2006). The average Ga concentration was 4.15 times higher than the one provided by XRF. Notably, Li concentration ranges from 31.87 µg/g in CD1_09 at the 4-5 m interval to 79.75 µg/g in CD1_07 at the 2-3 m interval, with an average of 56.27 µg/g, indicating a fair distribution of Li across different intervals for each sample. The average concentration of Li was 2.13 times less than 120 µg/g the cut-off grade (Sun et al., 2014; Wang et al., 2022). The minor concentrations of Be, Co, Mo, and Nb remain stable throughout the intervals for each sample.

The trace concentrations of REYs have been detected by ICP-MS compared to XRF. The REY concentrations also vary across different intervals for each sample. For example, the Sc concentration ranges from 1.79 µg/g in CD1_05 at the 4-5 m interval to 22.80 µg/g in CD1_04 at the 2-3m interval, while the Y concentration ranges from 0.88 µg/g in CD1_06 at the 0-1 m interval to 10.25 in CD1_03 at the 3-4 m interval. Similarly, the La concentration ranges from 0.29 µg/g in CD1_14 at the 0-1 m interval to 9.50 µg/g in CD1_06 at the 0-1 m interval, while the Ce concentration ranges from 0.61 µg/g in CD1_14 at the 0-1 m interval to CD1_06 at the 0-1m interval. The concentration of Nd ranges from 0.28 µg/g in CD1_10 at the 1-2 m interval to 10.78 µg/g in CD1_05 at the 3-4 m interval. The total average concentration of REY was 23.57 µg/g. La and Ce were enriched in the weathered sample at the lower interval, while Y and Nd were enriched in the lower interval and reduced at shallower depth intervals.

Table 14: Concentration of trace elements (µg/g) in CD1.

0-1 m	Ba	Be	Co	Ga	Li	Mo	Nb	Sr	Ce	La	Nd	Sc	Y
CD1_01	1099.52	1.57	14.16	154.07	48.21	2.34	15.85	380.42	11.13	2.86	nd	10.67	7
CD1_02	1004.95	1.79	14.74	127.52	53.34	2.46	13.1	313.79	9.9	2.52	nd	11.5	7.68
CD1_03	1292.65	2.15	16.05	203.3	59.25	1.89	12.56	384.23	5.17	1.74	0.32	5.69	2.98
CD1_04	1492.49	3	19.31	221.95	64.34	2.38	13.52	411.85	7.98	2.19	3.81	8.48	7.12
CD1_05	575.64	2.55	10.92	106.9	53.17	1.64	10.72	320.03	5.2	1.59	nd	2.11	2.21
CD1_06	498.01	3.04	21.95	89.92	63.49	1.88	14.7	220.61	nd	nd	nd	6.89	0.88
CD1_07	605.23	2.42	12.35	105.72	61.4	1.28	10.75	310.89	3.04	0.97	nd	4.77	2.42
CD1_08	615.71	2.52	11	106.13	61.02	1.34	11.26	335.55	2.44	0.78	nd	2.45	1.4
CD1_09	694.28	2.24	13.14	120.17	43.99	1.76	10.96	321.95	7.03	2.32	1.16	1.91	1.73
CD1_10	1062.26	2.72	14.23	184.37	68.63	2.04	12.62	399.04	5.73	1.9	0.58	7.86	4.94
CD1_11	1027.03	2.93	13.42	150.73	68.22	1.9	12.94	397.97	4.83	1.57	nd	5.22	3.29
CD1_12	954.33	2.12	9.21	132.46	61.08	1.59	10.13	387.54	5.82	1.99	0.38	5.67	5.09
CD1_13	867.05	1.58	9.53	114.97	46.77	0.99	8.44	317.64	4.17	1.48	nd	4.53	3.11
CD1_14	792.05	2.4	11.5	121.08	66.68	1.38	11.3	323.69	0.61	0.29	nd	5.47	1.42
1-2 m	**Ba**	**Be**	**Co**	**Ga**	**Li**	**Mo**	**Nb**	**Sr**	**Ce**	**La**	**Nd**	**Sc**	**Y**
CD1_01	1047.19	1.49	12.48	136.57	52.25	2.27	13.07	291.13	10.41	2.75	nd	12.21	7.49
CD1_02	1271.07	1.66	15.22	158.65	59.22	2.43	12.98	314.35	9.41	2.42	nd	11.35	6.65
CD1_03	817.58	1.57	10.3	107.3	34.4	1.83	11.04	314.07	14.18	4.07	nd	2.82	3.77
CD1_04	938.19	2.57	15.84	142.83	56.72	2.09	13.05	436.9	8.97	2.62	4.99	11.07	3.24
CD1_05	693.06	2.68	9.63	104.15	41.13	1.61	10.02	344.63	7.99	2.73	1.61	2.74	1.68
CD1_06	687.95	2.49	12.6	116.45	48	1.4	10.92	343.01	13.51	4.48	4.68	4.84	3.01
CD1_07	667.71	1.55	10.05	110.77	46.71	0.98	8.17	231.85	3.09	1.03	nd	6.02	2.75
CD1_08	624.34	2.33	13.21	102.88	60.94	1.35	11.3	312.86	6.79	1.91	0.95	5.24	5.26
CD1_09	1111.11	2.42	23.47	181.67	62.55	2.54	13.79	349.57	5.38	1.7	0.3	5.88	4.02
CD1_10	970.88	1.47	11.33	156.34	33.37	1.21	8.18	291.47	5.56	1.93	0.28	3.18	2.3
CD1_11	1071.19	2.52	14.65	151.91	66.82	2.06	12.79	399.41	5.3	1.74	0.39	6.88	3.83
CD1_12	1167.06	2.12	12.98	160.42	45.47	1.36	10.88	380.41	19.22	6.86	7	1.86	4.07
CD1_13	727.59	2.4	10.9	100.54	62.31	1.58	11.11	323.44	13.24	4.35	4.96	5.6	7.23
CD1_14	780.47	1.68	10.15	112.72	43.55	1.03	8.39	303.58	3.9	1.36	nd	3.51	2.38
2-3 m	**Ba**	**Be**	**Co**	**Ga**	**Li**	**Mo**	**Nb**	**Sr**	**Ce**	**La**	**Nd**	**Sc**	**Y**
CD1_01	916.9	1.51	12.55	121.95	58.68	2.42	14.65	280.75	9.03	2.07	nd	8.56	6.33
CD1_02	799.15	1.07	18.5	104.62	42.96	2.45	11.57	292.37	12.67	3.52	nd	8.07	4.74
CD1_03	789.17	1.78	15.56	98.46	59.96	2.15	12.89	305.22	12.02	3.63	3.24	8.64	6.57
CD1_04	1308.06	1.44	14.54	186.88	43.68	1.53	8.2	268.05	8.34	2.28	4.22	22.8	5.75
CD1_05	516.48	2.6	9.48	96.03	53.33	1.14	9.22	250.22	2.58	0.87	nd	4.45	1.97
CD1_06	733.43	2.22	13.29	125.7	62.49	1.73	11.98	304.07	7.07	2.23	1.14	6.57	5.09
CD1_07	998.71	2.62	17.53	163.27	79.75	2.04	13.35	392.39	6.74	2.13	1.3	8.91	5.89

CD1_08	535.02	1.54	9.01	87.46	40.19	0.97	7.5	236.73	3.3	1.15	nd	2.8	1.9
CD1_09	787.71	1.98	21.41	132.33	65.99	2.38	13.94	324.84	2.89	0.91	nd	5.51	3.29
CD1_10	937.67	2.06	12.81	145.88	49.21	1.42	9.93	307.55	1.83	0.67	nd	3.68	1.46
CD1_11	1471.58	2.58	18.24	205.3	57.1	1.93	12.96	395.22	6.77	2.24	1.11	3.52	2.9
CD1_12	1301.3	2.67	13.86	178.26	51.49	1.4	11.93	350.02	6.11	1.99	0.65	2.32	2.43
CD1_13	1029.13	2.34	14.44	143.93	63.76	1.66	12.64	304.98	1.96	0.64	nd	4.49	2.75
CD1_14	1092.79	2.21	14.82	157.1	54.85	1.88	11.72	320.38	3.91	1.33	nd	5.96	2.67
3-4 m	**Ba**	**Be**	**Co**	**Ga**	**Li**	**Mo**	**Nb**	**Sr**	**Ce**	**La**	**Nd**	**Sc**	**Y**
CD1_01	894.55	1.24	16.02	115.5	39.97	2.52	13.31	365.4	15.45	4.46	nd	6.83	4.69
CD1_02	807.08	1.03	11.4	102.53	52.15	2.85	12.12	375.02	11.08	2.83	nd	8.63	8.5
CD1_03	957.42	1.87	16.69	116.16	62.89	2.86	13.29	388.2	14.01	4.61	5.36	16.03	10.25
CD1_04	2371.4	2.27	34.35	331.93	77.27	2.77	14.81	467.81	12.14	4.03	4.7	15.09	9.49
CD1_05	919.27	3.06	15.83	136.97	54.38	3.07	16.01	556.51	25.49	9.5	10.78	3.49	3.63
CD1_06	764.29	2.8	15.61	132.82	68.74	1.95	12.33	336.87	3.96	1.27	nd	5.87	2.22
CD1_07	805.94	2.43	14.78	138.32	55.29	1.82	10.75	294.23	1.96	0.64	nd	4.61	1.81
CD1_08	609.51	1.75	10.81	105.4	50.9	1.09	9.36	293.04	3.92	1.31	nd	3.23	1.69
CD1_09	602.52	2.41	14.64	102.47	62.78	2.52	13.42	322.04	1.25	0.45	nd	2.71	1.3
CD1_10	1400.19	2.18	20.69	212.05	77.2	1.84	13.04	475.14	8.97	3.04	2.4	7.81	5.54
CD1_11	1140.86	2.6	14.5	164.75	51.65	1.63	11.95	427.07	16.05	5.8	5.56	1.93	2.23
CD1_12	1385.33	2.34	20.34	188.36	68.69	2.17	12.29	372.16	6.6	2.27	1.14	7.85	5.09
CD1_13	1210.44	2.26	17.3	163.85	59.02	1.52	11.72	369.69	5.64	1.85	0.37	4.7	2.94
CD1_14	1244.64	2.42	16.83	170.2	59.42	2.26	12.27	377.98	4.52	1.48	nd	3.93	2.05
4-5 m	**Ba**	**Be**	**Co**	**Ga**	**Li**	**Mo**	**Nb**	**Sr**	**Ce**	**La**	**Nd**	**Sc**	**Y**
CD1_01	888.89	1.67	13.36	115.57	55.46	2.48	13.92	376.34	13.3	3.59	nd	10.04	7.81
CD1_02	555.92	0.97	10.12	70.98	32.03	2.08	9.72	277.38	8.58	2.07	nd	4.77	3.05
CD1_03	683.55	1.15	19.16	84.74	50.21	2.77	12.42	345.33	8.98	2.97	2.76	11.85	6.83
CD1_04	3426.22	2.68	16.79	456.8	71.4	3.38	12.59	523.7	12.27	4.53	4	9.99	9.5
CD1_05	572.1	2.01	7.99	87.59	37.61	1.5	8.25	267.89	3.7	1.26	nd	1.79	1.46
CD1_06	907.57	3.22	18.2	155.71	77.86	2.12	11.47	504.87	12.36	3.95	4.51	5.16	5.74
CD1_07	538.93	1.53	11.22	89.26	45.1	2.72	17.15	266.87	7.79	2.58	1.83	7.3	5.99
CD1_08	735.24	2.45	11.58	113.21	62.2	1.24	7.91	390.01	4.06	1.4	nd	5.4	3.25
CD1_09	374.54	2.12	22.26	73	31.87	2.34	19.81	91.91	6.75	0.78	nd	14.5	1.4
CD1_10	1185.58	2.24	17.67	170.35	69.07	2.14	12.48	432.22	8.84	3.1	2.62	10.5	6.3
CD1_11	923.56	2.42	17.36	137.81	67.74	2.19	12.7	393.42	4.95	1.57	nd	6.46	3.94
CD1_12	1143.68	2.72	19.21	151.54	68.4	1.62	12.45	363.72	6.07	1.99	0.98	10.05	5.49
CD1_13	807.48	2.63	12.77	110.8	58.04	1.25	10.68	377.14	5.96	1.97	0.66	4.63	3.6
CD1_14	1028.88	1.97	17.43	146.82	55.2	1.8	11.27	319.25	2.26	0.78	nd	4.33	1.63
Average	**960.85**	**2.16**	**14.79**	**141.07**	**56.27**	**1.92**	**11.95**	**344.94**	**7.57**	**2.38**	**2.67**	**6.6**	**4.14**

4.8.4 Trace Elements Concentration via ICP-MS in CD2

Table 15 shows that the concentration of Ba ranged from 528.57 µg/g in CD2_19 to 768.80 µg/g in CD2_18, with an average concentration of 628.12 µg/g, suggesting a relatively stable concentration across the samples. The average concentration of Ba in CD2 was 1.53 times smaller than in CD1. The Sr concentration ranged from 242.30 µg/g in CD2_15 to 413.52 µg/g in CD2_07, with an average of 339.33 µg/g. The Sr concentration in CD2 was slightly lower than in CD1. The Ga concentration ranged from 88.20 µg/g in CD2_06 to 129.23 µg/g in CD2_18, with an average of 105.25 µg/g, lower than in CD1. Similarly, the Li concentration ranged from 65.51 µg/g in CD2_11 to 84.38 µg/g in CD2_01, with an average of 76.42, quite higher than the one found in CD1. The low concentrations of Be, Co, Mo, and Nb remain stable throughout the samples. The total average concentration of REY (Ce+La+Nd+Sc+Y) was 16.35 µg/g, which was 1.44 times lower than the total average concentration of REY in CD1.

Table 15: Concentration of trace elements (µg/g) in CD2.

Sample_ID	Ba	Be	Co	Ga	Li	Mo	Nb	Sr	Ce	La	Nd	Sc	Y
CD2_01	618.79	3.2	14.12	97.69	84.38	2.97	15.41	352.07	0.31	0.2	nd	4.41	1.29
CD2_02	600.86	3.21	15.52	94.64	81.27	3.39	14.86	371.91	0.66	0.3	nd	4.78	1.15
CD2_03	557.9	2.85	16.37	89.8	78.59	2.91	14.51	337.79	0.33	nd	nd	4.61	1.23
CD2_04	678.19	2.89	14.84	107.64	79.01	3.73	15.76	291.33	nd	nd	nd	6.14	1.1
CD2_05	642.64	2.86	14.31	103.1	74.9	3.09	13.86	352.21	2.57	0.53	nd	nd	1.27
CD2_06	533	2.72	15.71	88.2	73.32	2.81	13.48	333.96	3.57	1.21	nd	nd	1.46
CD2_07	638.12	2.99	16.96	104.23	76.53	3.63	14.88	413.52	4.8	1.24	0.57	nd	1.84
CD2_08	618.31	2.93	17.38	102.55	77.62	3.68	18.18	342.41	5.06	1.44	0.87	nd	2.15
CD2_09	531.48	2.52	13.75	89.51	74.87	3.16	13.89	320.14	4.88	1.99	2.64	nd	1.62
CD2_10	723.02	3	16.11	115.89	74.03	5	14.4	408.28	7.48	2.69	3.24	nd	4.88
CD2_11	611.11	2.97	13.38	98.99	62.51	2.67	14.19	364.42	13.89	2.77	9.79	nd	5.37
CD2_12	625.96	2.77	13.04	105.33	74.69	2.52	14.48	317.11	6.75	8.13	4.76	nd	7.77
CD2_13	602.98	2.84	13.12	101.83	72.7	2.8	12.67	351.36	11.73	4.16	1.11	nd	3.49
CD2_14	651.74	3.12	15.25	111.17	81.45	3.45	16.51	351.97	2.73	0.79	nd	nd	1.47
CD2_15	670.2	2.54	14.58	114.84	70.36	3.1	14.94	242.3	1.37	nd	nd	nd	0.4
CD2_16	651.26	2.68	18.32	113.4	80.77	3.17	15.07	378.87	3.95	1.54	nd	nd	1.12
CD2_17	635.87	3.03	16.54	113.76	81.43	3.17	15.91	283.7	5.75	1.53	2.22	nd	1.31
CD2_18	768.8	2.76	17.32	129.23	82.61	3.57	17.76	269.2	3.33	1.04	0.28	nd	1.1
CD2_19	528.57	2.69	13.47	93.1	62.84	3.25	16.37	260.97	3.71	0.94	0.58	nd	2.09
CD2_20	615.61	2.67	14.08	105.99	74.79	2.87	14.75	321.87	5.88	2.67	0.25	nd	1.89
CD2_21	635.53	3.56	13.75	112.17	72.85	2.81	14.45	346.83	2.48	0.62	nd	nd	1.63

CD2_22	687.3	2.86	18.02	119.08	78.42	3.34	15.17	392.69	5.91	1.32	nd	nd	2.55
CD2_23	606.52	2.47	24.28	105.04	79.9	2.95	16.01	375.9	5.5	1.71	2.47	nd	6.7
CD2_24	641.09	2.6	34.97	108.76	84.28	2.88	17.06	363.08	5.79	1.33	1.17	nd	5.95
Average	**628.12**	**2.86**	**16.47**	**105.25**	**76.42**	**3.21**	**15.19**	**339.33**	**4.71**	**1.82**	**2.3**	**4.99**	**2.53**

Nd-not detected

4.8.5 Summary

The average concentrations of trace elements, as determined by XRF and ICP-MS, are summarized and compared in a horizontal bar graph in Figure 44 and 45 respectively, revealing distinct patterns and differences as depth interval changes.

4.8.5.1 CD1

1. **0 –1 m Interval**

   In this interval, Ba and Sr have high concentrations of 1117.43 ppm and 1222.64 ppm respectively, while Ni is sitting at 72.57 ppm. The concentration of REE remained relatively low, for example the La at 1.71 µg/g and Nd at 1.25 µg/g have reached their lowest concentrations. Cu was at its lowest peak among the intervals. Be was at the highest concentration in CD1.

2. **1 - 2 m Interval**

   The concentrations of Ba and Sr increased to 1176.50 ppm and 1260.71 ppm respectively, in this interval Sr and Ni have reached their peak concentration. Similarly, the concentrations of REY (La, Nd, Y, and Ce) increased while Sc showed a slight decrease from 5.95 µg/g at the 0 – 1 m interval to 5.94 µg/g. The concentration of Cu to increase to 73.79 ppm.

3. **2 – 3 m Interval**

   Ba increased to 1199.93 ppm, while Sr decreased to 1159.21 ppm and Ni decreased slightly to 78.14 ppm. Cu shows exponential increase. Ga, Zn and Sc reached their highest peak at CD1. REY (La, Ce, Nd, and Y) showed a slight drop but remains significant.

4. **3 – 4 m Interval**

   Ba reached its highest peak of 1328.79 ppm, while Sr showed a sharp increase. Mo and Co also reached their highest peak of 37.78 ppm and 17.13 µg/g. Rb, and Zr remain relatively

stable. Ce, La and Nd reached their highest values. This indicates a strong REE enrichment in carbonate and phosphate minerals.

5. **4 –5 m Interval**

   Ba dropped significantly, while dropped slightly and Zr, Sc, Cu reached its highest peak. Ni reached its lowest peak, while Y reached its highest concentration of 4.71 µg/g, indicating an increase in clay, carbonate, or phosphate minerals. The concentrations of Nd, Mo, Li, La, Ga, Co, Ce and Be remain significant.

4.8.5.2 CD2

Ba has reached its lowest concentration of 668.25 ppm, similarly Ni and Cu have also reached their lowest concentration of 68.39 ppm and 71.17 ppm, respectively. The concentrations of Be, Sr, and Zr were above their average concentration in CD1. REY such as Ce, La, Sc, Y have reached the lowest concentration while Nd was relatively stable, this suggests a sharp in decrease carbonate minerals as well as slight decrease in phosphate minerals. Li exhibited its highest concentration of 76.42 µg/g, in the same manner Mo, Nb, Pb and Co reached their concentrations.

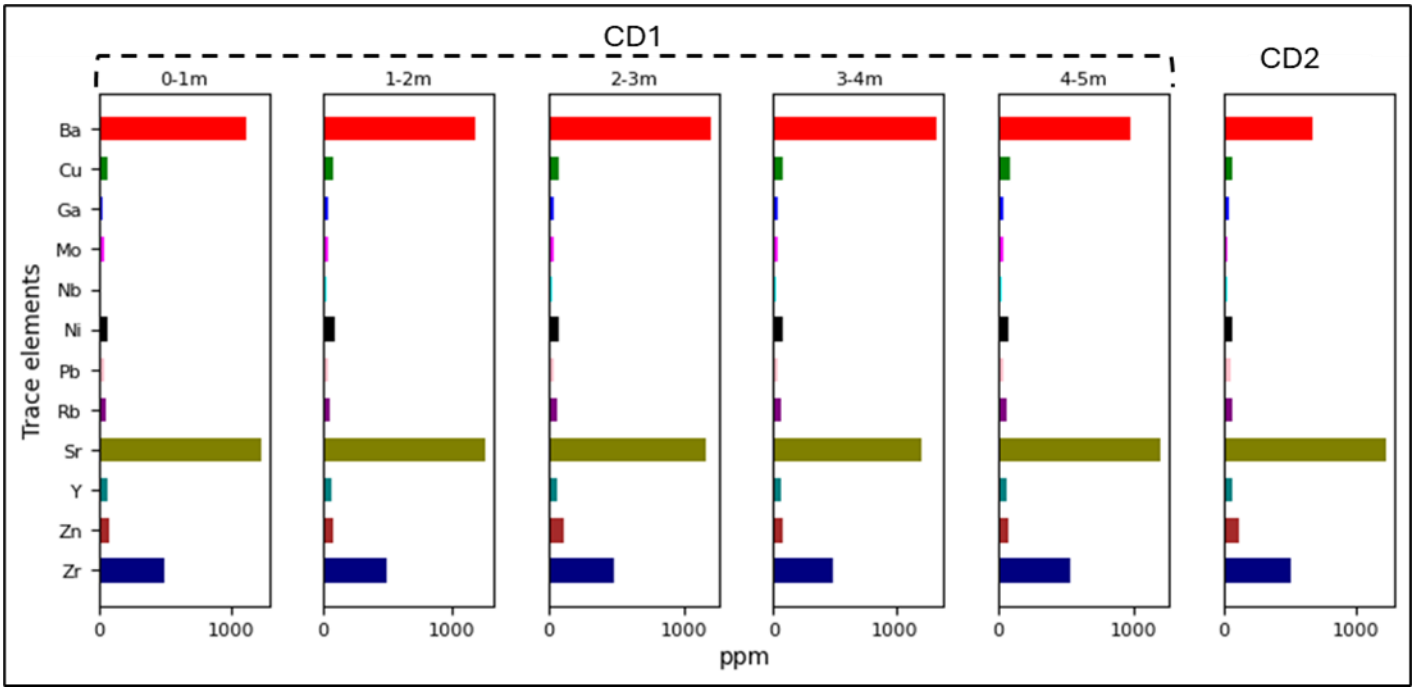

Figure 46: Summary of trace elements via XRF: CD1 and CD2 Comparison.

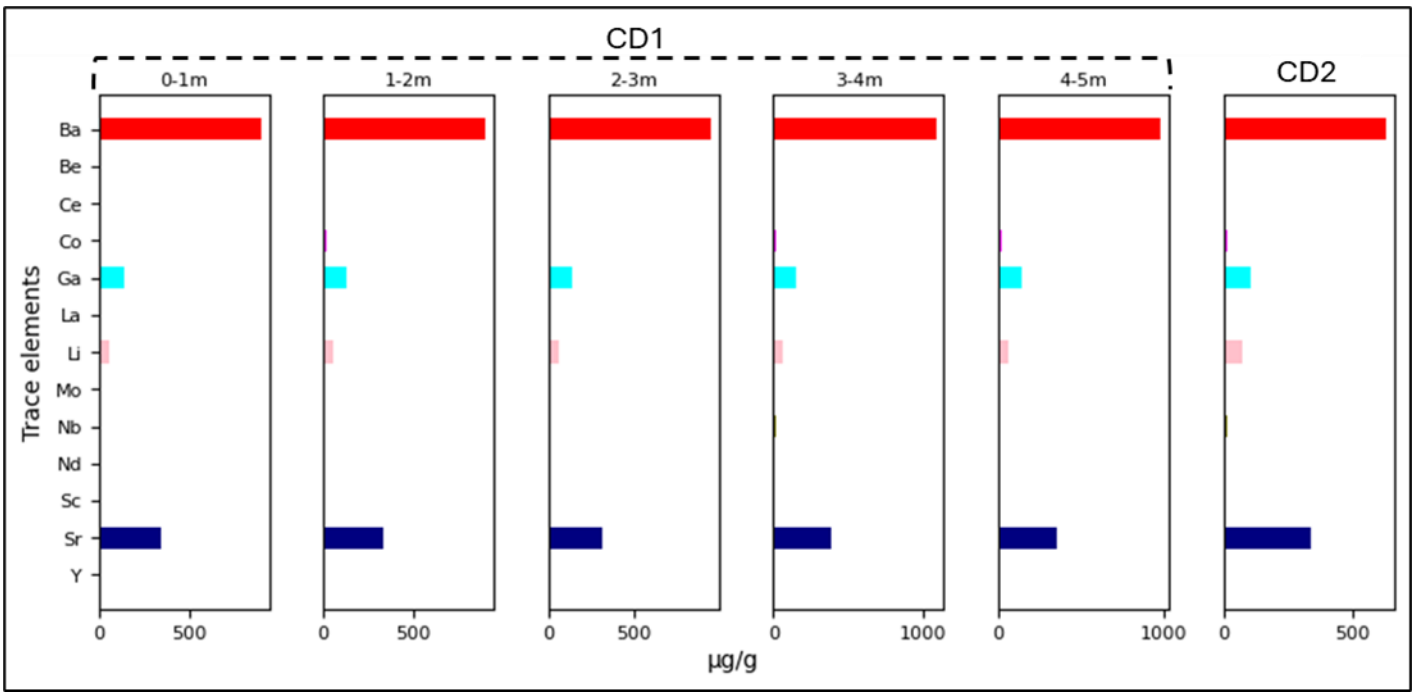

Figure 47: Summary of trace elements via ICP-MS: CD1 and CD2 comparison.

These results provided a comprehensive understanding of the coal quality, mineral phases, and concentrations of CRMs in coal discard samples, highlighting their potential as a valuable secondary source of CRMs. The next chapter will focus on the mode of occurrence, distribution, and enrichment of these CRMs in coal discards.

Chapter 5: Discussion

This discussion examines the mode of occurrence, distribution, and concentration of CRMs in coal discard samples, providing insight into the geochemical characteristics of coal discards and the factors influencing elemental associations. By analyzing the relationship between these factors, this chapter aims to shed light on the complex interactions between coal discard composition, geological processes, and elemental behavior. It will explore the implications of the findings, highlighting patterns, trends and correlations that inform our understanding of elemental distribution in coal discards.

5.1 Distribution

5.1.1 Vertical and Lateral Distribution of CRMs in CD1 Dump

China and India dominate the production of Ba, while Iran and Spain dominate the production of Sr, raising the supply risk for other countries (European Commission, 2023). In this study Ba and Sr are well above their cut-off grades, highlighting their economic viability, geochemical importance and may make South Africa to be a role player in the global supply chain. Coals with a Ba concentration greater than 750 µg/g (5 times greater than Ba cut-off grade of 150 µg/g) are considered super high Ba coals (Dai et al., 2012a). The Ga and Ba concentrations exceed the industrial minimum requirement of 30 µg/g and 150 µg/g in all the samples, while Li concentrations fall below the cut-off grade of 120 µg/g in all the coal discard samples of both dumps. Zr is distributed uniformly throughout the samples. Samples with Ba > 1000 µg/g are distributed at the 2-3 m interval (Figure 48c), to a lesser extent at the 3-4 m (Figure 48d) and 4-5 m (Figure 48e) intervals. These samples dominate the northern side of the dump and a few on the southern side. In the same way samples with Ba > 1000 µg/g are distributed at the 1-2 m (Figure 48b), and 3-4 m (Figure 48d) intervals, and to a lesser extent at the 2-3 m interval (Figure 48c). The samples enriched with Sr are found at the 4-5 m interval (Figure 48e) and with few samples at the 0-1 m (Figure 48a), 1-2 m (Figure 48b) and 2-3 m (Figure 48c) intervals. Samples with high Ba and Sr are distributed throughout the dump at the 0-1 m interval (Figure 48a), while are in the northwest at the 1-2 m (Figure 48b) and 2-3 m (Figure 48c) intervals and in the northern at deep intervals (Figure 48d and e). Samples with high Ba and Sr are only present in the deeper intervals (Figures 48d and e). Variations in element distribution within coal discard dump may be attributed

to differences in the age of the deposits, changes in mineralogy, and fluctuations in environmental conditions during the initial coal formation. Additionally, when exposed to current surface climatic conditions, elements in coal waste exhibit varying degrees of mobility and leachability, influenced by factors such as pH, redox state, and weathering processes.

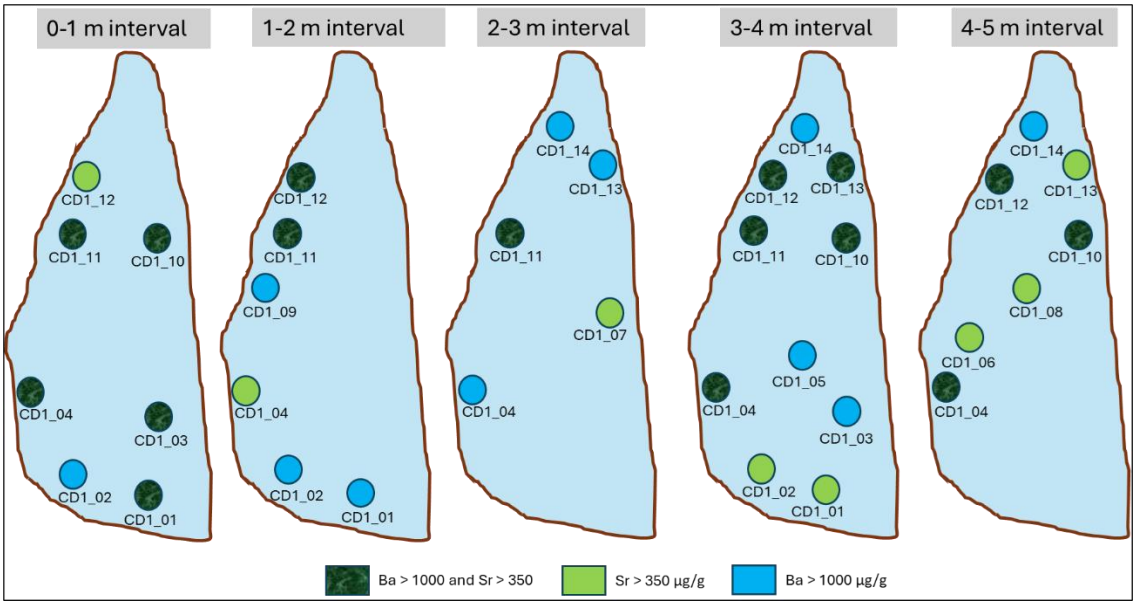

Figure 48: Vertical and lateral distribution of CRMs in CD1 dump.

5.1.2 CRMs Lateral Distribution in CD2

The distribution of Ba is mostly uniform in CD2, with only one sample (CD2_18) exhibiting high concentration of Ba, greater than 750 µg/g. Even though the concentration of Ba exceeds the cut –off grade of 150 µg/g (Dai et al., 2012a; Ketris & Yudovich, 2009). This dump may be considered to have Ba. The distribution of Ga is also uniform throughout the dump, but CD2 dump may also be considered to have Ga. Since all the samples exhibit Ga higher than the cut-off grade of 30 µg/g (Dai et al., 2006). Sr is evenly distributed throughout the dump as shown in Figure 49. Samples with high Zr concentration are distributed on the southern side of the dump. These variations may be due to changes in the deposition of coal discards and changes in the environment of coal accumulation.

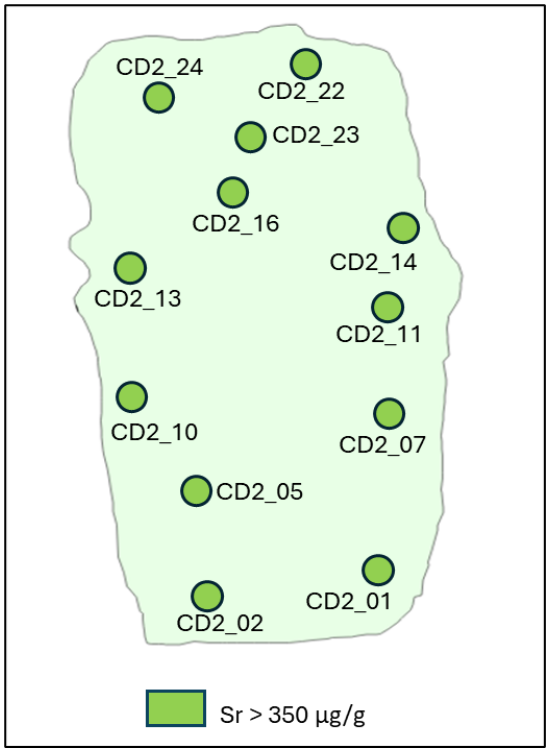

Figure 49: Lateral distribution of CRMs in CD2 dump.

5.2 Mode of Occurrence of CRMs

The mode of occurrence of CRMs in coal discards, which include mineral-associated, organic-associated, adsorbed and included forms, is crucial in understanding their potential sources, behavior, and environmental implications. This section aims to elucidate the specific mode of occurrence of these CRMs in the coal discard samples, using correlation analyses to investigate relationship between trace and major elements, as well as physicochemical properties such as volatile matter, fixed carbon and ash content, to gain a comprehensive understanding of their geochemical associations and controls.

5.2.1 Major Elements

The XRD, FTIR, TIMA, and SEM-EDS data show that that Si mainly occurs quartz (Figures 31, 35a, and 44), zircon (Figures 43b and 44) and Al in montmorillonite (Figure 35b) and kaolinite (Figures 29, 35c and 44). Fe is incorporated in the crystal structure of pyrrhotite (Figure 39), siderite (Figures 37 and 44), Ti-hematite (Figures 43a and 44), and magnetite (Figures 33 and 44),

with small portions of clay minerals and organic matter (Figure 42a). Similarly, Ca is found in the chemical structure of calcite, dolomite, brushite, ankerite, gypsum and apatite, and organic matter (Figure 42a). A small proportion of Ti is in the chemical form of anatase (Figure 44) and Ti-hematite (Figures 43a and 44). Ankerite is the main carrier of Mn (Figure 30), while Mg is hosted by dolomite (Figures 30, 38a and 44) and ankerite (Figure 30). A small content of Na in samples is controlled by minor albite (Figure 44). K occurred in the chemical form of muscovite (Figures 32, 36b and 44) and illite (Figures 36a and 44) while P is incorporated in berlinite (Figure 32) and apatite (Figures 44).

5.2.2 Trace Elements

Ba

SEM-EDS results show that Ba was incorporated into the chemical structure of barite (Figures 40 and 41). However, Ba in coal has multiple modes of occurrence (Dai et al., 2021). Zhao et al. (2014) reported that Ba substitutes isomorphically for K in medium-volatile bituminous coals, predominantly associating with clay minerals, barite, boehmite, and organic matter. In the Permian bituminous coals of the Guizhou Province, it was found to be positively correlated with ash content (Dai et al., 2005), and in the lignite coals of the Can Basin in Turkey, it exhibited a moderate negative correlation with ash content (Gürdal, 2008). The correlation difference in these coals was due to the different rank of coals. Therefore, the mode of occurrence for Ba is highly dependent on the coal rank. Both coal discards in this study are from bituminous coal.

Sr

Sr has multiple occurrence forms; it is associated with sulfates, phosphates, carbonates, clay minerals, and occasionally with organic compounds. Liu et al. (2021) showed that leached Sr has a remarkably positive correlation with leaching behaviour in low-Ge and high-Ge coals. SEM-EDS analyses indicate that Sr is present in barite (Figure 41), consistent with earlier research identifying sulfate minerals as common Sr hosts in coal (Karayigit et al., 2000; Nkwamza & Malumbazo, 2025). As shown in Figure 50, Sr displays a positive correlation with P_2O_5 and CaO, respectively, suggesting that Sr can isomorphically substitute for Ca in apatite and additionally occurs in carbonate minerals such as calcite, dolomite, and ankerite. Overall, these findings imply that Sr occurs mainly in barite in CD1 and in phosphate, and carbonate minerals in CD2.

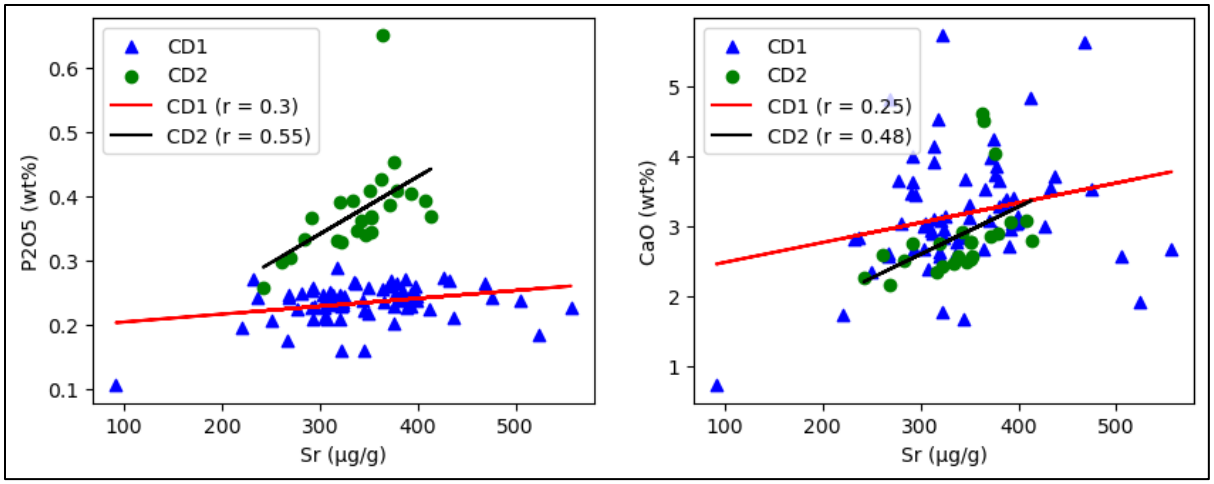

Figure 50: Correlation analysis illustrating the relationships between Sr and P_2O_5, and between Sr and CaO concentrations.

Ga

Ga isomorphically coexist with Al in Al-bearing minerals owing to their similar electronegativity, ionic radii, and charges (Wang et al., 2011). However, Ga has multiple modes of occurrence (Dai et al., 2021). For instance, in the high-volatile bituminous coals of the Jungar Coalfield, it is primarily hosted in collotelinite (Jiu et al., 2023). In contrast, in the medium-volatile bituminous coals of the Muli Coalfield, Ga is mainly associated with kaolinite (Shao et al., 2018). This difference in Ga occurrence is related to the coal rank. Although minerals like boehmite and goyazite, which can contain Ga, were not identified by SEM-EDS, XRD, or TIMA in this study apart from kaolinite, most research indicates that Ga predominantly resides in Al-bearing minerals, particularly kaolinite (Wang et al., 2011; Shao et al., 2018; Zhao et al., 2019) as well as in boehmite (Dai et al., 2006, Wang et al., 2011; Shao et al., 2018) and goyazite (Dai et al., 2012; Zhao et al., 2019). In this investigation, kaolinite ranks as the second most abundant mineral in coal discards. Considering the notably high Ga concentrations, which exceed typical values found in most hard coals worldwide, it is plausible that kaolinite and organic matter serve as the main Ga hosts in these samples (Nkwamza & Malumbazo, 2025). However, this conclusion should be made cautiously due to the limited direct mineralogical confirmation.

Zr

The SEM-EDS analysis identified zircon as the main host of Zr (Figures 42b, 43b, and 44). Additionally, statistical correlation showed a strong relationship between Zr and TiO_2 in CD1 (Figure 51), suggesting that zircon is commonly found alongside Ti-bearing minerals rather than Zr being incorporated within them. Both zircon and Ti-bearing minerals are dense and durable, which often leads to their joint deposition in place (Nkwamza & Malumbazo, 2025). However, Zhao et al. (2017) reported the presence of Zr within anatase in tuff from southwestern China. The moderate positive correlation between Zr and Al_2O_3 seen in Figure 51 also points to minor Zr occurrences within aluminum-bearing minerals.

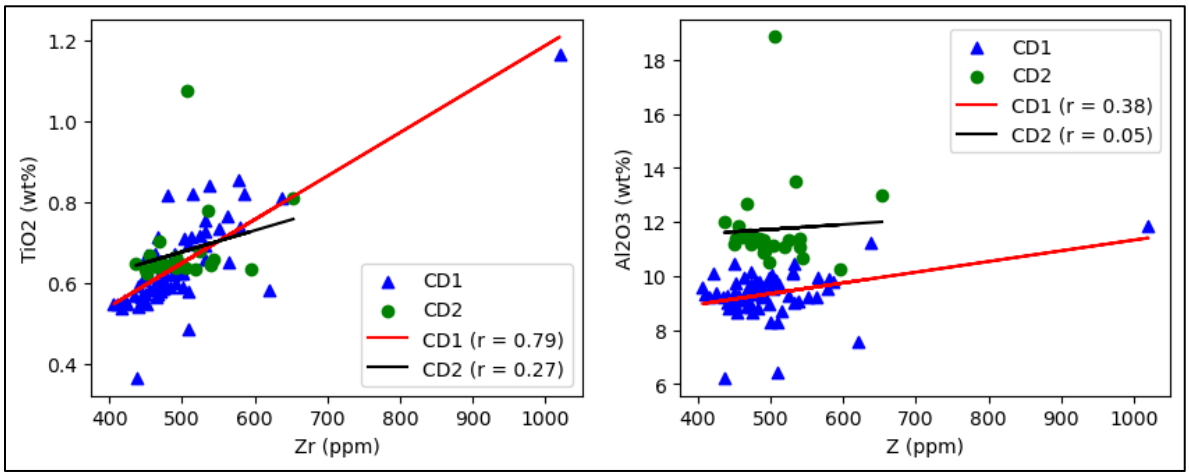

Figure 51: Correlation analysis illustrating the relationships between Zr and TiO_2, and between Zr and Al_2O_3 concentrations.

Li

Li typically substitutes isomorphically in silicate minerals such as mica and tourmaline (Finkelman et al., 2018). Several studies infer Li's mode of occurrence based on correlation analyses, due to limited direct mineralogical evidence and weak correlations in some cases. For example, Sun et al. (2022) found strong positive correlations between Li and ash content, SiO_2, and Al_2O_3 in high-volatile bituminous coals from the Ningwu Coalfield, suggesting an association with aluminosilicate minerals. However, a weak negative correlation between Li and the SiO_2/Al_2O_3 ratio indicated possible links to kaolinite or other Al-bearing minerals. Similarly, Shao et al. (2022)

reported strong positive correlations of Li with SiO_2 and Al_2O_3 in the Datong Coalfield's high-volatile bituminous coals, supporting its occurrence in aluminosilicates like kaolinite. Wang et al. (2022) observed moderate positive correlations between Li and clay minerals, ash content, and volatile matter in medium-rank coals, indicating Li's association with both inorganic and organic matter. Using Pearson correlation, Han et al. (2024) concluded that Li shows an inorganic affinity and occurs in Ti-rich aluminosilicates, illite, and phosphate minerals in the Gaoping Coal. Given the reliance on correlation data and the scarcity of direct mineral evidence, these interpretations should be considered cautiously. For the samples studied here, it is most reasonable to infer an intimate organic affinity for Li.

REY

REYs have multiple modes of occurrence, most of them are associated with carbonate, phosphate, aluminosilicate minerals, and organic compounds (Dai et al., 2021). Shao et al. (2022) showed that REEs had a moderate positive correlation with SiO_2, Al_2O_3, P_2O_5 and CaO in the Datong coal. They further explained that because apatite contains only a low amount of Ca, REEs are instead incorporated primarily into Ca-bearing clay minerals. Figure 52 shows that there were no correlations between REY and SiO_2 and REY and Al_2O_3, a very weak negative correlation between REY and P_2O_5, a weak positive correlation between REY and CaO, a moderate positive correlation between CaO and P_2O_5 and a moderate positive correlation between REY and Fe_2O_3 in CD1. These findings suggest that REY did not occur in aluminosilicate minerals, a small portion of REY occurred in apatite, and REY mainly occurred in Fe-rich minerals such as magnetite, ilmenite and pyrite, probably through substitution and adsorption and to a lesser extent in ankerite and other Ca-bearing minerals. The CaO/P_2O_5 ratio ranges from 6.94 to 25.02, this ratio was higher than 3.33, the CaO/P_2O_5 in apatite (Kolker et al., 2017), suggesting that REYs occurred in Fe and Ca-bearing minerals in CD1.

In CD2, REY had strong positive correlations with Al_2O_3, P_2O_5, moderate positive correlations with SiO_2 and CaO, and a weak positive correlation with Fe_2O_3. CaO has a strong correlation with P_2O_5. These findings align with previous studies that REYs were concentrated in Al and Si rich aluminosilicates (Thompson et al., 2018) and in Al and P rich aluminosilicates (Pan et al., 2018) and to a lesser with Ca and Fe-rich aluminosilicates (Kolker et al., 2017). These observations

suggest that REYs occurred in both phosphate and aluminosilicate minerals. The CaO/P_2O_5 ratio ranges from 6.27 to 10.78 higher than 3.33, the CaO/P_2O_5 in apatite (Shao et al., 2022), indicating a low concentration of Ca in phosphate minerals. This suggests that REYs predominantly occur in Ca-rich aluminosilicates. REY and Ca have similar ionic radii and electronegativity (Bindeman & Davis, 2000). REY^{+3} substitutes Ca^{+2} in Ca-rich aluminosilicates, and this was achieved through coupled substitution, where Al^{+3} replaces Si^{+4} in a tetrahedral framework (Bindeman & Davis, 2000). This suggests that REYs not only occur as adsorbents through substitution of Ca on the surface of kaolinite, but they were incorporated into smectite and illite through substitution.

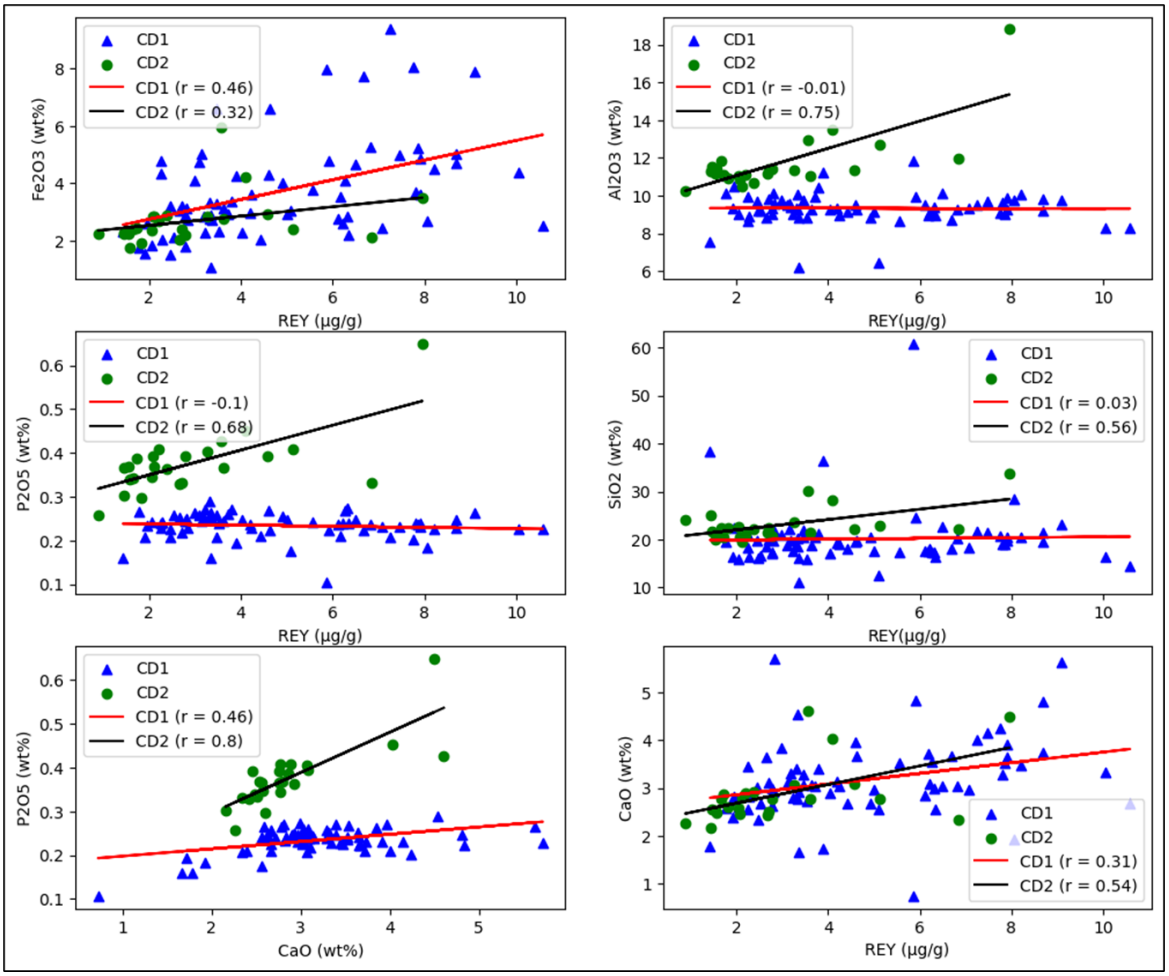

Figure 52: Correlation analysis between REY and major oxides including Fe_2O_3, Al_2O_3, P_2O_5, SiO_2, CaO as well as the relationship between CaO and P_2O_5.

Nb and Mo

As shown in Figure 53, Nb exhibits moderate positive correlations with TiO_2 and SiO_2 in CD1, while Mo shows a moderate positive correlation with TiO_2 in the same sample. This suggests their occurrence within anatase, likely through isomorphic substitution within its crystal structure. In contrast, in CD2, Nb has an extremely weak negative correlation with TiO_2 and a weak positive correlation with SiO_2, whereas Mo displays a weak negative correlation with TiO_2. These weaker associations indicate a more limited occurrence of Nb and Mo in both inorganic and organic matter in CD2. The strong affinity of Zr and Nb for anatase in CD1 aligns with Zhao et al. (2017), who proposed anatase as the main host mineral for these elements. The differences in mineral associations between CD1 and CD2 may be attributed to the lower SiO_2 and TiO_2, combined with higher Nb and Mo concentrations in CD1, compared to higher SiO_2 and TiO_2 and lower Nb and Mo in CD2.

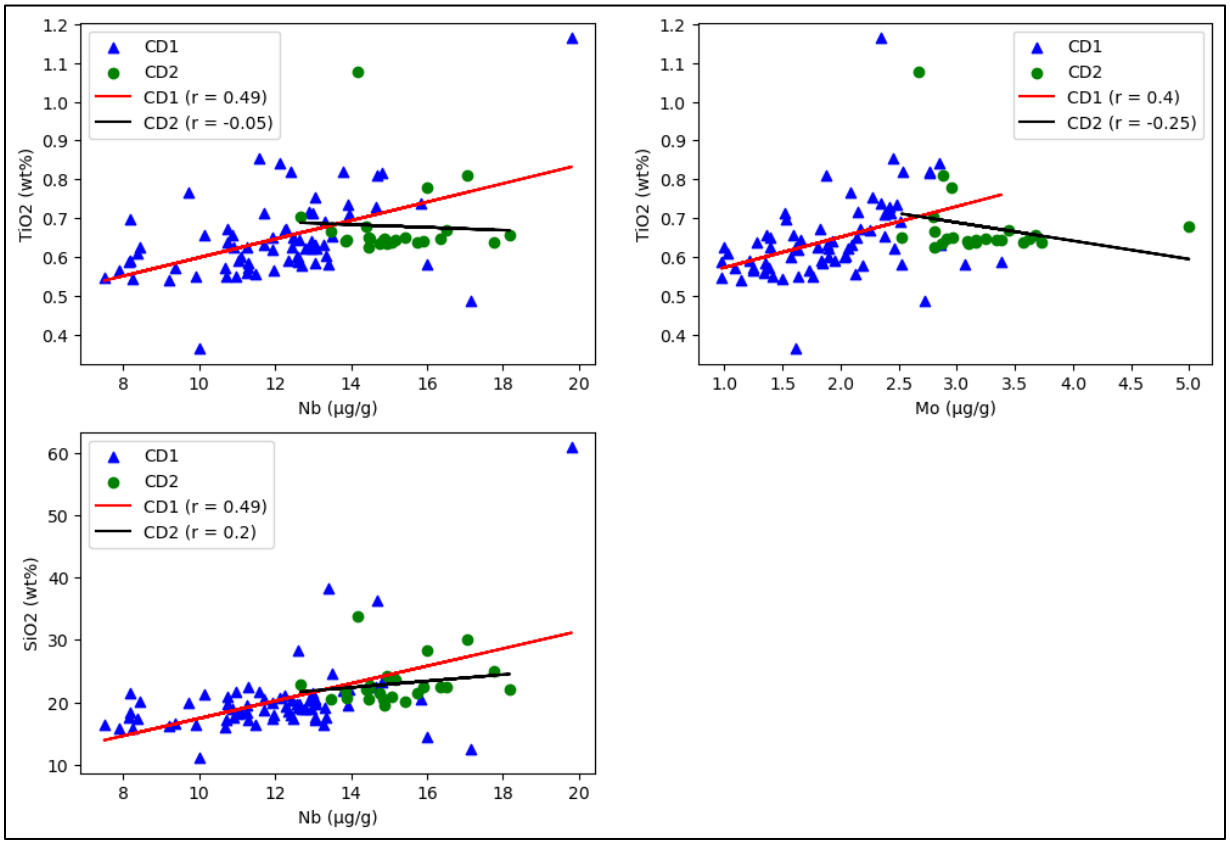

Figure 53: Correlation analysis between Nb and TiO_2 and SiO_2 as well as Mo and TiO_2.

Co

Figure 54 shows that Co has moderate positive correlations with SiO_2, Fe_2O_3, MnO, TiO_2, and Na_2O, and a weak positive correlation with CaO in CD1. These relationships suggest that Co is associated with silicates, Fe-, Mn-, and Ti-bearing minerals. In CD2, Co exhibits strong positive correlations with Fe_2O_3, MnO, and CaO, a moderate positive correlation with SiO_2, and weak positive correlations with TiO_2 and Na_2O. This indicates that Co is primarily associated with Fe-, Mn-, and Ca-bearing minerals and silicates, with some association to anatase and albite. These observations are consistent with earlier studies, which report that Co mainly occurs in carbonate and aluminosilicate minerals in hard coals (Querol et al., 2001; Swaine, 1990). The main difference in mineral associations between these coal discards may stem from lower Co and SiO_2 but higher Fe_2O_3, MnO, and CaO in CD1, compared to higher Co and SiO_2 but lower Fe_2O_3, MnO, and CaO in CD2.

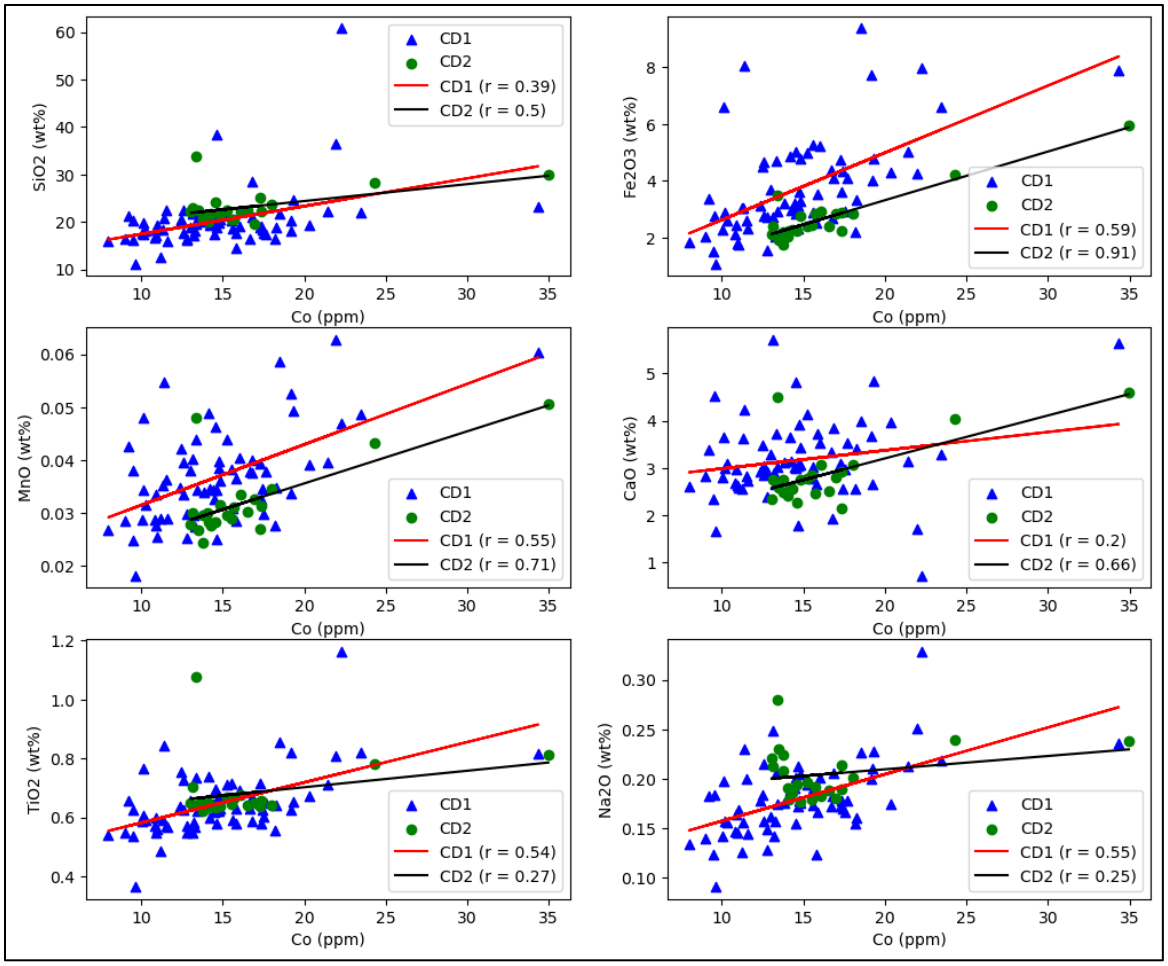

Figure 54: Correlation analysis between Co and SiO_2, Fe_2O_3, MnO, CaO, TiO_2 and Na_2O.

Cu

Cu in coal is typically associated with sulfide minerals, especially pyrite and chalcopyrite. In high-rank coals, Cu is mainly incorporated in chalcopyrite, while in low-rank coals, it tends to associate with organic matter (Dai et al., 2021; Swaine, 1990). Kolker et al. (2021) found that pyrite was the major carrier of Cu in the Illinois Basin coal. Riley et al. (2021) concluded that Cu exhibits multiple modes of occurrence in Australian coals, typically existing in sulfides, silicates, and organic matter. The modes of occurrence of Cu in coal discards from the Witbank Coalfield differ according to the correlation analysis (Figure 55). In CD1, Cu shows a weak negative correlation with Al_2O_3 and Cr_2O_3 suggesting limited association with Al-bearing minerals and chromite. Instead, a moderate positive correlation with ash content indicates a potential inorganic mineral association.

Additionally, a weak positive correlation with P_2O_5 points to a minor association with phosphate minerals.

In contrast, in CD2, Cu exhibits a strong positive correlation with ash content, indicating a strong association with inorganic matter. Weak positive correlation with Al_2O_3, suggesting potential minor association with Al-bearing minerals. A moderate positive correlation with P_2O_5 and Cr_2O_3 implies association with phosphate minerals and chromite.

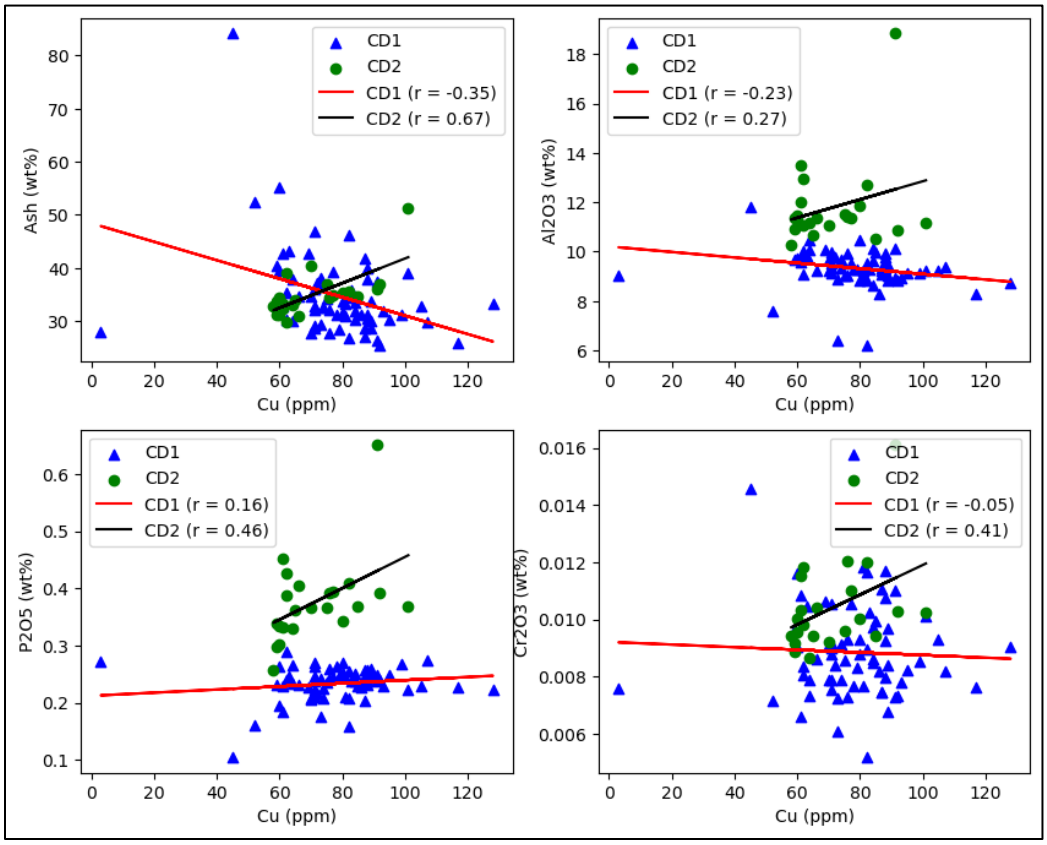

Figure 55: Correlation analysis between Cu and ash content, Al_2O_3, P_2O_5, and Cr_2O_3.

Pb

Lead Pb in coal is mainly incorporated in sulfide minerals such as galena (Riley et al., 2012; Sia & Abdullah, 2012). It is also found in Se-bearing sulfide and silicate minerals (Riley et al., 2012). Sia & Abdullah (2012) reported a notably negative correlation (r = -0.12) between Pb and ash content in Balingian bituminous coals, implying an organic association. However, Kolker et al.

(2021) identified pyrite as the major carrier of Pb in Illinois Basin high-volatile bituminous coals. Dai et al. (2021) also noted that Pb occurs in pyrite, organic matter, galena, and clausthalite.

As shown in Figure 56, Pb in CD1 displayed moderate negative correlations with CaO, TiO_2, and Cr_2O_3, suggesting limited association with carbonate, Ti-bearing minerals, and chromite. A moderate positive correlation with FC suggests an organic matter association. In contrast, Pb in CD2 showed moderate positive correlations with CaO, TiO_2, P_2O_3, Cr_2O_3, and MgO, indicating primarily inorganic mineral associations. These contrasting correlation patterns likely reflect differences in physicochemical, geochemical, and mineralogical compositions.

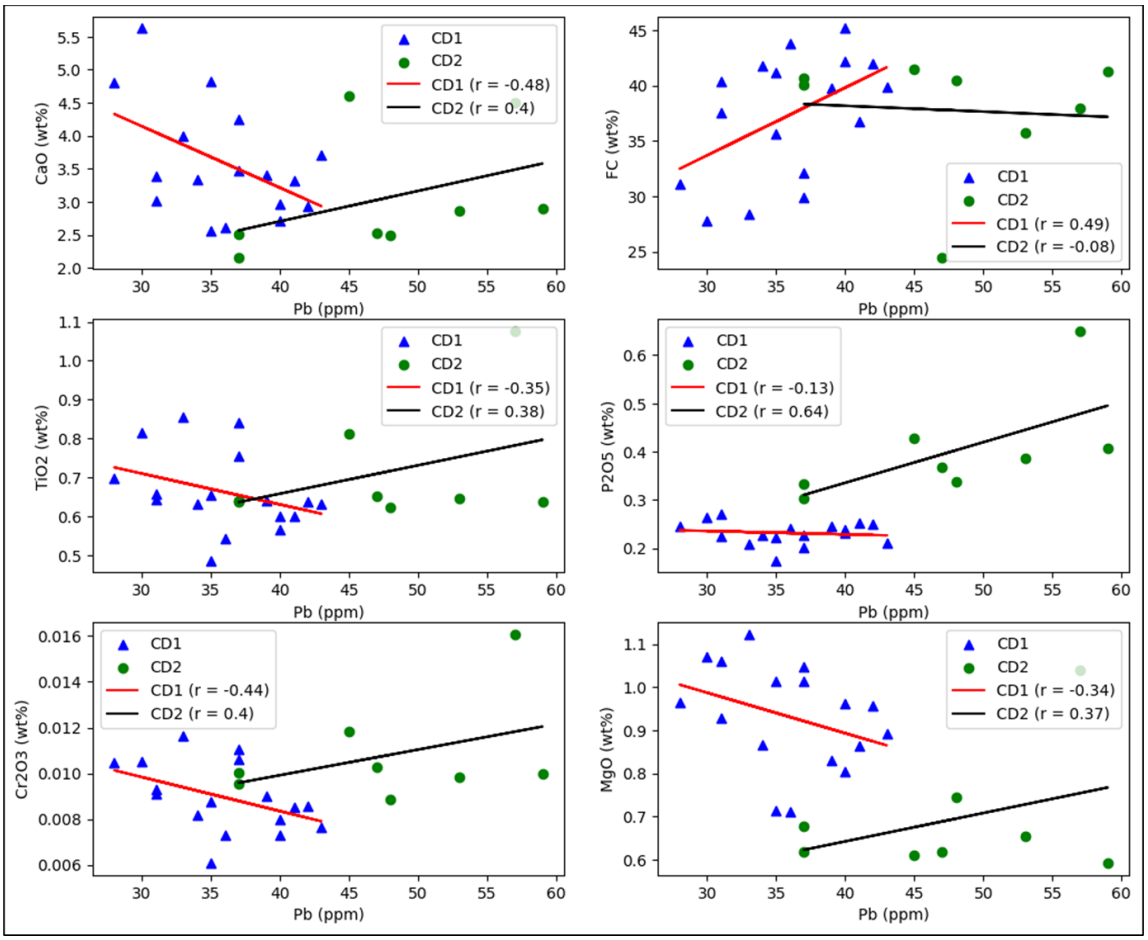

Figure 56: Correlation analysis between Pb and CaO, FC, TiO_2, P_2O_5, Cr_2O_3 and MgO.

Ni

Sequential leaching studies showed that Ni mainly occurs in sulfides, silicates, organic matter, and in carbonate minerals in coals (Riley et al., 2021). Dai et al. (2021) concluded that organic matter is the major carrier of Ni primarily in low-rank coals, such as lignite and sub-bituminous coals. This is consistent with general observations that organic associations for elements like Ni tend to decrease with increasing coal rank, becoming less common in bituminous and higher-rank coals. Figure 57 shows that Ni has a strong negative correlation with ash content and a strong positive correlation with fixed carbon in CD1, indicating a strong organic association. This observation contrasts with Dai et al. (2021), who concluded that organic matter is the primary host of Ni mainly in low-rank coals, with organic association generally decreasing as coal rank increases. In contrast, in CD2, Ni exhibits a moderate positive correlation with ash content and moderate negative correlation with FC, indicating its association with inorganic matter.

These differences in the mode of occurrence of Ni could be attributed to the difference in the age and environmental conditions of the dumps. CD1, as the older dump, may have undergone more extensive weathering, biological activity, or geochemical changes that enhanced Ni's association with organic matter. Conversely, CD2, the newer dump, likely retains more of the original inorganic mineral associations of Ni with ash-forming minerals. This highlights how dump age and post-depositional processes can influence the distribution and mode of occurrence of Ni in coal discards.

Be

Be in low-rank coals is commonly associated with organic compounds, especially those composed of hydroxyl and carboxyl groups (Wei and Zhao, 2024). As shown in Figure 57, Be has a weak negative and positive correlation with ash and FC contents, respectively, in CD1, implying its minor potential association with organic matter. In contrast, CD2, Be exhibits a weak positive and negative correlation with ash and FC contents, respectively, implying its association with inorganic matter. These differences in Be's mode of occurrence could be attributed to the relative age and weathering history of the dumps. CD1, being the older dump, likely experienced more extensive weathering and geochemical alteration, which may have favored redistribution or enhanced association of Be with organic matter. Conversely, the newer CD2 dump may retain more of the original inorganic mineral associations of Be due to limited weathering. This highlights how the

age of coal waste dumps can influence trace element distribution and mode of occurrence despite similar coal rank.

Zn

Zn in coal is incorporated in sphalerite (Dai et al., 2021; Finkelman et al., 2018; Riley et al., 2021; Swaine, 1990) and is associated with organic matter in low-rank coals (Swaine, 1990). Finkelman et al. (2018) reported that 15% of Zn occurs in pyrite in bituminous coals. Figure 57 shows that Zn had a negative correlation with ash content in CD1, indicating its limited occurrence in inorganic matter, while it had a strong positive correlation with ash content in CD2 implying its strong association with sulfide minerals such as pyrrhotite.

Rb

Rb is isomorphic with K in silicate minerals, it tends to replace K due to their similar ionic radius, charge, and electronegativity. Zhao C et al. (2017) reported that Rb has a strong positive correlation with K_2O, and a moderate positive correlation with SiO_2 and Al_2O_3 in high-bituminous coals. Based on these findings, they concluded that illite and kaolinite were the major carriers of Rb in Iqe coals. In Figure 57, Rb exhibited a strong positive correlation with K_2O in both coal discards suggesting its occurrence in K-bearing minerals such as illite and muscovite. These findings resonate with Zhao C et al. (2017) findings in the Iqe coals.

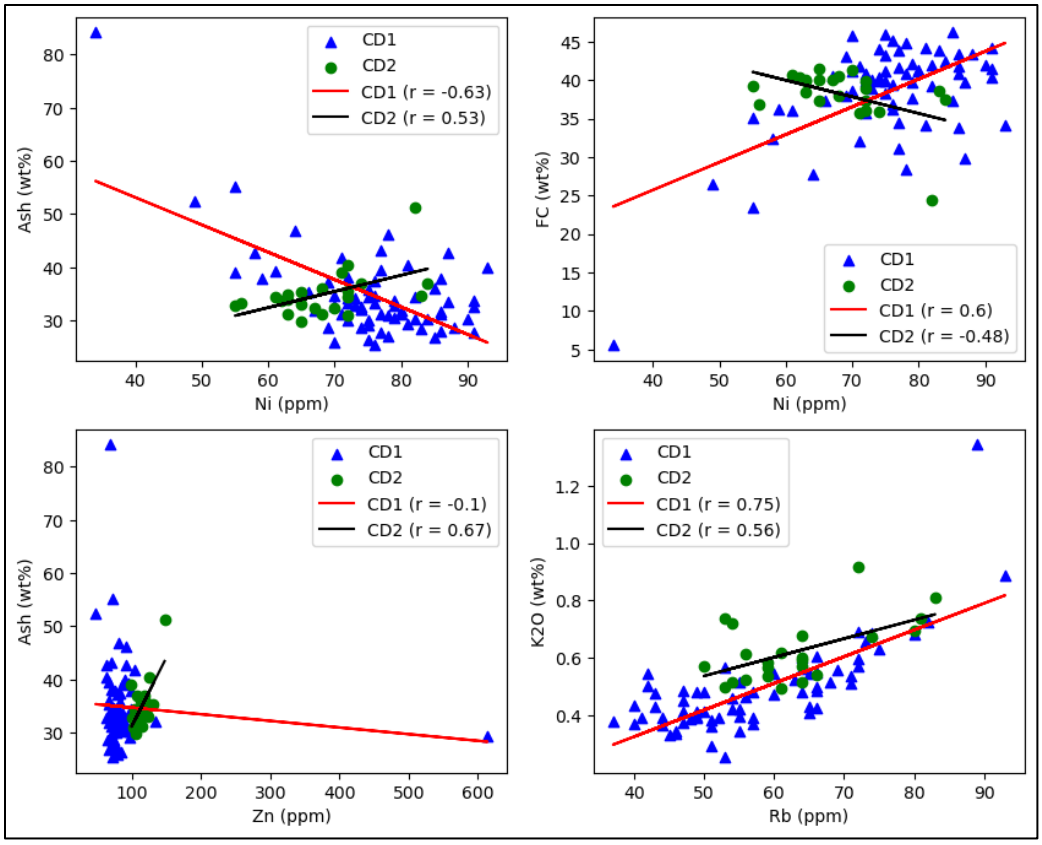

Figure 57: Correlation analysis: Ni vs ash and FC; Zn vs ash and Rb vs K_2O.

The distinct modes of occurrence of CRMs between CD1 and CD2 reflect a complex interplay of physicochemical, mineralogical, and geochemical factors, all influenced by the age of the coal dumps. Although both dumps contain coal discards of the same rank, their different ages mean they have undergone varying degrees of weathering and geochemical alteration. Over time, exposure to surface conditions can alter mineral phases, redistribute elements, and transform the associations of CRMs with organic matter and inorganic minerals.

In the CD1, prolonged weathering and biogeochemical processes may have enhanced the association of CRMs with organic matter or caused partial leaching and secondary mineral formation. In contrast, CD2 retains more of the original mineralogical characteristics of the coal, resulting in CRMs being primarily hosted by inorganic phases such as sulfides, phosphates, silicates, or carbonates. These dynamics highlight how dump age, beyond coal rank alone,

critically controls the behaviour, distribution, and mode of occurrence of CRMs in coal waste environments.

5.3 Influence of Geological Factors on the Occurrence, Distribution and Concentration of CRMs in Coal Discards

Coal discards like coal are complex and heterogeneous materials. The mode of occurrence, distribution, and concentration of CRMs in coal seams are influenced by several geological factors such as source materials, freshwater/seawater, and igneous intrusion/hydrothermal activities while coal discards are mainly influenced by telogenic processes. Vassilev et al. (1997) stated that leaching, coalification stages, depositional and paleoenvironmental conditions play a pivotal role in controlling the chemical composition in coal.

5.3.1 Source Materials

The Al_2O_3/TiO_2 ratio has been used extensively to determine the provenance of sedimentary rock (Hayashi et al., 1997) and coal seam (Zhao et al., 2019a; Zheng et al., 2017). Hayashi et al. (1997) reported that sedimentary rocks with an Al_2O_3/TiO_2 ratio between 3 and 8 are derived from mafic igneous sources, those with a ratio between 8 and 21 originate from intermediate igneous rocks, and ratios from 21 to 70 indicate derivation from felsic igneous rocks. They noted that weathering, deposition, transportation, and diagenesis generally do not significantly alter the Al_2O_3/TiO_2 ratio in source materials. During weathering, Al, Ti, and Zr are typically retained due to their low solubility, whereas elements such as Ca, K, and Mg are more readily leached through hydrolysis, dissolution, and ionic exchange because of their higher solubility in water.

Previous studies have shown that coal seams influenced by alkaline felsic volcanic ashes are enriched in Nb, Ta, Zr, Hf, Ga, and rare earth elements (REY), whereas those influenced by mafic volcanic ashes are enriched in Co, V, Cr, Ni, and V (Dai et al., 2014; Wang et al., 2016; Zhao et al., 2017). Although there has been no recent volcanism within the main Karoo Basin, volcanic ash deposits are present and associated with the underlying Transvaal Supergroup (Eriksson & Clendenin, 1990). Zhao et al. (2019a) showed that most of coal and non-coal samples in the Datanhao mine fall in the felsic field, with few samples falling in the intermediate field in the Al_2O_3- TiO_2 plot whilst Zheng et al. (2017) showed that all the coal samples from the Shungentian

coalfield fall in the mafic field and those coal samples were rich in Sc, Cr, V, Co, Zn and Ni. The Al_2O_3/TiO_2 ratios of the coal discards exclusively fall in the range between 8-21 in the Al_2O_3- TiO_2 plots (Figure 58), indicating the influence of intermediate igneous rock. In addition, coal discard compositions were characterized by elevated concentrations of Si, Ba, Sr, Ga, and Zr, and moderate concentrations of Al, Fe, Zn, Ti, Co, Cu, Nb and Ca, and traces of K, Mg, Mn, P, Ti, Cr, Mo, and Li. These findings align with previous studies indicating that the Witbank Coalfield experienced a series of dolerite (mafic) intrusions (Coetzee & Kisters 2017) alongside deposition of rhyolitic (felsic) volcanic material from the Rooiberg Group (Eriksson & Clendenin, 1990). The dolerite intrusions have led to the formation of epigenetic minerals in the coal seams, including pyrite, carbonate minerals such as dolomite and calcite, and alteration products like quartz and clay minerals. These minerals typically form from hydrothermal fluids released during the cooling of dolerite and through thermal metamorphism, altering the coal's mineralogy, geochemistry, and trace element distribution.

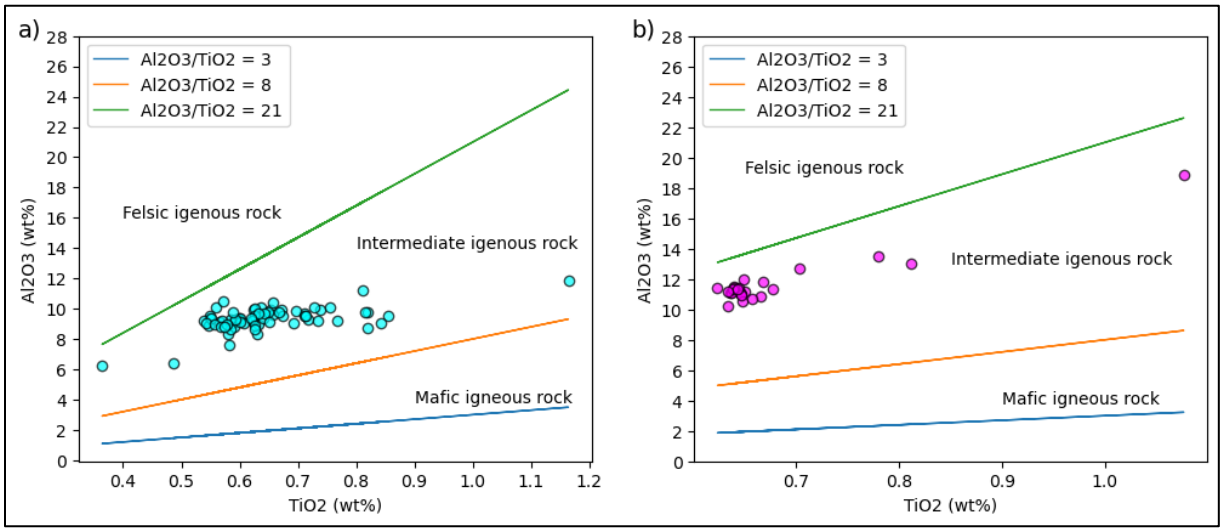

Figure 58: Relationship between Al_2O_3 and TiO_2 in a) CD1and b) CD2 samples, illustrating the geochemical signatures indicative of provenance.

5.3.2 Freshwater

The Witbank Coalfield is known for its high Ba concentration in coal seams (Netshitungulwana et al., 2022; Pinetown, 2007). This Ba enrichment is linked to the presence of Ba-bearing minerals

such as barite (Figures 40 and 41). The mineralogical and geochemical characteristics influencing Ba concentrations reflect regional depositional environments and post-depositional processes like hydrothermal alteration. Reimann & De Caritat (2012) noted that freshwater has low concentrations of K, Mg, Li, F, and Sr while seawater has elevated concentrations of these elements. Wang et al. (1979) used the Sr/Ba ratio as an indicator of depositional environment during the peat-forming stage, asserting that ratios greater than one reflect marine influence, while ratios less than one indicate freshwater conditions. This ratio helps infer paleosalinity during coal deposition. Post-depositional processes, such as dolerite intrusions, may alter the mineralogy and geochemistry of the coal, potentially influencing trace element distribution. Additionally, telogenic processes occurring after mining such as weathering, processing, and storage in stockpiles can further modify mineral associations and geochemical signatures. Petrographic evidence is crucial to distinguish these different mineral classes formed during each stage and to validate interpretations of the Sr/Ba ratio.

The Sr/Ba ratios in Figure 59 indicate that coal seams were subjected to freshwater influence. These findings are consistent with previous studies which reported that coal seams in the Witbank Coalfields formed in freshwater environments such as fluvial, wetlands, river system and lacustrine settings (Netshitungulwana et al., 2022; Soeder & Borglum, 2019; Weeber et al., 2000). The coal discards of the Witbank coalfield are characterized by low composition of MgO, MnO, Na_2O, K_2O, REY and small phases of marine derived minerals such as pyrite, dolomite and calcite. The high content of quartz and kaolinite suggests clastic sedimentary rocks such as sandstones, shale and mudstones are typically present in riverine and lake environments.

Subangular quartz (Figure 35a) indicates minimal transportation by water. Bright, platy-like crystal of magnetite with small inclusions of organic matter (Figure 42a), indicates that magnetite was subjected to late-stage incursion of organic-rich freshwater. Well-rounded zircon grain (Figure 42b) and sub-rounded massive siderite (Figure 37b) indicate abrasion and slight transport by water. However, carbonates such as dolomite and siderite in coal seams are rarely detrital, they typically form epigenetically during peatification and coalification. This is because carbonate minerals precipitate in situ from pore waters under specific diagenetic conditions rather than being transported as detrital grains. The dolomite grains embedded in calcite (Figure 38b) suggest

epigenetic dolomitization likely caused by the incursion of Mg-rich freshwater during coal maturation.

Most coal discard samples fall below the 50 wt% ash content thresholds for high ash (Figure 59), with only a few exceeding this value. Although the low Sr/Ba ratio and low ash content initially suggest freshwater influence due to Ba abundance in freshwater from terrestrial sources such as soil and rock weathering, the chemistry and ash content measured in these discards do not represent their in-situ conditions. These discard samples were previously processed, which alters their original mineralogy and geochemistry through removal of minerals, salts, and suspended particles. Therefore, interpretations regarding depositional environment based on discard ash content or Sr/Ba ratios should be made cautiously, considering the effects of coal beneficiation and handling.

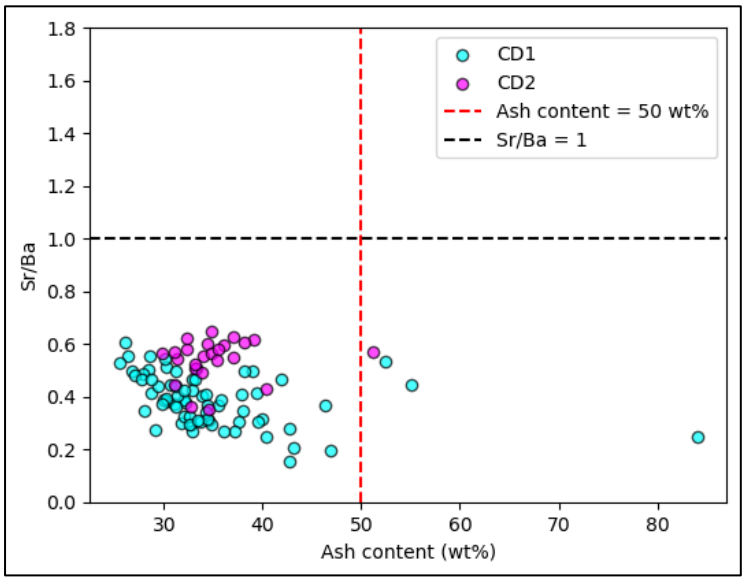

Figure 59: Diagram showing the relationship between Sr/Ba ratios and ash content in coal discard samples from CD1 and CD2. Sr/Ba ratios indicate paleosalinity during deposition, while ash content reflects mineral matter levels, with variations influenced by processing, weathering, and post-depositional changes.

5.3.3 Igneous Intrusion and Hydrothermal Fluids

The coal seams in the Witbank coalfield were intruded by a series of igneous intrusions in the form of dolerite sills and dykes (Coetzee & Kisters 2017). Carbonate minerals such as calcite, ankerite,

and dolomite commonly form near igneous intrusions due to thermal and hydrothermal alteration, resulting from fluids released during cooling of the intrusions (Moroeng et al., 2024). These epigenetic carbonates reflect post-depositional mineralogical changes rather than detrital origin. Li et al. (2016) highlighted that pyrite formed due to the precipitation of epithermal fluids during coal formation rather than indicating the influence of seawater in coal seams. They also mentioned that rectorite form when kaolinite reacts with low hydrothermal fluids during diagenesis processes. On the other hand, Dai et al. (2017) reported that when kaolinite reacts with ammonium under high-temperature hydrothermal conditions it forms tobelite. However, there was no evidence of rectorite and tobelite formation in the Witbank coalfield. Dai et al. (2015) reported that epigenetic hydrothermal fluids facilitate the replacement of Al by Ti in kaolinite and the enrichment of REEs in coals. The coal discards in this study have elevated concentrations of quartz and kaolinite, which would have been destroyed by hydrothermal activities (Dai et al., 2013). A complementary study by Zhao et al. (2019a) highlighted that the enrichment of Li and REEs in coals is due to hydrothermal fluids generated by magmatic activities. Dai et al. (2016) inferred that coal seams influenced by hydrothermal fluids have elevated concentration of U, V, Se, Mo, Re and V. This study was characterized by low Li, Mo, Pb, and REY+Sc contents suggesting the minimal effect of hydrothermal fluids on the coal seams. High quartz and kaolinite contents in the coalfield are primarily syngenetic, reflecting input from terrigenous sediments during peat formation. The Fe is mainly present in pyrrhotite, which may be either syngenetic or epigenetic in origin. Ca is likely hosted in carbonate minerals such as calcite or dolomite, which are generally epigenetic and form during coalification rather than being detrital. In addition, elevated concentrations of Ba, Zr, and Sr points towards igneous and sedimentary minerals, that might have been altered.

5.4 Potential Economic Significance of CRMs in Coal Discards

The elevated concentrations of trace elements such as Ba, Be, Ga, Sr, Zr, REY, Zn, Co, Cu, Ni, Li, Rb, Pb, Mo, and Nb in coal discard samples suggest a heightened potential for recovery of these CRMs compared to typical geological materials. The extraction of these elements from coal discards could help easy supply chain constraints and stop reliance on primary sources (Dai et al., 2017; Lin et al., 2018b; Thompson et al., 2018; Wang et al., 2022; Zhao et al., 2019). The economic viability of CRMs depends on several factors such as concentration, as well as mode of occurrence and distribution.

The average Ba concentrations in coal discard samples are 960.85 µg/g in CD1 and 628.12 µg/g in CD2, approximately four times higher than the 150 µg/g cut-off grade established by Dai et al. (2012a) and Ketris & Yudovich (2009). Since Ba primarily occurs as barite in these samples (Figure 40 and 41), its extraction could potentially mitigate the environmental impacts associated with high-Ba coal (Hao et al., 2022). However, successful industrial-scale extraction depends on the mineralogical form of Ba in the discard and requires comprehensive beneficiation and chemical processing techniques to recover Ba from barite. Similarly, the concentrations of Ga are 141.07 µg/g in CD1 and 105.25 µg/g in CD2, higher than 30 µg/g, its cut-off grade (Dai et al., 2006). The average concentrations of Sr are 344.94 and 339.33 µg/g in CD1 and CD2, respectively. Whereas Li, another sought-after element, fall significantly below its cut-off grade. The concentrations of Zr are extremely high in the coal discard samples, its averages are 495.39 ppm in CD1 and 502.96 ppm in CD2. Nonetheless, the world average concentrations of Zr are 35 ppm in low-rank and 36 ppm in hard coals (Ketris & Yudovich, 2009), while the Zr average concentration in US coal is 27 ppm (Orem and Finkelman, 2005), and Chinese coal is 89.5 ppm (Dai et al., 2012).

The average concentrations of REY + Sc are 4.67 µg/g in CD1 and 3.27 µg/g in CD2.The average concentrations of Cu are 78.19 and 71.17 ppm in CD1 and CD2, respectively. These concentrations are higher than 16 ppm in US coals (Orem and Finkelman, 2005) and 17.5 ppm in Chinese coals (Dai et al., 2012). Similarly, they are higher than the world average concentration in low-rack and high-rank coals, 15 and 16 ppm, respectively (Ketris & Yudovich, 2009). The average concentrations of Zn are 86.34 and 114 ppm in CD1 and CD2, respectively. These concentrations are higher than the world average concentrations reported by Ketris & Yudovich (2009), 18 ppm in low-rank coals, and 28 ppm in hard coals.

The average concentrations of Ni in CD1 and CD2 are 75.51 and 68.39 ppm, respectively. These concentrations are higher than 14 ppm in Chinese coals (Dai et al., 2012) and 13.7 ppm in US coals (Orem and Finkelman, 2005). In the same way, they are higher than those reported in low-rank and hard coals, 9 ppm and 17 ppm respectively (Ketris & Yudovich, 2009). Similarly, the average concentrations of Co in CD1 and CD2 are 14.79 and 16.47 ug/g, respectively, slightly higher than those reported in US and Chinese coals, 6.1 (Orem and Finkelman, 2005) and 7.1 ppm (Dai et al.,

2012). Similarly, they are slightly higher than the world average concentration reported in low-rank and hard coals, 4.2 and 6.0 ppm, respectively (Ketris & Yudovich, 2009).
The average concentrations of Pb in CD1 and CD2 are 36 and 49 ppm, respectively, six times higher than those reported in low-rank and hard coals, 6.6 and 9.0 respectively (Ketris & Yudovich, 2009). They are also higher than the average concentration of Pb reported in US and Chinese coals, 11 ppm (Orem and Finkelman, 2005) and 15.1 ppm (Dai et al., 2012). While the concentration levels of Be are lower in coals, for instance the average concentrations of Be are 2.16 and 2.86 ug/g, almost equal to the average of Be in hard coals, 2 ppm and slightly higher than its average in low-rank coals, 1.2 ppm (Ketris & Yudovich, 2009). Similarly, the average concentrations of Rb are57.53 and 63 ppm in CD1 and CD2, respectively. Ketris & Yudovich (2009) reported that the average world concentration of Rb in low-rank and high-rank coals was 10 and 18 ppm, respectively, extremely lower than those reported in this study.

The average concentrations of Nb are 11.95 and 15.19 ug/g in CD1 and CD2, respectively. According to Ketris & Yudovich (2009) the world average concentration of Nb in low-rank coal was 3.3 ppm and 4.0 ppm in hard coal, lower than those reported in this study. Similarly, the average concentrations of Mo are 1.92 and 3.21 ug/g in CD1 and CD2, respectively. The average concentration of Mo in CD1 is lower than the world average concentration of Mo, while Mo in CD2 was slightly higher than the world average concentration, which are 2.2 and 2.1 ppm in low-rank and hard coals, respectively (Ketris & Yudovich, 2009). Similarly, the average concentration of Mo in CD1 are lower than those reported in US and Chinese Coal, but in CD2 was equal to them, which are 3.2 ppm (Orem and Finkelman, 2005) and 3.1 ppm (Dai et al., 2012), respectively.

These coal discards should be considered as a potential source for Ba, Ga, Sr, Zr, Cu, Zn, Ni, Co, Pb, Be, Mo, and Nb recovery as they were higher compared to their word average concentrations. The extraction of chalcophile elements such as Cu, Ni, Pb, Be, and Mo from coal discards can contribute to sustainable development and mitigate environmental risks like AMD. Technically, their extraction is feasible using methods such as sequential acid leaching. Extraction efficiency depends on the form in which these elements occur, whether associated with organic matter or locked in mineral phases, which influences the choice of processing techniques. Industrial-scale recovery requires integration of beneficiation to concentrate the target elements, followed by

hydrometallurgical methods including mild acid leaching, bioleaching, or chemical adsorption to separate and purify the metals. However, challenges remain, including processing costs, recovery from complex matrices, and competing uses of coal, which must be addressed to realize practical, large-scale extraction.

Chapter 6: Conclusion and Recommendations

6.1 Conclusion

This study successfully addresses the key research questions regarding the presence, modes of occurrence, concentrations and distribution of CRMs in coal discards from the Witbank Coalfield. The coal discards were found to contain various CRMs, including Ba, Ga, Sr, Zr and other valuable elements, distributed unevenly between and within dumps. Notably, the older CD1 dump showed stratigraphic control on CRM concentrations, while CD2 exhibited lateral heterogeneity. The mode of occurrence of CRMs is complex, influenced by dump age, depth, and geological factors such as mineralogy, hydrogeochemical and hydrothermal alteration. Mineralogical and geochemical data confirmed that CRMs are primarily hosted by kaolinite, carbonate, sulfide, and phosphate minerals with variable organic associations. Despite challenges in processing due to heterogeneous mineral associations and element speciation, the elevated concentrations of CRMs compared to global averages illustrate coal discards' economic potential as secondary CRM resources. This valorization can contribute to sustainable resource management and reduce environmental impacts such as acid mine drainage. Future work should focus on refining beneficiation and extraction technologies to optimize CRM recovery and support the sustainable development of coal discard resources.

The research questions of this study were responded in the following manner:

Research Question 1: Which CRMs are present in the coal discards of the Witbank Coalfield?

Response: These are the dominating CRMs present in both coal discards (Zr, Sr, Ga, Li, REY, Co, Cu, and Ni).

Research Question 2: How are these CRMs distributed spatially and concentrated across two selected coal discard dumps?

Response: These CRMs are heterogeneously distributed with varying concentrations at different intervals, indicating stratigraphic control in CD1 due to distinct mineral layering observed and corresponding oxide profiles. The stratigraphic control of the presence of CRMs observed in CD1 is as a result of the coal discard dump being well compacted and

managed. In CD2, the distribution is also heterogeneous but less stratigraphically coherent, reflecting more mixing and post-depositional alteration processes. These conclusions are based on the sampling methods and observations: CD1 was obtained by drilling, providing continuous vertical intervals that reveal clear stratigraphic variations in CRM concentrations, while CD2 samples were collected from the surface, resulting in more mixed and less stratigraphically preserved CRM distributions.

Research Question 3: How do the characteristics of coal discard, such as age, depth, and geological composition affect the occurrence and concentration of CRMs?

Response: The occurrence and concentration of CRMs in coal discards reflect the combined influence of age, depth, and geological composition, resulting in complex and variable distribution patterns. CD1 often record the effects of prolonged weathering, oxidation, and mineral transformation, which can modify CRM concentrations and mineral stability. Depth governs the pressure, temperature, and fluid movement within the discard, influencing the redistribution and enrichment of certain CRMs through geochemical reactions and recrystallization. Geological composition establishes the mineralogical context, determining which CRMs are present and their specific modes of occurrence, such as association with silicates, sulfides, or phosphates. In contrast, CD2 typically display CRM distributions that are mainly a consequence of coal processing, with little modification from post-depositional telogenic processes. Consequently, CD1 tend to exhibit more complex CRM patterns due to cumulative environmental and mineralogical changes over time.

6.2 Recommendations

To further investigate the mode of occurrence, distribution, and concentration of CRMs in the coal discards of the Witbank Coalfield, it is recommended that the following studies be conducted:

1. Conduct petrographic studies to investigate the distribution, speciation, and mobility of these CRMs in organic matter.
2. Conduct and optimize floatation to fully liberate minerals and avoid the observed intimate organic associations of some CRMs.

3. Conduct selective leaching to improve the quantification of mode of occurrence of CRMs in coal discards.
4. Estimate the resource potential of coal discards, considering factors such as tonnage, grade, and extractability.

References

1. Adriano, D.C., 1986. Trace elements in the terrestrial environment. *Springer Verlag google schola*, *2*, pp.335-348.
2. Aja, S.U., 2019. On the thermodynamic stability of illite and IS minerals. Clays and Clay *Minerals*, 67(6), pp.518-536.
3. Arbuzov, S.I., Volostnov, A.V., Mezhibor, A.M., Rybalko, V.I. and Ilenok, S.S., 2014. Scandium (Sc) geochemistry in coals (Siberia, Russian Far East, Mongolia, Kazakhstan, and Iran). *International Journal of Coal Geology*, *125*, pp.22-35.
4. ASTM (American Society for Testing Materials), 2007. A standard Test Method for Gross Calorific Value of Coal and Coke: ASTM D5865/D5865-07.
5. ASTM (American Society for Testing Materials), 2009. Standard test Method for Proximate Analysis of the Analysis Sample of Coal and Coke by Instrument Procedures1: ASTM D5142/D5142-09.
6. Bindeman, I.N. and Davis, A.M., 2000. Trace element partitioning between plagioclase and melt: investigation of dopant influence on partition behavior. *Geochimica et cosmochimica acta,* 64(16), pp.2863-2878.
7. Brown, D.J., 1962. Coal flotation. *Froth Flotation*, *50*, pp.518-538.
8. Bytnar, K. and Makowska, D., 2017. Concentration of main elements in mineral matter of Polish coking coal and its cleaning products. In E3S web of conferences (Vol. 14,02013). EDP Sciences.
9. Cairncross, B., 2001, An overview of the Permian (Karoo) coal deposit of Southern Africa, *Journal of Earth of Sciences*, University of Johannesburg, 33, pp. 529-562.
10. Cairncross, B., 2001. An overview of the Permian (Karoo) coal deposits of southern Africa. *Journal of African Earth Sciences*, *33*(3-4), pp.529-562.
11. Çelik, Y., Karayigit, A.I., Oskay, R.G., Kayseri-Özer, M.S., Christanis, K., Hower, J.C. and Querol, X., 2021. A multidisciplinary study and palaeoenvironmental interpretation of middle Miocene Keles lignite (Harmancık Basin, NW Turkey), with emphasis on syngenetic zeolite formation. *International Journal of Coal Geology*, 237, p.103691.
12. Cloete, H.C.C., 2012. The estimation of uncertainty of measurement by X-ray fluorescence spectrometry. MSc thesis, Department of Chemistry, University of Johannesburg.

13. Coetzee, A. and Kisters, A., 2016. The 3D geometry of regional-scale dolerite saucer complexes and their feeders in the Secunda Complex, Karoo Basin. *Journal of Volcanology and Geothermal Research*, 317, pp.66-79.
14. Czajka, K.M., 2018. Proximate analysis of coal by micro-TG method. *Journal of analytical and Applied Pyrolysis*, *133*, pp.82-90.
15. Dai S., Yuegang, T., Mei, Y. and Liming, H., 2005. Concentration and distribution of elements in Late Permian coals from western Guizhou Province. China, 61(1), pp.119-137.
16. Dai, S., Finkelman, R.B., French, D., Hower, J.C., Graham, I.T. and Zhao, F., 2021. Modes of occurrence of elements in coal: A critical evaluation. *Earth-Science Reviews*, *222*, p.103815.
17. Dai, S., Guo, W., Nechaev, V.P., French, D., Ward, C.R., Spiro, B.F., Finkelman, R.B., 2018a. Modes of occurrence and origin of mineral matter in the Palaeogene coal (no. 19-2) from the Hunchun Coalfield, Jilin Province, China. *Int. J. Coal Geol*. 189, 94–110.
18. Dai, S., Jiang, Y., Ward, C.R., Gu, L., Seredin, V.V., Liu, H., Zhou, D., Wang, X., Sun, Y., Zou, J. and Ren, D., 2012a. Mineralogical and geochemical compositions of the coal in the Guanbanwusu Mine, Inner Mongolia, China: Further evidence for the existence of an Al (Ga and REE) ore deposit in the Jungar Coalfield. *International Journal of Coal Geology*, 98, pp.10-40.
19. Dai, S., Li, T., Jiang, Y., Ward, C.R., Hower, J.C., Sun, J., Liu, J., Song, H., Wei, J., Li, Q. and Xie, P., 2015. Mineralogical and geochemical compositions of the Pennsylvanian coal in the Hailiushu Mine, Daqingshan Coalfield, Inner Mongolia, China: Implications of sediment-source region and acid hydrothermal solutions. *International Journal of Coal Geology*, *137*, pp.92-110.
20. Dai, S., Luo, Y., Seredin, V.V., Ward, C.R., Hower, J.C., Zhao, L., Liu, S., Zhao, C., Tian, H. and Zou, J., 2014. Revisiting the late Permian coal from the Huayingshan, Sichuan, southwestern China: Enrichment and occurrence modes of minerals and trace elements. *International Journal of Coal Geology*, 122, pp.110-128.
21. Dai, S., Ren, D., Chou, C.L., Finkelman, R.B., Seredin, V.V. and Zhou, Y., 2012. Geochemistry of trace elements in Chinese coals: A review of abundances, genetic types, impacts on human health, and industrial utilization. *International Journal of Coal Geology*, *94*, pp.3-21.

22. Dai, S., Ren, D., Chou, C.L., Li, S. and Jiang, Y., 2006. Mineralogy and geochemistry of the no. 6 coal (Pennsylvanian) in the Junger Coalfield, Ordos Basin, China. *International Journal of Coal Geology*, 66(4), pp.253-270.
23. Dai, S., Wang, X., Zhou, Y., Hower, J.C., Li, D., Chen, W., Zhu, X. and Zou, J., 2011. Chemical and mineralogical compositions of silicic, mafic, and alkali tonsteins in the late Permian coals from the Songzao Coalfield, Chongqing, Southwest China. *Chemical Geology*, *282*(1-2), pp.29-44.
24. Dai, S., Xie, P., Jia, S., Ward, C.R., Hower, J.C., Yan, X. and French, D., 2017. Enrichment of U-Re-V-Cr-Se and rare earth elements in the Late Permian coals of the Moxinpo Coalfield, Chongqing, China: Genetic implications from geochemical and mineralogical data. *Ore Geology Reviews*, *80*, pp.1-17.
25. Dai, S., Zhang, W., Ward, C.R., Seredin, V.V., Hower, J.C., Li, X., Song, W., Wang, X., Kang, H., Zheng, L. and Wang, P., 2013. Mineralogical and geochemical anomalies of late Permian coals from the Fusui Coalfield, Guangxi Province, southern China: influences of terrigenous materials and hydrothermal fluids. *International Journal of Coal Geology*, 105, pp.60-84.
26. Davison, R., and Van Rythoven, A., 2023. Critical mineral: Germanium: Montana Bureau of Mines and Geology Fact Sheet 5, p.2.
27. Dawson, G.K.W., Golding, S.D., Esterle, J.S. and Massarotto, P., 2012. Occurrence of minerals within fractures and matrix of selected Bowen and Ruhr Basin coals. *International Journal of Coal Geology*, 94, pp.150-166.
28. De Waal, S.A., Schweitzer, J.K. and Hatton, C.J., 1995. Regional lithochemical stratigraphy of the Rooiberg Group, upper Transvaal Supergroup: a proposed new subdivision. South African Journal of Geology, 98(3), pp.245-255.
29. DMP (Division of Mine Permits), 2008. Where does coal come from? Division of Mine Permits, Kentucky. http://www.minepermits.ky.gov/miningeducation/coal_formation.htm. [Accessed 10 May 2024].
30. DOE (Department of Minerals and Energy), 2001. National Inventory of Discard and Duff coal, Pretoria, South African Government, https://www.energy.gov.za/coal-discard-report. [Accessed 26 January 2024].

31. Donahue, C.J. and Rais, E.A., 2009. Proximate analysis of coal. *Journal of Chemical Education*, *86*(2), p.222.
32. Equeenuddin, S.M., Tripathy, S., Sahoo, P.K. and Ranjan, A., 2016. Geochemical characteristics and mode of occurrence of trace elements in coal at West Bokaro coalfield. *International Journal of Coal Science & Technology*, *3*, pp.399-406.
33. Eriksson, P.G. and Altermann, W., 1998. An overview of the geology of the Transvaal Supergroup dolomites (South Africa). *Environmental Geology*, 36, pp.179-188.
34. Eriksson, P.G. and Clendenin, C.W., 1990. A review of the transvaal sequence, South Africa. *Journal of African Earth Sciences* (and the Middle East), 10(1-2), pp.101-116.
35. Eriksson, P.G., Schweitzer, J.K., Bosch, P.J.A., Schereiber, U.M., Van Deventer, J.L. and Hatton, C.J., 1993. The Transvaal sequence: an overview. *Journal of African Earth Sciences* (and the Middle East), 16(1-2), pp.25-51.
36. Erkoyun, H., Kadir, S. and Huggett, J., 2019. Occurrence and genesis of tonsteins in the Miocene lignite, Tunçbilek Basin, Kütahya, western Turkey. *International Journal of Coal Geology*, 202, pp.46-68.
37. European Commission, 2008**.** Commission Recommendation of 10 April 2008 on the management of intellectual property in knowledge transfer activities and Code of Practice for universities and other public research organisations (notified under document number C (2008) 1329) (Text with EEA relevance), *Official Journal of the European Union*, L 146, 05.06.2008, pp. 19–24. ELI: http://data.europa.eu/eli/reco/2008/416/oj. [Accessed 04 November 2023].
38. European Commission, 2011. Tackling the Challenges in Commodity Markets and on Raw Materials, Communication from the Commission to the European Parliament, the Council, the European Economic and Social Committee and the Committee of the Regions. https://eur-lex.europa.eu/LexUriServ/LexUriServ.do?uri=COM:2011:002. [Accessed 04 November 2023].
39. European Commission, 2014. On the Review of the List of Critical Raw Materials for the EU and the Implementation of the Raw Materials Initiative. Communication from the commission to the European parliament, the council, the European economic and social committee and the committee of the regions. https://ec.europa.eu/growth/sectors/raw-materials/areas-specific-interest/critical-raw-materials_en. [Accessed 05 November 2023).

40. European Commission, 2017. On the 2017 List of Critical Raw Materials for the EU, 2017. Communication from the commission to the European parliament, the council, the European economic and social committee and the committee of the regions. https://ec.europa.eu/transparency/regdoc/rep/1/2017/EN/COM-2017-490-F1-EN-MAIN-PART-1.PDF. [Accessed 05 November 2023].
41. European Commission, Directorate-General for Internal Market, Industry, Entrepreneurship and SMEs, Grohol, M., Veeh, C., *Study on the critical raw materials for the EU 2023 – Final report,* Publication Office of the European Union, 2023, https://data.europa.eu/doi/10.2873/725585. [Accessed 04 October 2023].
42. European Commission, Directorate-General for Internal Market, Industry, Entrepreneurship and SMEs, *Charting a Path towards Greater Security and Sustainability – Final report*, Publication Office of the European Union, 2020, https://ec.europa.eu/docsroom/documents/42849**.** [Accessed 01 November 2023].
43. European Commission, Directorate-General for Internal Market, Industry, Entrepreneurship and SMEs, *Study on the review of the list of critical raw materials – Final report,* Publication Office of the European Union, 2017a, https://data.europa.eu/doi/10.2873/876644.[Accessed 01 November 2023].
44. European Commission, Joint Research Centre, Alves Dias, P., Pavel, C., Plazzotta, B. et al., *Raw materials demand for wind and solar PV technologies in the transition towards a decarbonised energy system,* Publication Office, 2020a, https://data.europa.eu/doi/10.2760/160859. [Accessed 04 November 2023].
45. Falcon, LM* & Falcon, R., 1987. The petrographic composition of Southern African coals in relation to friability, hardness, and abrasive indices. *Journal of the Southern African Institute of Mining and Metallurgy*, *87*(10), pp.323-336.
46. Falcon, R.* & Ham, A., 1988. The characteristics of South African coals. *Journal of the Southern African Institute of Mining and Metallurgy*, *88*(5), pp.145-161.
47. Falcon, R.M.S., 1977. Coal in South Africa-Part 1: The quality of South African coal in relation to its uses and world energy. *Minerals Science and Engineering*, *9*(4), pp.198-217.
48. Falcon, R.M.S., 1978. Coal In South AFfrica-2. The Application Of Petrography To The Characterization Of Coal. *Miner Sci Eng*, 10(1), pp.28-52.

49. Farjana, S.H., Mahmud, M.A. and Huda, N., 2021. Life cycle assessment of ilmenite and rutile production in Australia.
50. Finkelman, R.B., 1994. Modes of occurrence of potentially hazardous elements in coal: levels of confidence. *Fuel processing technology*, 39(1-3), pp.21-34.
51. Finkelman, R.B., Dai, S. and French, D., 2019. The importance of minerals in coal as the hosts of chemical elements: A review. *International Journal of Coal Geology*, 212, p.103251.
52. Finkelman, R.B., Palmer, C.A. and Wang, P., 2018. Quantification of the modes of occurrence of 42 elements in coal. *International Journal of Coal Geology*, 185, pp.138-160.
53. Fu, B., Hower, J.C., Zhang, W., Luo, G., Hu, H. and Yao, H., 2022. A review of rare earth elements and yttrium in coal ash: Content, modes of occurrences, combustion behavior, and extraction methods. *Progress in Energy and Combustion Science*, *88*, p.100954.
54. Fuller, M.P., Hamadeh, I.M., Griffiths, P.R. and Lowenhaupt, D.E., 1982. Diffuse reflectance infrared spectrometry of powdered coals. *Fuel*, 61(6), pp.529-536.
55. Georgakopoulos, A., 2003. Study of low rank Greek coals using FTIR spectroscopy. *Energy sources*, 25(10), pp.995-1005.
56. Ghosh, S., Mukhopadhyay, J. and Chakraborty, A., 2019. Clay mineral and geochemical proxies for intense climate change in the Permian Gondwana Rock Record from Eastern India. *Research*.
57. Gong, C., Wang, Z., Sun, C., Wang, Y. and Huo, L., 2024. Phosphorus removal of coal-based bottom ash: Performance evaluation and mechanism exploration. *Journal of Cleaner Production*, 445, p.141244.
58. Grigore, M. and Sakurovs, R., 2016. Inorganic matter in Victorian brown coals. *International Journal of Coal Geology*, *154*, pp.257-264.
59. Gürdal, G., 2008. Geochemistry of trace elements in Çan coal (Miocene), Çanakkale, Turkey. *International Journal of Coal Geology*, 74(1), pp.28-40.
60. Han, P., Zhao, F., Liu, D., Zhang, Q., Zhang, Q. and Ullah, S., 2024. Occurrence and Favorable Enrichment Environment of Lithium in Gaoping Coal Measures: Evidence from Mineralogy and Geochemistry. *Applied Sciences* (2076-3417), 14(16).

61. Hao, H., Zhang, M., Wang, J., Fu, Z., Balaji, P. and Jiang, S., 2022. Barium in coal and coal combustion products: Distribution, enrichment, and migration. *Energy Exploration & Exploitation*, *40*(3), pp.889-907.
62. Harrar, H., Eterigho-Ikelegbe, O., Modiga, A. and Bada, S., 2022. Mineralogy and distribution of rare earth elements in the Waterberg coalfield high ash coals. *Minerals Engineering*, *183*, p.107611.
63. Hartzer, F.J., 1995. Transvaal Supergroup inliers: geology, tectonic development and relationship with the Bushveld Complex, South Africa. *Journal of African Earth Sciences*, 21(4), pp.521-547.
64. Hassan, A.S., 2023. Modeling the linkage between coal mining and ecological footprint in South Africa: does technological innovation matter?. *Mineral Economics*, *36*(1), pp.123-138.
65. Hayashi, K.I., Fujisawa, H., Holland, H.D. and Ohmoto, H., 1997. Geochemistry of~ 1.9 Ga sedimentary rocks from northeastern Labrador, Canada. *Geochimica et cosmochimica acta*, 61(19), pp.4115-4137.
66. Hower, J.C., Berti, D., Hochella Jr, M.F. and Mardon, S.M., 2018. Rare earth minerals in a "no tonstein" section of the Dean (Fire Clay) coal, Knox County, Kentucky. *International Journal of Coal Geology*, *193*, pp.73-86.
67. Hrstka, T., Gottlieb, P., Skala, R., Breiter, K. and Motl, D., 2018. Automated mineralogy and petrology-applications of TESCAN Integrated Mineral Analyzer (TIMA). *Journal of Geosciences*, 63(1), pp.47-63.
68. Huggins, F.E. and Huffman, G.P., 1996. Modes of occurrence of trace elements in coal from XAFS spectroscopy. International Journal of Coal Geology, 32(1-4), pp.31-53.
69. IEA, 2020. Coal Explained: how Much Coal is Left? https://www.eia.gov/energyexplained/coal/how-much-coal-is-left.php. [Accessed 30 September 2023].
70. IEA, 2025. *Coal*. International Energy Agency. https://www.iea.org/energy-system/fossil-fuels/coal. [Accessed 05 October 2025].
71. ISO (International Organization for Standardization), 2008. Hard Coal – Determination of Total Moisture, ISO 589:2008.

72. ISO (International Organization for Standardization), 2010. Hard Coal and Coke – Determination of Volatile Matter, ISO 562:2010.
73. ISO (International Organization for Standardization), 2010a. Solid Mineral Fuels - Determination of Ash, ISO 171:2010a.
74. Jiu, B., Huang, W., Spiro, B., Hao, R., Mu, N., Wen, L. and Hao, H., 2023. Distribution of Li, Ga, Nb, and REEs in coal as determined by LA-ICP-MS imaging: A case study from Jungar coalfield, Ordos Basin, China. *International Journal of Coal Geology*, 267, p.104184.
75. Jones & Wagener, 2017, Rietspruit mine -mine closure operations, Old tailings dam – Geotechnical investigation and probability of failure assessment. Report No.: JW185/16/F070 -Rev 2.
76. Kang, Y., Zhu, R., Liu, K., Zhang, J. and Zhang, S., 2024. Detrital and authigenic clay minerals in shales: A review on their identification and applications. *Heliyon*, *10*(20).
77. Karayigit, A.I., Gayer, R.A., Querol, X. and Onacak, T., 2000. Contents of major and trace elements in feed coals from Turkish coal-fired power plants. *International Journal of Coal Geology*, *44*(2), pp.169-184.
78. Ketris, M.Á. and Yudovich, Y.E., 2009. Estimations of Clarkes for Carbonaceous biolithes: World averages for trace element contents in black shales and coals. *International journal of coal geology*, *78*(2), pp.135-148.
79. Kolker, A., Scott, C., Hower, J.C., Vazquez, J.A., Lopano, C.L. and Dai, S., 2017. Distribution of rare earth elements in coal combustion fly ash, determined by SHRIMP-RG ion microprobe. *International journal of coal geology*, *184*, pp.1-10.
80. Kolker, A., Scott, C., Lefticariu, L., Mastalerz, M., Drobniak, A. and Scott, A., 2021. Trace element partitioning during coal preparation: Insights from US Illinois Basin coals. *International Journal of Coal Geology*, *243*, p.103781.
81. Kolker, A., Senior, C., van Alphen, C., Koenig, A. and Geboy, N., 2017a. Mercury and trace element distribution in density separates of a South African Highveld (# 4) coal: Implications for mercury reduction and preparation of export coal. *International Journal of Coal Geology*, *170*, pp.7-13.
82. Li, B., Zhuang, X., Li, J., Querol, X., Font, O. and Moreno, N., 2017. Enrichment and distribution of elements in the Late Permian coals from the Zhina Coalfield, Guizhou Province, Southwest China. *International Journal of Coal Geology*, 171, pp.111-129.

83. Li, J., Zhuang, X., Yuan, W., Liu, B., Querol, X., Font, O., Moreno, N., Li, J., Gang, T. and Liang, G., 2016. Mineral composition and geochemical characteristics of the Li-Ga-rich coals in the Buertaohai-Tianjiashipan mining district, Jungar Coalfield, Inner Mongolia. *International Journal of Coal Geology*, *167*, pp.157-175.
84. Li, X., Dai, S., Nechaev, V.P., Graham, I.T., French, D., Wang, X., Zhao, L. and Zhao, J., 2020. Mineral matter in the Late Permian C1 coal from Yunnan Province, China, with emphasis on its origins and modes of occurrence. *Minerals*, 11(1), p.19.
85. Lin, R., Soong, Y., and Granite, E.J., 2018. Evaluation of trace elements in US coals using the USGS COALQUAL database version 3.0. Part I: Rare earth elements and yttrium (REY). *International Journal of Coal Geology*, *192*, pp.1-13.
86. Lin, R., Soong, Y., and Granite, E.J., 2018a. Evaluation of trace elements in US coals using the USGS COALQUAL database version 3.0. Part II: Non-REY critical elements. *International Journal of Coal Geology*, *192*, pp.39-50.
87. Lipiarski, I., Muszyński, M. and Wyszomirski, P., 2004. Alunites in the red beds of the "Marcel" coal mine, Upper Silesian Coal Basin, Poland. Mineralogia Polonica.
88. Liu, J., Spiro, B.F., Dai, S., French, D., Graham, I.T., Wang, X., Zhao, L., Zhao, J. and Zeng, R., 2021. Strontium isotopes in high-and low-Ge coals from the Shengli Coalfield, Inner Mongolia, northern China: New indicators for Ge source. *International Journal of Coal Geology*, *233*, p.103642.
89. Liu, J., Ward, C.R., Graham, I.T., French, D., Dai, S. and Song, X., 2018. Modes of occurrence of non-mineral inorganic elements in lignites from the Mile Basin, Yunnan Province, China. *Fuel*, *222*, pp.146-155.
90. Ma, M., Wang, W. and Zhang, K., 2022. Occurrence Characteristics of Fine-Grained Pyrite in Coal and Its Scaling Effect on Flotation Desulfurization. *ACS omega*, 7(46), pp.42467-42481.
91. Majumder, A.K., Jain, R., Banerjee, P. and Barnwal, J.P., 2008. Development of a new proximate analysis-based correlation to predict calorific value of coal. *Fuel*, *87*(13-14), pp.3077-3081.
92. Mapeo, R.B.M., Wendorff, M., Ramokate, L.V., Armstrong, R.A., Mphinyane, T. and Koobokile, M., 2019. Zircon geochronology of basement granitoid gneisses and sedimentary rocks of the Tsodilo Hills Group in the Pan-African Damara Belt, western Botswana: age

constraints, provenance, and tectonic significance. *Journal of African Earth Sciences*, *159*, p.103576.

93. Marchant, P, B., and Lawrence R.W., 1991. Acid Rock Drainage Prediction Manaul (Issue October).
94. Martin, K.A. and Chao, S.S., 1988. Structural group analysis of argonne premium coals by FTIR spectroscopy. Prepr. Pap., Am. Chem. Soc., Div. Fuel Chem.;(United States), 33(CONF-8809161-).
95. Mashishi, R.M., Okonkwo, O.J. and Malehase, T., 2023. Selected trace element concentrations in run-of-mine coal, discard, and coal product, and environmental implications. *Journal of the Southern African Institute of Mining and Metallurgy*, *123*(12), pp.573-577.
96. Mastalerz, M., Bustin, R.M. and Lamberson, M.N., 1993. Variation in chemistry of vitrinite and semifusinite as a function of associated inertinite content. *International Journal of Coal geology*, *22*(2), pp.149-162.
97. Mastalerz, M., Drobniak, A., Eble, C., Ames, P. and McLaughlin, P., 2020. Rare earth elements and yttrium in Pennsylvanian coals and shales in the eastern part of the Illinois Basin. *International Journal of Coal Geology*, *231*, p.103620.
98. Matin, S.S. and Chelgani, S.C., 2016. Estimation of coal gross calorific value based on various analyses by random forest method. *Fuel*, *177*, pp.274-278.
99. Matjie, R.H., Li, Z., Ward, C.R., Bunt, J.R. and Strydom, C.A., 2016. Determination of mineral matter and elemental composition of individual macerals in coals from Highveld mines. *Journal of the Southern African Institute of Mining and Metallurgy*, *116*(2), pp.169-180.
100. Maya, M., Musekiwa, C., Mthembi, P. and Crowley, M., 2015. Remote sensing and geochemistry techniques for the assessment of coal mining pollution, Emalahleni (Witbank), Mpumalanga. *South African Journal of Geomatics*, 4(2), pp.174-188.
101. McCarthy, T. and Rubidge, B., 2013. The story of earth & life: a southern African perspective on a 4.6-billion-year journey. Penguin Random House South Africa.
102. Misz-Kennan, M. and Fabiańska, M.J., 2011. Application of organic petrology and geochemistry to coal waste studies. *International Journal of Coal Geology*, *88*(1), pp.1-23.

103. Modiba, D.G. and Wagner, N.J., 2024. An assessment of Rare Earth Elements in borehole cores from the Ermelo, Witbank and Waterberg Coalfields, South Africa: Focus on mode of occurrence. *Journal of the Southern African Institute of Mining and Metallurgy*, 124(10), pp.559-566.
104. Moore, J.M., Tsikos, H. and Polteau, S., 2001. Deconstructing the Transvaal Supergroup, south Africa: implications for Palaeoproterozoic palaeoclimate models. *Journal of African Earth Sciences*, 33(3-4), pp.437-444.
105. Moroeng, O.M., Murathi, B. and Wagner, N.J., 2024. Enrichment of rare earth elements in epigenetic dolomite occurring in contact metamorphosed Witbank coals (South Africa). *International Journal of Coal Geology*, *282*, 104405.
106. Netshitungulwana, K.R.T., Gauert, C., Vermeulen, D., Yibas, B., Shai, M. and Lusunzi, R., 2022, November. Geochemical characterisation of the Witbank coalfield geological strata and assessment of potential metal impact on the receiving environment. In Proceedings of the International Mine Water Association 2022 Conference Reconnect, Christchurch, New Zealand (pp. 6-10).
107. Nguyen, X., Li, J., Zhuang, X., Li, B., Querol, X., Moreno, N. and Cordoba, P., 2022. Significant enrichment of Rb and Cs in the Late Triassic coals from the Coc Sau surface mine, Cam Pha Coalfield, Quang Ninh Province, Vietnam. *Ore Geology Reviews*, 142, p.104700.
108. Nkwamza, X. and Malumbazo, N., 2025. The modes of occurrence, distribution and enrichment of critical raw materials (Ga, Sr, Zr and Ba) within coal discards of the Witbank Coalfield, South Africa. *International Journal of Coal Geology*, 104870.
109. Oikonomopoulos, I.K., Perraki, M., Tougiannidis, N., Perraki, T., Frey, M.J., Antoniadis, P. and Ricken, W., 2013. A comparative study on structural differences of xylite and matrix lignite lithotypes by means of FT-IR, XRD, SEM and TGA analyses: An example from the Neogene Greek lignite deposits. *International Journal of Coal Geology*, 115, pp.1-12.
110. Orem, W.H. and Finkelman, R.B., 2005. US Geological Survey, Reston, VA, USA. *Sediments, Diagenesis, and Sedimentary Rocks: Treatise on Geochemistry, Volume 7*, *7*, p.191.
111. Ottaway, M., 1982. Use of thermogravimetry for proximate analysis of coals and cokes. *Fuel*, *61*(8), pp.713-716.

112. Öztaş, N.A. and Yürüm, Y., 2000. Pyrolysis of Turkish Zonguldak bituminous coal. Part 1. Effect of mineral matter. *Fuel*, 79(10), pp.1221-1227.
113. Painter, P.C., Snyder, R.W., Starsinic, M., Coleman, M.M., Kuehn, D.W. and Davis, A., 1981. Concerning the application of FT-IR to the study of coal: a critical assessment of band assignments and the application of spectral analysis programs. *Applied Spectroscopy*, 35(5), pp.475-485.
114. Pan, J., Zhou, C., Liu, C., Tang, M., Cao, S., Hu, T., Ji, W., Luo, Y., Wen, M. and Zhang, N., 2018. Modes of occurrence of rare earth elements in coal fly ash: A case study. *Energy & fuels*, *32*(9), pp.9738-9743.
115. Permana, A.K., Ward, C.R., Li, Z. and Gurba, L.W., 2013. Distribution and origin of minerals in high-rank coals of the South Walker Creek area, Bowen Basin, Australia. *International Journal of Coal Geology*, 116, pp.185-207.
116. Pierce, W.T. and Ferreira, B.A., 2022. Statistics of utility-scale power generation in South Africa in 2021.
117. Pinetown K.L., 2007. Quantitative evaluation of minerals in coal deposits in the Witbank and Highveld Coalfiels and the potential impact on acid mine drainage (Masters' thesis, University of the Free State).
118. Pinetown, K.L., Ward, C.R. and Van der Westhuizen, W.A., 2007. Quantitative evaluation of minerals in coal deposits in the Witbank and Highveld Coalfields, and the potential impact on acid mine drainage. *International Journal of Coal Geology*, 70(1-3), pp.166-183.
119. Pone, J.D.N., Hein, K.A., Stracher, G.B., Annegarn, H.J., Finkleman, R.B., Blake, D.R., McCormack, J.K. and Schroeder, P., 2007. The spontaneous combustion of coal and its by-products in the Witbank and Sasolburg coalfields of South Africa. *International Journal of Coal Geology*, *72*(2), pp.124-140.
120. Qiao, J., Du, F., Wang, S., Tan, F. and Zhang, Y., 2020. Enrichment and Occurrence of Mn in 5–2 Coal from Qinglongsi Coal Mine, Northern Ordos Basin, China. *ACS omega*, *5*(32), pp.20202-20214.
121. Querol, X., Klika, Z., Weiss, Z., Finkelman, R.B., Alastuey, A., Juan, R., López-Soler, A., Plana, F., Kolker, A. and Chenery, S.R.N., 2001. Determination of element affinities by density fractionation of bulk coal samples. *Fuel*, 80(1), pp.83-96.

122. Reimann, C. and De Caritat, P., 2012. Chemical elements in the environment: factsheets for the geochemist and environmental scientist. Springer Science & Business Media.
123. Rerani, V.P., Mabowa, H.M. and Wagner, N.J., 2024. Characterization of rare earth element-bearing mineral phases present in South African coal ash using Mineral Liberation analysis. *Fuel*, *368*, p.131661.
124. Riley, K.W., French, D.H., Farrell, O.P., Wood, R.A. and Huggins, F.E., 2012. Modes of occurrence of trace and minor elements in some Australian coals. *International Journal of Coal Geology*, 94, pp.214-224.
125. SANS. 2006. ISO 17246 :2005, SANS 17246 :2006, Coal- Proximate analysis. Pretoria.
126. SANS. 2006. ISO 17247 :2005, SANS 17247 :2006, Cola – Ultimate analysis. Pretoria.
127. Seredin, V.V. and Dai, S., 2012. Coal deposits as potential alternative sources for lanthanides and yttrium. *International Journal of Coal Geology*, *94*, pp.67-93.
128. Shao, P., Hou, H., Wang, W., Qin, K. and Wang, W., 2022. Distribution and enrichment of Al-Li-Ga-REEs in the High-Alumina coal of the Datong Coalfield, Shanxi Province, China. *Ore Geology Reviews*, *140*, p.104597.
129. Shao, P., Wang, W., Chen, L., Duan, P., Qian, F., Ma, M., Xiong, W. and Yu, S., 2018. Distribution, occurrence, and enrichment of gallium in the Middle Jurassic coals of the Muli Coalfield, Qinghai, China. *Journal of Geochemical Exploration*, 185, pp.116-129.
130. Sia, S.G. and Abdullah, W.H., 2012. Enrichment of arsenic, lead, and antimony in Balingian coal from Sarawak, Malaysia: Modes of occurrence, origin, and partitioning behaviour during coal combustion. *International journal of coal geology*, 101, pp.1-15.
131. Soeder, D.J. and Borglum, S.J., 2019. The fossil fuel revolution: Shale gas and tight oil. *Elsevier*.
132. Spears, D.A, Booth, C.A., 1999. The determination of trace elements in British coals using energy dispersive polarizerd XRF and element disitributions by statistical analysis. In: Proceedings of the sixteenth annual international Pittsburgh coal conference and workshop. Pittsburgh, PA, USA, 11-15 Oct 1999. Pittsburgh, PA, USA, Univrsity of Pittsburgh, p. 1-18. Poster Session P2. Paper Ag/5-66.pdf, CD-ROM.
133. Speight, J.G., 2016. The Chemistry and technology of coal, Third edition, CRC Press, Boca Raton.

134. Spiro, B.F., Liu, J., Dai, S., Zeng, R., Large, D. and French, D., 2019. Marine derived 87Sr/86Sr in coal, a new key to geochronology and palaeoenvironment: Elucidation of the India-Eurasia and China-Indochina collisions in Yunnan, China. *International Journal of Coal Geology*, 215, 103304.
135. Steyn, M. and Minnitt, R.C.A., 2010. Thermal coal products in South Africa. *Journal of the Southern African Institute of Mining and Metallurgy*, *110*(10), pp.593-599.
136. Sun, B., Liu, Y., Tajcmanova, L., Liu, C. and Wu, J., 2022. In-situ analysis of the lithium occurrence in the No. 11 coal from the Antaibao mining district, Ningwu Coalfield, northern China. *Ore Geology Reviews*, *144*, 104825.
137. Sun, Y.Z., Zhao, C.L., Li, Y.H. and Wang, J.X., 2014. Minimum mining grade of the selected trace elements in Chinese coal. *Journal of China Coal Society*, 39(4), pp.744-748.
138. Swaine, D.J., 1990, Trace Elements in Coal. Butterworths, London (278).
139. Thompson, R.L., Bank, T., Montross, S., Roth, E., Howard, B., Verba, C. and Granite, E., 2018. Analysis of rare earth elements in coal fly ash using laser ablation inductively coupled plasma mass spectrometry and scanning electron microscopy. *Spectrochimica Acta Part B: Atomic Spectroscopy*, *143*, pp.1-11.
140. Thwala, K., 2020. Geochemical characterization of the Witbank coalfields, South Africa (Doctoral dissertation, University of the Free State).
141. Tian, H.Z., Lu, L., Hao, J.M., Gao, J.J., Cheng, K., Liu, K.Y., Qiu, P.P. and Zhu, C.Y., 2013. A review of key hazardous trace elements in Chinese coals: abundance, occurrence, behavior during coal combustion and their environmental impacts. *Energy & fuels*, 27(2), pp.601-614.
142. U.S Department of Energy, 2010. Critical material strategy.
143. U.S Department of Energy, 2019. Critical material strategy.
144. U.S DOD (United states Department of Defense), 2019. Strategic and Critical Materials 2019 Report on Stockpile Requirements, https://www.dla.mil/Portals/104/Documents/J3Logistics/StrategicMaterials/Reports/2019%20NM&SP%20Report.pdf [Accessed 20 February 2024]
145. U.S Geological Survey, 2022. Final List of Critical Minerals, Federal Register, 87(37), pp. 10381-10382.
146. U.S Geological Survey, 2024. USGS critical minerals review, *Mining Engineering*, 76(5).

147. Van Alphen, C., (2007), Automated mineralogical analysis of coal and ash products-challenges and requirements, *Minerals Engineering*, vol. 20 no. 5, pp. 496-505.
148. Vassilev, S.V. and Vassileva, C.G., 1996. Occurrence, abundance and origin of minerals in coals and coal ashes. *Fuel processing technology*, 48(2), pp.85-106.
149. Vassilev, S.V., Kitano, K. and Vassileva, C.G., 1997. Relations between ash yield and chemical and mineral composition of coals. *Fuel*, 76(1), pp.3-8.
150. Vo, T.L., Nash, W., Del Galdo, M., Rezania, M., Crane, R., Nezhad, M, M., & Ferrara, L., 2022, Coal mining wastes valorization as raw geomaterials in construction: A review with new perspectives, *Journal of Cleaner Production*, 336, pp. 1-19.
151. Wagner, M., Bielowicz, B. and Misiak, J., 2019. Analysis of the occurrence of critical elements and raw materials in Polish lignite deposits with particular emphasis on coal ashes. In IOP Conference Series: *Earth and Environmental Science* (Vol. 214, No. 1, 012026). IOP Publishing.
152. Wang, P.P., 2017. Enrichment and Differentiation Mechanism of Minerals and Trace Elements in the Late Permian Coals from Eastern Yunnan and Western Guizhou Province [D]. Beijing, China University of mining and Technology (Beijing).
153. Wang, Q., Yan, Q., Zhang, Y. and Zhou, F., 2022. Enrichment Mechanism of Lithium in Late Permian Coals in the Bijie Area, Guizhou, China. *ACS omega*, 7(19), pp.16361-16370.
154. Wang, W., Qin, Y., Liu, X., Zhao, J., Wang, J., Wu, G. and Liu, J., 2011. Distribution, occurrence and enrichment causes of gallium in coals from the Jungar Coalfield, Inner Mongolia. *Science China Earth Sciences*, 54, pp.1053-1068.
155. Wang, W., Sang, S., Bian, Z., Duan, P., Qian, F., Lei, S. and Qin, Y., 2016. Fine-grained pyrite in some Chinese coals. *Energy Exploration & Exploitation*, 34(4), pp.543-560.
156. Wang, X., Dai, S., Chou, C.L., Zhang, M., Wang, J., Song, X., Wang, W., Jiang, Y., Zhou, Y. and Ren, D., 2012. Mineralogy and geochemistry of Late Permian coals from the Taoshuping Mine, Yunnan Province, China: Evidences for the sources of minerals. *International Journal of Coal Geology*, 96, pp.49-59.
157. Wang, Y.Y., Guo, W.Y. and Zhang, G., 1979. Application of some geochemical indicators in determining of sedimentary environment of the Funing Group (Paleogene), Jin-Hu Depression, Kiangsu Province. *Journal of Tongji University*, 7(2), pp.51-60.

158. Ward, C.R., 2002. Analysis and significance of mineral matter in coal seams. *International Journal of Coal Geology*, 50(1-4), pp.135-168.
159. Ward, C.R., 2016. Analysis, origin and significance of mineral matter in coal: An updated review. International Journal of Coal Geology, 165, pp.1-27.
160. Weeber, SL., Cairncross, B. & Falcon, R., 2000. Mineralogical, petrographic and geological controls on coal ash fusion temperature from New Clydesdale Colliery, Witbank Coalfield, South Africa. *Journal of the Southern African Institute of Mining and Metallurgy*, 100(3), pp.181-190.
161. Wei, Q. and Zhao, L., 2024. Modes of occurrence of beryllium in the Ge-rich coal deposit, Lincang, SW China: Theoretical insight into organic association and distribution. *Journal of Hazardous Materials*, 480, 135913.
162. Word Bank Group (WBG), 2020. Minerals for Climate Action: The Mineral Intensity of Clean Energy Transition.
163. Xue, H., Dong, X., Fan, Y., Ma, X. and Yao, S., 2023. Study of structural transformation and chemical reactivity of kaolinite-based high ash slime during calcination. *Minerals*, 13(4), 466.
164. Yuan, Y., Tang, S. and Zhang, S., 2019. Concentrations and modes of occurrence of some potentially valuable and toxic elements in the No. 5 coal from the Yanzishan Mine, Datong Coalfield, Shanxi Province, China. *Energy Exploration & Exploitation*, *37*(6), pp.1694-1720.
165. Zhao, C., Liu, B., Ma, J., Liu, S. and Blokhin, M.G., 2017. Occurrence of rubidium and cesium in Iqe coal, Qinghai-Tibet Plateau: Evidence from sequential chemical extraction experiment. *Energy Exploration & Exploitation*, 35(3), pp.376-387.
166. Zhao, C.L., Sun, Y.Z., Xiao, L., Qin, S.J., Wang, J.X. and Duan, D.J., 2014. The occurrence of barium in a Jurassic coal in the Huangling 2 Mine, Ordos Basin, northern China. *Fuel*, 128, pp.428-432.
167. Zhao, L., Dai, S., Finkelman, R.B., French, D., Graham, I.T., Yang, Y., Li, J. and Yang, P., 2020. Leaching behavior of trace elements from fly ashes of five Chinese coal power plants. *International Journal of Coal Geology*, *219*, 103381.
168. Zhao, L., Dai, S., Nechaev, V.P., Nechaeva, E.V., Graham, I.T. and French, D., 2019. Enrichment origin of critical elements (Li and rare earth elements) and a Mo-U-Se-Re

assemblage in Pennsylvanian anthracite from the Jincheng Coalfield, southeastern Qinshui Basin, northern China. *Ore Geology Reviews*, *115*, 103184.

169. Zhao, L., Dai, S., Nechaev, V.P., Nechaeva, E.V., Graham, I.T., French, D. and Sun, J., 2019a. Enrichment of critical elements (Nb-Ta-Zr-Hf-REE) within coal and host rocks from the Datanhao mine, Daqingshan Coalfield, northern China. *Ore Geology Reviews*, *111*, 102951.
170. Zhao, L., Ward, C.R., French, D. and Graham, I.T., 2012. Mineralogy of the volcanic-influenced Great Northern coal seam in the Sydney Basin, Australia. *International Journal of Coal Geology*, 94, pp.94-110.
171. Zhao, L., Zhu, Q., Jia, S., Zou, J., Nechaev, V.P. and Dai, S., 2017. Origin of minerals and critical metals in an argillized tuff from the Huayingshan Coalfield, southwestern China. *Minerals*, 7(6), p.92.
172. Zheng, X., Wang, Z., Wang, L., Xu, Y. and Liu, J., 2017. Mineralogical and geochemical compositions of the lopingian coals and carbonaceous rocks in the Shugentian coalfield, Yunnan, China: With emphasis on Fe-bearing minerals in a continental-marine transitional environment. *Minerals*, 7(9), p.170.
173. Zhu, H.X., Chen, H.Y., Zhang, W., Ning, S.Z. and Han, L., 2016. Metal mineral types and distribution characteristics in coal in Northern China. Journal of China Coal Society, (2).
174. Zou, J., Liu, D., Tian, H., Li, T., Liu, F. and Tan, L., 2014. Anomaly and geochemistry of rare earth elements and yttrium in the late Permian coal from the Moxinpo mine, Chongqing, southwestern China. *International Journal of Coal Science & Technology*, *1*, pp.23-30.

Appendix A: Data Visualization

Table A 1: Physiochemical properties of CD1.

0-1 m	**CD1_01**	**CD1_02**	**CD1_03**	**CD1_04**	**CD1_05**	**CD1_06**	**CD1_07**	**CD1_08**	**CD1_09**	**CD1_10**	**CD1_11**	**CD1_12**	**CD1_13**	**CD1_14**
M	5.27	6.03	7.42	7.13	5.53	4.6	5.39	6.5	3.85	5.31	5.92	6.22	4.82	4.7
VM	22.93	22.57	23.12	22.59	21.94	16.86	22.37	22.57	23.29	22.71	21.96	22.45	22.38	21.16
A	37.96	34.58	32.72	29.15	28.58	55.08	30.27	30.1	32.9	32.15	32.07	33.76	35.46	37.87
FC	33.84	36.82	36.74	41.13	43.95	23.46	41.97	40.84	39.96	39.82	40.05	37.57	37.33	36.26
CV	15.34	16.96	16.94	17.88	19.99	0.12	19.83	18.58	18.17	18.46	18.04	16.50	17.74	17.88
1-2 m	**CD1_01**	**CD1_02**	**CD1_03**	**CD1_04**	**CD1_05**	**CD1_06**	**CD1_07**	**CD1_08**	**CD1_09**	**CD1_10**	**CD1_11**	**CD1_12**	**CD1_13**	**CD1_14**
M	40,91	39,76	46,24	52,30	48,78	53,16	47,32	44,22	41,29	44,87	45,09	43,87	44,82	45,86
VM	24,02	24,33	22,70	14,46	25,33	25,63	22,49	25,35	21,97	22,74	23,08	23,22	22,91	22,40
A	9,25	9,43	9,09	9,29	8,61	9,05	9,00	9,04	9,21	9,26	9,10	9,20	9,09	9,10
FC	14,36	14,82	14,11	14,52	13,13	6,93	13,91	13,98	14,24	14,47	14,08	14,24	14,01	14,04
CV	1,84	2,16	1,50	1,84	0,77	1,42	1,35	1,39	1,97	1,76	1,54	1,69	1,43	1,49
2-3 m	**CD1_01**	**CD1_02**	**CD1_03**	**CD1_04**	**CD1_05**	**CD1_06**	**CD1_07**	**CD1_08**	**CD1_09**	**CD1_10**	**CD1_11**	**CD1_12**	**CD1_13**	**CD1_14**
M	45,13	40,15	50,47	50,86	51,93	54,07	46,19	44,81	43,25	47,80	44,02	44,05	44,33	48,08
VM	19,91	18,35	14,64	12,33	19,65	25,69	22,49	24,92	22,00	23,08	23,10	23,74	23,55	19,92
A	9,13	9,43	9,09	9,63	8,84	8,95	9,05	9,00	9,14	8,86	9,18	9,11	9,10	9,09
FC	14,07	14,72	14,06	15,27	13,59	6,81	14,02	13,92	14,14	13,63	14,31	14,12	14,05	14,09
CV	1,68	2,54	1,74	2,43	1,09	1,27	1,48	1,34	1,76	1,11	1,69	1,57	1,53	1,56
3-4 m	**CD1_01**	**CD1_02**	**CD1_03**	**CD1_04**	**CD1_05**	**CD1_06**	**CD1_07**	**CD1_08**	**CD1_09**	**CD1_10**	**CD1_11**	**CD1_12**	**CD1_13**	**CD1_14**
M	46,70	42,45	48,96	45,78	51,56	55,09	47,69	45,24	59,66	45,57	43,05	41,78	42,59	47,11
VM	18,07	17,77	17,74	12,03	18,24	23,94	17,14	25,13	10,14	21,20	25,50	23,37	23,12	18,65
A	9,25	9,48	9,18	9,89	8,96	9,00	9,23	8,96	8,66	9,23	9,07	9,37	9,12	9,33
FC	14,40	14,88	14,27	15,83	13,81	6,89	14,34	13,82	13,21	14,40	14,04	14,70	14,10	14,62
CV	1,93	2,50	1,77	3,04	1,32	1,40	1,86	1,28	0,95	1,79	1,48	2,02	1,71	1,95
4-5 m	**CD1_01**	**CD1_02**	**CD1_03**	**CD1_04**	**CD1_05**	**CD1_06**	**CD1_07**	**CD1_08**	**CD1_09**	**CD1_10**	**CD1_11**	**CD1_12**	**CD1_13**	**CD1_14**
M	46,72	45,69	46,14	56,28	54,34	55,17	48,17	48,24	92,70	45,80	46,36	43,80	47,15	50,20
VM	18,34	16,47	15,55	13,20	16,38	24,98	21,87	21,69	1,58	20,42	21,01	23,56	21,77	17,12
A	9,35	9,33	9,34	8,71	8,93	8,94	8,91	8,98	nd	9,25	9,08	8,97	9,03	8,94
FC	14,54	14,49	14,50	13,31	13,78	6,75	13,74	13,85	nd	14,41	14,07	13,82	13,99	13,74
CV	1,96	2,12	2,24	1,04	1,23	1,25	1,33	1,32	nd	1,82	1,58	1,47	1,44	1,46

Table A 2: Physiochemical properties of CD2.

Sample_ID	M	VM	A	FC	CV
CD2_01	40,08	37,23	4,38	4,63	3,50
CD2_02	41,13	37,41	4,49	4,96	1,39
CD2_03	45,39	36,29	2,40	4,68	1,27
CD2_04	42,89	37,78	2,45	4,86	1,38
CD2_05	43,57	37,08	2,40	5,67	1,25
CD2_06	41,05	33,33	2,36	5,56	3,77
CD2_07	39,18	36,81	2,47	4,89	1,40
CD2_08	44,23	35,91	2,49	5,02	1,46
CD2_09	41,32	37,56	2,47	4,86	1,33
CD2_10	44,28	33,16	2,56	5,18	1,52
CD2_11	63,64	20,63	1,55	1,50	1,15
CD2_12	44,55	38,44	3,36	3,35	1,15
CD2_13	45,82	30,95	2,48	8,30	1,35
CD2_14	44,78	37,44	2,47	4,72	1,35
CD2_15	48,35	36,62	2,28	2,26	1,13
CD2_16	41,85	35,57	2,48	8,68	1,43
CD2_17	44,90	33,32	2,39	8,27	1,24
CD2_18	50,06	34,35	3,27	2,16	1,09
CD2_19	45,03	40,16	2,44	2,60	1,23
CD2_20	42,88	38,81	2,36	6,02	1,17
CD2_21	41,13	28,52	2,40	7,46	2,23
CD2_22	47,18	35,37	2,57	3,07	1,51
CD2_23	56,58	22,06	2,87	4,03	2,04
CD2_24	60,06	17,00	2,98	3,21	2,44

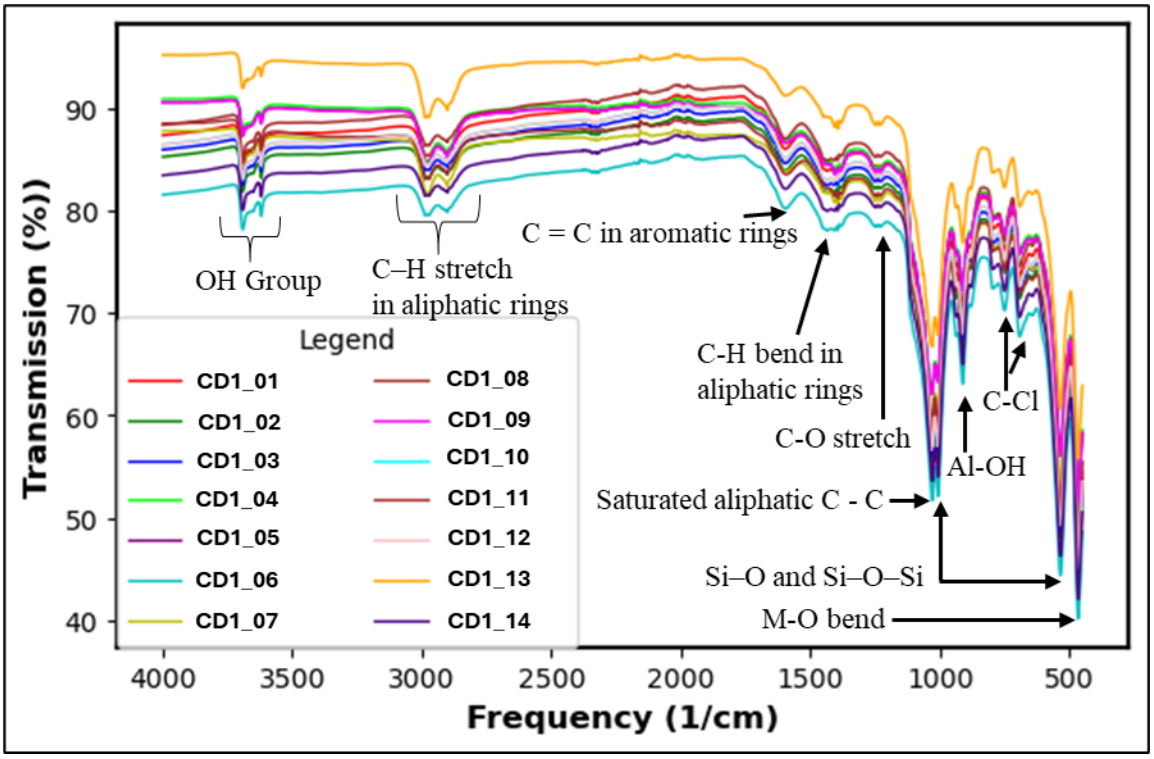

Figure A 1: FTIR spectra for samples at the 2-3 m interval.

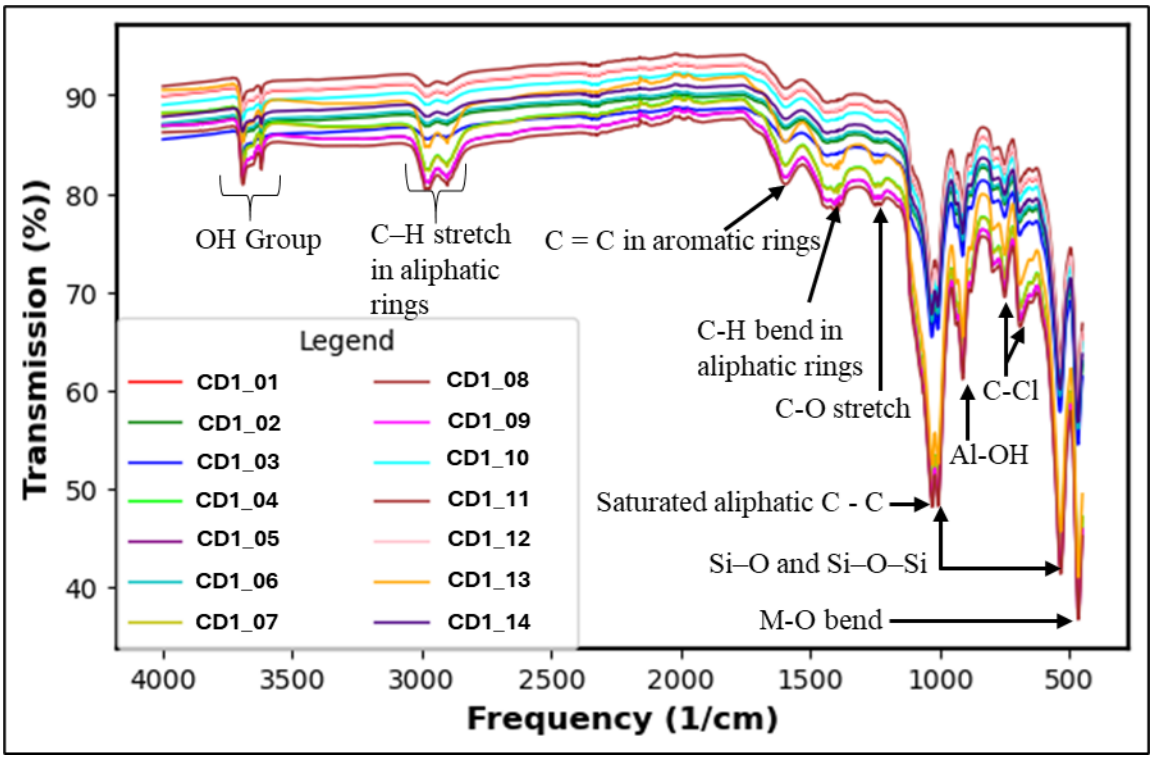

Figure A 2: FTIR spectra for samples at the 3-4 m interval.

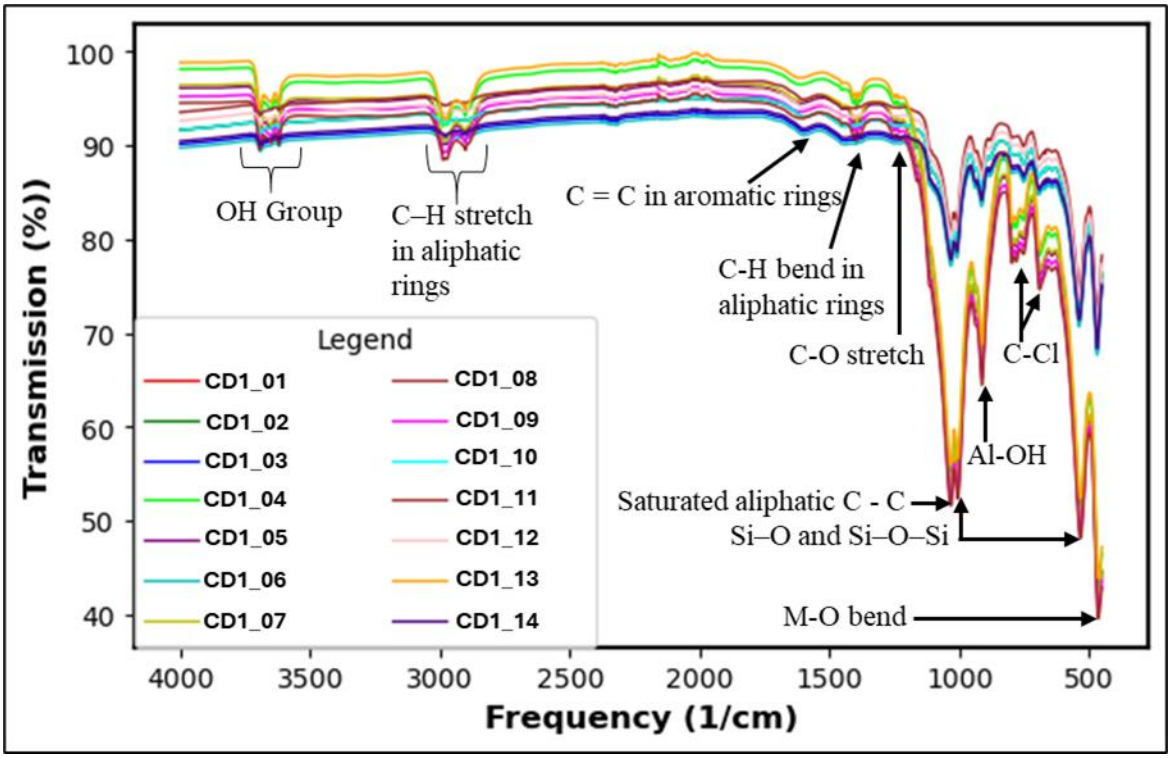

Figure A 3: FTIR spectra for samples at the 4-5 m interval.